INFLUENCE OF Si, Sb AND Sr ADDITIONS ON THE MICROSTRUCTURE, MECHANICAL PROPERTIES AND CORROSION BEHAVIOR OF AZ91 MAGNESIUM ALLOY

Thesis submitted to
Cochin University of Science and Technology
in partial fulfillment of the requirements
for the Degree of

DOCTOR OF PHILOSOPHY
in the **Faculty of Technology**

By
A. SRINIVASAN

MATERIALS AND MINERALS DIVISION
NATIONAL INSTITUTE FOR INTERDISCIPLINARY SCIENCE AND TECHNOLOGY (CSIR)
THIRUVANANTHAPURAM - 695 019
INDIA

April 2008

राष्ट्रीय अंतर्विषयी विज्ञान तथा प्रौद्योगिकी संस्थान
(वैज्ञानिक एंव प्रौद्योगिकी अनुसंधान परिषद्)
(पहले क्षेत्रीय अनुसंधान प्रयोगशाला)
NATIONAL INSTITUTE FOR INTERDISCIPLINARY SCIENCE AND TECHNOLOGY
(Council of Scientific & Industrial Research)
(formerly Regional Research laboratory)
इन्डस्ट्रियल इस्टेट डाक घर, तिरुवनन्तपुरम 695 019, भारत
Industrial Estate P.O., Thiruvananthapuram 695 019, India

CERTIFICATE

*This is to certify that the thesis entitled "**Influence of Si, Sb and Sr Additions on the Microstructure, Mechanical Properties and Corrosion Behavior of AZ91 Magnesium Alloy**" that is being submitted by **Mr. A. Srinivasan** for the award of the degree of **Doctor of Philosophy in Technology**, in the Faculty of Technology of the **Cochin University of Science and Technology, Cochin,** is a record of bonafide research work carried out by him under my guidance and supervision. The results embodied in this thesis have not been submitted to any other University or Institute for the award of any other degree or diploma.*

Dr. U. T. S. Pillai
Scientist
Materials and Minerals Division
National Institute for Interdisciplinary
Science and Technology (CSIR)
Trivandrum

DECLARATION

I hereby declare that the thesis entitled *"Influence of Si, Sb and Sr Additions on the Microstructure, Mechanical Properties and Corrosion Behavior of AZ91 Magnesium Alloy"* embodies the results of bonafide research work done by me for the degree of **Doctor of Philosophy** in Faculty of Technology of the ***Cochin University of Science and Technology, Cochin*** under the guidance of **Dr. U.T.S. Pillai**, National Institute for Interdisciplinary Science and Technology (CSIR), Trivandrum. I further declare that this thesis or part thereof has not previously been formed the basis for the award of any degree or diploma.

(A. SRINIVASAN)

ACKNOWLEDGEMENTS

It is indeed very much overwhelming feeling when a sailor in a deep sea senses the end of a tiring journey. He forgets all the obstacles that he has come across during the course of his journey. He would like to express his sincere gratitude and thanks to all the crews who have been his source inspiration and given enough strength and perseverance since the beginning. While doing this, he is bit wordless.

I like to express my deep sense of respect and gratitude to my mentor, Dr. U. T. S. Pillai Scientist, Materials and Minerals Division, National Institute for Interdisciplinary Science and Technology (NIIST), Trivandrum, for his invaluable and fruitful constructive suggestions and guidance that have enabled me to overcome all the problems and difficulties while carrying out multi-functionaries of the present investigation. He stayed along with me and motivated constantly and stimulated me to the fullest extent. I feel fortunate for the support, involvement and well wishes of my mentor and this is virtually impossible to express them in words.

I wish to thank my well wishers Dr. B.C. Pai, Senior Deputy Director, NIIST, Trivandrum and Dr. U. Kamachi Mudali, Head, Corrosion Science and Technology Section, Indira Gandhi Center for Atomic Research, Kalpakkam for their persistent encouragement and advice during the course of this work.

I thank Dr. R. M. Pillai Senior Deputy Director, Head, Materials and Minerals Division for his valuable advice and encouragement.

I am grateful to Prof. T.K. Chandrashekar, Director, National Institute for Interdisciplinary Science and Technology, Trivandrum and Prof. S. P. Mehrotra, Director, National Metallurgical Laboratory (NML), Jamshedpur for the support during the course of this research work.

I am thankful to the Council of Scientific and Industrial Research (CSIR), New Delhi for granting Senior Research Fellowship to carry out this research work.

I am very much grateful to Mr. K. Sukumaran, and Mr. K.K. Ravikumar, NIIST for their help in mechanical testing, Mr. S.G.K. Pillai, NIIST for optical metallography, Dr. V. John and Mr. M.C. Shaji, NIIST for foundry facilities, Dr. M. Ravi, NIIST for image analysis, Dr. Peter Koshy, Dr. P. Prabhakar Rao and Mr. M.R. Chandran, NIIST for SEM and EDS facilities and Dr. U. Syamprasad and Mr. P. Gurusami, NIIST for the XRD work.

I wish to place on record my sincere thanks to Dr. J. Swaminathan, Scientist, NML, Jamshedpur for his valuable help to carry out the creep testing and optical micrographs. It is worth to mention that the thesis would not have come to the final shape with out his help.

My sincere thanks also to Mr. S.K. Das and Mr. Manoj Kunjan, NML, Jamshedpur for their kind help in doing SEM and EDS work

I am also grateful to Dr. Ningshen, Corrosion Science and Technology Section, Indira Gandhi Center for Atomic Research (IGCAR), Kalpakkam for his help to conduct corrosion testing and Dr. (Mrs) Saroja Saibaba, Physical Metallurgy Divison, IGCAR, Kalpakkam for her kindness to provide the SEM-EDS facility.

I wish to thank my colleagues in NML, Jamshedpur, Dr. Sukomal Ghosh, Mr. P. K. De, Dr. V. C. Srivastava, Dr. K. L. Sahoo, Dr. D. Mandal and Mr. P. Poddar for their support during the course of this work.

I express my sincere thanks to Dr. T.P.D. Rajan and Dr. S. Sreeja Kumari, NIIST for the technical discussions and the help given to me during the course of this research work.

My sincere thanks to Mr. T. Soman and Mr. V. Antony, NIIST for the help received from them throughout the research work. I thank Mr. P. Balan,

Mr. S. Ramakrishnan, Mr. N. Narayanan, Mr. T.A. Balakrishnan, Mr. P. Sisupalan and P. Soman, NIIT for the machining, fabrication and other works at workshop.

I am very much grateful to Mr. V.M. Sreekumar, Mr. K.R. Ravi, Mr. .M Suresh, Mr. K. Venkatesh, Mr. G. Jaganathan and Mr. M. Saravanan NIIST, Trivandrum for the technical discussions and their assistance in my work. I also thank all members of Light Metals, Alloys and Composite Group, NIIST, Trivandrum for the help throughout my work.

A special mention is worth to Mr. N. Balasubramani, NIIST, Trivandrum for his tireless help throughout this work.

I like to thank Dr. K. Venkateswarlu, Mr. M. Madan, Mr. V. Rajinikanth and all other friends in Jamshedpur for their help and encouragement.

I would also like to recall the inspiring words of my Professor Dr. K. Raghukandan, Head, Manufacturing Dept., Annamalai University, which always rejuvenate me.

Heartfelt thanks to my parents and sister, who always concern about my progress, for their encouragement and untiring support. Special thanks to my wife J. Mohana Priya for the encouragement and support given to me. I also thank my son Akash and daughter Thendral, who I believe, bring happiness and luck to my life. Last but not least, I thank **GOD** for giving me the knowledge and helping me throughout my life.

A. Srinivasan

ABSTRACT

The use of magnesium has grown considerably since early 1990 and continues to rise in the automotive industry. This is mainly attributed to the lightness of magnesium-one –third lighter than aluminum, three-fourth lighter than zinc, and four-fifths lighter than steel. Magnesium also has the highest strength-to- weight ratio compared to many of the structural metals commonly used. Although magnesium alloys have been developed and used widely during World War II, research and development of magnesium alloys significantly declined after 1960 due to various reasons. As a result, the metallurgical knowledge of magnesium and its alloys is immature compared to that of aluminum and its alloys, leaving a significant amount of work waiting for the attention of researchers. AZ91, whose composition is Mg-9%Al-1%Zn-0.2%Mn is one of the major alloy systems in magnesium alloys. This alloy offers excellent mechanical, chemical and foundry properties. However, the major problem is with its high temperature properties. Its elevated temperature tensile and creep properties drops drastically, which restricts its usage above 120°C. The presence of low temperature melting point intermetallic $Mg_{17}Al_{12}$ at the grain boundary is said to be the culprit for the above said problem. Introduction of high thermally stable intermetallics in the microstructure through minor alloying additions is an old but still effective way of improving its high temperature behavior.

Hence, the primary objective of the present research work, **"INFLUENCE OF Si, Sb AND Sr ADDITIONS ON THE MICROSTRUCTURE, MECHANICAL PROPERTIES AND CORROSION BEHAVIOR OF AZ91 MAGNESIUM ALLOY"**, is to study the influence of individual and combined additions of Si, Sb and Sr on the creep behavior of gravity cast AZ91 alloy. In addition, the role of these elemental additions on the ageing behavior, tensile properties and corrosion behavior of AZ91 alloy is also studied. The thesis contains totally well organized five chapters with the following details.

Chapter 1 gives the over all idea of the thesis. The general introduction to magnesium alloys and its importance are given. The limiting properties of AZ91 alloy

for its wide applications are identified as creep and corrosion. Their creep and corrosion mechanisms are briefly discussed. The effect of various minor alloying additions on the microstructure and mechanical properties are also brought out. The theme of the thesis is given at the end of the chapter.

A comprehensive review on the parameters influencing the structure and properties of Mg-Al based alloys particularly AZ91, is given in **Chapter 2**. A great attention is given to understand the creep and corrosion behavior of AZ91 alloy and its mechanisms. The information available in the literature about the role of different alloying elements on the structure and properties, particularly the creep and corrosion is covered. Finally the areas are identified for the present research work and scope of the investigation is also given at the end of the chapter.

Chapter 3 gives the details of the materials and the experimental methods used in the present investigation. Magnesium alloys with various compositions were prepared under proper flux cover. To study the effect of minor alloying additions, various amounts of different alloying elements like Si, Sb and Sr are added to AZ91 alloy in the form of aluminum master alloys. The microstructures were characterized using optical microscope (OM) and Scanning Electron Microscopy (SEM) attached with EDS. To study the ageing behavior heat treatment studies were carried out at 200°C. Tensile properties were evaluated at room as well as at 150°C temperatures using Instron Universal Testing Machine. Creep properties were also evaluated at 150 and 200°C temperatures with an initial stress of 50 MPa using 3 ton 'MAYES' creep testing machine. 100 h immersion test in 3.5% NaCl solution, Potentiodynamic Polarization and Electrochemical Impedance Spectroscopy measurements in ASTM 1384 solution, which contains 148 mg l^{-1} of Na_2SO_4, 138 mg l^{-1} of $NaHCO_3$ and 165 mg l^{-1} NaCl (pH≈8.3), were carried out to estimate the corrosion behavior of AZ91 alloy with and without alloying additions.

Chapter 4 presents the results of the present investigation and the detailed discussions on the results with microstructural evidences and suitable theories.

The microstructure of base alloy consists of α-Mg matrix and β-$Mg_{17}Al_{12}$ intermetallic at the grain boundary. Additions of Si, Sb, and Sr to AZ91 introduce Mg_2Si, Mg_3Sb_2 and Al_4Sr intermetallics respectively. The morphology of Mg_2Si intermetallic is found to be a coarse Chinese script where as both Mg_3Sb_2 and Al_4Sr have needle shape. Combined addition of Si with 0.2% Sb and 0.1% Sr has modified the Chinese script morphology of Mg_2Si intermetallic in to a fine polygonal and rectangular shape. The reason for the modification is that the added Sb and Sr has restricted the growth of Mg_2Si intermetallic during solidification.

During solution treatment at 410°C for 48 h, the $Mg_{17}Al_{12}$ intermetallic gets dissolved where as the other intermetallics such as Mg_2Si, Mg_3Sb_2 and Al_4Sr are not affected due to their high thermal stability. On the other hand, the thermal stability of $Mg_{17}Al_{12}$ intermetallic is improved to a certain extent by Sr addition. Ageing of AZ91 alloy at 200°C leads to the formation of $Mg_{17}Al_{12}$ precipitates in two morphologies: discontinuous lamellar and continuous fine plate morphology. Continuous morphology is favorable for the age hardening. Addition of Si, Sb suppresses the discontinuous precipitation and thereby helps to form more continuous precipitates. Due to this, the peak hardness increase considerably. On the other hand, Sr addition slightly increases the volume of the discontinuous precipitates. Moreover, the improvement in peak hardness with Sr addition is not much. This is due to the availability of less amount of Al for the precipitation process during ageing. Since the stability of the $Mg_{17}Al_{12}$ intermetallic is increased by the Sr addition, it is not completely dissolved during solution treatment. Moreover, most of the Al is in the form of undissolved Al_4Sr intermetallics and the total amount of aluminum available for the precipitation process is less.

Addition of Si marginally reduces the tensile properties of AZ91 alloy because of the presence of the Chinese script Mg_2Si intermetallic but with the Sb addition improves it for the room as well as at 150°C, which is due to the presence of fine Mg_3Sb_2 intermetallics and the grain refinement effect. However, 0.7% Sb addition reduces the tensile properties due to the presence of more numbers of needle shaped Mg_3Sb_2 intermetallics. Not much increase in UTS but significant improvement in

yield strength is observed with Sr addition. Again optimum amount of Sr addition is restricted to 0.5%. Due to the refinement in grain size, yield strength is improved with Sr additions. However, not much improvement in UTS is seen with Sr additions which are due to the fact that the formation of Al_4Sr intermetallics reduces the volume of $Mg_{17}Al_{12}$ intermetallics, which is considered as the strengthening phase at room temperature. Both the combined additions of Si with Sb and Si with Sr provide superior properties compared to the individual addition of Si due to the modification in morphology of Mg_2Si intermetallics.

At 150°C, substantial improvement in the creep properties with alloying additions is observed. Addition of Si and Sb greatly increases the total creep life of AZ91 alloy. This is attributed to the presence of hard and stable Mg_2Si, Mg_3Sb_2 intermetallics in Si and Sb added alloys respectively and more volume fraction of continuous precipitates, which strengthen the grain boundary during creep. It is interesting to note that both Chinese script and polygonal shaped Mg_2Si intermetallic in Si added alloys exhibit similar creep properties. This is in contrast to the tensile behavior where the tensile properties are reduced by the Chinese script morphology of Mg_2Si. This indicates that Chinese script morphology is advantageous as far as the creep property is concerned. The multiple arms of the Chinese script extended to the neighboring grain boundaries effectively hold the boundaries during creep and restricts it against sliding. The 500 h short term creep test has revealed that the Sr addition also capable of improving the creep properties of AZ91. However, the creep behavior of AZ91 alloy at 200°C is not improved significantly by the additions. This is attributed to the fact that the softening effect by the coarsening of $Mg_{17}Al_{12}$ is more predominant at 200°C due to the high mobility of aluminum atoms, which overcomes the strengthening effect by the stable intermetallics.

The post crept microstructural analyses indicate that dynamic continuous precipitates of $Mg_{17}Al_{12}$ occur during creep in all the alloys, which in turn improved the strength. These continuous precipitates nucleate on the dislocations found near the hard intermetallics. Cavities are noticed at the matrix-massive $Mg_{17}Al_{12}$ intermetallic interface due to the incompatibility between them. Multiple cracking of $Mg_{17}Al_{12}$

intermetallic are also observed. These cavities at the interface and cracking of massive $Mg_{17}Al_{12}$ intermetallics along with the coarsening of continuous precipitates due to the low melting point, lead to the final fracture in AZ91 alloy. It is found that addition of alloying elements promotes more number of continuous precipitates. Addition of alloying elements introduces various hard intermetallics which increases the dislocation density near the intermetallics during solidification, due to the difference in co-efficient of thermal expansion between the intermetallic and matrix. These dislocations act as a heterogeneous nucleation site for the continuous precipitates. Fine precipitates along with the stable intermetallics (Mg_2Si, Mg_3Sb_2 and Al_4Sr) strengthen the grain boundary and thereby improve the creep resistance.

Addition of Si and Sr reduces the corrosion rate of AZ91 alloy whereas, Sb addition increases it. Interesting result is observed with the Si and Sb combined addition of which results highest corrosion resistance compared to all the alloys. Both the intermetallics Mg_2Si and Al_4Sr are less harmful to corrosion compared to $Mg_{17}Al_{12}$ whereas Mg_3Sb_2 intermetallic acts as an active cathode. Fine and evenly distributed Mg_2Si intermetallic with the combined addition provides continuous protective layer to retard the growth of corrosion more effectively compared to the massive sized particle.

The summary of the findings of this investigation along with its contributions made to the knowledge and the avenues for further work are presented in **Chapter 6**.

CONTENTS

Page No.

Page No.

Page No.

LIST OF TABLES

LIST OF FIGURES

CHAPTER 1: INTRODUCTION

1.1 MAGNESIUM

Increase in luxury and safety features in the modern cars have caused an increase in vehicle weight translating into increased fuel consumption and ultimately increased CO_2 emissions [1]. Hence, the automotive industry is increasingly looking for stronger and lightweight materials in order to meet these emission regulations. Magnesium with a major advantage of low density plays a dominant role in automobile industry to overcome this problem. With a density that is approximately two-third that of aluminum, the potential weight savings due to increase in magnesium usage has substantial environmental impact, including reduction of greenhouse gas emissions. Furthermore magnesium also provides solution for the global environmental problems like reusability and recyclability due to the fact that magnesium unlike many polymers is a recyclable [2].

Magnesium is the sixth most abundant element on earth; one cubic mile of sea water contains 6 million tones of magnesium. The first commercial production of magnesium was recorded in Germany in 1916 [3]; however, a lack of markets caused the world production of magnesium to be a meager of 300 tonnes [4]. It was not until the Second World War the magnesium industry developed significantly. By the end of 1945, magnesium production had increased to 237,000 tonnes worldwide [4]. Two years later, magnesium consumption had dropped dramatically to 50,000 tonnes [4]. It took another 30 years for the annual production of magnesium to recover to the 1945 level, and in the year 2000, 366,900 tonnes of magnesium were consumed. The worldwide primary magnesium production in 2004 was 584,000 metric tons according to the U.S. Geological Survey Minerals Yearbook-2004 [5]. Recently, the American Foundry Society Magnesium Division has developed the Magnesium Casting Industry Technology Roadmap [6]. According to that report, in 2004, the U.S. magnesium casting industry culminated ten years of remarkable growth by shipping nearly 100,000 tons of castings to a wide range of markets [7]. During the last decade alone, growth in magnesium castings for light vehicles has averaged 16% per year and

is predicted to grow at an annual rate of 11.5% for the next decade. Even then, it is believed that magnesium is not being utilized as should it be. This is mainly due to the fact that the metallurgical knowledge of magnesium and its alloys is immature compared to that of aluminum and its alloys, leaving a significant amount of work waiting for the attention of researchers.

As far as the crystal structure is concerned, magnesium has a hexagonal crystal structure, with a c:a ratio of 1.6236, very close to the ideal value of 1.633 for the atomic packing of spheres. [8]. Figure 1.1 shows the planes and directions in the magnesium unit cell. At room temperature only three slip systems are active all parallel to the basal plane (0001) [9]. However, at higher temperatures, both prismatic and pyramidal slip planes are also become active leading to the work hardening. Its alloying behavior because of a favorable size factor (atomic diameter 0.320 nm), is characterized by an ability to form a solid solution with a variety of elements particularly those which are of commercial importance including Al, Zn, Sn, Li, Ce, Ag, Zr and Th [10]

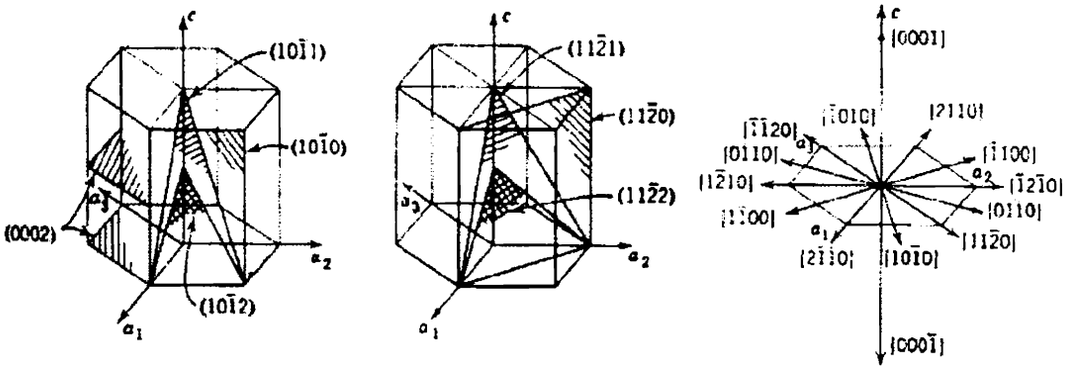

Figure 1.1: Schematic diagram showing principal planes and directions in the magnesium unit cell [8]

1.2 AZ91 MAGNESIUM ALLOY

Among the various magnesium alloy systems, Mg-Al alloys are the most important alloy systems since aluminum provide better castability. Table 1.1 shows some of the major alloy systems in this group (Mg-Al) and its major compositions [11]. Mechanical properties of some of the alloys are also provided in Table 1.2 [12].

AZ91 alloy, which contains 9% Al-1% Zn-0.2% Mn is the most widely and commercially used Mg alloy in automotive industries. This alloy provides very good room temperature tensile properties, excellent casting properties and corrosion resistance [13]. Aluminum in this alloy offer better castability, strength and corrosion properties. Zinc improves the solid solution strengthening whereas Mn provides corrosion resistance. Due to this, among 90% of Mg alloy components used in transport industries are made from AZ91 alloy [14]. However, AZ91 alloy does not exhibit good creep resistance which is a major setback [15].

Table 1.1: Major compositions of some of the Mg-Al based alloys [11]

Alloy	Al	Zn	Si	Mn	RE	Cu	Fe	Ni	others
AM20	1.7-2.2	< 0.1	< 0.1	>0.5	--	<0.008	<0.004	<0.001	<0.01
AM50	4.5-6.3	< 0.1	< 0.1	>0.27	--	<0.008	<0.004	<0.001	<0.01
AM60	5.7-6.3	< 0.2	< 0.05	>0.27	--	<0.008	<0.004	<0.001	<0.01
AS41	3.7-4.8	< 0.1	0.6-1.4	0.22-0.48	--	<0.04		<0.01	<0.30
AZ91	8.5-9.5	0.45-0.9	< 0.05	>0.17	--	<0.015	<0.004	<0.001	<0.01
AE42	3.6-4.4	< 0.2	--	>0.27	2.0-3.0	<0.04	<0.004	<0.004	<0.01

Table 1.2: Mechanical properties of different Mg-Al based alloys [12]

Alloy	Condition	Yield strength (MPa)	Tensile strength (MPa)	Elongation (%)
AZ91	Die cast	150	230	3
AM60	Die cast	115	205	6
AS41	Die cast	150	220	4
AS21	Die cast	130	240	9
AE41	Die cast	103	234	15

1.3 CREEP BEHAVIOR OF AZ91 ALLOY

Creep is a special kind of plastic deformation which takes place when the material is loaded at high temperature for a prolonged time. The load is very much low compared to its yield strength. So, the deformation is not mainly due to the applied load but temperature plays a major role. Based on applied stresses and operating temperatures, the creep deformation mechanisms for most engineering materials classified into main groups: the dislocation creep and the diffusion creep. They can also be further subdivided into dislocation glide, dislocation climb, grain boundary sliding, boundary diffusion (Nebrro-Herror creep) and bulk diffusion (Coble creep) [16].

Very little is known about the high temperature properties of AZ91 alloy. Only few elaborative creep studies were conducted on die cast AZ91 [17-27]. Most of the literature suggests that the dislocation climb is the major creep mechanism in the temperature range of 100-300°C with an initial load 20-100 MPa. However, some literature proposed a grain boundary sliding mechanism at the low stress levels of 20-40 MPa [28]. Dynamic discontinuous precipitates occur at the grain boundary during creep is said to be responsible for such sliding. Detailed creep studies on gravity cast AZ91 alloy is lack in literature. It is said that dislocation creep is the only dominant mechanism at all temperatures and stress ranges in ingot gravity casting [29].

Structural instability is observed during creep exposures in both die cast and gravity cast AZ91 alloy [29-31]. However, this effect is more pronounced in die cast alloy where the amount of Al supersaturated Mg matrix is large due to the faster solidification. All the literature supports the formation of dynamic precipitation during creep but it is still inconclusive about its influence on the creep behavior. Occurrence of more dynamic discontinuous precipitates at the grain boundary in the die cast AZ91 alloy and grain boundary sliding due to the precipitate formation is reported [28]. In contrast, it is also observed that the formation of continuous precipitates in die cast AZ91 provides precipitation hardening [29]. Strengthening due continuous precipitates in ingot cast AZ91 is also reported [29].

In summary, both diffusion controlled dislocation climb and grain boundary sliding are reported as creep mechanisms depending upon the temperature and stress levels. The poor thermal stability of $Mg_{17}Al_{12}$ and formation of dynamic discontinuous precipitation (DP) can result in substantial grain boundary deformation at elevated temperatures. Higher diffusivity of aluminum in magnesium matrix and the self-diffusion of magnesium at elevated temperature are also contributing to high creep rate in AZ91 alloy.

1.4 CORROSION BEHAVIOR OF AZ91 Alloy

Another hurdle in the potential use of AZ91 is their susceptibility to corrosion. Its corrosion resistance depends on two different factors: the level of impurity elements and the microstructure. Fe, Ni, Co, Cu is considered as impurity elements which have negative effect on corrosion resistance. The tolerance limits for these elements are defined by the ASTM standards [32]. As far as the microstructure is concerned, the aluminum level and the distribution of β phase in the microstructure are vital [33-37]. When the β -$Mg_{17}Al_{12}$ phase is fine and distributed evenly along the grain boundary, it acts as a barrier for corrosion, on the other hand it acts as an effective cathode for corroding α matrix when it is in bulk form and the inter particle distance is large [36]. In general, the corrosion start from the centre of the matrix where the aluminum content is less compared to near the grain boundary [37].

1.5 ROLE OF MINOR ALLOYING ADDITIONS

Many new Mg-Al based alloy systems are developed for high temperature applications [38-40]. However, none of them are commercialized so far due to the very fact that those alloy systems does not have the die castability as like AZ91 alloy. Later the idea of modifying the alloy chemistry of existing AZ91 by addition of minor alloying elements is found to the effective way of improving the creep resistance and it has become popular.

It is well established that the β-$Mg_{17}Al_{12}$ phase in AZ91 alloy is the reason for the poor creep properties. Coarsening of β at high temperature and discontinuous form of β phase are said to be the culprit for such behavior. Altering the alloy composition

by minor alloying additions suppress the discontinuous precipitates and slow down the coarsening of $Mg_{17}Al_{12}$ intermetallic during the high temperature exposure. More over, addition of alloying elements forms hard and stable intermetallics at the grain boundaries which act as barriers for both dislocation and grain boundary sliding.

Surface active elements like Ca, Bi, Sb, RE etc., are added to AZ91 alloy to improve the creep resistance [41-47]. Reduction in the quantity of $Mg_{17}Al_{12}$ intermetallic and formation of thermally stable Al_2Ca intermetallic is observed with Ca addition which improves the high temperature properties of AZ91 alloy [41]. Bi addition also capable of forming stable intermetallic Mg_3Bi (melting point of 823 °C) and thereby improving the high temperature properties [42]. When Sb is added to AZ91 alloy a favorable microstructure is obtained which consists of thermally stable Mg_3Sb_2 intermetallics (melting point of 1228° C) at the grain boundary along with the refined $Mg_{17}Al_{12}$ intermetallics [43, 44]. RE addition like La, Ce, etc., are also found to improve the creep behavior of AZ91 alloy by reducing the amount of $Mg_{17}Al_{12}$ intermetallic as a consequence of the formation of Al-RE compounds [45-47].

Improvement in corrosion behavior is also noticed with the addition of alloying elements like La, Ce, Ca, Ho and Er to AZ91 [46-50]. Such improvement is attributed to the following reasons (i) the added elements refine the β- phase and forms more continuous network (ii) the added element suppresses the formation of β-phase by forming other intermetallics with Al which has less harmful to corroding α-Mg matrix (iii) the added alloying elements may be incorporated into the protective film and increases the stability of it.

1.6 THEME OF THE THESIS

All the exciting work on developing new and better alloys has led older alloys, such as AZ91, being abandoned by researchers. It is believed that the full potential of AZ91 in automotive design has not been realized. Whatever works have been carried out on AZ91alloy to improve its mechanical properties are insufficient in terms of its potential usage in auto industries. Due to the fact that AZ91 offers high room temperature mechanical properties and good castability, still this alloy is a primary

choice for the auto component manufactures. Small improvement in its creep properties will have a huge impact in the transportation industries. Hence, in the present work, ***"Influence of Si, Sb and Sr Additions on the Microstructure, Mechanical Properties and Corrosion Behavior of AZ91 Magnesium Alloy"***, an attempt has been made to improve the creep properties of AZ91 alloy through minor alloying elemental additions and to understand its strengthening mechanisms. The effect of alloying additions on the ageing and tensile properties of AZ91 is also studied. In addition to that, role of various intermetallics formed due to the alloying additions on the corrosion properties of AZ91 alloy is investigated.

CHAPTER 2: LITERATHRE REVIEW

2.1 INTRODUCTION

The weight of the average family car has increased by 20% over the last 20 years [51]. Most of the increased weight is a result of increased average engine size and the additions of safety features. On the other hand, customer's awareness of fuel efficiency has been made more acute by increasing fuel prices and the popularity of environmental issues. So, weight reduction is an imperative task for automobile producers. The attractive benefit of reduction in automobile weight can be seen in terms of improved fuel efficiency as shown in Figure 2.1 [52]. "Concept cars" produced in recent years have been lightweight, for example, the Ford P2000, which weighs only 544.3 Kg [53]. The weight reductions have been made possible by the replacement of steel by light metal alloys, usually aluminum or magnesium. In production vehicles, the weight is saved through the use of lightweight metals, which have reduced the weight of cars by 10% since 1978, without compromising safety [54]. Earlier, aluminum alloys replaced most of steel or cast iron components in automobiles. But at this moment, the major aim and task of the researchers is to find suitable material, which is more efficient than aluminum so as to reduce the weight of automobile further. Magnesium and its alloys are one such promising material, whose light weight advantage could be used for the above said purpose.

Magnesium, with a density of 1.7 g/cc is the lightest of the structural materials. It is two third of its counterpart aluminum density (2.7 g/cc) and one third of steel density (7 g/cc). So, it has high specific strength properties over aluminum alloys. However, the total annual world consumption of magnesium at around 250 thousand tones is a fraction of the 20 million tones of aluminum used. Both metals were discovered in the early 19^{th} century and industrial refining processes for each metal were announced in 1886. So, the lower usage of magnesium is due to different complex of factors. However, developments in magnesium refining and processing technology have coincided with new demands from many industries for high precision light-weight die-castings. Now the use of magnesium is growing at a faster

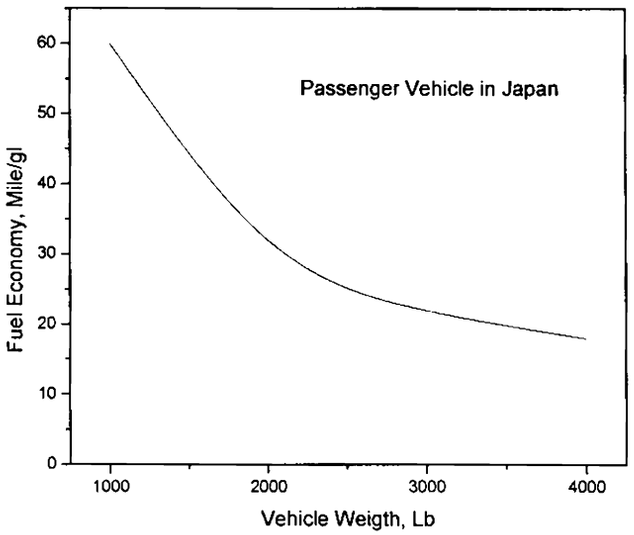

Figure 2.1: Effect of weight reduction on the fuel efficiency of automobile [52]

2.2 ADVANTAGES

Magnesium alloys has several advantages. Table 2.2 lists some of the key attributes of magnesium alloys that make them more attractive to automotive, aerospace and other industries [12]. The most important of these is light weight. This leads to relatively high specific stiffness and specific strength for magnesium alloys. Another very important advantage is the design flexibility and manufacturability. Typical magnesium die-casting alloys such as AZ91, AM50 and AM60 can be cast into larger, more complex shapes with thinner sections. Thus they lend themselves to produce large die cast components that, in a single-shot die casting, integrate the functions of structure that would otherwise be fabricated from a large number of pieces in several manufacturing steps.

2.3 APPLICATIONS

2.3.1 Aerospace Industries

Magnesium is employed extensively in aircraft engines, air frames and landing wheels [56]. The main factors dictating the use of magnesium in aircraft have been strength/density ratio in castings and stiffness/density ratio in wrought forms, combined, as required, with factors such as good elevated temperature, fatigue and impact properties, always with good machinability. Alloys such as ZE41 (Mg-4.2%

Zn-0.7% Zr-1.3% MM), QE22 (Mg-0.7% Zr-2.5% Nd-2.5% Ag) and particularly WE43 (Mg-4% Y-3.25% Nd-0.5% Zr) are commonly used for aircraft applications due to their improved corrosion and creep resistance.

2.3.2 Defense Industries

High specific strength and rigidity coupled with ease of fabrication are important for missile and space applications. EZ33 (Mg-2.7% Zn-0.7% Zr-3.2% MM) sand castings are used in the "Skylark" research rockets. ZK51 (Mg-4.5% Zn-0.7% Zr) and ZE41 castings have been used extensively for structural parts in British missiles [57].

2.3.3 Automobile Industries

Automobile industries are the latest beneficiary of magnesium, currently exploring its maximum usage. Table 2.3 gives a number of applications of magnesium that are currently being addressed by the automotive industry. Components at the top of this list, such as steering wheel armatures, cylinder head covers and instrument panel beams are already in significant production, while items at the bottom of the list require several years of intensive development before they can be implemented [12]. Figure 2.2 gives some of the automobile components made from magnesium alloys [58].

Table 2.2: Advantages of magnesium alloys [56]

1.	Strength/Weight ratio
2.	Excellent damping capacity
3.	Non-magnetic, EMF shielding
4.	Good heat dissipation
5.	High castability
6.	Complex, thin walled castings
7.	Excellent machinabiltiy

Table 2.3: Some of the magnesium alloy automobile components [12]

1.	Steering wheels
2.	Cylinder head covers
3.	Instrument panel beams
4.	Sear frames
5.	Door frames
6.	Transmission housings
7.	Grill opening reinforcements
8.	Structural supports
8.	Rear deck lid/engine hood
10.	Wheels
11.	Engine blocks
12.	Steering wheels

2.3.4 Nuclear Industry

With natural uranium as a fuel, it is essential to conserve neutrons by using materials in the reactor, which will not absorb them readily. Natural uranium plants with operating temperatures suitable for power production essentially determine the general reactor design and limit the canning material to magnesium and the coolant gas to magnesium dioxide [57]. The advantages of magnesium as a canning material over competing materials are: (a) low tendency to absorb neutrons, (b) does not alloy with uranium, (c) adequate resistance to carbon dioxide up to the highest service temperatures envisioned, and (d) good thermal conductivity [57].

2.3.5 Sporting and Electronic Industries

Apart from transport and missile components magnesium also finds application in electronics and house holding items. Some of the examples are computer housing and mobile telephone cases, where lightness, suitability for thin wall casting and the characteristic of electromagnetic shielding are the particular advantages [57]. Figure 2.3 shows some of such applications [58].

2.4 LIMITATIONS

In spite of the above said advantages and applications, there are some limitations, which restrict its full utilization for industry applications. Some of the challenges that are facing magnesium in order for its wholesale acceptance for industrial applications are summarized in Table 2.4 [12].

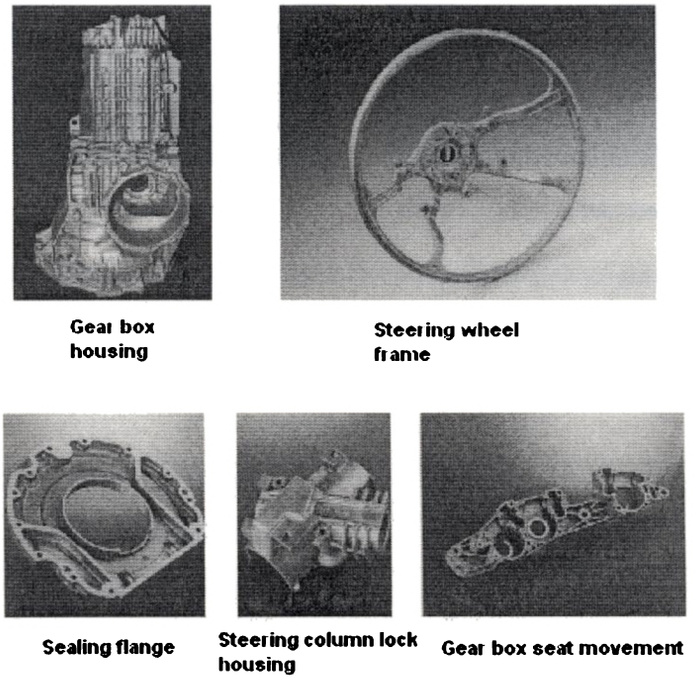

Figure 2.2: Some of the automobile components made up of Mg alloys [58]

2.5 MELTING PRACTICE

2.5.1 Flux Melting and Refining

When magnesium and its alloys are melted, they tend to oxidize and explode, unless care is taken to protect the molten metal surface against oxidation. Molten magnesium alloys behave differently from aluminium alloys, which tend to form a continuous, impervious oxide skin on the molten bath and limits further oxidation. Magnesium alloys, on the other hand, form a loose, permeable oxide coating on the molten metal surface. This allows oxygen to pass through and support burning of melt below the oxide surface. The two main reasons that lead to the ignition of magnesium during melting process are given below [59];

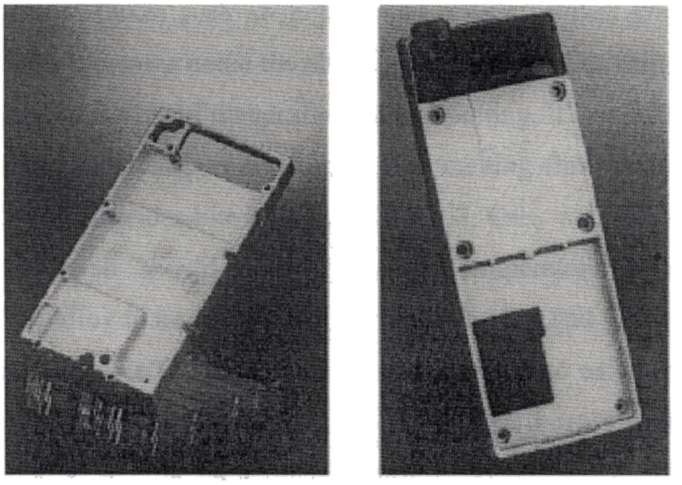

Screen housing Units for mobile handset

Figure 2.3: Magnesium parts used in communication engineering [58]

Table 2.4: Limitations of magnesium alloys [12]

1.	High metal cost
2.	Small supply base
3.	High cost of recycling
4.	Replacement of SF_6 cover gas (melting difficulties)
5.	Low high temperature properties
6.	Corrosion problem
7.	Lack of joining technologies
8.	Poor workability

1. The volume of magnesium shrinks after it is oxidized, and the structure of magnesia (MgO) is loose and many small holes appear on the surface thus become porous. So it cannot prevent the passage of oxygen and the oxidation of inner magnesium.

2. The heat formation of magnesia is too large so that the local area temperatures can even reach 2850°C by the heat generated in the oxidation process.

Two kinds of fluxes such as melting and refining fluxes are normally used during melting of Mg to over come the above said problems [59, 60]. Melting flux is used to prevent the oxidation of magnesium during melting. It is added throughout the melting when ever the local burning occurs. The melting flux normally consists of various chloride and fluorides like $MgCl_2$, KCl, NaCl, CaF_2, etc. The requirements of a melting flux are: It should have a liquidus temperature below the solidus temperature of the alloy to be melted and sufficient fluidity and wetting power above this temperature to enable the flux to spread out on melt so as to form a complete protective layer over the metal. The flux melts first and form a protective chloride layer over the solid as well the liquid metal during melting [59-61].

Many non metallic inclusions suspends in the molten metal of magnesium. These inclusions have to be removed before pouring otherwise, would enter in to the casting and reduces the casting quality [60]. For this purpose an inspissated flux (Refining flux) is used. The removal of oxides by inspissated flux is known as "refining process". In this process, the flux is added into the melt while it is rigorously stirrered. The refining flux disintegrates into globules, and is able to wet and absorb particles of suspended oxides, thereby becoming denser, so that they readily settle to the bottom of the crucible [59, 60]. 10-30 minutes, depend upon the size of the melt, should be given for settling inspissated impurities. The essential constituent of the inspissated flux is $MgCl_2$.

2.5.2 Flux-less Melting

Although extremely effective in controlling oxidation, fluxes create corrosive fumes in the foundry and are difficult to separate from the metal, contributing to a high incidence of corrosive inclusions in magnesium casting parts. The quest for technology to protect magnesium from oxidizing without the negative ramifications associated with flux lead to flux-less melting. It is very effective way of melting in which, inert gases are used to protect the molten metal. The most common gas used in flux-less melting is SF_6 mixed with dry air and CO_2 [62]. To maintain an adequate and homogenous level of SF_6 at all area of the melt surface it is usually desirable to supply the protective atmosphere through a manifold with several outlets so as the gas

to spread out over the melt surface. The gas mixtures take away the oxygen out of the melting area and hence, provide an oxygen free atmosphere for melting.

The SF_6 based shielding gas is non-toxic, odourless and corrosion free. However, SF_6 is having a heavy green house effect. Its Global Warming Potential (GWP) is 23900 times higher than CO_2 and will be banned from industrial use [63]. Therefore, researchers in magnesium industries are trying to find the alternatives. Recently International Magnesium Association (IMA) found out suitable substitutes for SF_6. These are HFC-134, HFE-7100 and HFE-7200, Novec^{TM} 612 (FKs) [64]. These alternatives are all fluorides and their protective effects are no less than that of SF_6 but their GWP values much less tat that of SF_6 [65].

2.6 CASTING PROCESSES

Normally the magnesium alloys are cast by die casting method. This is to overcome the material cost disadvantages compared to aluminium alloys [66]. All magnesium alloys development activities for different mechanical properties are thus also focused with die-castability. Magnesium alloy containing Al as a major alloying element has high die castability compared to other Mg alloys. The most commercial and widely used die cast magnesium alloys are AZ91, AM60, and AE42 etc.

The choice of a particular casting method depends upon many factors, e.g., the number of castings required, the properties required, dimensions and shape of the part and the castabiltiy of the alloy [67]. Although pressure die casting is predominantly used to produce many of the magnesium alloy components, other casting processes such as gravity and low pressure castings using sand and permanent moulds are also familiar. Investment casting process has also presently become popular in producing Mg alloy components. Mg-Al and Mg-Al-Zn alloys are also easy to cast in gravity sand casting method; however they are limited in certain respects. They exhibit micro shrinkage when they are sand-cast, and the alloy is not suitable for applications in temperatures of above 120°C. Magnesium alloys containing RE as a major alloying element are mainly produced in sand casting route for this purpose and they are used in

aerospace applications. However these alloys are not suitable for die-casting application due to the poor die castability.

In addition, developments are well advanced with squeeze casting and semi solid processing like Reho casting and thixo casting [68-74]. Components produced through these casting methods show less defects and porosity and they can be heat treated to get maximum mechanical properties. These casting methods are also suitable for thick and thin sections. Low Pressure Casting (LPC) is another casting technique used to produce magnesium castings with improved mechanical properties [75-77]. Uniform filling rate throughout the casting in LPC eliminates turbulence and cold shut, which are inherent defects in gravity castings while making thin wall component castings [75].

2.7 MAJOR ALLOY SYSTEMS

The alloy designation system has been standardized by the American Society for Testing Materials (ASTM). In this system the first two letters indicate the principal alloying elements according to the following code:

A- Aluminum

E- Rare earth metals

H- Thorium

K- Zirconium

L- Lithium

M- Manganese

Q- Silver

T- Tin

Z- Zinc

The letters corresponding to the element present in the greater quantities in the alloy is given first followed by number which represents the nominal compositions in weight percent of the principal alloying elements. Magnesium casting alloys may be classified in to two major groups: zirconium free alloys and zirconium containing alloys. Zr is an effective grain refiner for Mg alloys. However, in presence of Al, the

efficiency of Zr reduces because Al removes Zr from the solid solution to form Al-Zr based intermetallics. Hence in zirconium free alloys, Al presence as the major alloying element along with zinc and manganese (Mg-Al-Zn, Mg-Al-Si, Mg-Al-RE, etc.,) where as alloy systems like Mg-Zn-Zr, Mg-RE-Zr all are examples for zirconium containing alloys.

2.7.1 Zirconium Containing Alloys

The maximum solubility of zirconium in molten magnesium is 0.6%. As binary Mg-Zr alloys are not sufficiently strong for commercial applications, the addition of other elements is necessary. The ability to refine the grains in Mg-Zn alloys with zirconium led to the introduction of ternary alloys such as ZK51 (Mg-4.5Zn-0.7Zr). However, these alloys are susceptible to micro porosity and are not weldable, they have found little practical application [78, 79]. However, Zn along with RE addition provides high strength and finds many applications.

Magnesium forms solid solutions with a number of RE elements. The addition of cheaper mischmetal based on cerium or neodymium to magnesium gives good casting characteristics and mechanical properties. These properties are improved by adding Zr to refine grain size and further increases in strength occur if zinc is added as well. EZ33 (Mg-3RE-2.5Zn-0.6Zr) is one such alloy, which retains strength and creep resistance at temperatures up to 250°C [80].

Recently Mg-Y age hardenable alloy systems are developed to utilize the benefit of high solid solubility of yttrium in magnesium. Series of Mg-Y-Nd-Zr alloys have been produced, which provides high strength at ambient temperature and good creep resistance up to 300°C temperature [81, 82]. Maximum strength combined with an adequate level of ductility is found to occur in an alloy containing approximately 6% Y and 2%Nd and the commercially available alloy in this category is WE54 (Mg-5.25Y-3.5RE-0.45Zr).

Addition of thorium also confers to increase creep resistance in magnesium alloys, and these alloys have been used in service temperatures up to 350°C. Ternary

compositions such as HK31 (Mg-3Th-0.7Zr) is developed for high temperature applications. However, in spite of their application in missiles and spacecraft, the alloy usage is reduced because of environmental considerations. Silver is also added to magnesium and Mg-Ag-RE-Zr alloys are developed with improved room and high temperature mechanical properties [83]. The alloy QE22 (Mg-2.5Ag-2RE-0.7Zr) has been used for a number of aerospace applications including landing wheels, gear box housings and rotor heads for helicopters.

2.7.2 Zirconium Free Alloys (Mg-Al Alloys)

Aluminium is the principal alloying element to magnesium. The binary Mg-Al system is the basis for the first magnesium casting alloys but most current compositions also contain small amounts of zinc and manganese. The most widely used alloys in this group are AZ91 and AM50 [78]. These alloys have a wide range of mechanical properties and good castability and mostly used in die casting application. However, the draw back of using these alloys is its poor elevated temperature tensile and creep properties above 150°C. [15].

Alloys like AS21, AS41 (Mg-Al-Si), which contain Si in it are developed for better creep properties compared to AZ91 [66]. Later on, solubility of rare earth (RE) in magnesium led to the development of AE alloys systems, which contain less amount of aluminium and small percent of RE [84]. One such alloy system, AE42 (Mg-4Al-3RE-0.3Mn)) has a good combination of properties including creep strength, which is superior to the Mg-Al-Si alloys [85]. The major drawback of these alloys is addition of RE increase the alloy cost drastically [66]. Recently, it is also found that the thermal stability of Al_4RE intermetallic in RE containing Mg alloys does not extend beyond 150°C and hence the AE42 alloy loses creep strength above this temperature.

The addition of calcium to Mg-Al based alloys for improved creep resistance is reported in a British patent [86]. This patent disclosed that calcium additions of 0.5-3% provide creep resistance to magnesium alloys containing up to 10% Al. However, the patent also revealed that calcium containing alloys prone to hot cracking.

Volkswagen attempted the use of Mg-Al-Ca alloys in the 1970's and claimed an improvement in creep resistance with the addition of about 1% Ca to magnesium alloy AZ81. However, the application of this alloy to die casting was not possible owing to die sticking and hot cracking. Later, a through investigation on the optimum amount of Ca addition to Mg-Al alloy to avoid these problems was carried out by Institute of Magnesium Technology (ITM) in Canada and General Motor [87, 88]. It is found that Mg-Al-Ca based alloys, which contain Ca more than 1%, are susceptible to the hot cracking problem.

Mg-Al-Sr (AJ) alloys are new addition to the creep-resistant Mg-Al based magnesium alloys [89]. Various alloy compositions such as AJ51 (Mg-5Al-1Sr), AJ52 (Mg-5Al-2Sr) and AJ62 (Mg-6Al-2Sr) have been developed. The creep resistance of theses alloys is found to be better than many Mg-Al alloys [90, 91]. However still, the microstructure and its creep mechanism are not fully understood.

2.7.2.1 AZ91 (Mg-9% Al-1% Zn-0.2% Mn) alloy

AZ91 alloy is one of the old but most commercially used Mg-Al based alloys. Among 90% of Mg alloy components used in transport industries are made from AZ91 alloy [14]. Currently, this alloy is being used in manufacturing instrumental panels, steering column, steering wheel, seat frame etc in automotive vehicles. This alloy provides wide range of properties and castability. Of course, AZ91 is the bench mark alloy for castability compare to all Mg alloys.

AZ91 alloy contain 8.1-9.3% Al, 0.4-1% Zn, 0.3 % max Mn, other impurities like Si, Fe, Cu and Ni. Aluminum in this alloy offers mechanical, corrosion and foundry properties like castability. Zinc offers little solid solution strengthening and corrosion resistance. Manganese neutralizes the ill effect of Fe and hence provides corrosion resistance. However, AZ91 alloy does not exhibit good creep resistance, which is a major setback [15].

2.8 FACTOR INFLUENCING THE STRUCTURE AND PROPERTIES OF Mg-Al ALLOYS

The physical and mechanical properties attainable in these alloys are strongly influenced by the alloy composition, impurity elements, solidification characteristics, and heat treatment.

2.8.1 Effect of Alloy Compositions

2.8.1.1 Aluminum

Aluminum is one of the major alloying elements to magnesium. Aluminum has a very good solid solubility in magnesium. The Mg-Al binary phase diagram is given in Figure 2.4 shows that the maximum solubility of Al in Mg at 437°C (eutectic temperature) is around 12.7% [92]. Figure 2.5 illustrates the effect of Al addition on the tensile properties of Mg-Al alloys [93]. The yield strength increases with addition of Al whereas UTS increase up to 6% and then decreases. However the ductility increases initially up to 3% of Al addition and then start to decrease steeply [93]. The solid solubility of aluminum in magnesium at room temperature is around 2%. So the excess aluminum forms $Mg_{17}Al_{12}$ intermetallic with Mg. This phase is hard and brittle and hence, acts as a strengthening element at room temperature. Al in this alloy also improves the castabiltiy [94]. However, Al also increases the tendency for shrinkage micro porosity up to 9% and then reduces it [95]. The reason the peak porosity at 9% can be related to the worst combination of mushy zone size, interdendritic feeding, permeability and eutectic volume friction. Aluminum also increases the corrosion behavior of Mg-Al alloys.

2.8.1.2 Zinc

Zinc has very good solubility in Mg. The role of zinc in AZ91 alloy is to improve the strength of alloy by solid solution strengthening. Zinc also improves the fluidity of the alloy. But higher amount of Zn to Mg-Al alloys can lead to hot cracking problem. It is further reported that the addition of zinc reduces the ductility of the alloy. Zinc strongly affects solidification pattern of AZ91 alloy and thereby forming micro-porosity. Studies report that addition of 2% Zn increases micro porosity in sand-cast magnesium alloys containing 2, 4, 8 and 10% Al [96]. The

presence of zinc decides the type of eutectic (completely or partially divorced) during final stage of solidification.

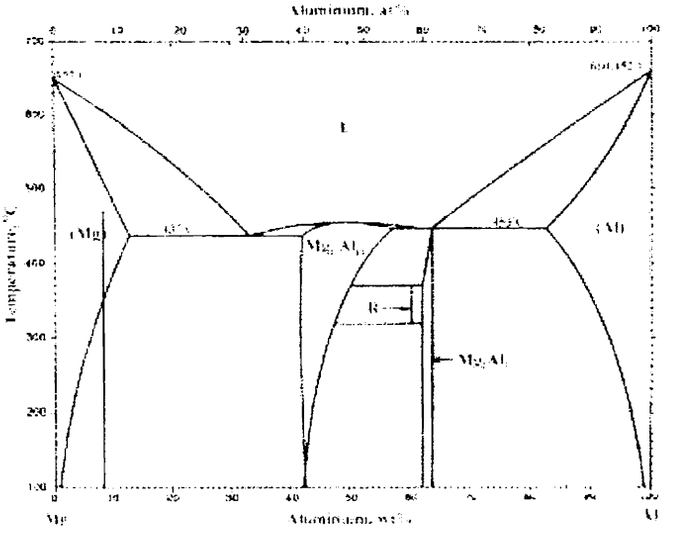

Figure 2.4: Phase diagram of Mg-Al binary alloy system [92]

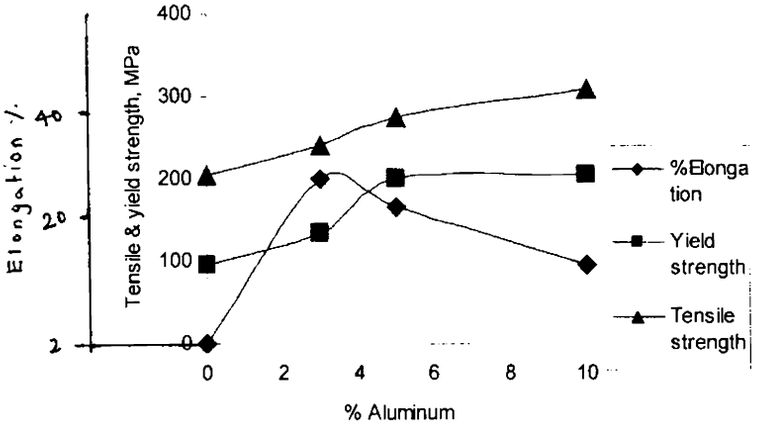

Figure 2.5: Effect of aluminum on the mechanical properties of Mg-Al binary alloys [*reproduced from ref. 93*]

2.8.1.3 Manganese

The main purpose of addition of Mn to AZ91 alloy is to improve the corrosion properties. The role of manganese in the improvement of corrosion resistance is twofold.

1. When manganese is added to Mg-Al alloys several types of AlMnFe intermetallic particles are formed [97]. These particles settle at the bottom of the melt, by which the iron content in the melt is reduced.
2. Manganese also renders the iron containing particles left in the melt during solidification less harmful by making them less efficient as cathodes, compared to the Al-Fe intermetallics, which are formed in Mn-free Mg-Al alloys.

2.8.1.4 Impurities

The heavy metal impurities like iron, nickel and copper in AZ91 alloy mainly affects the corrosion behavior. These elements form particles, which are highly cathodic to the matrix, and thus, leading to micro-galvanic corrosion. So, there exists a tolerance limit for these elements, above which the corrosion rate increases rapidly [98].

Nickel and copper are usually not create much problem due to the very low content of these elements in alloys from primary production. Iron is the most troublesome element in high purity alloys, as there always is a risk of iron pick-up form crucibles made of carbon steel.

2.8.2 Solidification

The solidification sequence of Mg-Al alloys starts with nucleation of primary magnesium (α- Mg) in the temperature range of 650-600°C, i.e. ranging from the melting point of pure magnesium to the liquidus temperature of Mg-9Al, covering the various aluminum contents used in commercial alloys. Later solidification reactions involve the formation of eutectic phases, with Mg-$Mg_{17}Al_{12}$ eutectic reaction occurring at 437°C [99]. Both these liquidus and eutectic (solidus) temperatures are cooling rate dependent. According to the phase diagram with equilibrium

solidification the liquidus and solidus temperatures of AZ91 is ~600°C and ~500°C respectively. But, in most of the casting practice the solidification never approach the equilibrium. Luo [99] reports the change in liquidus and solidus temperature of AZ91 at wide range of cooling rate and the data is presented in Table 2.5. The eutectic [Mg (α) +$Mg_{17}Al_{12}$ (β)] of AZ91 is a divorced eutectic. In a slow cooled alloy, when casting cools from eutectic to the room temperature, the solid deformation takes place, in which the highly super saturated eutectic Mg decompose into alternative layers of solute deployed Mg and $Mg_{17}Al_{12}$ phase.

2.8.2.1 Eutectic solidification

The eutectic solidification controls the size, shape and distribution of the more brittle $Mg_{17}Al_{12}$ phase in the final microstructure, which, in turn, is likely to influence mechanical properties particularly ductility and creep strength of the alloy. Moreover eutectic growth affects feedability at a crucial stage when feeding is interdendritic and large pressure differentials are required to draw liquid through the dendritic network. [96]. The Mg-$Mg_{17}Al_{12}$ eutectic in Mg-Al alloy, exhibits a wide range of morphologies depending on the alloy composition and cooling conditions. The Mg-33% Al (eutectic composition) alloy, exhibits a lamellar morphology and at low growth rates and a fibrous morphology at higher growth rates. However, in low aluminum content Mg-Al alloys such as AZ91 and AM60, the eutectic has different morphologies, described as either completely or partially divorced [96].

Table 2.5: Liquidus and solidus temperature of AZ91 alloy at various cooling rates [99]

Cooling Rate (dT/dt, °C/s)	0.03	0.06	0.4	7.8	20.6	41.1
Liquidus (TL, °C)	600.2	600	599.5	598	595.5	593.8
Solidus (TS, °C)	435	435	430	328	-	-

Both fully and partial divorced eutectic morphology is shown in Figure 2.6. In fully divorced morphology, as shown in Figure 2.6 (a), the two eutectic phases are

completely separated in microstructure. Each interdendritic region consists of a single β- $Mg_{17}Al_{12}$ particle surrounded by eutectic α-Mg. A partially divorced eutectic morphology, as shown in Figure 2.6 (b), is characterized by an 'islands' of eutectic α-Mg within the β- $Mg_{17}Al_{12}$ phase, but the bulk of the α-Mg is still outside the $Mg_{17}Al_{12}$ particle, i.e. the volume fraction of α-Mg within the $Mg_{17}Al_{12}$ particle is much lower than the proportion by the equilibrium phase diagram [96].

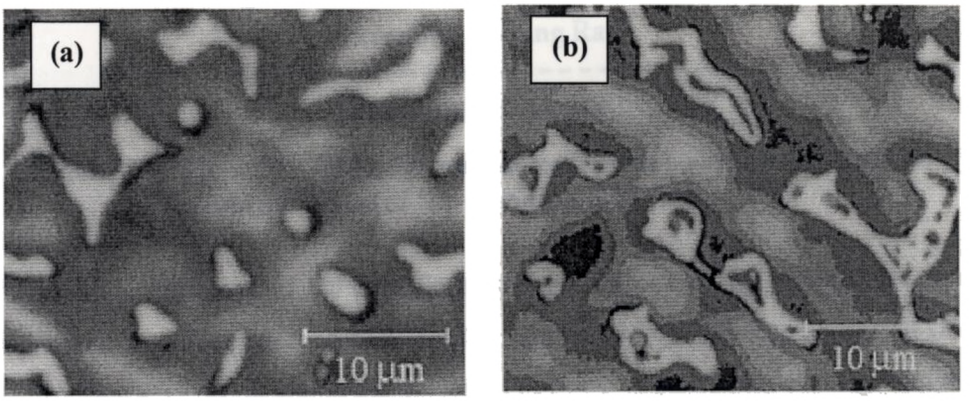

Figure 2.6: Microstructure of AZ91 alloy showing (a) fully divorced eutectic (b) partially divorced eutectic [16]

M.D. Nave et al [100] have shown that as the aluminum content of Mg-Al alloy increases, the eutectic progresses through the morphological sequence: fully divorced—partially divorced---granular---fibrous---lamellar. They also demonstrated that increase in cooling rates, increase the tendency towards divorced eutectic formation in a particular alloy. The effects of aluminum content, zinc content and cooing rate on eutectic morphology in permanent mould cast alloys are shown schematically in Figure 2.7 [96]. Hence the eutectic tends to become less divorced with increasing aluminum content, but more divorced with increases zinc content and cooling rate.

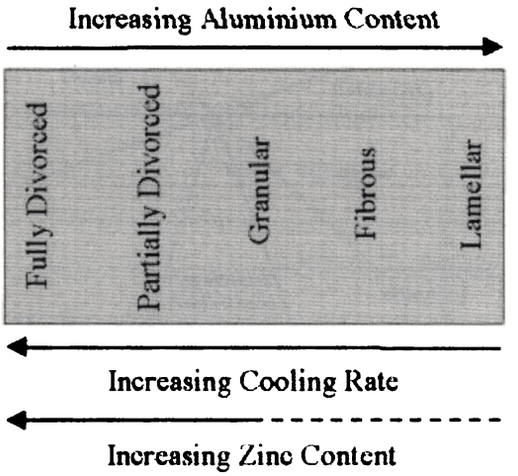

Figure 2.7: The effect of Al, Zn content and cooling rate on the eutectic morphologies of Mg-Al alloys [96]

The morphology of the eutectic is strongly influenced by the morphology of the primary dendrites, which determines the size and degree of interconnection of the interdendritic regions, in which the eutectic solidifies. Some under cooling below the eutectic temperature is required before solidification of the eutectic can commence. As the primary Mg dendrites continue to grow below the eutectic temperature, the composition of the liquid is enriched in aluminum past the eutectic coupled zone and into the region of the phase diagram where the $Mg_{17}Al_{12}$ phase grow faster than the coupled eutectic as shown in Figure 2.8. When nucleation of the $Mg_{17}Al_{12}$ occurs, a halo of this phase is deposited on the primary dendrites. If the amount of under cooling is not great and the eutectic region is sufficiently large, the formation of this halo consumes the excess solute in the boundary layer adjacent to the dendrite and the composition come back to the coupled zone (T_1 in Figure 2.8). This leads to the lamellar growth. This situation occurs with high aluminum content and at slow cooling rates. The higher amount of aluminum ensures the quite large interconnected regions of liquid between the primary dendrites. However, if the amount of aluminum is less and the cooling rate is fast, the composition of the liquid could increase well past the eutectic composition before nucleation of $Mg_{17}Al_{12}$ phase occurs. The entire pocket of the liquid could then become enriched to a composition, which is outside the coupled zone at that temperature. This leads to the formation of a partially or fully divorced eutectic.

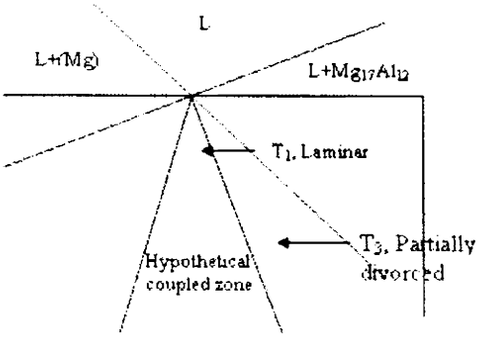

Figure 2.8: Mg-Al phase diagram showing the effect of Al and cooling rate on the eutectic solidification *[reproduced from ref. 96]*

Like aluminum content and the cooling rate, zinc also affects the morphology of the eutectic in Mg-Al alloys as shown in Figure 2.7 [101]. There are a number of possible ways in which zinc may affect the growth morphology of the eutectic. Zn, with a partition coefficient of 0.1 in Mg at 600°C, segregates more strongly to the liquid than aluminum (whose partition coefficient is 0.33 at 600°C). This increases the degree of constitutional under cooling ahead of the solid-liquid interface during the early stages of primary dendrite growth. The dendrites are therefore likely to grow with a more highly branched morphology. A more divorced eutectic is then favored because of the reduced size of the interdendritic spaces [101].

2.8.2.2 Solid state transformation

Solid state reaction takes place after the eutectic reaction when the cooling rate is slow. Normally this happens in gravity casting like sand and permanent mould cast AZ91 alloy. During this, the highly supersaturated eutectic α-Mg rejects the excess Al in the form of laminar kind of $Mg_{17}Al_{12}$ at grain boundary, known as discontinuous precipitates. An alternative layer of depleted α-Mg and $Mg_{17}Al_{12}$ precipitates form from the super saturated eutectic α- Mg during this reaction.

2.8.3 Grain Refinement

Grain refinement is an important practice used to improve the mechanical properties of castings. It is an essential and fundamental approach since grain size significantly influences the strength properties without compromising the ductility

much, and the grain size is usually determined at an early stage of solidification by nucleation of dendrites.

2.8.3.1 Effect of aluminum

Figure 2.9 shows the grain size change with increasing aluminum content in Mg-Al alloys [96]. A small addition of aluminum to pure magnesium leads to a morphological change of the primary phase from a cellular to a dendritic structure. Rosette-like globular equiaxed grains form with aluminum-rich solid solution between the dendrite arms. As the aluminum content increases further to 5%, dendrites with pools of eutectic phase between the dendrite arms start to develop and, when the aluminum content is further increase, a fully developed dendritic structure with sharp tips is observed.

The addition of small amounts of alloying elements such as zinc, manganese and rare-earths to Mg-Al alloys has little effect on nucleation of the primary phase since these elements are mostly segregated to form secondary phases well after the primary phase has nucleated [99].

2.8.3.2 Super heating treatment

Several methods of grain refinement have been developed. The first method of grain refinement is by a simple thermal treatment prior to casting, known as 'superheating treatment'. This method involves rapid cooling of the melt to the desired casting temperature after short holding time at an elevated temperature, generally between 150°C and 260°C above the equilibrium liquidus temperature of the alloy [102]. This method is only useful for Mg-Al alloys like AZ91, where as in other magnesium alloys refinement by the means described is marginal [103, 104]. Usually, superheating treatment is not much effective, owing to the small number of nucleation sites forms during this treatment [105]. It is assumed that superheating of Mg-Al alloys facilitate the formation of many intermetallic compounds, which serves as the nucleation site for α-Mg. One hypothesis is that hexagonal Al_4Mn forms as a result of the manganese content in the commercial alloys of the AZ series [106]. According to another theory the compound is of the type Al_4C_3, or iron Aluminide, both of which

has been observed experimentally [107]. The presence of these compounds can be justified with the fact that superheated Mg-Al alloy melt strongly dissolves crucibles made of iron or steel. Such dissolution, or the presence of organic impurities, could be the source of the iron or carbon necessary for inoculation. Despite the successful grain refinement achieved by the superheating method, this techniques has several practical problems, mainly related to the higher operating temperatures involved [108].

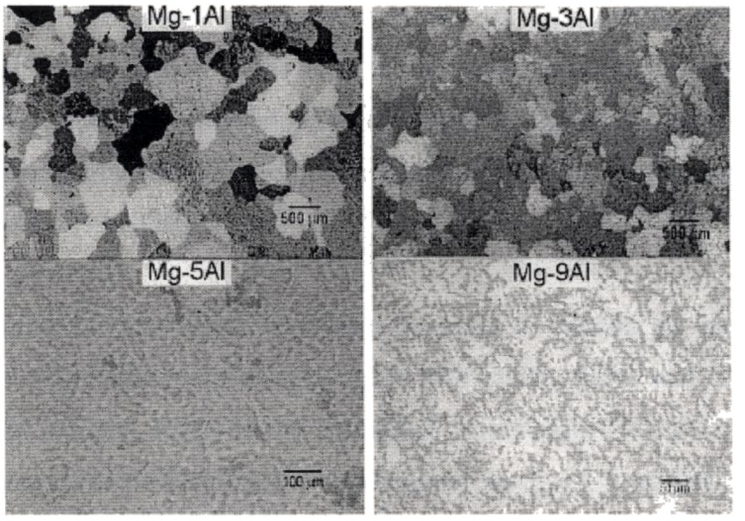

Figure 2.9: Micrographs of Mg-Al alloys showing the effect of aluminum on grain refinement [96]

2.8.3.3 Elfinal process

Successful grain refinement has been reported by the addition of ferric chloride (Elfinal process) in magnesium alloys containing aluminum and manganese [109, 110]. The amount of grain refinement achieved by the Elfinal process is somewhat similar to that achieved by superheating. The mechanism by which the grain refinement takes place by Elfinal process is still not clear. Partridge [111] has reported that a rusty mild steel crucible that loosely adherents rusty iron produced grain refining effect. Nelson et al [103] have pointed out that the Elfinal process did not work for Mg-Al alloys containing no manganese. Emley apparently preferred the Al_4C_3 hypothesis for the grain refinement [107]. Recent studies by Cao et al [112] have reconfirmed that the Elfinal process has lead to grain refinement when high-

purity Mg-Al alloys melted in carbon free aluminum titanite crucibles and suggesting that the Elfinal process has little to do with the Al_4C_3 hypothesis proposed by Emley. However, due to the detrimental effect on corrosion resistance from the addition of Fe, the Elfinal process has not attracted industrial attention.

2.8.3.4 Carbon inoculation

The addition of carbon to the melt (carbon inoculation) offers more practical advantages accompanied by lower operating temperatures and less fading. Various carbon-containing agents such as organic materials like C_2Cl_6, CCl_4, SiC particles or granular graphite and carbon in the form of wax-fluorspar-carbon compound have been reported to produce successful grain refinement in Mg-Al alloys [111,113, 114]. Similar to superheating, carbon inoculation is effective only to magnesium alloys that contain aluminum [115-118].

A number of hypotheses have been proposed to explain the mechanism by which carbon inoculation methods cause grain refinement. Once such mechanism is that aluminum carbide, Al_4C_3 is the compound responsible for the refining effect [103]. But there are some literatures, which suggest that Al-C-O particles, probably in the form of Al_2OC, could be a much more potent nucleant than Al_4C_3 in terms of lattice match [119-122]. Qinglin Jin et al [123] have proposed a different theory for the grain refinement by C addition. The addition of carbon in the Mg-Al melt, segregate during the solidification and provide constitutional super cooling. This restricts the grain growth. However, recently, M. Qian et al [118] have rejected this hypothesis. Moreover, the efficiency of grain refinement with Carbon inoculation process is depending upon the holding time and temperature of the melt. Extending the time of interaction between inoculant and melt adversely affects the refinement, as illustrated in Figure 2.10 [124]. According to the figure, inoculation produces finer grains after much shorter holding times and at lower temperatures.

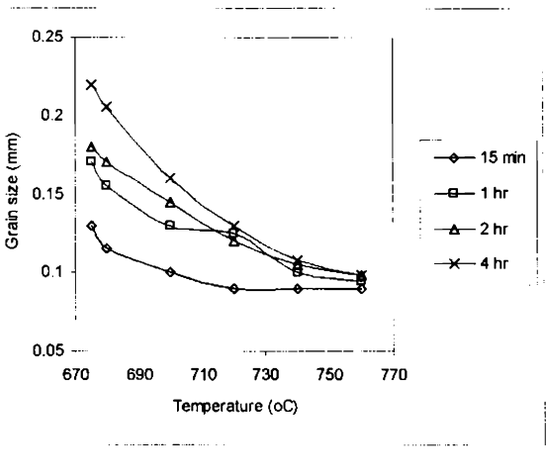

Figure 2.10: Effect of temperature and holding time on the fading effect of Carbon inoculant in Mg melt ***[reproduced from ref. 124]***

It is also shown that the grain size of AZ91 varies substantially depending on the purity of the ingots used to make the alloy [125]. It is found that the structure of the high purity alloys is finer than that of ordinary alloys both with and without superheating. The reason for the grain refinement in the high purity alloys is the absence of manganese, iron, carbon and oxygen, which otherwise canceling the refining effect of Al-C compounds [125].

2.8.3.5 Thermo mechanical treatment

Mechanical working like rolling, extrusion, forging are other potential way of achieving grain refinement. Number of publications is available on the effect of these processes on the grain refinement of Mg-Al based alloys particularly wrought alloy AZ31 [126-128]. Ravikumar et al [129] have reported that 5μm grain size is obtained in AZ91 using hot extrusion at a temperature of 335°C. There are other studies, which reports on grain refinement of AZ alloys by severe plastic deformation processes like Equal Channel Angular Pressing (ECAP), Accumulative Roll Bonding (ARB), Large Strain Rolling (LSR) and hot multiple forging [130-133].

2.8.4 Heat Treatment

2.8.4.1 General behavior

The maximum solubility of aluminum at eutectic temperature (437°C) is around 12%, which reduces down to around 2% at the room temperature. This solubility variation provides AZ91 alloy system to be age hardenable. The precipitation processes in AZ91alloy have been studied extensively [134, 135]. The precipitation in this alloy system is relatively simple; plates of the equilibrium phase, $Mg_{17}Al_{12}$, are formed without any intervention of a transition phase. No evidence of G.P zones is so far reported in this alloy. The normal sequence of heat treatment is solution treatment at 410°C for 48 h and ageing at a temperature range from 150 to 250°C. During solution treatment, dissolution of eutectic $Mg_{17}Al_{12}$ phase is slow mainly due to its massive size. With 24 h of solution treatment, complete dissolution of this phase take places, however, 48 h of solution treatment is normally required to get completely homogenous microstructure of Al in Mg matrix [134]. Cold water quenching is followed by solution treatment to retain the aluminum in solid solution.

A typical ageing curve at different temperatures for AZ91 alloy after solution treatment is shown in Figure 2.11 [134]. In general, the ageing curve can be divided in to four distinct regions as follows [136]:

1. A incubation period where the hardness is not increased with time
2. A rapid increase in hardness with respect to time
3. Slow down in the rate of hardening nearer to the peak hardness
4. Leveling off at the peak hardness

It can be seen from Figure 2.11 that a large decrease in peak hardness when the ageing temperature increases from 100 to 150°C and another large decrease in peak hardness observed between 250 and 300°C. The hardness for ageing at 200 and 150°C remained at the maximum value for a significant period before gradually decreasing. Ageing kinetic is increased with increases in ageing temperature. The ageing kinetic also increases with the amount of aluminum in the solid solution. S. Celotto et al [134] have reported that the higher peak hardness in shorter time obtained in AZ91 alloy compared with Mg-6Al alloy is due to the difference in

aluminum content. He also observed that the presence of zinc in the AZ91 alloy improves the hardness and ageing kinetics over its counter part Mg-9Al by reducing the solubility of aluminum in magnesium matrix [134].

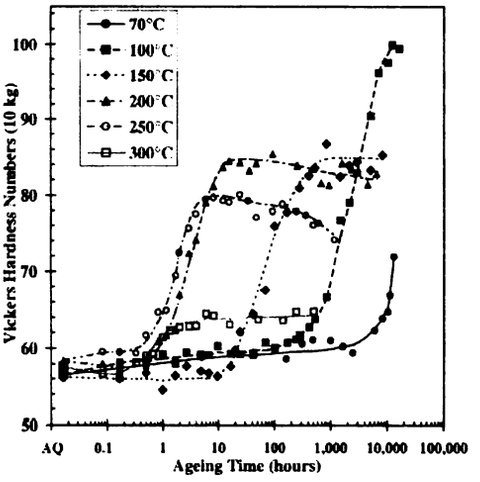

Figure 2.11: Typical ageing curve for AZ91 alloy at different temperatures [134]

2.8.4.2 Continuous precipitate

The microstructural development of Mg-Al binary alloys and Mg-Al-Zn ternary alloys for a range of ageing temperatures has been investigated in a number of studies [134, 135]. During ageing the $Mg_{17}Al_{12}$ precipitates out in two forms: discontinuous (cellular) and continuous (intragranular) form. Discontinuous precipitation (DP) is the cellular growth of alternating layers of $Mg_{17}Al_{12}$ phase and near equilibrium magnesium matrix at high angle grain boundaries. Growth of the discontinuous precipitates regions ceases relatively early in the precipitation process. Then, continuous precipitation (CP) takes place in the remaining regions of the matrix that are not already occupied by discontinuous precipitation.

Clark [135] and Crawley and Lagowski [137] have reported that the continuous precipitates consist of relatively large plates on the basal plane of the matrix. The predominant orientation relationship (OR) between the β-phase plates and the magnesium matrix is reported to be the Burgers OR, namely: (0001)m//(110)p and [12'10]m//[11'1]p [137, 138]. Some precipitates have also been observed perpendicular to the basal plane of the matrix [139]. Two different ORs have been

reported for these precipitates: (0001)m//(110)p, [12'10]m//[11'2']p by Crawley and Lagowski [137] and Crawley and Milliken [137]; and (12'11)m//(11'0)p, [I2'10]m//[11'2']p from Poter reported by Duly et al [139]. It is also found that dislocations acts as a nucleation site for continuous precipitation [135, 140]. Clark [135] has observed that introduction of dislocations by cold work prior to aging markedly improve the ageing kinetics and increase the peak hardness. Figure 2.12 shows the effect of 1% prior strain by cold work on the age hardening of Mg-9Al alloy. He found the density of continuous precipitates for a given time of aging in the pre strained by the cold working is higher. He also observed that nucleation of continuous precipitates occurs most rapidly in the interfaces of, and within, {1012} twins.

It is continuous, not discontinuous precipitate, which is responsible for most of the age hardening in AZ91 alloy [141]. Lagowski and Crewley [138] have carried out a double stage (96 h for 100°C and 192 h at 140°C) ageing on AZ91 after solution treatment and observed increase in strength. It is found that the double stage aging leads to the formation of higher amount of continuous precipitation and the decrease in inter precipitates spacing. The hardening mechanism explained by Clark [**135**] suggested that the continuous precipitation suppresses the basal slip and {101'2} twinning and promotes cross slip in the prismatic plane. This generates complex dislocation tangle, which harden the alloy. However, the hardening response of AZ91 is generally less than that observed in many heat-treatable aluminum alloys. There are two reasons suggested for the poor hardening response of AZ91. The order of magnitude difference in the number of continuous precipitates per unit volume compared with many age-hardenable aluminum alloys. Another reason is the orientation of the precipitates with respect to the predominant slip plane of the matrix. The effectiveness of a single precipitate as an obstacle to dislocations is improved if it is oriented such that it intersects more operating slip plane. According to Celotto [134], the continuous precipitation, rod or lath-shaped precipitates lying perpendicular or at an angle to the basal plane are more effective than symmetric lozenge or lath-shaped precipitates lying parallel to the basal plane in preventing slip in the magnesium matrix.

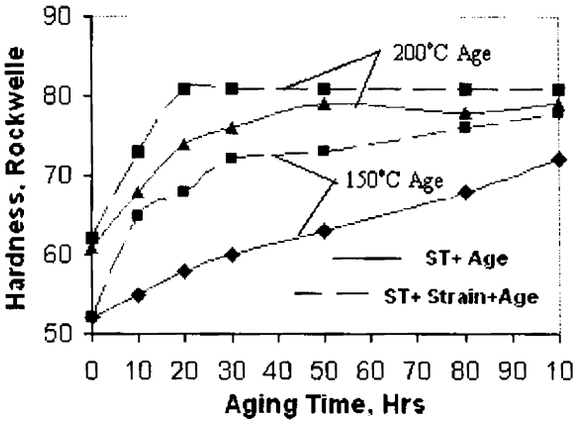

Figure 2.12: Effect of cold work on the ageing behavior of AZ91 alloy [135]

2.8.4.3 Discontinuous precipitate

Discontinuous precipitation (DP) is a heterogeneous reaction, which leads to the formation of a lamellar structure behind a moving grain boundary [142]. The schematic diagram representing the discontinuous precipitation process is shown in Figure 2.13 [143]. Two phases (α, β) forms simultaneously from a supersaturated single α_0 matrix. The moving grain boundary, called reaction front (RF), act as a short circuit path for the diffusion of the solute atoms [144-147]. DP is arrested when CP relives the solute super-saturation in front of the advancing nodule. The nucleation of discontinuous precipitates are mainly depends upon grain size, initial solute content, temperature. Three main nucleation mechanisms have been identified for discontinuous precipitation:

1. A precipitate first nucleates at the grain boundary and then acts to pull it from its initial position; the movement is associated with a reduction of interfacial energy as proposed by Tu and Turnbull [148-150]
2. The initial displacement of the grain boundary is due to chemical forces (similar to the DIGM (diffusion induced grain boundary migration) driving force) as for steady state growth, as proposed by Purdy and Lange [151]

3. The force responsible for the initial grain boundary motion are capillarity forces, identical to those that act during grain growth or recrystallization, as proposed by Fournelle and Clark [152]

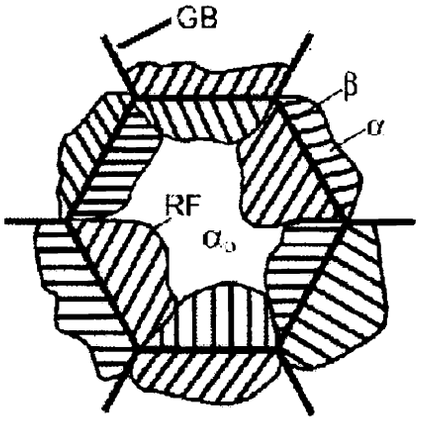

Figure 2.13: Schematic diagram showing DP process [143]

Duly and Brechet [153] studied the nucleation phenomena with respect to ageing temperature. It appears that at high temperatures (T.>220°C) Clark's nucleation mechanisms dominates where as at lower temperatures (T~140°C) Tu and Turnbull's mechanism dominates. At intermediate temperatures it is found that Purdy and Lange's mechanism is the one, which dominates.

Effect of discontinuous precipitation on the mechanical properties particularly creep properties of AZ91 are studied and reported [28, 154]. Since the discontinuous precipitation takes place at the grain boundary and the reaction associated with movement of grain boundary, it leads to the grain boundary sliding particularly in die cast alloy at elevated temperature exposure. This reduces the creep properties of AZ91 alloys [28].

2.8.5 Tensile Behavior

Tensile properties of AZ91 find scatter. This is because the tensile properties are highly sensitive to the microstructure. The tensile properties are mainly depends on grain size and volume and size of second phase [155, 156]. Porosity is another

major factor, which affects the tensile properties much [157-160]. The tensile properties are also sensitive to temperature and strain rate.

2.8.5.1 Effect of temperature and strain rate

The tensile properties of AZ91 alloy at high temperatures are well documented in literature. A drastic reduction in both yield and Ultimate strength occurs while the ductility improves considerably. As far as AZ91 alloy is concerned the main room temperature strengthening element is $Mg_{17}Al_{12}$ intermetallics. But this intermetallic has a low melting point (437^0C) and has a tendency to become coarsen at elevated temperature i.e. above 100^0C and no longer act as a barrier for dislocations [161]. More over $Mg_{17}Al_{12}$ has a cubic crystal structure, which is incoherent with the hcp magnesium matrix. Therefore this phase leads to the poor elevated temperature properties of AZ91 alloy. It is also important to note that temperature has a great effect on the tensile properties at lower strain rate whereas at higher strain rate, the temperature effect is less significant [162].

Figure 2.14 shows the variation in flow stress of AZ91 as a function of deformation temperature for various strain rates. The flow stress for each strain rate is determined at a fixed strain of 0.1. It is noted that the decrease in flow stress with temperature at strain rate at 10^{-3} S^{-1} is far grater than that at a strain rate of 10^3 S^{-1}. It is suggested that climb controlled dislocation creep could be a dominant deformation process in the low strain rate range. However, the operating deformation mechanisms at high strain rates are suggested to be dislocation glide and twinning even at elevated temperatures [162].

2.8.5.2 Effect of grain size

Several studies have been made of grain size strengthening in magnesium and in several of its alloys. Due to the fact magnesium is basically a HCP materials, it is more sensitive to the grain size. In general, the yield strength as a function of grain size can be represented as Hall-Petch equation;

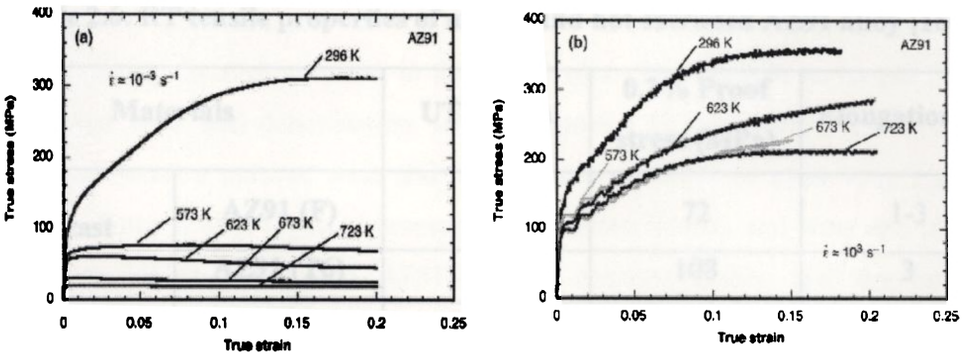

(a) (b)

Figure 2.14: Typical tensile behavior of AZ91 alloy at different temperatures and strain rates (a) at strain rate 10^{-3} s^{-1}(b) at 10^{3} s^{-1} [162]

$$\sigma = \sigma_0 + Kd^{-1/2}$$

where σ is the yield stress, σ_0 is the yield stress of a single crystal, K is a constant and d is the grain size. The value of K increases with increasing the Taylor factor [163]. The Taylor factor generally depends on the number of the slip systems. Because the slip systems are limited and the Taylor factor is larger for HCP metals than for FCC and BCC metals, HCP metals exhibit the strong influence of grain size on strength [164]. Reduction in grain size improves both strength and ductility. The higher strength and ductility obtained by thermo mechanical treatment and severe plastic deformation is due to the same fact that these processes provide fine grain size in the order of 1μm. Table 2.6 provides the room temperature tensile properties of as cast and hot extruded AZ91 alloy [164]. It can be seen that both strength as well as ductility is improved significantly. This is attributed to the fine grain structure obtained in hot extrusion. It is observed that intergranular fracture is occurred in magnesium alloy with a large grain size: however, intergranular fracture is limited in magnesium alloy with a small grain size [165], indicating that the fracture mechanism is changed by grain refinement. This is because the critical stress for crack propagation at grain boundaries increases with decreasing grain size [165].

Table 2.6: RT tensile properties of as cast and hot extruded AZ91 alloy [164]

Materials		UTS, MPa	0.2% Proof stress (MPa)	Elongation, %
As cast	AZ91 (F)	131	72	1-3
	AZ91 (T6)	235	108	3
Extruded	AZ91	341	244	13

The fine grained AZ91 alloy not only shows high strength and ductility at room temperatures, but also superplasticity at elevated temperatures. Recently, it has been reported that an extruded AZ91 exhibits a maximum elongation of 425% at a testing temperature of 250°C with a strain rate of 3 X 10^{-4} s^{-1} [166]. Y.H. Wei et al [167] have also reported that the rolled AZ91 shows excellent super plasticity with the maximum elongation to failure of 455% tested at 350°C and a strain rate of 10^{-3} s^{-1}. The dominant deformation mechanism in high strain rate superaplasticity is reported as grain boundary sliding (GBS). Moreover, recently it is reported that the AZ91 processed by ECAE (Equal Channel Angular Extrusion), shows superplastic behavior at even low temperatures of 175-200°C [168]. This is attributed to a very small grain size in order of 1 μm.

2.8.6 Wear Behavior

Wear properties are important especially when magnesium alloys are to be applied for critical automobile applications. Wear, in the broadest sense, may be defined as the removal of surface material of a component. There are several mechanisms of wear, which include seizure, melting, oxidation, adhesion, abrasion, delamination, fatigue, frettling, corrosion, and erosion [169, 170]. Wear may normally be reduced by using a lubricant with appropriate anti-wear additives or changing the materials and/or the operation parameters affecting the wear rate. There are few studies available on wear behavior of AZ91 alloy. H. Chen et al [171] have carried out a dry sliding wear testing on AZ91 alloy against AISI 52100 steel ring within a load range of 1-350 N and a sliding velocity range of 0.1 – 2 m/s. They observed two main wear regimes, namely a mild wear regime and a severe wear regime. In the mild

wear regimes, it is found that the volume loss due to sliding wear increased linearly with the sliding distance where as in the severe wear regimes, it is no longer linear. Oxidational wear and delamination wear is reported in mild wear regime. Sever plastic deformation induced wear and melt wear is observed in sever wear regime. Recently, Song et al [172] have investigated wear mechanism and wear rate of two magnesium alloys, AS21 and AZ91D under constant sliding and dry loading conditions and concluded that the wear rate of the alloy mainly depends on the alloy hardness. D.S Mehta et al [173] also have reports that AS21 alloy shows higher wear rate than the AZ91D alloy due to its lesser hardness. Peter et al [174] have conducted both unidirectional and reciprocation sliding motion wear test on die cast and thixomolded AZ91D alloy. In reciprocating tests, the thixomolded specimens have slightly lower wear rates than die cast specimens where as in unidirectional sliding, both have similar wear rates, indicating that the microstructural differences do not have a pronounced effect on wear when the direction of surface shearing remained the same for each pass of the slider [174].

2.8.7 Creep Behavior

Creep is time-dependent deformation occur at high temperature normally above $0.5T_m$ (T_m – melting temperature). While elastic-plastic deformation, strain is a function of stress only whereas, creep strain is a function of stress, time and temperature [175]. Figure 2.15 shows a typical creep-strain versus time curve for a metal, where three distinct regions can be observed [176]. After an initial and instantaneous restructuring of the metal, primary stage creep occurs with decreasing creep rate. Here, the work hardening is higher than the stress recovery (work softening). In the secondary creep stage (stead-state) the metal experiences a two-way balance between work-hardening and stress recovery resulting in steady-state creep (constant creep-rate). The tertiary creep stage exhibits increasing creep rate due to necking and cracking resulting finally in fracture.

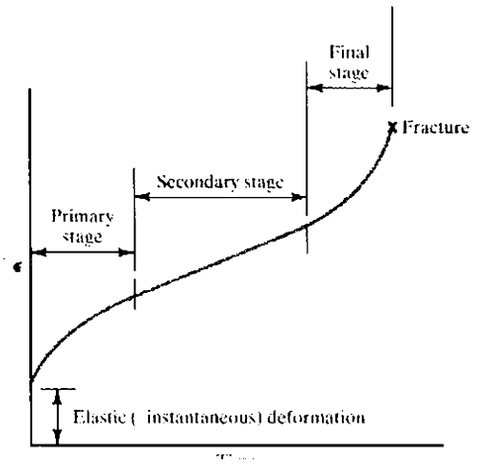

Figure 2.15: Typical creep-strain versus time curve for metals [176]

2.8.7.1 Creep behavior of pure magnesium

The creep response of pure magnesium has been extensively investigated [177-181]. In the temperature regime of around 200°C, the creep response of pure magnesium is fully comparable to that observed in other pure metals, where creep is controlled by dislocation climb [181]. In these cases, the activation energy for creep is equivalent to that of self-diffusion ($Q=Q_l$), and the stress exponent in the conventional Norton equation is around 5. It is generally accepted that at temperatures below 300-330°C dislocation glide (<11'20> {0001} slip system) on basal planes is dominant, whereas slip on pyramidal systems, {101'1} or {112'1} in the <11-20> directions, is the rate controlling mechanism above these temperature [182].

2.8.7.2 Creep behavior of die cast AZ91

Number of creep studies have been published on die cast AZ91 Mg alloys [17-27]. But still the creep deformation mechanism is not clearly understood. Some authors found the dynamic precipitate occurs during creep exposure is a fine particles and it strengthen the alloy. Coarsening of these precipitates is the softening mechanism. But it is also stated by others, that discontinuous precipitate form during creep and leads to the grain boundary sliding.

Regev et al [183] have reported that the creep rates of AZ91 are found to be a few orders of magnitude lower than these of pure magnesium and elongation to

fracture is to be at least 1.5 times higher than the pure magnesium. Regev [183] also reported a stress exponent 'n' value of 6.9 at 150°C and 5.4 at 180 °C and related the creep mechanism to dislocation creep. Blum [184] conducted a compressive creep testing on AZ91 die casting in the temperature range of 70-150°C and reported that the dislocation creep is the dominant mechanism and no grain boundary sliding contribute to the deformation. William K. Miller [185] has found that AZ91 alloy is creeping even at room temperature under the stress level of 60-120 MPa. The measured stress dependency of the secondary creep rate suggests that diffusion driven dislocation climb may be the rate controlling creep mechanism.

M.S. Dargusch [28] observed grain boundary sliding in AZ91 alloy and suggested that it play a dominant role at least in low stress levels. Creep testing of die cast AZ91at stresses in the range of 20-60 MPa and temperature in the range of 125-175°C, gives an 'n' value of 1.5 and a 'Q' value of 44 KJ/mol [28]. This value of Q is close to 30 KJ/mol determined for the apparent activation energy for the formation of discontinuous β precipitation in Mg-9Al alloy. As it is evident that DP normally forms at a grain boundary and migrates in to the nearby grains, it damages the grain boundary. This will lead to the grain boundary sliding and formation of cavities and subsequent failure. Indeed they observed grain boundary sliding in AZ91 alloy as shown in Figure 2.16 in which the splitting of marked line across the grain boundary is clearly seen.

2.8.7.3 Creep behavior of AZ91 against other Mg-Al alloys

The creep behavior of AZ91, AS21, AS41 alloys are compared by Dargusch et al [28, 186] and have found that under all stress conditions and temperatures, the relative behavior of the alloys is similar with the creep strength of AE42 and AS21 being considerably better than AZ91. The comparison creep curves of three alloys at 150°C and 50 MPa is shown in Figure 2.17.

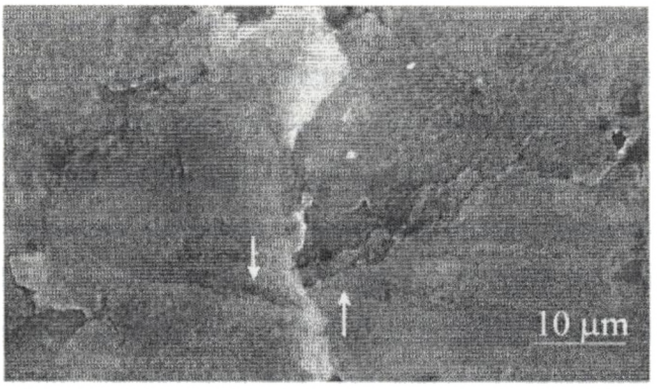

Figure 2.16: Micrograph showing grain boundary sliding in die cast AZ91 alloy [28]

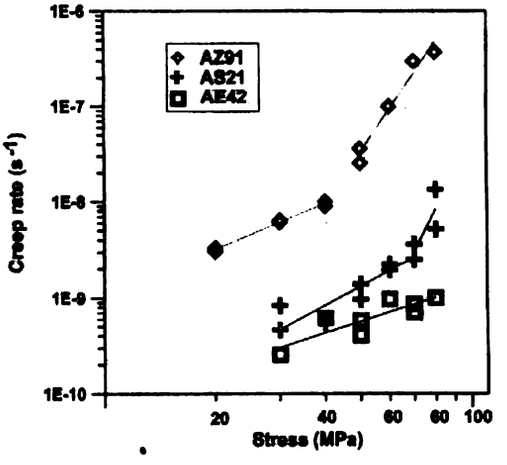

Figure 2.17: Stress dependency on secondary creep rates of different Mg-Al based alloys [186]

The superior creep resistance by other alloys over AZ91 alloy is explained by the amount of dynamic β precipitates form during high temperature exposure [28, 186]. The cast microstructure of AS21 and AE42 contain less amount of supersaturated α Mg because of less aluminum content compared to AZ91 alloy and as a result, their microstructures are much more stable and considerably less discontinuous precipitates occurs during exposure at elevated temperatures. Moreover these alloys also contain strong stable intergranular phases, Mg_2Si, in the case of AS21 and Al_4RE in the case of AE42, which can be expected to pin grain boundaries and hinder both grain boundary movement.

On the other hand W.Blum [30, 31, 184,] compared the creep behavior AZ91 die cast alloys with the other Mg-Al alloys like AS41, AS21 and AE42. From stress-strain curve obtained under compressive loading they found that AZ91 alloy has highest work hardening and has higher yield stress at all the testing temperature. They measured the maximum deformation resistance during compressive creep and represented in Z-σ plot, which is shown in Figure 2.18. AZ91 has a higher maximum deformation resistance at stress above 150 MPa and inferior to AS21 below this stress level. Apart from this, the values of AZ91 and AM60 lie on the one hand and AS21 and AE42 on the other hand. They showed that AZ91 alloy has the highest creep resistance of all alloys in the whole investigated range, with the exception of AS41 which becomes more creep resistant than AZ91 at stresses below 130 MPa. They attributed this behavior to high rate of work hardening of AZ91, combined with the precipitation hardening due to the dynamic precipitation of $Mg_{17}Al_{12}$. AZ91 alloy is expected to have highest super saturation of Al and subsequent precipitation of β during creep, strengthening the alloy. At low stresses, the alloys like AS21, AS41 exhibits good creep behavior because of the Mg_2Si precipitates, which is more stable than $Mg_{17}Al_{12}$ phase. The same author has proved this precipitation hardening in AZ91 alloy by conducting creep test on annealed, which exhibited higher creep resistance [187].

2.8.7.4 Creep behavior of ingot cast AZ91

There is not much creep studies are available on the gravity cast AZ91 alloy. However, a detailed work on the creep behavior of ingot AZ91 alloy carried out by Regev et al [29, 188] suggested that no grain boundary sliding contribute to the creep deformation. The creep mechanism observed is either dislocation creep or dislocation glide. Dynamic precipitation is also observed in ingot casting. It is suggested that creep induced precipitates are strengthening the alloy against creep.

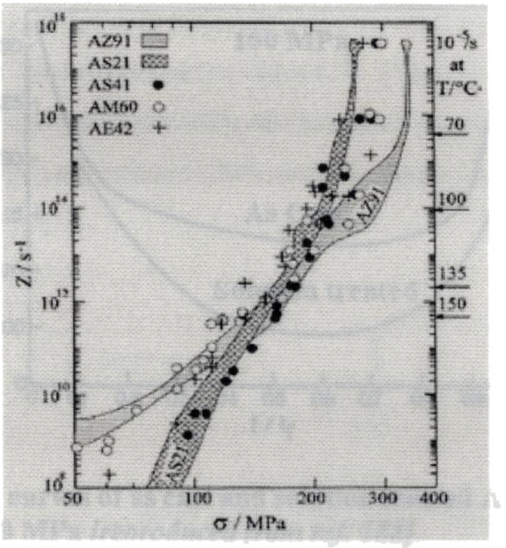

Figure 2.18: Maximum deformation resistance of die cast Mg-Al alloys in Z-σ plot [184]

The precipitation hardening is verified by conducting creep testing on AZ91 alloy ingot casting at various tempered conditions i.e., as cast, solutionized and aged [188]. Superior creep resistance of solution treated ingot AZ91 alloy castings over the as cast and aged alloy is observed as shown in Figure 2.19. The minimum creep rate of the solution-treated specimens is lower than that of the as cast specimen tested under the same condition (0.135%/h at 100 MPa compared with 0.05%/h for the as cast). It is also observed that the aged specimens showed higher minimum creep rates than the as cast specimens (0.11%/h at 50 MPa and 150°C compared with 0.025%/h for the as cast). More over that the minimum creep rate occurred app.2/3 of the time to failure in as cast and solutionized specimens where as in aged specimens, the minimum creep rate is attained at the earlier stage. This behavior is attributed to the β-$Mg_{17}Al_{12}$ precipitates formation during high temperature exposure. According to Regev [188], in the solutionized samples the hardening process starts with solid solution hardening as more aluminum in the solid solution and then changes to precipitation hardening whereas in aged sample neither solid solution nor precipitation strengthening takes place. The poor performance of the aged specimens is due the softening effect takes place because of the precipitates coarsening straightway. This indicates that submicron precipitates formed during creep exposure in ingot casting strengthens the alloy.

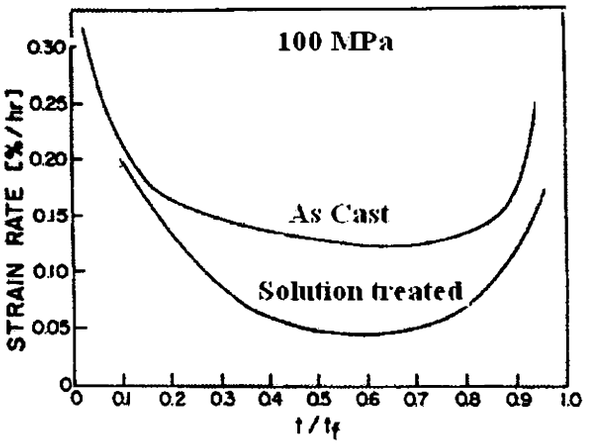

Figure 2.19: Creep curves of as cast and solution treated AZ91 alloy at 150°C and 50 MPa *[reproduced from ref. 188]*

While comparing the creep behavior of die and ingot cast AZ91, Regev et al [189] have found that the minimum creep rate was reached approximately two thirds of the time to rupture in the ingot specimen compared to one third of that time in the pressure die-casting as shown in Figure 2.20. Apart from that, the minimum creep rate at given test parameter is much higher in the pressure die casting than in ingot. These behaviors are related to the difference in hardening mechanisms due to the dynamic precipitation process involved during creep. Due to the faster cooling rate, the die cast alloy contains more amount of eutectic β- $Mg_{17}Al_{12}$ and less amount of Al in α- matrix. On the other hand, due to the slow cooling rate in gravity ingot casting, more amount of Al goes into the α-Al matrix. The higher content of Al in the matrix leading to prolonged precipitation until steady state is reached in ingot casting. This leads to the slow creep rate in ingot casting. In contrast the precipitation process comes to end at earlier in the die casting and coarsening of precipitates takes places, which degrade the microstructure [189, 190].

S.Spigarelli [191] also compared the creep behaviour of AZ91 alloy processed by die casting and thixo casting with the ingot casting at 150°C with an initial stress of 100 MPa. Similar kind of results are observed as the creep behaviour of die-cast and the thixo-formed samples exhibited a similar response, characterized by a relatively short primary stage followed by a short minimum-creep-rate range rather than by a secondary regime, and by a prolonged tertiary region. The ingot exhibited a longer

primary stage. Rupture in this case occurred abruptly after a short tertiary stage and exhibited the greatest creep strength as shown in Figure 2.21. The higher creep resistance of the ingot alloy is attributed to the extended precipitation of fine particles during creep exposure and marked difference in grain size with the die and thixoformed alloy samples.

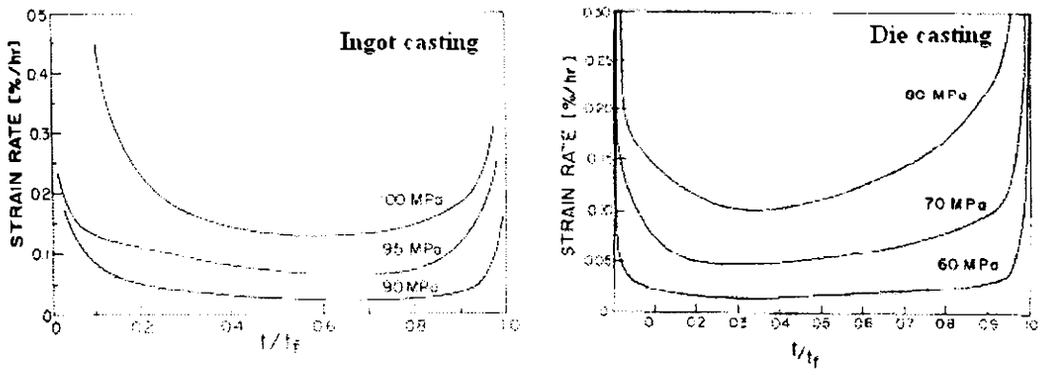

Figure 2.20: Creep curves of ingot and die cast AZ91 alloy at 150°C [189]

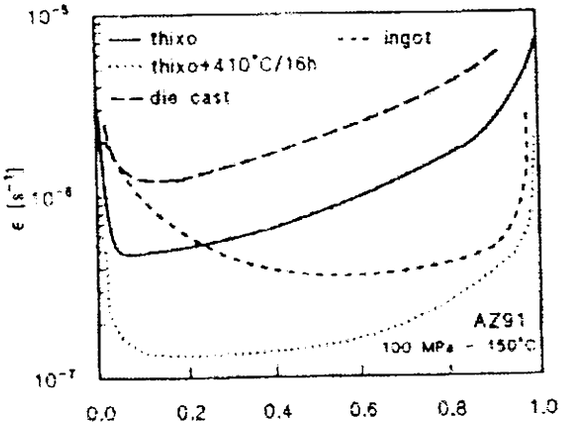

Figure 2.21: Comparison of creep behaviour of AZ91 alloy processed through different Casting processes [191]

2.8.8 Corrosion Behavior

Poor corrosion resistance is a recognized property of magnesium. Hence, this property is playing a prominent role in preventing more widespread use of magnesium, especially in aerospace applications. Of course, magnesium is the most active metal used in engineering applications and corrodes so readily in some

environments where magnesium alloys often serve as sacrificial anodes on structures such as ships' hulls, buried pipelines, and steel piles [192].

The standard electrochemical potential of magnesium is -2.4 V (NHE), and even though in aqueous solutions it shows a potential of -1.5 V due to the formation of $Mg(OH)_2$ film. Consequently, magnesium dissolves rapidly in aqueous solutions by evolving hydrogen below pH 11.0, the equilibrium pH value for $Mg(OH)_2$ [193, 194]. The reaction is relatively insensitive to the oxygen concentration. The overall reaction is described as

$$Mg+2H_20 \longrightarrow Mg(OH)_2 + H_2$$

As corrosion proceeds, the metal surface experiences a local pH increase because of the formation of $Mg(OH)_2$, whose equilibrium pH is about 11. The protection supplied by this film is highly dependent on the conditions of exposure. For example, magnesium is very resistant to corrosion in small volumes of water that are free of species aggressive to the film. In the atmosphere, Mg reacts further with carbon dioxide, forming magnesium carbonate, which acts as a sealer for the hydroxide film. High purity magnesium therefore has the potential to be extremely better in the atmosphere than iron [195]. Problems arise when impurity elements are present at levels that promote micro galvanic cell action, when the metal or alloy is galvanically coupled to an effective cathode materials, or when the nature of the environment prevents formation or maintenance of a protective film.

2.8.8.1 Corrosion behavior of AZ91

The corrosion behavior of AZ91 alloy is very sensitive to the microstructure. As mentioned already the AZ91 alloy consists of three microstructural constituents in the cast microstructure. These are primary α, eutectic α and β-$Mg_{17}Al_{12}$ intermetallic. The primary α phase normally contains much less aluminum compared to that of eutectic α and β phase. The β phase reported to have more cathodic potential than that of α phase [33]. Thus, α and β phases when in contact will easily cause galvanic corrosion. Song et al [34] by examining the individual phases, have shown that in

chloride solution, the rest potential of the β phase (-1.6 V) is some 300 mV positive to α phase (potential, -1.3V). Lunder et al [33] also found that the positive drift of the rest potential of $Mg_{17}Al_{12}$, which could be attributed to the passivation of this phase.

That way in AZ91 alloys, size and distribution of β phase together with the coring of α phase makes the alloy surface electrochemically heterogeneous. The corrosion behavior of the material thus depends on how these microconstituents interact when it is exposed to aqueous environment. The above said parameters changes with processing route, gives rise of different corrosion behaviors for materials prepared by different processing routes.

2.8.8.2 Effect of micro constituents

(i) α-Mg

The α phase plays an important role in the corrosion behavior of AZ91 [36], and its corrosion performance determines corrosion behavior of the alloy. The composition of α should be crucial to its corrosion behavior. In general, within α grain, the composition distribution is not always uniform. It has been shown that the aluminum concentration can vary from a few percent in the grain interior to 10% in the vicinity of the β phase [35]. The effect of aluminum on the corrosion behavior of Mg alloys has been subject to many investigations [98, 196, 197]. It has been generally agreed that the presence of aluminum is beneficial in improving the corrosion behavior of magnesium. Later it is found that for effective protection an optimum level of aluminum is required. Ambat et al [36] observed the region preferentially corroded is one with less than 8% aluminum. Lunder et al [33] also reported that this quantity is about 8% where as Warner et al [198] using TEM studies on rapidly solidified ribbons of composition Mg-9Al, arrived at the conclusion that it is >5%. Hehmann et al [199] studied corrosion behavior of rapidly solidified ribbons with aluminum concentration varying between 9 and 62.3%. They observed a decrease in the corrosion rate and E_{corr}, from 9.6 to 23.4% Al in aerated 0.01 M sodium chloride solution. Daloz et al [197] have reported that the increase in aluminum content in the material shifts the potential towards anodic side. But many authors find the corrosion initiates in α – Mg where the aluminum content is lesser.

This discrimination is explained by the presence of zinc in the solid solution. It is also reported that in Mg-Al alloys, presence of Zn influences the E_{corr} of both matrix and precipitates and has a beneficial effect on the corrosion resistance of the alloys [197].

(ii) β-$Mg_{17}Al_{12}$

The β-$Mg_{17}Al_{12}$ phase is cathodic with respect to the matrix and exhibits a passive behavior over a wider pH range than either of its components Al and Mg. β-$Mg_{17}Al_{12}$ is found to be inert in chloride solutions in comparison with the surrounding Mg matrix and could act as a corrosion barrier [200]. It is reported that the resistance of β-$Mg_{17}Al_{12}$ to corrosion is due to the presence of a thin passive film on its surface.

However, literature also suggests that β phase serves dual role in corrosion; the β phase can acts either as a barrier or as a galvanic cathode [37, 201-203]. If it is present as a small fraction, it serves mainly as a galvanic cathode, and accelerates the overall corrosion of α matrix. However, if its fraction is high, then it may act mainly as an anodic barrier [35].

If the α grains are very fine, the β phase fraction is not too low, and the β phase is nearly continuous like a net over the α matrix, then the β phase particles don not easily fall out by undermining. Instead, in this case the α matrix is much more easily corroded and even undermined because many more α grains are completely separated by the β phase net. Therefore, it can be expected that β fraction increase with time during corrosion, and finally the fraction becomes high enough to make the β phase become nearly continuous. The corrosion rate should be low after this steady state surface condition is reached. Hence, if α grains are fine, the gaps between β precipitates are narrow and the β phase is nearly continuous, the corrosion is greatly retarded [201, 202]. Figure 2.22 provides a schematic illustration of change of surface composition of die cast during corrosion. This kind of behavior normally observed with die cast AZ91 alloy.

On the other hand, if α grain size is large, the β phase is agglomerated and the distance between the β phase is large then at the final stage of the corrosion, the α

phase is not effectively blocked either by β phase or by the corrosion products deposited between the β phase and α phase. In an even worse case, the β can be undermined instead of α phase. In this case β fraction decreases with time during corrosion and the corrosion rate increases with time. This is what happens during corrosion of gravity cast AZ91 [37].

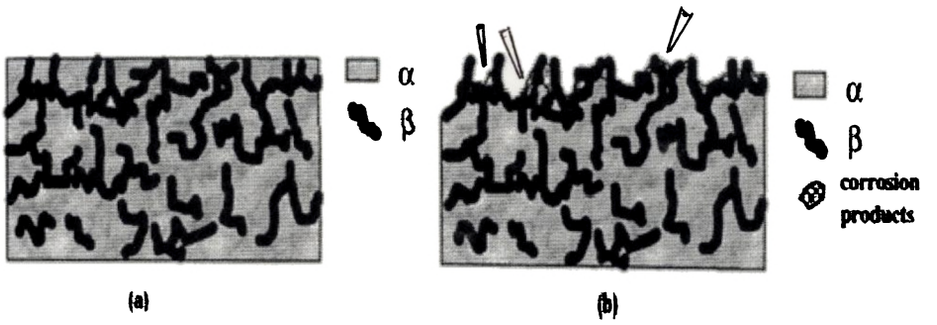

Figure 2.22: Schematic presentation of change of surface composition during corrosion (a) initial surface (b) final surface [201]

2.8.8.3 Effect of impurities

Another important factor, which affects the corrosion behavior of AZ91 alloy, is the kind and level of impurities presence in the alloy. Fe, Ni, Co, Cu are the impurity elements that have negative effect on corrosion resistance [204]. The tolerance limits for these elements are defined by the ASTM standards [205]. Iron is the most critical element since it reacts with aluminum forming a binary intermetallic compound Al_3Fe. This compound segregates at grain boundaries and it acts as an active cathodic phase relative to the magnesium rich matrix. One of the first observations by Hanawalt and co workers [98] was the effect of purity on the corrosion rate of pure magnesium, as measured by weight loss in 3% sodium chloride. The commercially pure metal (99.9%) has a corrosion rate of 5-100 $mg/cm^2/d$ (410-8300 mpy), while the corresponding rate for high purity magnesium (99.994%) is about 0.15 mg/cm/d (12mpy). The generalized curve in Figure 2.23 illustrates schematically the effects of common impurity elements observed in the Hanawalt study [98]. The curve shows a well defined impurity level, above which the corrosion rate increases dramatically. For high purity magnesium, these values are 170, 1000, and 5 ppm for iron, copper and nickel respectively.

Reichek et al [206] also showed that the salt water corrosion performance of the AZ91 alloy is a direct function of the alloy purity. They are able to define the specific tolerance limits of the three common contaminants of Mg alloys, i.e., Fe, Ni and Cu with respect to corrosion behavior. By keeping the respective limits of these contaminants to values below the defined values (Fe=3.2%Mn max.; Ni=50 ppm max.; and Cu=400 ppm max.), they found that AZ91 consistently exhibited a better salt spray corrosion performance than pressure die cast SAE 380 (Al-4.5% Cu-2.5% Si) and cold rolled steel. [206].

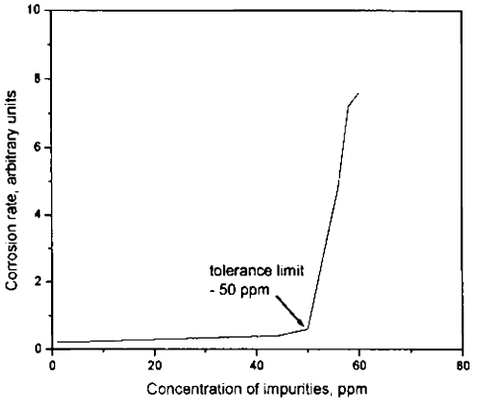

Figure 2.23: Generalized curve showing the effect of impurities on corrosion rate of magnesium [98]

To reduce the effect of iron in Mg-Al alloys, manganese is generally used. Manganese, combine with iron and improve the corrosion behavior in two possible ways: either removing iron by settling at the bottom of the melt, or forming intermetallic compounds with iron, which apparently have no negative effects. It has been shown by several authors that the corrosion rate of Mg-Al castings is better correlated to the Fe/Mn ratio of the alloy, rather than the absolute Fe content [198].

2.8.8.4 Effect of heat treatment

The effect of ageing on corrosion resistance of die cast AZ91 also reported in literature. Suman [207] showed that ageing at temperatures up to 230°C for 36 h has little effect on corrosion resistance. However, ageing at a temperature above 230°C significantly reduces the corrosion resistance of die cast AZ91 under a salt spraying

condition. Lunder et al [33] reported that the alloy exhibits an improved corrosion resistance in the artificially aged condition (T6) compared to as cast and homogenized (T4) state.

Recently Song et al [208] have carried out a detailed study on the effect of ageing at 160°C on the corrosion behavior of die cast AZ91 alloy. It was found that the corrosion rate of the alloy decreases with ageing time in the initial stages and then increases again at ageing times greater than 45 h. The dependence of the corrosion rate on ageing time is related to the changes in microstructure and local composition change during ageing. The β precipitates occurred during ageing treatment at the grain boundary acts as a barrier, resulting in a decreasing corrosion rate in the initial stages of ageing. In the later stages, the decreasing aluminum content of α grain makes the matrix more active, causing an increase in the corrosion rate. They also reported that the continuous rod shaped precipitates, which occur in the later stage in the grain, do not act as an effective barrier for the corrosion.

In contrast, Singh Raman [209] studied the ageing effect on corrosion of gravity cast AZ91 and reported that T4 (solution treated) treated specimen exhibit superior corrosion resistance. On the other hand, the aged specimen (16h and 19h) and as cast shows higher corrosion rates. He observed that the corrosion is highly localized in the region of β phase and the surrounding eutectic α phase. It is said that the cathode to anode area ratio is one of the prime factors governing the severity of the galvanic corrosion. The increase in corrosion rate with increase in ageing time is attributed to the increase in the precipitates volume, which in turn increases the cathode to anode area ratio, leading to more galvanic corrosion (ref Figure 2.24).

2.8.8.5 Corrosion protection coatings

There are two different ways to improve the corrosion resistance of magnesium alloys. The first one is to purify the alloy from impurities like Fe, Ni, Cu, etc. the second method is to form a protective coating on the magnesium alloys. Various surface treatments have been used to generate protective films or surface coating [210-213]. These techniques basically classified as two types. The first one is

to produce a protective film by chemical or electrochemical conversion treatments. The second one is a coating usually containing organic materials like paint. Chemical conversion coating, electrochemical anodizing, chemical plating, electro plating are comes under the first type. The chemical treatments usually involve the dipping of the magnesium alloy into acidic or nearly neutral solutions containing Cr compounds, which form a passive oxide layer on the surface of the metal. In electrochemical process like anodizing, film composed of MgO containing Cr compounds are produced on the surface [214].

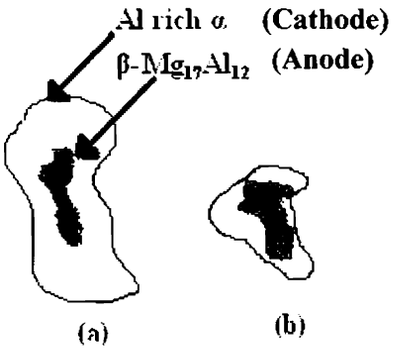

Figure 2.24: Schematic diagram illustrating the cathode-anode area change during ageing of AZ91 alloy (a) T6-16h (b) T6-19h ***[reproduced from ref. 209]***

Among the various electrochemical techniques, anodizing treatment is become most promising methods for magnesium even though this treatment is quite expansive compared to the chemical treatment [215]. Different process like DOW 17, HAE and MGZ has been developed. These coating has environmental problem as most of the electrolyte used in these process contain dichromate and phosphoric acid [216]. Recently, due to the health and environmental pressure, some new coatings such as Anomag and Tagnite have been developed [210, 211, 217]. These coating methods have less hazards and more effective in terms of corrosion resistance over HAE and DOW17 [218].

Laser treatment is another surface modification technique in which, formation of metastable solid solutions as promoted at metal surfaces by laser annealing where cooling rates as high as 10^{10} Ks^{-1}. This is also a kind of rapid solidification technique

in which only surface layer melt and solidifies [214]. Akavipat et al [219] studied the effects of thin layers of Al, Cr, Cu, Fe and Ni on the pitting resistance of AZ91C and found that improved breakdown potential for all cases. This improvement is attributed to the surface structure consists of mixture of amorphous mixed oxides. C. Padmavathi et al. [220] have reported that pulsed Nd:YAG laser melting treatment on AZ91C alloy improve its corrosion behavior because of its fine microstructure and redistribution of β- phase.

2.9 ROLE OF MINOR ALLOYING ADDITIONS

Surface active elements like Sb, Ca, Bi, Sr, RE, etc., are added to the AZ91 alloy to improve its mechanical and corrosion properties [221-224]. These elements mainly form intermetallics either with Mg, or with Al, which is high thermally stable than the $Mg_{17}Al_{12}$, thereby improve the creep properties. Some elements like Ca and Sr are effective in refine the grain size of AZ91 alloy. Ca and RE is also found to improve the corrosion resistance of AZ91 alloy.

2.9.1 Antimony

Qudong Wang et al [42] and Guangyin et al [44] studied the effect of Sb on the microstructure and mechanical properties of AZ91 alloy. Addition of small amount of Sb (0.5 to2%) lead to the microstructure of AZ91 alloy with needle shaped Mg_3Sb_2 particles at the grain boundary and refinement of $Mg_{17}Al_{12}$ precipitates to some extent [221]. Since the melting point of Mg_3Sb_2 is around 1228°C, it is thermally stable at high temperature. Maximum tensile properties are observed with 0.5% Sb added alloy. Improved creep properties at 150°C with 50 MPa initial stress is also observed [221]. With addition of 0.4% Sb, the minimum creep rate of AZ91 alloy is reduced from 5.6×10^{-8} to 1.5×10^{-8} s^{-1}. The total strain for 100 h is also reduced from 2.4% to 1.2% [222]. The hard and stable Mg_3Sb_2 precipitates pin both the grain boundary and dislocations at high temperature and thus improves the creep resistance. The microstructural analysis on the creep tested samples indicates that Sb rich particles hindering the dislocation movement and lead to the formation of dislocation tangles during creep process (ref Figure 2.25) [221]. However the problem associated with Sb addition is that if the addition exceeds 0.5% the number of Mg_3Sb phase also

increases and the needle shape morphology of this intermetallic brings down the properties.

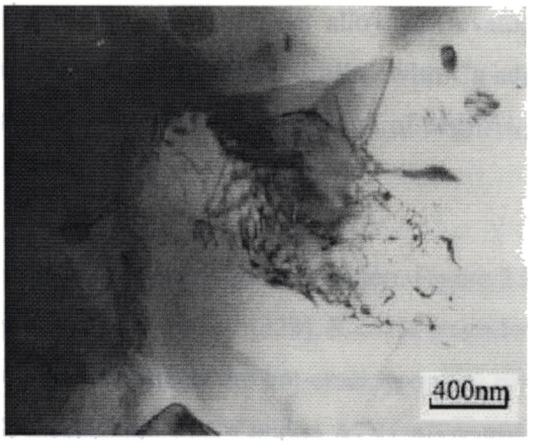

Figure 2.25: TEM micrograph showing dislocation pileups around the Mg_3Sb_2 intermetallics in Sb added AZ91 alloy crept at 200°C[221]

2.9.2 Calcium

Wang Qudong et at [41] added up to 2% Ca to AZ91 alloy and studied its microstructure and mechanical properties. Ca addition found to refine the microstructure and reduce the quantity of $Mg_{17}Al_{12}$ phase by forming new Al_2Ca phase. Addition of Ca is also effective in reduction in grain size of AZ91. Hirai et al [222] reported that the initial grain size of as cast AZ91 alloy is reduced from 65 μm to 20 μm when 1% of Ca is added. However, when the amount of added Ca is more than 1%, no change in grain size is observed. Peijie Li and S.S. Li also [223, 224] reported that the grain refinement efficiency is high with initial additions of Ca up to 0.4% and then the degree of grain size reduction decreases with further additions.

The addition of Ca improves the ambient temperature yield strength but ultimate tensile strength and ductility are found to reduced [41, 223]. The improvement in yield strength is attributed to the grain refinement effect of Ca but the Al_2Ca phase forms at grain boundaries is brittle and face centered cubic structure that may deteriorate the bond strength and result in worse UTS and elongation [223]. However, Ca addition confers elevated temperature strengthening of this alloy because at high temperature, the Al_2Ca phase is thermally stable compared to

$Mg_{17}Al_{12}$ precipitates and acts as an effective dislocation barrier [41]. In addition to that, increase in the stability of $Mg_{17}Al_{12}$ intermetallic is also observed with Ca addition. Part of the added Ca dissolves into the $Mg_{17}Al_{12}$ phase, which raises its thermostability, consequently, strengthen the alloy at elevated temperatures [225]. Improvement in corrosion resistance of AZ91 alloy with Ca addition is also reported [48]. This is due to the reduction in volume fraction of $Mg_{17}Al_{12}$ phase and formation of less harmful Al_2Ca intermetallic.

Hot-crack problem is noticed with Ca addition. Figure 2.26 shows the effect of Ca on the hot-crack grade of AZ91 alloy [223]. It could be understood from the figure that 1% of Ca addition greatly affects the hot-crack property of AZ91. Bi Tang [226] studied the hot crack mechanism of Ca added AZ91 alloy and reported that the Ca addition elevates the tendency of the divorce eutectic and forming the new Al_2Ca phase, which is distributed as a net-shape on the grain boundary and debases the boundary tension of the liquid film, deteriorating the filling capacity and lowering the hot-crack property of magnesium alloy [224].

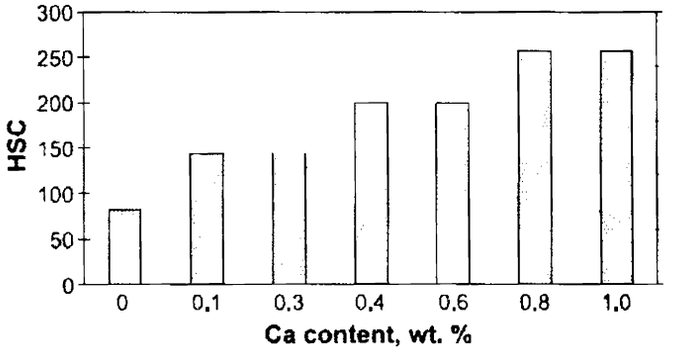

Figure 2.26: Effect of Ca on the hot-crack grade of AZ91 alloy [223]

2.9.3 Bismuth

Bi addition to AZ91 alloy forms a hard compound Mg_3Bi, which has a melting point of 823°C. Compared to Sb, Bi addition has, only little effect on the improvement of creep properties of Mg alloy. But when it combines with Sb, the effect is appreciable [43]. Microstructure observations reveal that the additions of

bismuth refines the $Mg_{17}Al_{12}$ precipitate in the as cast alloys and effectively suppresses the discontinuous β-$Mg_{17}Al_{12}$ precipitation during the aging process [43].

2.9.4 Rare earth

Rear earths are important alloying elements to magnesium alloys, which can improve casting characteristics, high temperature properties and corrosion resistance [227-230]. With addition of rare earth elements a rod-like $Al_{11}RE_3$ intermetallic forms at the grain boundary. Due to the formation of $Al_{11}RE_3$, the Al available for the formation of $Mg_{17}Al_{12}$ phase reduces. The effect of RE addition on the tensile properties of AZ91 alloy is scatter in the literature. Y. Lu [45] has reported that RE has little effect on the UTS of AZ91 at ambient temperature but greatly increase the high temperature tensile strength and elongation. Fan [46, 47] has reported a sharp increase in both UTS and ductility with the addition of La and Ce to AZ91 alloy. On the other hand, G. H. Wu et al [48] have found that with increasing RE additions, the UTS increases but the elongation decreases. S. Lee et al [231] have reported that addition of Y and Nd improves hardness and fracture toughness of AZ91. He observes planer slip bands and transgranular crack propagation along these slip bands. When planer slip bands are forms, a heavier load is requires for fracture than in the case of intergranular fracture, thereby yielding an overall improvement of mechanical properties [231].

G. Pettersen [232] indicates that RE could reduce the range of crystallization temperature of magnesium alloy, and hence the Mg-RE eutectic has good fluidity. However, Y. Lu [45] has reported a decrease in fluidity up to 2% RE addition and then it increase with higher percentage addition to AZ91 alloy. Qudong et al [233] observed the fluidity of RE added alloy is depending on the mould section thickness also. The fluidity decreases with increase in RE addition in mould section thickness under 2 mm whereas it decrease first with section thickness above 2 mm when RE content increases from 1 to 2% and increase when RE content increases from 2 to 3% to AZ91 alloy.

Wang et al [234] studied the effect of RE on hot tearing susceptibility. Small quantity of RE additions have little effect on the hot susceptibility coefficient (HSC) of Mg-9Al alloy, while RE content is exceeded 1.6%, HSC increases notably. The increase in HSC is attributed to the formation of rod-like Al_4RE precipitates, which has high latent heat. During the formation of this phase, much heat is given out, which slow down the temperature decease at the initial stage of solidification.

Rear earth addition has a significant role on corrosion behavior of Mg alloys. Lunder [235] found that the $Al_{11}MM_3$ (MM refers to misch metals, a mixture of rare earth metals) intermetallic phase in AE42 magnesium alloy is nobler than pure Mg. Its micro-galvanic corrosion is not severe since the $Al_{11}MM_3$ phase behaves as a passive cathode over a wide pH range. As a result, it is not expected to have a detrimental effect on the corrosion resistance of the alloy. Mercer [236] considered that the advantage of RE in magnesium alloys can be attributed to trapping deleterious elements and decreasing the activity of cathode. Nordlien et al. [237] indicated that the coexistence of aluminum with RE is an essential condition for improving the passivity of Mg-Al-RE alloy, suggesting a synergistic effect between these elements. Recently Fan et al. [46, 47] studied the effect of Ce and La addition on the corrosion behavior of AZ91 alloy and found improved corrosion behavior. They attributed the improvement is the ability of these elements to refine the β phase and thereby forming a continuous β network along the grain boundaries. Rosalbino et al [50] added erbium (Er) to AM50 alloy to improve it corrosion behavior. Electo chemical investigations revealed that the surface layers formed on Mg-Al-Er provide a better protective layer than the magnesium hydroxide or aluminum hydroxide layer normally form on AM60 in borate buffer solution. Zhou Xuehua et al [49] studied the corrosion behavior of holmium (Ho) added AZ91 alloy in 3.5% NaCl solution saturated with $Mg(OH)_2$ and reported that Ho enhanced the corrosion resistance of AZ91. The addition of Ho reduces the amount of β phase by forming Ho containing phase with Al and Mg and they are easily oxidized and passivated. They also reported that the corrosion product films on Ho added alloys contain more Al, which is more compact and stable [49].

2.9.5 Strontium

Not much studies available on the effect of Sr to AZ91 alloy. S. Lee [231] has reported a grain reduction of 82 μm to 48 μm with addition of 0.5% Sr to AZ91. The grain refinement obtained is attributed to the modified precipitation behavior observed with Sr addition [238]. With Sr addition, it is found that more amounts of $Mg_{17}Al_{12}$ phase are precipitates along the grain boundary. This can hinder the movement of grain boundaries and the subsequent grain growth leading to the greater effect of grain refinement. K. Hirai et al. [222] have noticed a grain reduction of only 65 μm to 40 μm with 0.5% Sr to AZ91 alloy. Moreover, when it is added along with 1% Ca, the grain size greatly reduced to 17 μm. It is also reported that the combined addition of Sr and Ca improves the room and high temperature properties due to the reduction in stacking fault energy [222]. However, low hardness and fracture toughness is obtained with 0.5% Sr added AZ91 alloy by S. Lee et al. [231]. This is due to the presence of coarse needle-shaped Sr based precipitates, which is mainly distributed on grain boundaries, beside the discontinuous $Mg_{17}Al_{12}$ precipitates. When load is applied, micro cracks are formed initially in these particles, and then are immediately connected to grain boundaries, causing intergranular facture. Thus its mechanical properties are reduces despite the fine grain size.

P. Zhao et al [239] studied the Sr effects on the tensile and creep properties of AM50 alloy. It is observed that trace additions of Sr to the alloy has a beneficial influence on the mechanical properties of Mg-5Al alloy, especially on UTS and elongation. The tensile properties increases with increasing Sr content when the Sr addition is lower than 0.1%. However, greater amount of Sr, deceases the UTS and elongation whereas increases the yield strength. He also observed the creep properties are increased with increase in Sr content.

2.10 SHORTCOMINGS IN LITERATURE

The creep behavior of die cast AZ91 alloy is extensively dealt in literature. In general two contradictory findings are reported: (i) dynamic discontinuous precipitate forms during creep leads to the sliding at low stress level. (ii) in contrast, continuous fine precipitates occurred at the same temperature and stress region provides

precipitation hardening and finally, coarsening of these precipitates at the later stage is the softening mechanism. Moreover, not much literature is available on the ingot cast alloy. Available literature, which deals the creep behavior of ingot AZ91 alloy, suggests dislocation creep is the dominant mechanism and no substantial grain boundary sliding contributes to the creep. In addition, most of the literature, which deals improvement in creep behavior of gravity cast AZ91 alloy by minor alloying addition suggests that the formation of thermally stable intermetallics and suppression of discontinues precipitates due to the additions are the reasons for the improvement. However, most of the studies are not provided the microstructural evidence for such a claim. Detailed post creep microstructural examination is hence, needed to understand the deformation mechanism of gravity cast AZ91 alloy added with various elements.

Moreover, most of work on AZ91 alloy is focused on its creep behavior and considerable effect has been put to improve its creep properties, particularly modify the alloy composition slightly through different alloying addition. While, considering the industrial application of magnesium alloys, particularly AZ91, creep is not the only concern. There are other properties like ageing behavior, tensile properties and corrosion properties, which are all important in practical applications. In specific, the corrosion behavior is another major concern, which restricts it wide spread application as a structural material. AZ91 alloy exhibit excellent corrosion resistance due to the high percentage of Al in the alloy. When alloy modification takes place to improve its high temperature performance, the microstructure changes considerably. Mainly these additions introduce various high temperature stable intermetallics in the microstructure. Since the corrosion behavior of this alloy is highly sensitive to microstructure, these intermetallics definitely play an important role. Hence studies on corrosion behavior of AZ91 alloy with different alloying additions are more valuable.

Even though the effect of elements like Sb, Ca, Bi, and RE addition on the tensile and creep properties of AZ91 is studied to certain extend and reported, there are other elements like Si, Sr whose influence on above said properties are not investigated in detail.

2.11 SCOPE OF THE WORK

The increase in the demand to reduce the weight of a passenger car thereby increase the fuel efficiency oblige the auto industries to paying more attention to discover the lighter material with high specific properties. It is not surprise that magnesium is one of the potential candidates as it is one of the lightest structural materials with a density of 1.77 g/cc. Since the material cost of magnesium is slightly higher than aluminum, die casting is always preferred for magnesium alloy castings. The magnesium alloys containing considerable amount of aluminum (6-9%) provides excellent die castability. AZ91 alloy, which containing 8-9%Al in it, is considered as a bench mark alloy for castabiltiy of Mg alloys. More over this alloy offer wide range of room temperature properties. In the as cast condition, the strengthening phase is the massive $Mg_{17}Al_{12}$, which is known as eutectic phase. However in the aged alloys, a fine and evenly distributed continuous form of $Mg_{17}Al_{12}$ precipitates in the basal plane strengthen the material according to Orowon theory of precipitation hardening. However, this alloy does not have adequate high temperature tensile and creep properties, which hamper its usage above 100°C. Literature said that the presence of higher amount of aluminum in this alloy not only increase the brittleness but also impair the creep properties. The coarsening of β-$Mg_{17}Al_{12}$ at elevated temperature, due to its low melting point (437°C), is said to be the cause for the poor creep properties. Due to this fact, it is believed that it does not act as a barrier for dislocation and grain boundary movement. Moreover, it is found that the structure is not stable at high temperature. Dynamic precipitation of $Mg_{17}Al_{12}$ occurs at the grain boundary. Hence, alloys with less amount of Al are developed for high temperature applications. These alloys containing only 2-4%Al along with third element results in no or fewer $Mg_{17}Al_{12}$ precipitates, in addition to the thermally stable intermetallics. Hence these alloys exhibit superior creep resistance over conventional AZ91. However, fewer amount of aluminum and presence of certain other elements like Ca and RE create die casting problem for these alloys.

Since AZ91 is still a work horse magnesium alloy system for automobile industries, even a slight improvement in its mechanical properties, particularly the creep, would be very much appreciated. Previous studies proved that addition of

minor alloying elements to AZ91 alloy is a successful way of improving its mechanical behavior. Surface active elements like Sb, Ca, Bi, RE and etc are added to Mg-Al alloys like AM60 and AZ91 alloys and noticed improvement in high temperature tensile and creep properties. This improvement is attributed to following reasons:

1. Introduction of intermetallics like Mg_3Sb_2, Al_2Ca, Mg_3Bi, and AlRE
2. Suppression of discontinuous $Mg_{17}Al_{12}$ precipitates at the grain boundaries
3. Increase the stability of $Mg_{17}Al_{12}$ precipitates

Corrosion is another concern of Mg alloys, which has been a major obstacle to its growth in structural applications. Magnesium with a standard electrochemical potential of -2.4 V (NHE), dissolves rapidly in aqueous solutions by evolving hydrogen below pH 11.0, the equilibrium pH value for Mg $(OH)_2$. As a consequence, researchers all over the world have shown much interest to study the corrosion behavior of Mg alloys and to develop protective measures. The corrosion behavior of AZ91 is highly sensitive to the microstructural features like, volume fraction and size of $Mg_{17}Al_{12}$ phase, amount and distribution of Al in the matrix, grain size, porosity etc. The alloying elements, which are added with the intention to improve the creep properties might changes the corrosion behavior of AZ91. Hence it is imperative to study the effect of intermetallics on the corrosion behavior of AZ91 alloy. So, the objectives of the present research work are:

1. To study the effect of individual and combined additions of Si, Sb and Sr on the microstructure, aging behavior and tensile properties of AZ91 alloy
2. To investigate the effect of additions on the creep behavior and understand its strengthening mechanism.
3. To estimate the change in corrosion resistance and behavior of existing AZ91alloy in presence of various intermetallics.

CHAPTER 3: MATERIALS AND EXPERIMENTAL RETAILS

3.1 MATERIALS

3.1.1 Metals and Master Alloys

The base alloy selected for the present study was AZ91 magnesium alloy. It was prepared by melting together the following metals.

1. Pure Magnesium ingots
2. Pure Aluminum ingots
3. Pure Zinc flaks
4. Al-10% Mn master alloy

The required alloying elements like Si, Sb and Sr were added in the form of master alloys to have effective recovery of elements. The following master alloys were used to prepare the required alloy systems.

1. Al-20% Si master alloy (for Si additions)
2. Al-10% Sb master alloy (for Sb additions)
3. Al-10Sr master alloy (for Sr additions)

3.1.2 Melting and Refining Flux

The flux ***'Magrex-60'*** supplied by ***FOSICO*** industries was used for covering and refining the molten metal during melting. MgCl, MgF, MgO, etc. are the major composition of the flux. Fine sulfur powder was used for dusting around the melt jet to remove the oxygen so as to avoid oxidization during pouring of molten metal in to the mould.

3.1.3 Mould

Cast iron mould shown in Figure 3.1 was used throughout the experiments. Initially, there was no pouring basin attachment with the sprue, which led to a restriction in pouring speed as higher pouring speed led to the spilling of molten metal into the floor. Moreover, since the fluidity of magnesium is less compared to

3.2 MELTING AND POURING

3.2.1 Cleaning of Materials

In order to remove the oxides sticking on the wall and bottom of the crucible from the previous melting the crucible was filled with water and kept for one day for oxides to get dissolved. Then it was cleaned with MS wire brush. All the steel tools used for melting and pouring purpose like skimmer, starrier etc and metal ingots were cleaned by metal wire brush. Metal ingots were then, cleaned with acetone. All the tools and metal ingots were preheated before use. The properly cleaned mould was given a graphite coat and preheated to 250°C in a heating oven for 1 h just before the casting.

3.2.2 Melting

The melting arrangement for magnesium alloys is presented in Figure 3.2. Resistance box furnace was used for melting. The preheated flux was sprinkled in the bottom and side of the cleaned crucible and kept inside the furnace. After the crucible reached the red hot condition, the preheated ingots were charged in to the crucible. Initially part of the total magnesium ingots were charged. After melting of charged ingots completed, the remaining ingots were then immersed into the molten metal. This kind of charging practice of metal ingots avoids the excessive oxidation during melting. Crucible was covered with furnace lid to minimize the air contact with the molten metal. Flux was sprinkled over the metal throughout the melting. Before addition of alloying elements, the top layer of oxides was completely removed and fresh layer of flux applied. The required amounts of master alloys were weighed and wrapped in aluminum foil and were slowly immersed into the melt. After additions, the melt was gently stirred for dissolution of the added elements. Again the top oxide layer was removed and fresh layer of flux was applied. The melt was held for 10 min to ensure the complete dissolution of elements in to the melt.

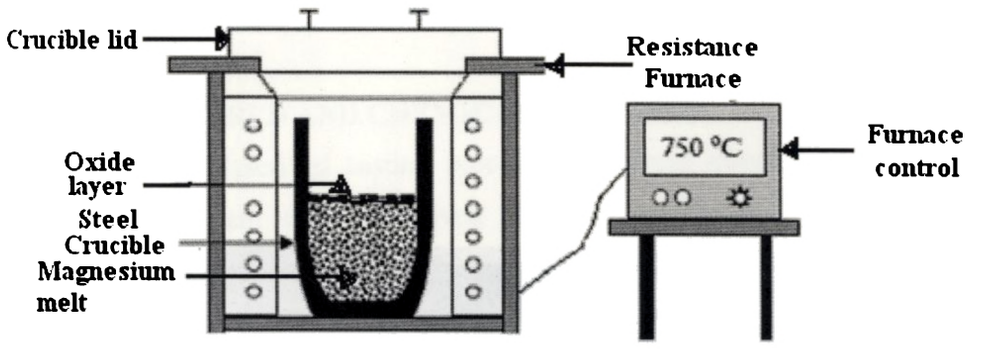

Figure 3.2: Schematic diagram showing the melting arrangement for magnesium

3.2.3 Refining

After the complete melting of the metals in the crucible, the refining of melt was carried out at a temperature of ≈720°C. Initially, the top layer (oxide layer) of the melt was removed and the melt was rigorously stirred for 2-3 min. Flux was applied during stirring. This stirring helps to mix the added flux with the melt uniformly. After thorough mixing, the top surface of molten melt was removed and a fresh layer of flux was applied. Then the melt was held for 10- 15 min without distributing, which enabled the added flux react with oxides inclusions presents in the melt and become heavier and settled down in the bottom of the crucible.

3.2.4 Pouring and Casting

After the refining and settling process was over, the molten metal was poured in to the pre heated moulds. During pouring much care was taken to avoid the breakage of top flux protective layer. The pouring was carried out gently without any jerk in the melt, since excessive jerk disturbs the settled oxide inclusions in the bottom. The flux layer near the lip of the crucible was pulled back gently by using a skimmer for smooth flow of molten metal. Sulfur powder dusting was carried out to remove the oxygen around the melt jet. Three fourth of the melt in the crucible was poured into the preheated mould. The remaining metal was poured separately as a scrap. Figure 3.3 shows a photograph of one such casting. Figure 3.4 shows a schematic diagram of casting and indicating the locations from where sample for different testing were taken.

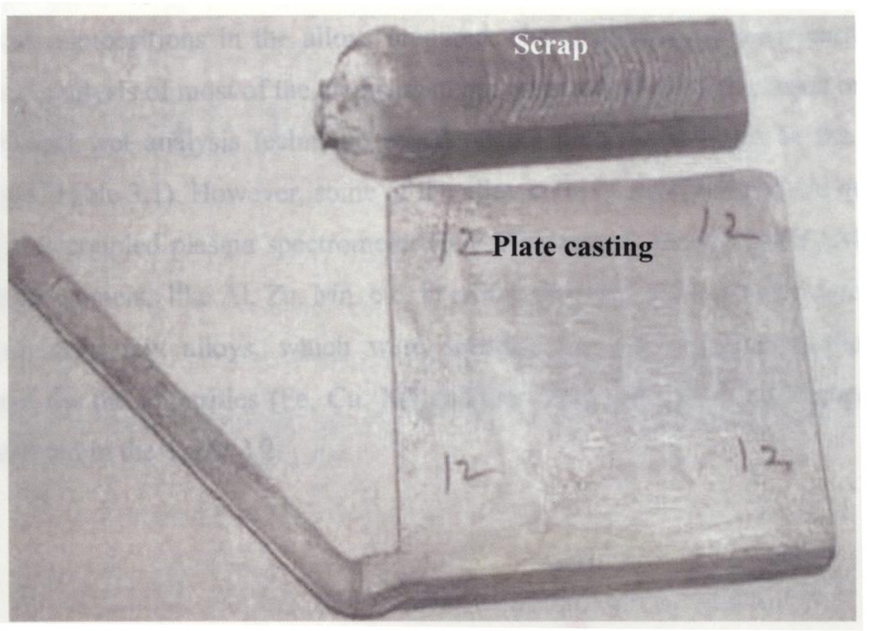

Figure 3.3: Photograph of the magnesium alloy castings

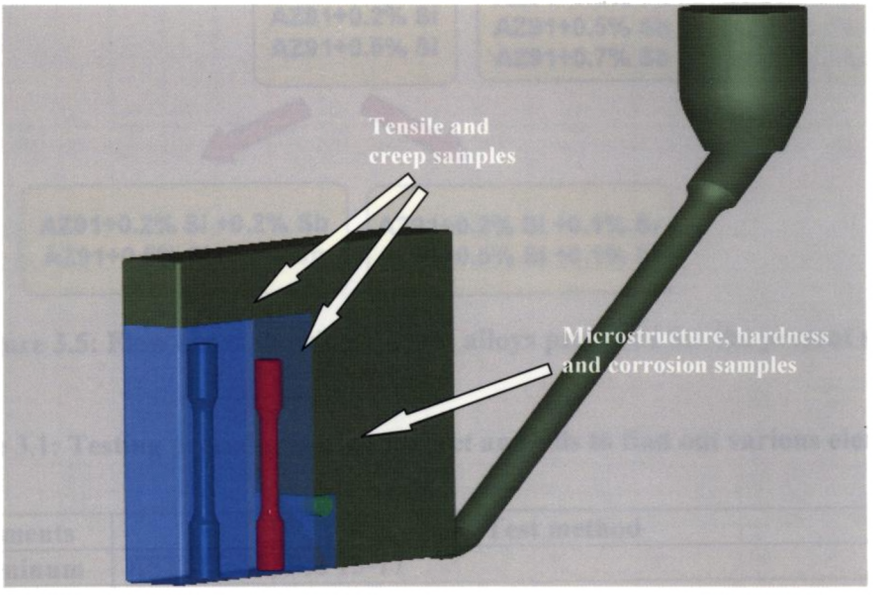

Figure 3.4: Schematic diagram showing the magnesium alloy casting and sample locations

3.3 ALLOYS PREPARED AND CHEMICAL ANALYSES

Using above described casting procedure, different alloys were presented prepared for the present study and given in Figure 3.5. To find out the actual elemental compositions in the alloys prepared, chemical analysis were carried out. Chemical analysis of most of the elements in the prepared alloys was carried out using conventional wet analysis technique based on the procedures given in the ASTM standards (Table 3.1). However, some of the alloy compositions were found out using inductively coupled plasma spectrometer (ICP Plasmascan, model LABTAM 8410). The major elements like Al, Zn, Mn, etc. in all the prepared castings were carried out; however, only few alloys, which were selected for the corrosion studies were subjected for the impurities (Fe, Cu, Ni) analyzes. The analyzed alloy compositions are presented in the Table 3.2.

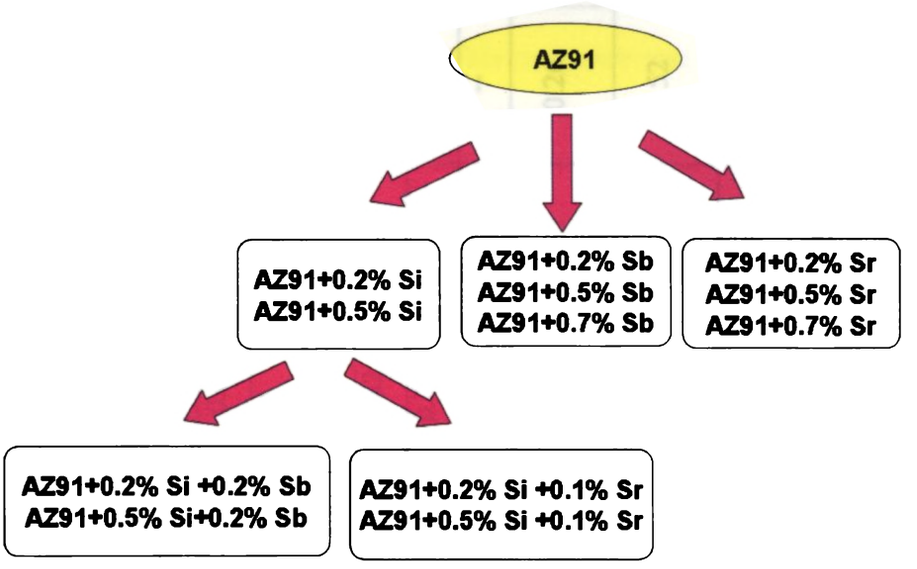

Figure 3.5: Flow chart showing various alloys prepared for the present study

Table 3.1: Testing procedures used for wet analysis to find out various elements

Elements	Test method
Aluminum	ASTM E 35, Sec 13-17
Silicon	ASTM E 35, Sec 88-92
Antimony	Vogel's quantitative inorganic analysis Part F, Chapter XVIII, 13, Page no 73
Strontium	Vogel's textbook of quantitative chemical analysis, 5th edition, chapter 11.42, page no. 468

Table 3.2: Analyzed chemical compositions of various alloys used in the present investigation

Alloy Designation	Analyzed compositions, wt %								
	Al	Zn	Mn	Si	Sb	Sr	Fe	Ni	Cu
AZ91	9.3	0.8	0.18	--	--	--	0.025	0.0035	0.0048
AZ91 + 0.2% Si	9.5	0.65	0.2	0.22	--	--	--	--	--
AZ91 + 0.5% Si	8.7	0.72	0.22	0.47	--	--	0.010	0.00204	0.0045
AZ91+0.2% Sb	8.35	0.6	0.15	--	0.16	--	--	--	--
AZ91 + 0.5% Sb	8.9	1	0.1	--	0.58	--	0.015	0.0046	0.0039
AZ91 + 0.7% Sb	8.7	0.5	0.28	--	0.85	--	--	--	--
AZ91 + 0.2% Sr	8.74	0.62	0.21	--	--	0.16	--	--	--
AZ91 + 0.5% Sr	8.92	0.71	0.2	--	--	0.42	0.018	0.0051	0.0032
AZ91 + 0.7% Sr	9.1	0.6	0.17	--	--	0.73	--	--	--
AZ91 + 0.2% + 0.2% Sb	8.3	0.84	0.31	0.26	0.16	--	--	--	--
AZ91 + 0.5% + 0.2% Sb	9.3	0.63	0.02	0.52	0.19	--	0.038	0.005	0.0049
AZ91 + 0.2% Si + 0.1% Sr	9.15	0.68	0.18	0.22	--	0.14	--	--	--
AZ91 + 0.5% + 0.1% Sr	8.78	0.92	0.28	0.42	--	0.126	--	--	--

3.4 HEAT TREATMENT

3.4.1 Sample Preparation

To avoid the variation in microstructure and properties along the thickness of the casting and maintain the uniformity in microstructure, all the samples were taken from the wall side of the castings. Cylindrical pieces of 15mm Φ X 10mm height were machined out from the castings as shown in Figure 3.4. The surface of the sample, which was nearer to the wall surface of the castings was selected for further characterization (microstructure and hardness measurement).

3.4.2 Solution Treatment

Solution heat treatment was carried out in a muffle furnace. Machined samples to be heat treated were placed in a mild steel tray in such way that no piece touches others. A sand bed prepared using carbon char coal and dry sand with a volume ratio of 20:80 was placed in the furnace. This helped to evacuate oxygen present in the furnace during heat treatment. To have a continuous protection, the sand bed was replaced in the time interval of every 5 h. This procedure was found satisfactory to avoid the oxidation of magnesium samples during the heat treatment. The samples were solution heat treated for 48 h followed by water quenching at room temperature without much delay and kept in desiccators for subsequent ageing treatment.

3.4.3 Ageing Treatment

The solution treated samples were aged at 200°C for 100 h in a heat treatment oven to study the ageing behavior. Since the ageing temperature was less than 350°C (the temperature, at which magnesium starts to oxidize), ageing was carried out in an open atmosphere. Samples were taken out from the furnace at regular interval and air cooled to room temperature for hardness measurements.

3.4.4 Hardness

INTENDEC hardness machine was used for brinell hardness measurement of as cast and heat treated samples. The samples faces were leveled on both sides. One side of the specimen, on which hardness was measured was polished up to 600 fine

emery paper to remove the oxide and other scales in order to see the edges of the indentation mark clearly. 2.5 mm ball was used to make indentation. Load was fixed at 66.5 Kg with a dwell time of 30 sec. On an average 5 indentations were made and average value is reported.

3.5 MICROSTRUCTURAL OBSERVATION

3.5.1 Sample Preparation

3.5.1.1 Polishing

Initially the samples (15mm Φ X 10mm height cylindrical sample) were polished using different grade of emery papers of progressively fine grades of 80, 220, 400 and 600 grits. During paper polishing water was used as a cleaning agent. After completing the paper polishing, the samples were polished in a rotating disc of proprietary cloth (Selvyte cloth) charged with a diamond paste of 6, 3 and 0.25 μm particle size in sequence. Filtered kerosene was used as lubricant during cloth polishing. Samples were gently pressed against the rotation wheel. Since magnesium is a soft material much care was taken during polishing to avoid sketches and excessive surface contamination. Cleaning the samples with water (even with distilled water) found inefficient to remove surface contaminants of the polished samples. So, after the finial polishing over, the surface of the samples was cleaned using ultrasonic cleaner in ethanol.

3.5.1.2 Chemical etching

Different kind of etchants were tried to get a clear microstructure. After various trails, picric acid based etchant was found to be an efficient one, which clearly revealed the microconstituents of magnesium alloys. The chemical composition of the etchant used in the present study is given below.

Picric acid – 6 grams

Acetic acid – 5 ml

Ethanol – 100ml

Distilled water – 10 ml

The etching time was found to be optimum with 2-3 seconds. Much care was taken during etching to avoid over etching otherwise, which would spoil the surface of the samples.

3.5.2 Optical Microscope

Microstructural specimens (after polishing and etching) were observed under a Leitz-Metalloplan optical microscope. Photographs were taken at different location with various magnifications.

3.5.3 Image Analysis

Quantitative analysis of the microstructure was carried out using a Leica 2001 Image Analyzer in conjunction with the optical microscope. Size of various intermetallics and grain size of various castings were measured by linear intercept method. The fields of observations were selected randomly at different locations of the sample. The size of Chinese script Mg_2Si intermetallic phase was measured manually since its shape is complicated. In each case, at least ten fields were analyzed from a single specimen and the average value is reported.

3.5.4 Scanning Electron Microscope (SEM)

To identify the type of precipitates in various castings and to study the micro-mechanisms of fracture during tensile and creep, samples were cleaned in ethanol using an ultrasonic vibrator and the surface were examined in a JEOL, JSM 35C Scanning Electron Microscope operating at an accelerating voltage of 15-30 KeV. Same optical microstructural samples were used for SEM studies. The composition of various phases and intermetallics were analyzed using Energy Dispersive Spectroscope (EDS) attached with SEM. An average of ten EDS measurement was used to approximate the composition of phases. For fracture studies, 5 mm height samples cut near from the fractured surface were used. Most SEM images were taken using secondary electron (SE) although some images have been acquired form back scattered electrons (BSE).

3.6 X-RAY DIFFRACTION (XRD)

The various microstructural constitutes of castings were identified using XRD. 15 mm Φ and 3mm thick samples were cut from the castings and the surface scales were removed by rough polishing. XRD spectrums were obtained using Phillips PW 1710 Powder Diffractometer with Cu-K_{α} radiation.

3.7 MECHANICAL PROPERTIES

3.7.1 Tensile Testing

Room as well as high temperature (150°C) tensile testing was carried out using computer controlled INSTRON 8801 Universal Testing Machine. Ultimate tensile strength, yield strength and elongation were obtained directly from the computer interfaced with the machine. For room temperature test extensometer was used to get the % elongation during testing whereas for high temperature test, the ductility was measured manually after the test. Samples for tensile testing were prepared according to ASTM E8 Standard. Figure 3.6 shows the schematic diagram of a tensile specimen. For high temperature testing, the samples were heated in an oven attached with the INSTRON machine and kept for 15 min after the required temperature (150°C) reached to ensure the homogenization of temperature throughout the sample.

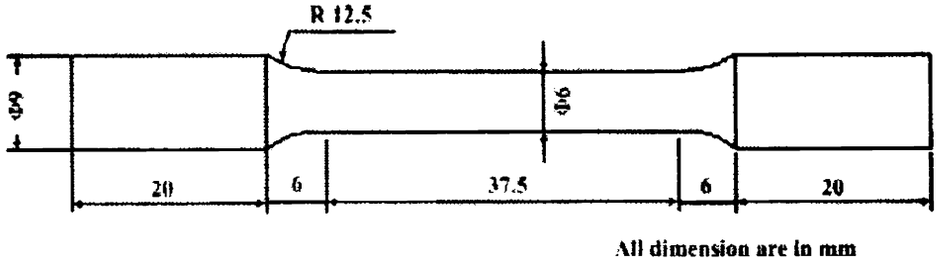

Figure 3.6: Schematic diagram of a tensile specimen (ASTM E8 Standard)

3.7.2 Creep Testing

Creep testing was carryout using 3 ton 'MAYES' creep testing machine with a lever ratio of 15:1 (Figure 3.7). Standard creep test samples (Figure 3.8) were machined out from the castings according to ASTM 138 standards. The displacement during creep was measured using two LVDTs mounted on the extensometer attached

on the gauge length (GL) of the test specimen. The required load was calculated according to the specimen diameter and lever ratio. The sample was heated using a three zone coil furnace. Specimen temperature was controlled with in ± 2° C of the set point temperature using a Eurotherm make three zone temperature controller. Two thermocouples were attached, one near the top ridge and another near the bottom ridge of the test specimen, to ensure uniform temperature throughout the GL (ref. Figure 3.8). The testing temperature was obtained around 1h and 30 min was given for the stabilization of temperature. Both the displacement and temperature was monitored and recorded at regular intervals (30 min) automatically through a Yokogawa make data logger.

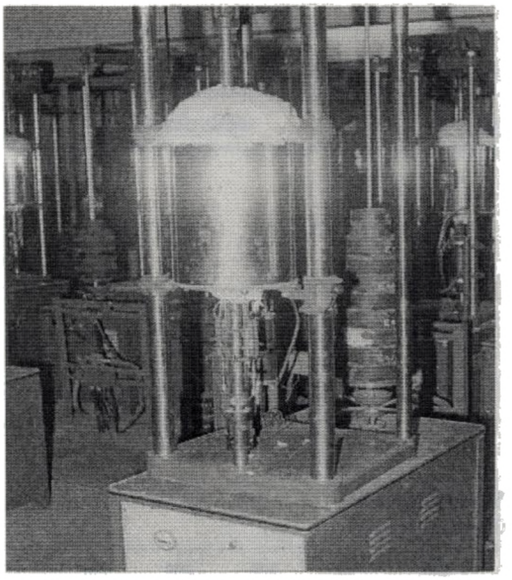

Figure 3.7: Photograph showing the creep testing machine

Cold run was carried out to check the sample alignment with the loading axis, during which the loading and unloading was done in an increment of 5 kg up to 80 % of the elastic limit. The incremental displacement during loading and unloading steps were plotted to check for equal displacement during loading and unloading. In case of any difference occurred (more than 10%), the alignment of the test sample was adjusted.

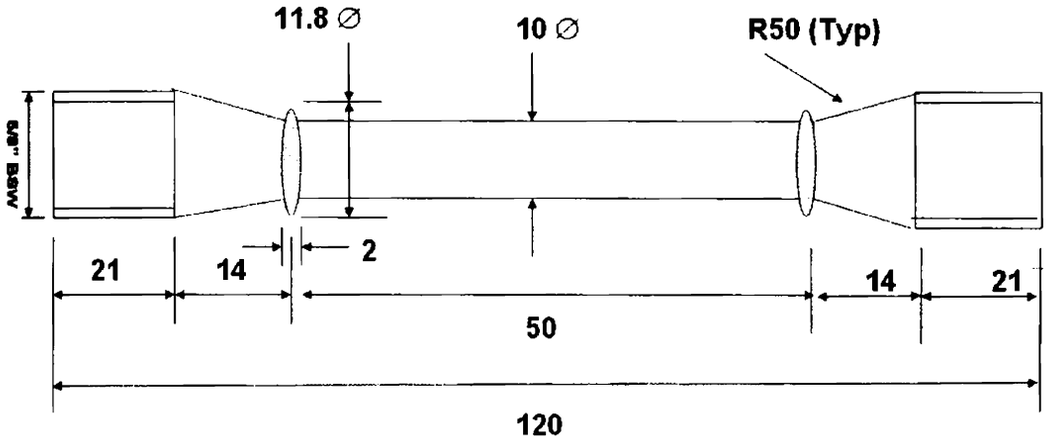

Figure 3.8: Schematic diagram showing standard creep testing specimen

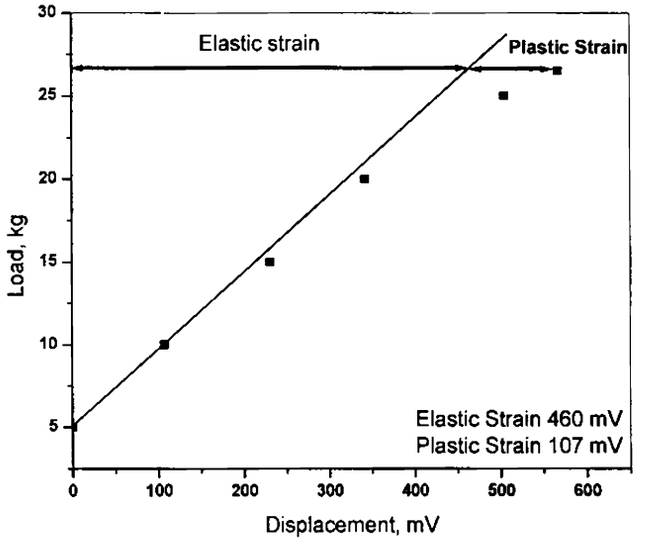

Figure 3.9: Typical hot run graph showing elastic and plastic strain region

Once the temperature of the specimen was stabilized the hot run was carried out. During hot run, loads were applied in a small possible increment to get a required finial load on pan. The total loading was carried out within 5 min. The LVDT readings were noted down immediately after every stage of loading and the displacement data were plotted against to the corresponding loads. **Figure 3.9** shows a typical hot run graph from which elastic and plastic strain was calculated. The elastic strain thus obtained was deducted from the total incremental strain recorded during

creep testing to obtain exact creep strain. Immediately after the completion of loading, strain readings were taken for 30 min in the time interval of 1 min to have more data points for getting smooth primary stage creep curve, where the creep rate changes very fast. From the displacement data obtained from data logger, strain was calculated and plotted against time.

3.8 CORROSION TESTING

3.8.1 Sample Preparation

15mm Φ X 10mm height specimens were cut from the castings and then polished up to 600 grit SiC emery paper on all sides prior to mounting in an epoxy resin using a brass rod for electrical connection for electrochemical corrosion test. This procedure avoided the formation of bubbles and crevices at the specimen/epoxy interface, which could have affected the electrochemical measurements.

3.8.2 Polarization Test

The electrochemical tests were carried out using potentiodynamic anodic polarization method in ASTM D 1384 solution. The ASTM D 1384 solution contain 148 mg l^{-1} of Na_2SO_4, 138 mg l^{-1} of $NaHCO_3$ and 165 mg l^{-1} NaCl (pH≈8.3). All the corrosion test experiments were carried out at room temperature using 1 liter, five neck ASTM electrochemical cell consisting of three electrodes; working electrode, reference electrode (Ag/AgCl-Sat) and counter electrodes (Pt). The typical polarization cell arrangement for conducting all the electrochemical experiments is shown in Figure 3.10. Solartron 1287 Electrochemical Interface was in the polarization experiments. During electrochemical corrosion test, the electrode potential was anodically scanned at a scan rate of 10 mV/min from a potential of – 1400 mV. All the electrode potential was measured against Ag/AgCl (in saturated KCl) reference electrode.

3.8.3 Electrochemical Impedance Studies

Electrochemical impedance spectroscopy (EIS) measurements were carried out using Solartron 1255 Frequency Response Analyzer (FRA) and Solartron 1287 Electrochemical Interface. The experiments were carried out in the frequency range

from 0.01 Hz to 100 kHz by superimposing an AC voltage of 10 mV amplitude at different potential. Data were presented as Nyquist and Bode plots. The Zplot/Zview software version 2.6 (Scribner Associates; Charlottesville, USA) was used for data acquisition and fitting of impedance spectra. The EIS results were interpreted using an "equivalent circuit" based on the electro physical model to ascribe a sub-electrochemical interface. The circuit description consist of an arrangement of ([R_s (C_{DL} || R_P)] elements, where R_s is the solution resistance, C_{DL} is the double layer capacitance in parallel connection with R_P, which is the polarization resistance at the interface (Figure 3.11). The selection of this circuit was a compromise between a reasonable fitting of the experimental values and a minimum of components in the equivalent circuit. The characteristic parameters of these elements values are then obtained directly by fitting the experimental impedance curves, it was apparent that this approach provide reasonably accurate values of the circuit parameters between the impedance data obtained experimentally and those calculated from the circuit parameters. The reproducibility of the data obtained with repeated measurements on a series of electrodes was within ± 5% for each measured impedance point.

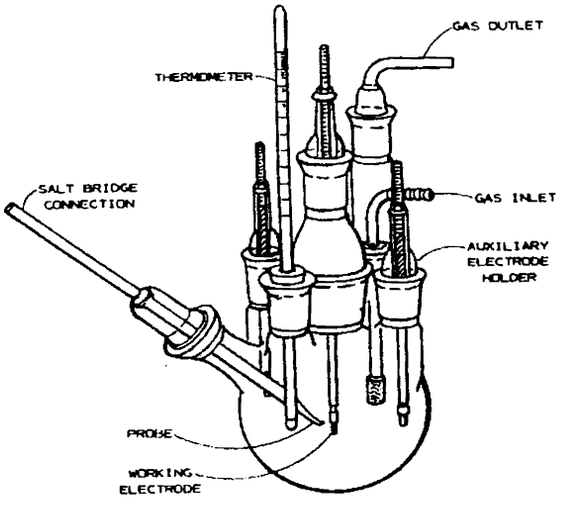

Figure 3.10: Typical polarization cell for conducting all the electrochemical experiments

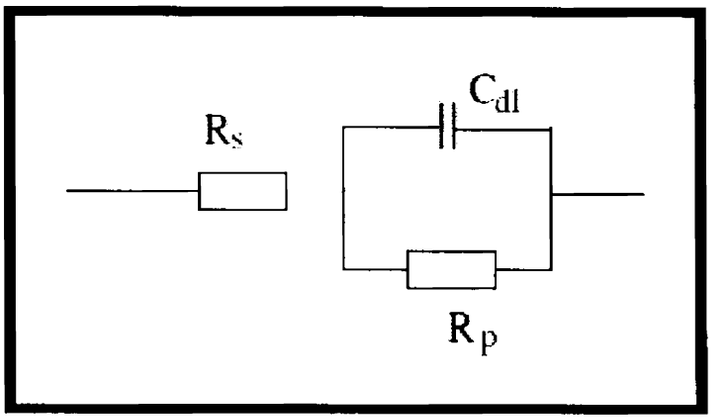

Figure 3.11: Schematic diagram showing simple 'equivalent circuit' and its elements

3.8.4 Immersion Test

For carrying out the constant immersion testing, samples of size 15mm Φ X 10mm height were polished with 80, 220, 400 and 600 grit emery papers and then polished with 0.25μm diamond paste and cleaned with acetone. The cleaned samples were weighed and exposed to a solution of 3.5% NaCl in a beaker for 100 h. After the immersion test, the samples were cleaned in a solution of 200g/l CrO_3 + 19 g/l $AgNO_3$ at room temperature for 10 min to remove the corrosion products. Finally, it was again washed with distilled water and weighted. The weight loss was calculated from the different between the initial and final weights. Form weight loss, corrosion rate was calculated using the formula given below:

$$\text{mpy (miles per year)} = 534W/DAT$$

where,

W – Weight loss during immersion in grams

D – Density of the sample in g/cc

A – Surface area of the sample exposed to the corrosive media in square inch

T – Immersion time in hours.

CHAPTER 4: RESULTS AND DISCUSSION

4.1 MICROSTRUCTURE AND PHASE IDENTIFICATION

This section of the chapter deals the effect of different alloying additions on the microstructural features of AZ91 alloy. Both optical and scanning electron microscope was used to examine the microstructural features of various alloys. Picric acid base etchant was used to etch the polished specimens. In addition to EDS analysis to identify the phases, XRD analysis was also used to confirm the type the phases. Grain size of the castings was measured at solution treated condition using image analyzer software attached with optical microscope.

4.1.1 AZ91 Alloy

Etching of Mg alloys with picric acid based etchant (6g picric acid, 5 ml acetic acid, 100 ml ethanol and 10 ml H_2O) is a complicated task. Slight change in the composition particularly, the acetic acid and water content in the etchant, spoil the surface. The etching time should also be maintained accurately i.e., 2-3 sec. Even slight extra etching time (5-6 sec) leads to the eutectic area of AZ91 alloy sample become black. This is due to the fact that the aluminium rich areas are etching faster than the other regions of the sample. Even then, it is found during this course of study that picric acid based etchant is more effective to reveal the microstructural features of Mg-Al based alloys compared to other etchants proposed in literature [240]. The optical microstructure of AZ91 alloy etched with picric acid based etchant for 5 sec (slightly over etching) and 2 sec (optimum etching) is shown in Figure 4.1. The slightly over etched microstructure in Figure 4.1(a) shows three different phases: primary α- Mg (Hexagonal crystal structure, space group $p6_3/mmc$, a=0.32094 and c=0.52105 nm) which is marked as A, massive precipitates at the grain boundary (marked as B), which is known as β-$Mg_{17}Al_{12}$ intermetallic (cubic crystal structure, space group *I*43, a=1.056 nm) and a dark area surrounding the massive sized particles, which is eutectic α- Mg (marked as C) [241]. Both the massive β-$Mg_{17}Al_{12}$ intermetallic and dark phase together is known as 'eutectic'. The primary phase i.e.,

α- Mg is a solid solution of Al and Zn. The eutectic observed at the grain boundary is divorced in nature, which is an irregular shaped particle with different sizes. As mentioned earlier, due to the higher amount of aluminium content in eutectic α- Mg compared to primary α- Mg, it etches faster and hence become darker. Figure 4.1 (b) shows the microstructure of AZ91 alloy etched with optimum time (2 Sec). The boundary (eutectic) region is clearly seen now. The dark area consists of lot of lamellar kind of precipitates. These lamellar precipitates form during the last stage of solidification. Micro constitutes of AZ91 alloy are further clearly seen in SEM photograph given in Figure 4.2.

Solidification of AZ91alloy is invoked to understand the microstructural features. During cooling, primary α-Mg forms from the super heated liquid at around 600°C. Then eutectic solidification takes place at around 400°C [96, 99]. The eutectic phase consists of massive β-$Mg_{17}Al_{12}$ and aluminum rich α-Mg, known as eutectic α-Mg. Eutectic occurs through divorced solidification reaction, not through coupled solidification as happens in most of the eutectic alloy systems like Al-Si alloys where both the eutectic phases solidifies simultaneously [99, 100]. In divorced eutectic solidification, the two eutectic phases solidify separately. Hence bulk of the $Mg_{17}Al_{12}$ solidifies separately and eutectic α-Mg solidifies around it [100]. After the eutectic reaction, a solid state transformation known as peritectic reaction takes place at the eutectic region. The eutectic α- Mg is highly supersaturated in Al compared to the primary α- Mg due to the fact it solidifies last and solidification never reach equilibrium. Due to this supersaturation, when alloy cools from eutectic temperature to the room temperature, the excess amount of aluminum in the solid solution precipitates out as $Mg_{17}Al_{12}$ and leaves aluminum depleted α- Mg. Hence this reaction leads to the formation of alternative layers of α- Mg and β phase as shown in Figure 4.2 (b) and known as discontinuous precipitates or secondary precipitates [144, 242, 243].

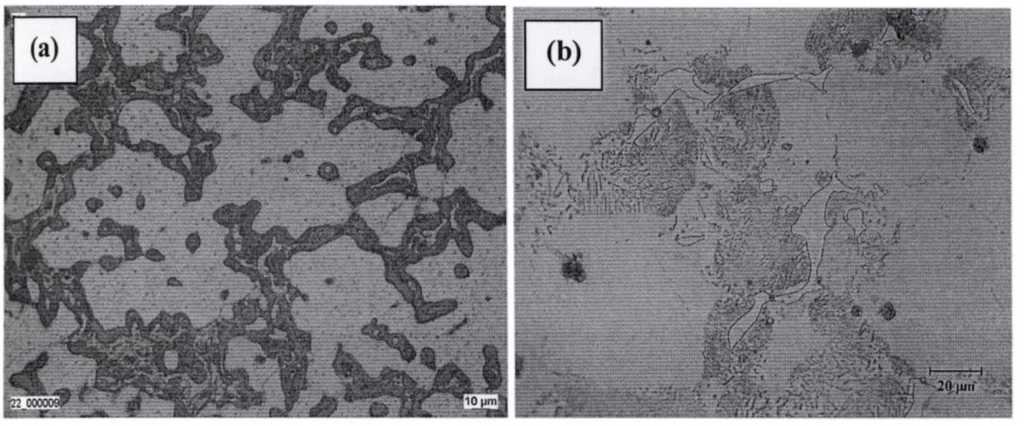

Figure 4.1: Optical micrograph of AZ91 etched in picric acid based etchant showing its different constituents (a) Etched for 5 sec (b) Etched for 2 sec

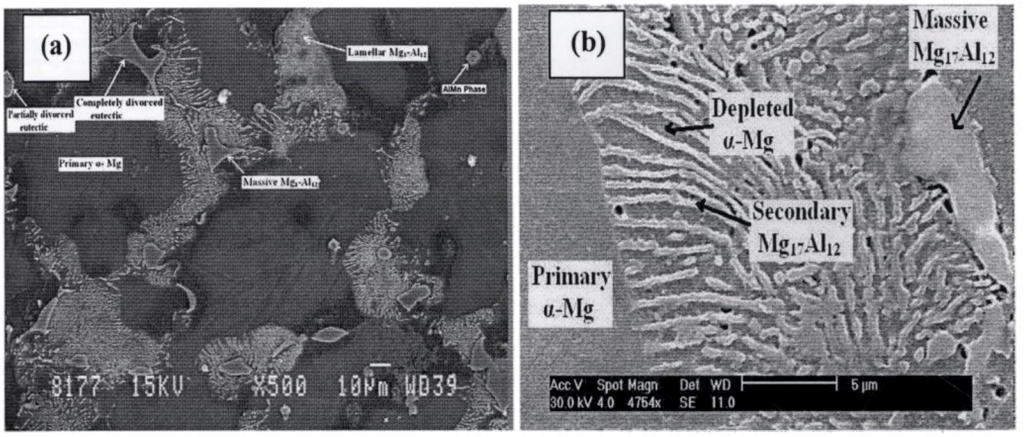

Figure 4.2: SEM photograph showing different phases in AZ91 (a) Low magnification (b) Higher magnification

The quantification of different alloying elements presents (Mg, Al and Zn) at different locations in AZ91 alloy microstructure is obtained from EDS analysis and is presented Table 4.1. It is seen that both massive and discontinuous lamellar $Mg_{17}Al_{12}$ has almost similar composition and hence has difference only in morphology. Interestingly, the EDS analysis also shows the presence of Zinc in $Mg_{17}Al_{12}$ intermetallic. Accommodation of zinc atoms in $Mg_{17}Al_{12}$ intermetallic during solidification is reported in literature [244]. Even though, the supersaturation of Al is relived by the formation of DP reaction during solidification, it is also observed at most of the areas near to the DP front that the Al and Zn content are still slightly higher.

Table 4.1: EDS results taken at different location/phases in AZ91 alloy

Location	Elements, % Wt		
	Mg	Al	Zn
Matrix near the center of grain	92.24	5.45	2.31
Matrix near the eutectic area	80.14	14.42	5.44
Massive $Mg_{17}Al_{12}$	57.46	37.34	5.20
Lamellar $Mg_{17}Al_{12}$	55.75	37.50	6.75

The eutectic observed in the microstructure consists of mostly fully divorced eutectic. However there are some partially divorced eutectic is also seen. A fully divorced eutectic is one, in which the two eutectic phases are completely separated as eutectic α- Mg and massive β-$Mg_{17}Al_{12}$. On the other hand, in partial divorced eutectic, 'islands' of eutectic α- Mg present within the β-$Mg_{17}Al_{12}$ and still bulk of the eutectic α- Mg present out side the β-$Mg_{17}Al_{12}$. Both the eutectics are shown in Figure 4.3. There are different factors like aluminium, zinc content and cooling rate, which decides the type of eutectics [100, 101, 245, 246]. The presence of considerable amount of zinc (up to 1%) and comparatively faster cooling in permanent mould (compared to sand casting) leads to the formation of fully divorced eutectic [100, 101, 245]. The mechanisms behind the formation of partial and complete divorced morphologies are already discussed in chapter 2.

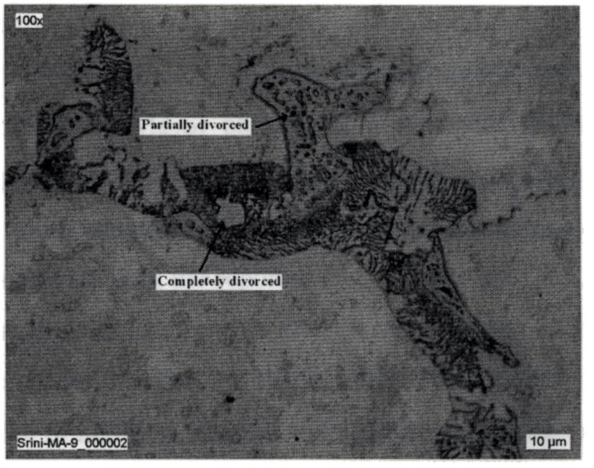

Figure 4.3: Microstructure of AZ91 showing both complete and partially divorced eutectic

Apart from the major phases, there are some AlMn intermetallic is also seen in the microstructure, which is identified as Al_8Mn_5 [241]. The morphology of this phase is round and very fine compared to the massive eutectic $Mg_{17}Al_{12}$ phase. However, the amount of this precipitates is very less. This is because the added amount of Mn is very low (0.2% max) and most of the Mn is utilized to remove the Fe by forming heavy intermetallics, which normally settle down in the crucible.

Figure 4.4 shows the XRD pattern of base alloy, which shows peaks for only two phases: α- Mg and β-$Mg_{17}Al_{12}$. Some of the peaks for β phase, which appears in the JCPDS software, are not revealed [247]. But, the major peak for β phase at 2θ values of 36.5, which represent (411) planes, is clearly seen. Even though Al_8Mn_5 intermetallic is seen in the microstructure, there are no X-ray peaks corresponding to this phase. This is due to the fact that the volume fraction of the phase is very much below to the detectable level in XRD.

4.1.2 AZ91+X Si Alloys (X=0.2%, 0.5%)

As per the Mg-Si phase diagram, (shown in Figure 4.5) Si has negligible solid solubility in magnesium at room temperature [248]. Hence all the added Si combines with Mg to form Mg_2Si intermetallics. Figure 4.6 shows the microstructure of Si added AZ91 alloys. When 0.2% Si is added to AZ91 alloy, black coloured Mg_2Si

intermetallics appears at the grain boundary in addition to the massive $Mg_{17}Al_{12}$ particles. With 0.5% Si added alloy, the only microstructural change observed is the increase in the amount of Mg_2Si phase and it has well defined Chinese script morphology. This phase is very coarse and has multiple arms extended along many of the neighbouring grain boundaries. The morphology of Mg_2Si precipitates observed in this study is in consistence with the reported one in literature [183, 249-251]. A close inspection on the microstructure reveals that the morphology of Mg_2Si intermetallic varies from needle shape to massive Chinese script. More needle shaped precipitates is noticed with 0.2% Si addition whereas with higher percentage of Si (0.5%), more number of Chinese script Mg_2Si appears in the microstructure. This is due to the segregation of more amount of Si to the solidifying Mg_2Si particles during slower solidification in gravity cast process (compared to die casting).

Figure 4.7 shows the SEM photograph focusing the Mg_2Si Chinese script intermetallic and its EDS pattern, which indicate that it contains only Mg and Si. However, variation in the composition along its arms is noticed. Higher concentration of Si is noticed at the tip of the arm. For further confirmation, X- ray analysis was also carried out in the solution treated sample (410°C for 48 h), which shows peaks for Mg_2Si intermetallic in addition to peaks for α-Mg (Figure 4.8).

There is no appreciable change in grain size observed with Si addition. The grain size measured for 0.2% Si and 0.5% Si added alloys read almost similar as around 70 μm (the base alloy grain size is 80 μm). It is further noticed from the microstructure that the addition of Si to AZ91 alloy does not change the quantity as well as the morphology of the massive β-$Mg_{17}Al_{12}$ phase. The β- $Mg_{17}Al_{12}$ intermetallic quantity is not changed since the possibility of forming of any other phase between Al and Si is nil. So, all the aluminium is available for the formation of $Mg_{17}Al_{12}$ phase. In addition, EDS analysis performed across the $Mg_{17}Al_{12}$ intermetallic indicates that there is no Si in it. This confirms that Si does not act as a modifier or refiner for $Mg_{17}Al_{12}$ phase.

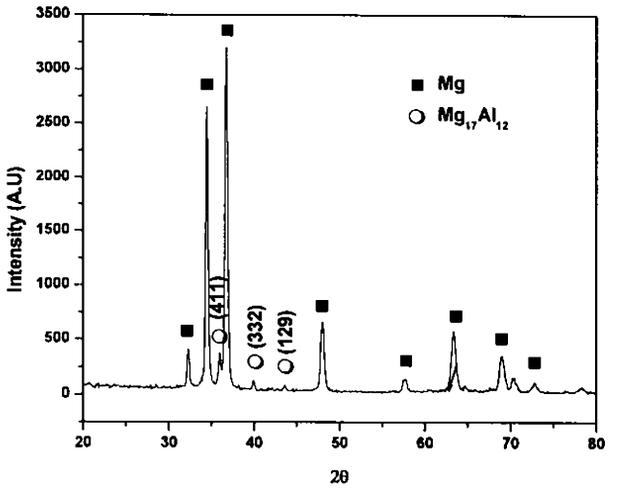

Figure 4.4: XRD pattern of AZ91 alloy showing peaks for Mg and $Mg_{17}Al_{12}$ Intermetallic

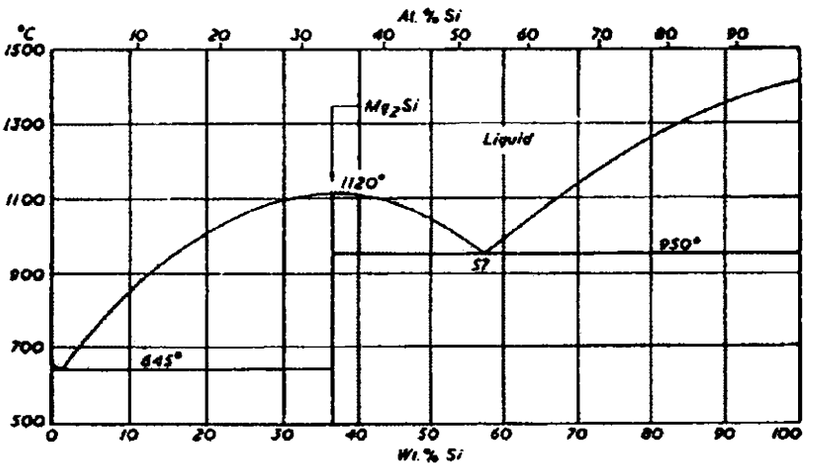

Figure 4.5: Phase diagram of binary Mg-Si alloy system [248]

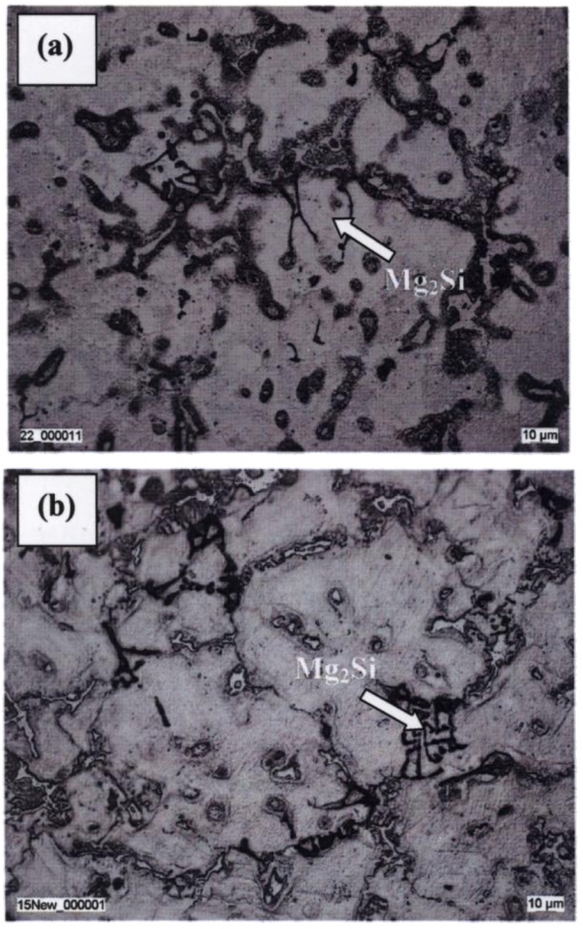

Figure 4.6: Microstructure of Si added alloys (a) AZ91+ 0.2% Si (b) AZ91+0.5%Si

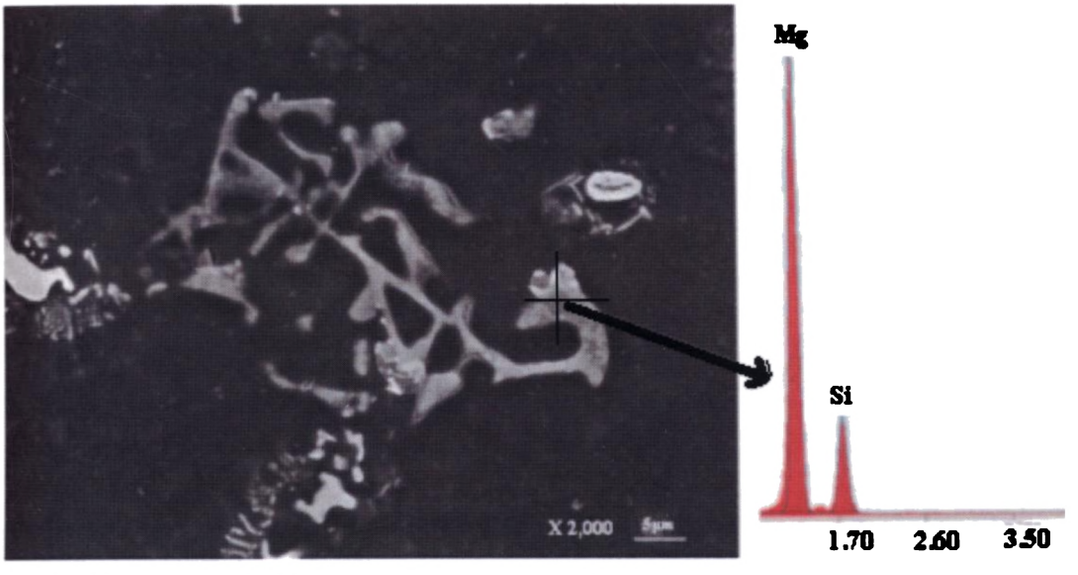

Figure 4.7: SEM photograph showing Chinese script Mg_2Si intermetallic and its EDS spectrum

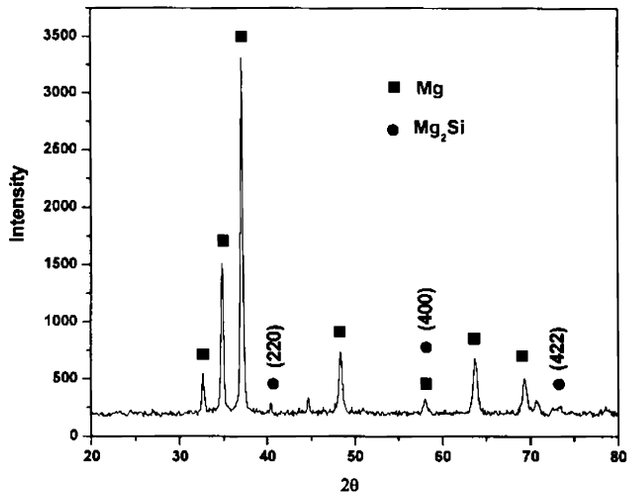

Figure 4.8: XRD pattern of solution treated AZ91+0.5% Si alloy indicates the presence of Mg_2Si intermetallic

4.1.3 AZ91+X Sb Alloys (X=0.2%, 0.5%, 0.7%)

Figure 4.9 shows the optical microstructure of Sb added AZ91 alloys. With 0.2% Sb addition, the microstructure of AZ91 alloy does not change much. However, a black colored phase is seen along with massive $Mg_{17}Al_{12}$ at the grain boundaries in 0.5% Sb added alloy as shown in Figure 4.9 (b). When Sb addition increases to 0.7%, the amount of black phase also increases, which is evidenced in Figure 4.9 (c). Reduction in grain size to certain extend is also noticed with 0.7% Sb addition. Size and morphology of the Sb bearing intermetallic compound is clearly seen in the SEM photograph shown in Figure 4.10, which reveals that the morphology is a needle or plate shape. According to the Mg-Sb phase diagram (Figure 4.11) it is understandable that Sb does not have any solubility in Mg at room temperature [252] and the possible intermetallic present at room temperature is Mg_3Sb_2. So, all the added Sb needs to form Mg_3Sb_2 intermetallic. It is further noticed from the microstructure that almost all the Mg_3Sb_2 intermetallics appears together with $Mg_{17}Al_{12}$ at the grain boundaries. Figure 4.12 shows the SEM photograph focusing Mg_3Sb_2 intermetallic and EDS spectrum taken at the phase, which indicates the presence of only Mg and Sb. Based on the quantitative analysis, the phase is identified as Mg_3Sb_2. The presence of Mg_3Sb_2 intermetallics is also confirmed by XRD analysis carried out on solution treated AZ91 + 0.5% Sb added alloy as shown in Figure 4.13.

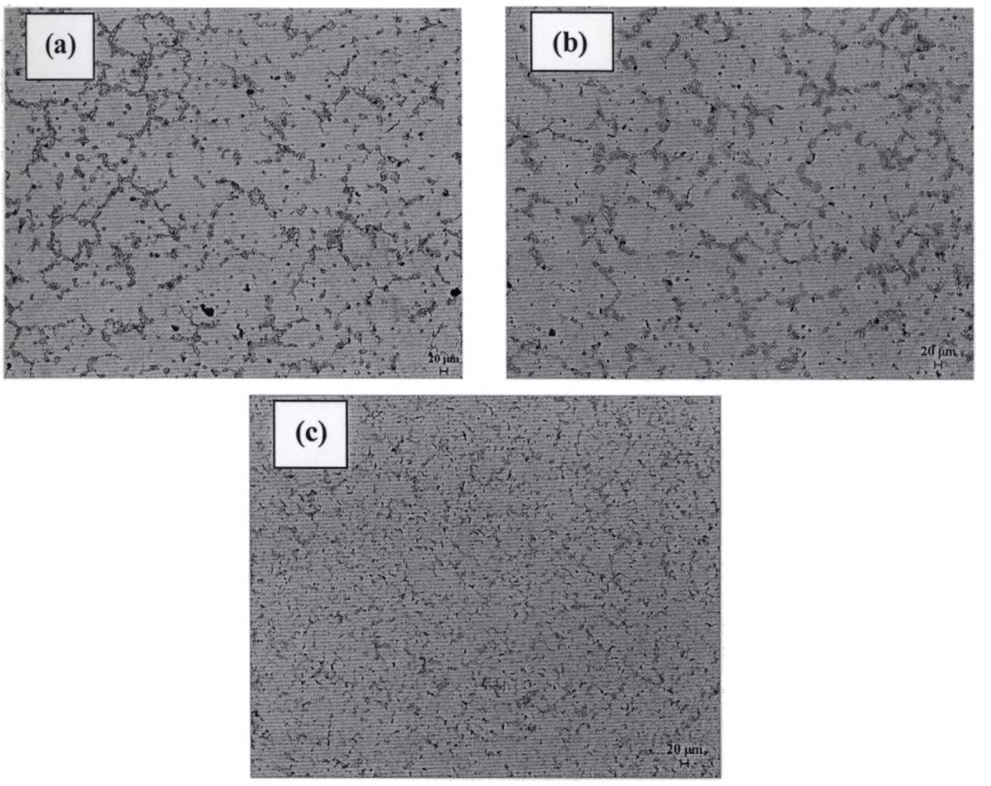

Figure 4.9: Optical microstructure of Sb added AZ91 alloys (a) AZ91+0.2% Sb (b) AZ91+0.5% Sb (c) AZ91+0.7% Sb

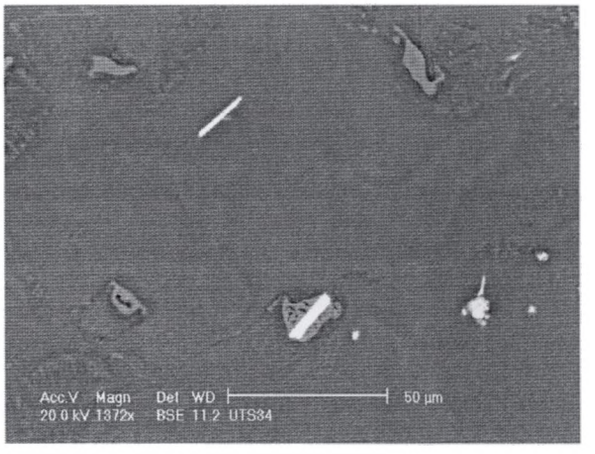

Figure 4.10: SEM photograph of AZ91+0.5% Sb alloy showing Mg_3Sb_2 intermetallic

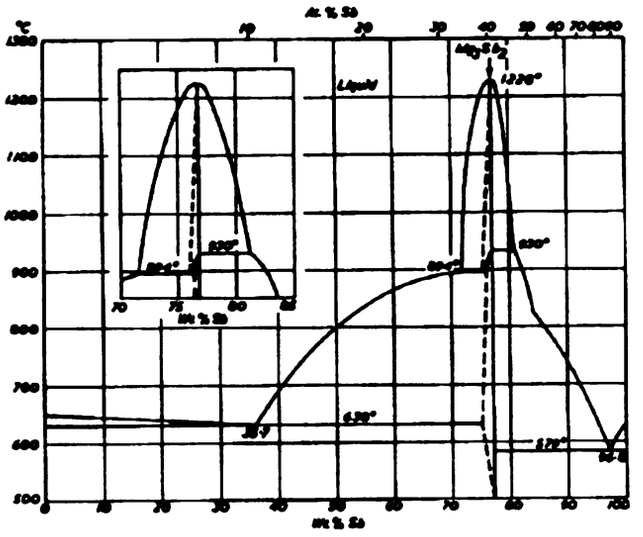

Figure 4.11: Phase diagram of Mg-Sb binary alloy system [252]

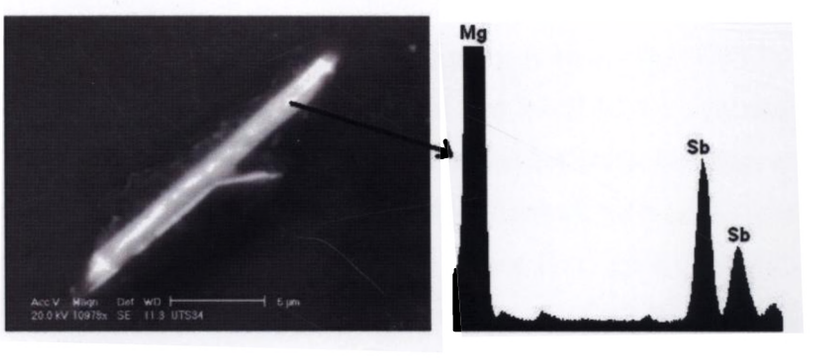

Figure 4.12: SEM photograph and EDS spectrum of Mg_3Sb_2 intermetallic

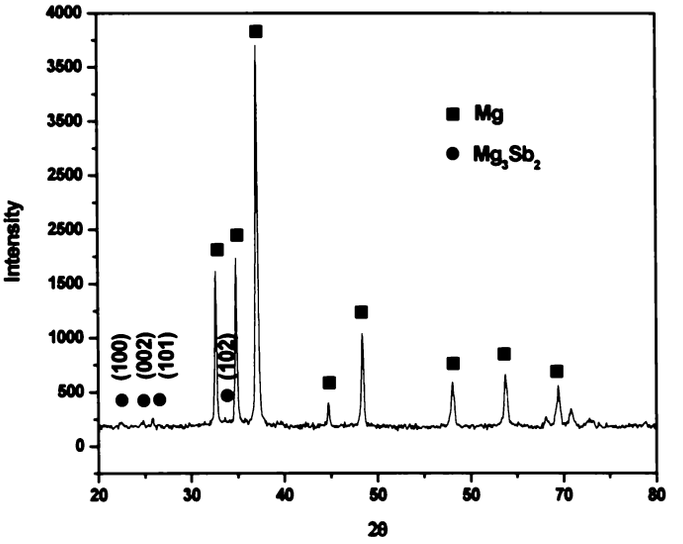

Figure 4.13: XRD pattern of 0.5% Sb added AZ91 alloy showing peaks for Mg_3Sb_2 intermetallic

4.1.4 AZ91+X Sr Alloys (X=0.2%, 0.5%, 0.7%)

From Mg-Sr phase diagram given in Figure 4.14, it is clear that the Sr addition has little solid solubility with Mg [253]. Hence the added Sr needs to form an intermetallic with either Mg or Al, since aluminum is also presented in the alloy. The microstructure of Mg-Al-Sr alloy system is well analyzed due to the development of Sr containing Mg-Al based alloys (Mg-5% Al-1% Sr, Mg-5% Al-2% Sr and Mg-6% Al-2% Sr) for high creep resistance [66, 239, 254-259]. However, the key obstacle is the lack of a well defined Mg-Al-Sr ternary diagram. At present the phases have been identified based on three binary diagrams of Al-Mg, Al-Sr and Mg-Sr [260]. In the Al-Sr system, in addition to solid solutions of Al, γ-Sr (bcc) and α-Sr (fcc), there are other three intermetallic compounds present: Al_4Sr, Al_2Sr and Al_7Sr_8 [261]. The Mg-Sr system also contains, in addition to solid solutions of Mg, γ-Sr and α-Sr, four intermetallic compounds: $Mg_{17}Sr_2$, $Mg_{38}Sr_9$, $Mg_{23}Sr_6$ and $MgSr_2$ [36].

Different phases are reported in ternary alloy system (Mg-Al-Sr) by different authors. Peng Zhao et al [239] have reported that Al_4Sr is the only intermetallic present in AM50+xSr (0.02-1%Sr) alloy. But in another study Bai Jing et al [256] have reported two types of Sr phases in Mg-4Al: network kind of Al_4Sr with body centered tetragonal structure (DI3 with a=4.46 A0 and C=11.07 Ao), a bulky Mg-Al-Sr ternary intermetallic with a chemical composition of 12.4% Al-9.6% Sr-Mg. Gzerwinski et al [259] have observed different kind of Sr bearing phases like Al_4Sr, $Mg_{17}Sr_2$ in Sr containing Mg-Al alloy.

Recently, Pekguleryuz et al [176] have reported that the Mg-Al alloys containing Sr exhibit different microstructures based on the Sr/Al ratio. For Sr/Al ratio below about 0.3, Al_4Sr intermetallic is the only second phase seen in the structure. When the Sr/Al ratio is higher than 0.3%, a second intermetallic phase, a ternary Mg-Al-Sr intermetallic, also appears along with binary phase.

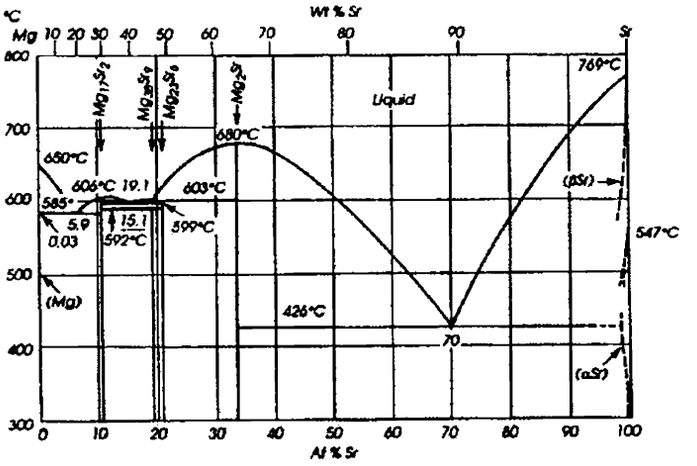

Figure 4.14: Binary phase diagram of Mg-Sr alloy system [253]

Figure 4.15 shows the SEM photograph of Sr added AZ91 alloys. With 0.2% Sr addition, there is no intermetallic, other then $Mg_{17}Al_{12}$, is found in the microstructure. However, this Sr addition slightly refines the grain size. With little higher percentage of addition i.e., 0.5%, few white-colored needle like precipitates are seen along with $Mg_{17}Al_{12}$ intermetallic at the grain boundary. On the other hand, the microstructure of 0.7% Sr added alloy shows more number of white needle shaped precipitates. The grain size of both 0.5 and 0.7% Sr added alloys are not differed much (around 50 μm). A closer inspection with 0.7% Sr added alloy, shown in Figure 4.16, indicate that there are two different kinds of precipitates appear at the grain boundary: one is a long needle shaped particle, which is presented in large number (marked as 1) and another one is a bulky precipitate (marked as 2) which appears rarely. The EDS analysis on the bulky precipitate indicate that it is a ternary precipitate of Al, Mg and Sr. Moreover, it is found that the bulky precipitate is not a general feature. No such intermetallic is found in 0.2% Sr and 0.5% Sr additions, which might be due to very low content of Sr to form ternary intermetallic.

In the present work, according to Sr/Al ratio, only Al_4Sr intermetallic is observed in the microstructure, which is confirmed by XRD studies. The XRD spectrum of solution treated 0.7% Sr added alloy is given in Figure 4.17, which shows peaks for both Mg and Al_4Sr intermetallic. But no peaks are observed for any ternary phases since the amount of ternary intermetallic present is very much low.

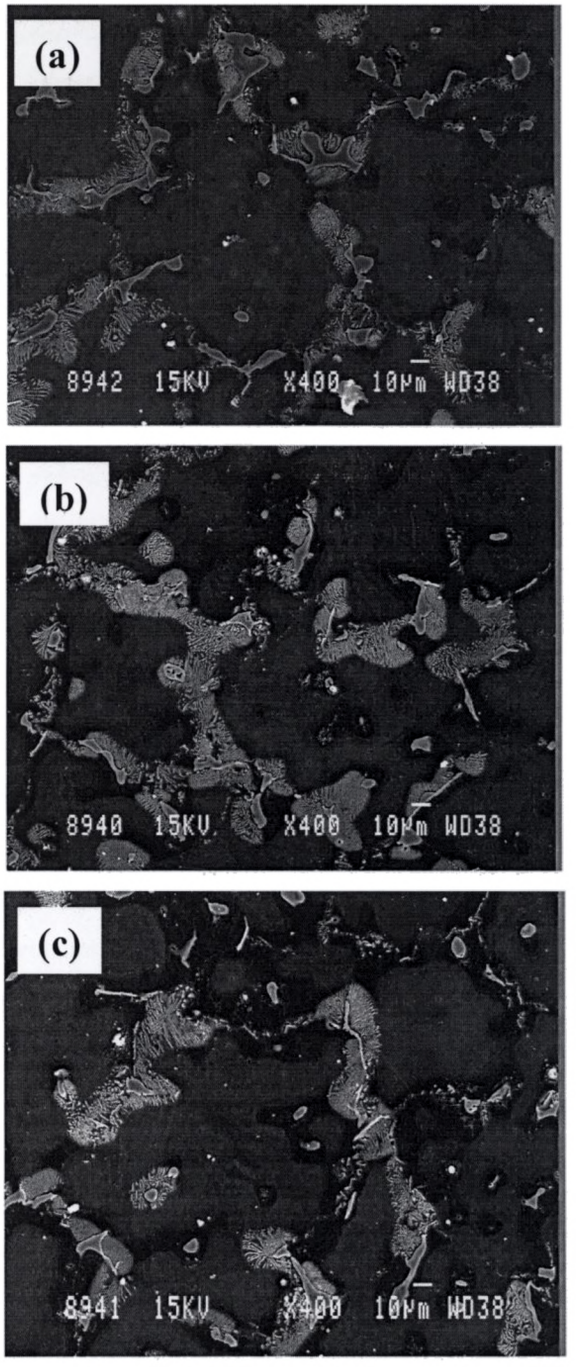

Figure 4.15: SEM photograph of Sr added AZ91 alloy (a) AZ91+0.2% Sr alloy (b) AZ91+0.5% Sr alloy (c) AZ91+0.7% Sr

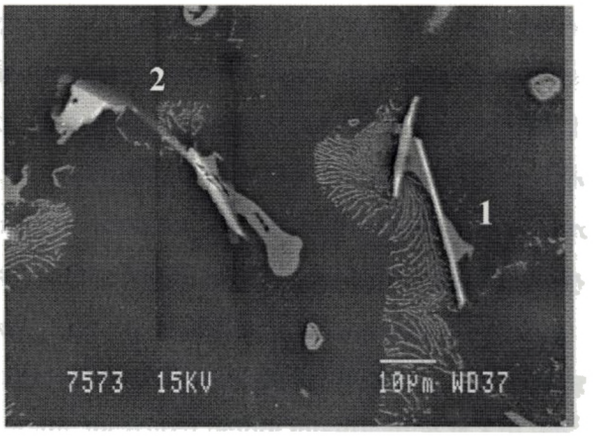

Figure 4.16: SEM photograph of AZ91+0.7% Sr alloy showing two kind of Sr bearing phases

In addition to Sr containing phases, presence of $Mg_{17}Al_{12}$ intermetallic is also observed with Sr added alloy microstructure. Since added Sr amount is low (0.7% max) and Al content is very high (9%), there would be insufficient amount of Sr to bind all Al and hence the excess Al is solidified as $Mg_{17}Al_{12}$ intermetallic. However, from the microstructures presented in Figure 4.15, it can also be seen that the size of the β-$Mg_{17}Al_{12}$ phase is refined to some extent. The massive shaped β-$Mg_{17}Al_{12}$ phase changes into a finer one as the Sr content increases from 0.2% to 0.7%. Similar kind of refinement is reported in literature previously with Sr addition to AM50 alloy [239]. The EDS spectrum taken at $Mg_{17}Al_{12}$ intermetallic, presented in Figure 4.18, confirms the presence of Sr in it. This indicates that little amount of added Sr dissolved into the β phase and restrict its growth during solidification.

4.1.5 AZ91+XSi+0.2% Sb and AZ91+XSi+0.1% Sr Alloys (X=0.2%, 0.5%)

Morphological modification of Mg_2Si intermetallic is needed to improve the mechanical properties of gravity cast Si containing Mg-Al alloys. 0.2% Sb and 0.1% Sr is added to Si containing AZ91 alloy in this present study to investigate its modification efficiency. Figures 4.19 and 4.20 show the microstructures of 0.2% Sb and 0.1% Sr added AZ91 alloy containing 0.5% Si. The addition of 0.2% Sb leads to an interesting microstructural change by changing the massive Chinese script morphology of Mg_2Si phase to a well define fine polygonal shape besides distributing

them evenly along the grain boundaries. However, there are few Mg_2Si intermetallics are also seen within the grain. From the figure 4.20, it is found that Sr is also found to be capable of modifying the morphology of Mg_2Si intermetallic but to lesser extend compared to the Sb addition. In this case, most of the modified particles are in irregular shape and few particles are in rectangular shape. Moreover, it is further observed that the size of the Mg_2Si precipitates in Sr modified alloy is bigger than that of the Sb modified alloy. It is difficult to measure the exact size of the Mg_2Si intermetallics because of its complex nature. However, the average size (in terms of area) of the intermetallic measured before modification is 320 μm^2 and after modified with Sb and Sr is 30 and 75 μm^2 respectively. Due to this size difference in Sb and Sr modification, the distribution of Mg_2Si in two additions is also differed. The Mg_2Si particles are more or less evenly distributed throughout the microstructure in case of Sb addition compared to Sr addition.

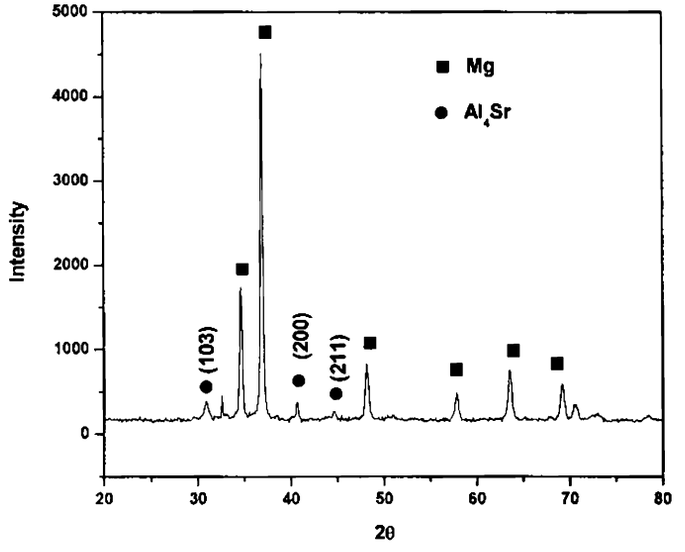

Figure 4.17: XRD spectrum of AZ91+0.7% Sr alloy confirm the presence of Al_4Sr Intermetallic

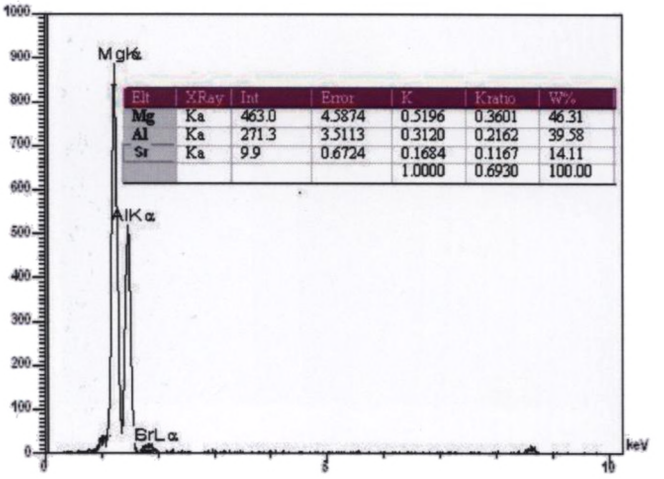

Figure 4.18: EDS spectrum of $Mg_{17}Al_{12}$ intermetallic in AZ91+0.7% Sr alloy confirms the presence of Sr

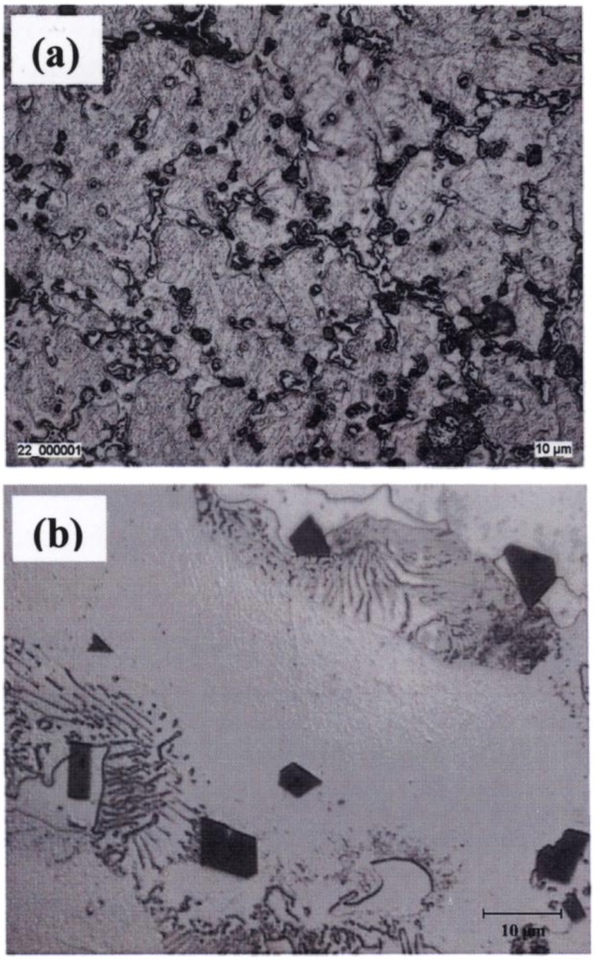

Figure 4.19: Microstructure of AZ91+0.5% Si+0.2% Sb showing modified Mg_2Si intermetallic (a) Lower magnification (b) Higher magnification

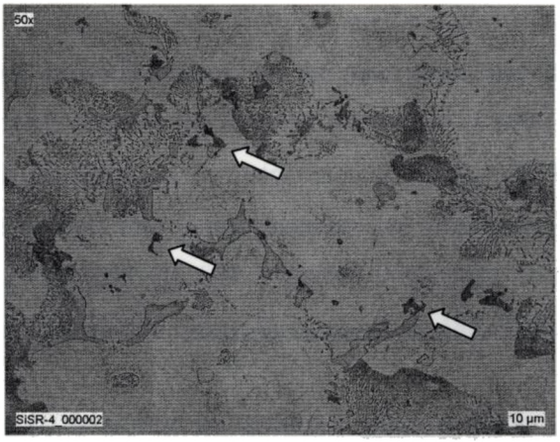

Figure 4.20: Microstructure of AZ91+0.5% Si+0.1% Sr alloy showing modified Mg_2Si intermetallic

Modification of Chinese script Mg_2Si intermetallic in gravity cast Mg-Al is already in practice [262-264]. AS21 and AS41 alloys, which contain 2% and 4% Al respectively, have Mg_2Si precipitates in larger volumes. These alloys provide higher creep resistance due to the presence of thermally stable Mg_2Si intermetallic [24, 262, 263]. However, these alloys are restricted only to die-casting. In sand casting, the Mg_2Si intermetallic solidifies as a coarse Chinese script, which reduces the mechanical properties [17, 22]. Normally P, Ca is added to modify this intermetallic into fine sized particles [249, 264, 265]. In the present study, it is found that both Sb and Sr are also capable of modifying the Mg_2Si precipitates.

The possible mechanisms for the refinement might be the added Sr and Sb either acted as a nucleation site for the Mg_2Si precipitates or suppresses the growth of the precipitates during solidification. Jae Joong Kim et al [249] have carried out extensive TEM studies on Ca and P added Si containing Mg-Al alloys and found the presence of $CaSi_2$ and $Mg_3(PO_4)_2$ compounds respectively in Ca and P added alloys, which act as a nucleation site for the Mg_2Si particles. Recently there are some studies, which report that Sb is also capable of refine the Mg_2Si Chinese script intermetallic [266, 267]. However, the mechanism for such refinement is not yet clear. Yuan et al [266] have suggested that the added Sb forms Mg_3Sb_2 intermetallic and acts as a nucleation site for the Mg_2Si precipitates. They have verified the presence of Mg_3Sb_2

precipitates using XRD. In the present study no such peaks corresponding to Mg_3Sb_2 precipitate is observed in XRD studies. On the other hand, the EDS analysis carried out on the Mg_2Si particle indicate the presence of Sb in it as shown in Figure 4.21. In order to have more information on the distribution of Sb over the Mg_2Si intermetallic, line scan across the particle and X-ray mapping was also carried out and given in Figures 4.22 and 4.23 respectively. These studies confirm no Sb concentration in the Mg_2Si particles, rather distributed evenly throughout the Mg_2Si intermetallic.

Elements like Ca. P and Sb are normally added to Al-Si alloys to modify the eutectic and primary Si particles. Sr is also a well-known modifier for Si in hypoeutectic Al-Si alloys [268, 269]. Based on this, it is believed that Sr can also change the morphology of Mg_2Si intermetallic. However, studies on Sr modification of Mg_2Si intermetallic in Mg alloys is not reported in literature. In the present study, Sr modification of Mg_2Si intermetallic in AZ91 alloy is carried out and found that Sr changes the morphology of Mg_2Si. Similar to Sb modified alloy the XRD pattern taken on the Sr modified alloy does not show any peaks for Sr containing component. However, EDS spectrum taken at the Mg_2Si precipitates shown in Figure 4.24 indicates the presence of Sr in it. X-ray mapping of the Sr modified Mg_2Si intermetallic (Figure 4.25) also indicates the distribution of Sr in Mg_2Si intermetallic is even.

From these results, it is more logical to conclude that both the Sb and Sr addition restrict the growth of Mg_2Si intermetallic during solidification and change the morphology rather than act as a nucleant. Uneven size and shape of the modified Mg_2Si particles are also support this modification mechanism. However, more rigorous TEM studied are needed to confirm the modification mechanism, which is included in the future course of work.

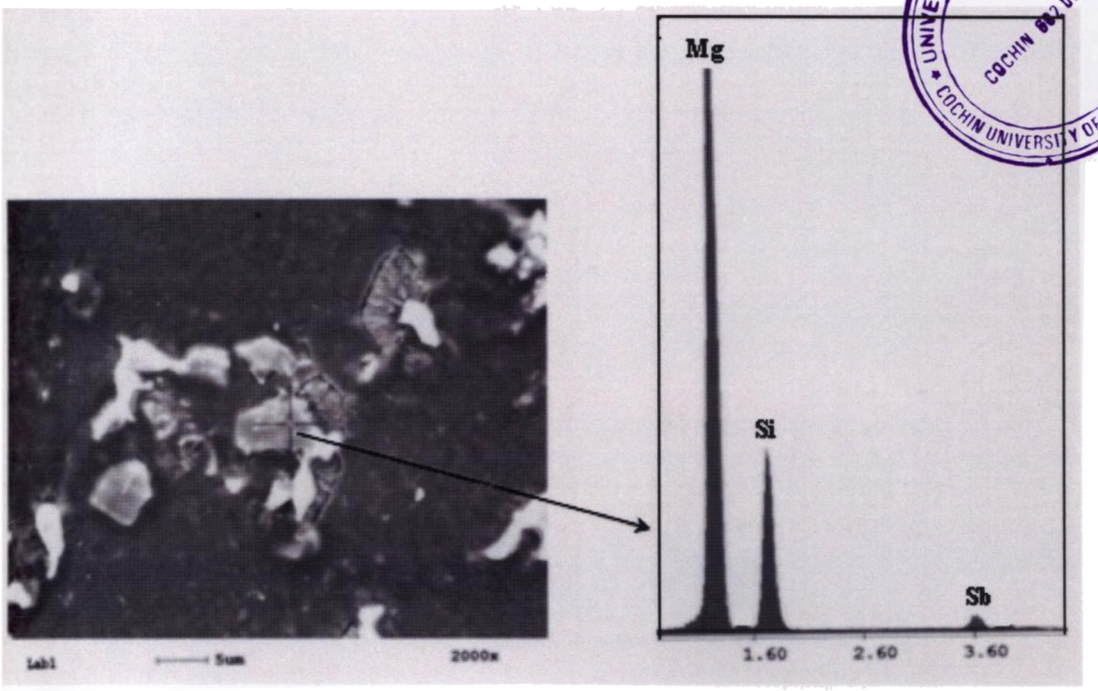

Figure 4.21: SEM photograph and EDS spectrum taken on Mg_2Si in Sb added AZ91+0.5% Si alloy indicates the presence of Sb in it

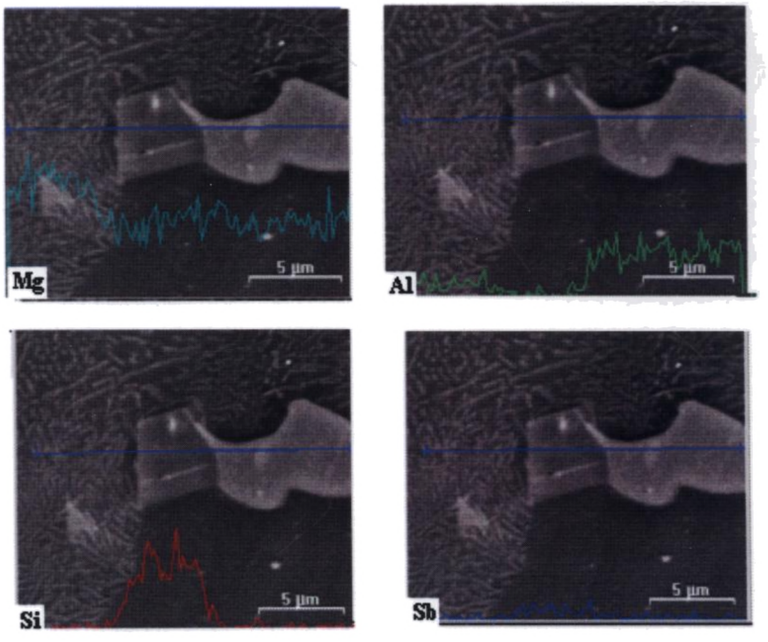

Figure 4.22: Line scanning taken across the modified Mg_2Si precipitate in Sb added AZ91+0.5% Si alloy

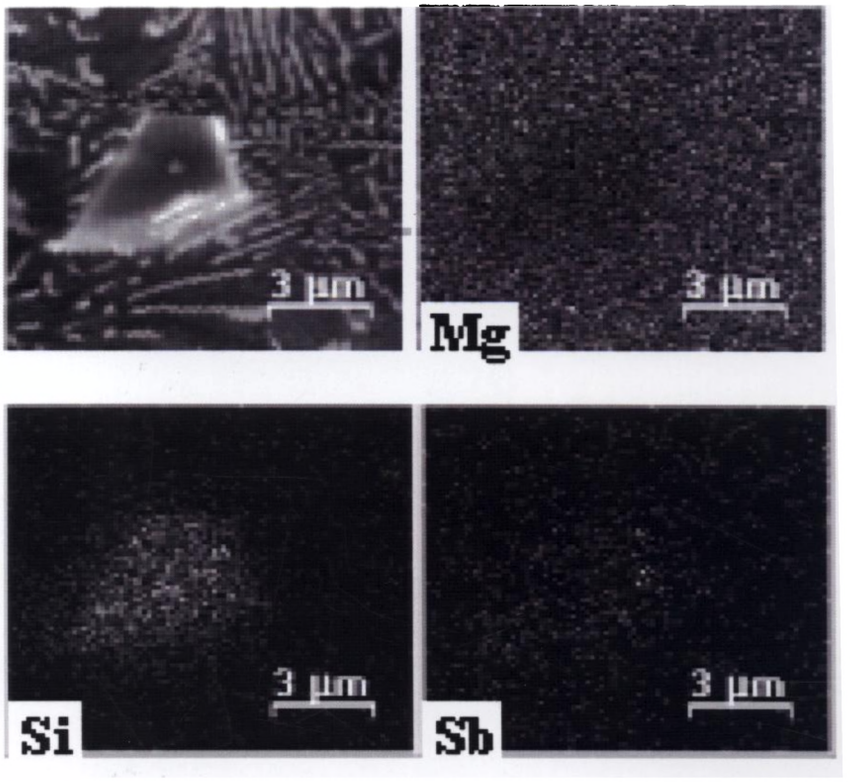

Figure 4.23: X- ray mapping taken on the modified Mg_2Si precipitate in Sb added AZ91+0.5% Si alloy

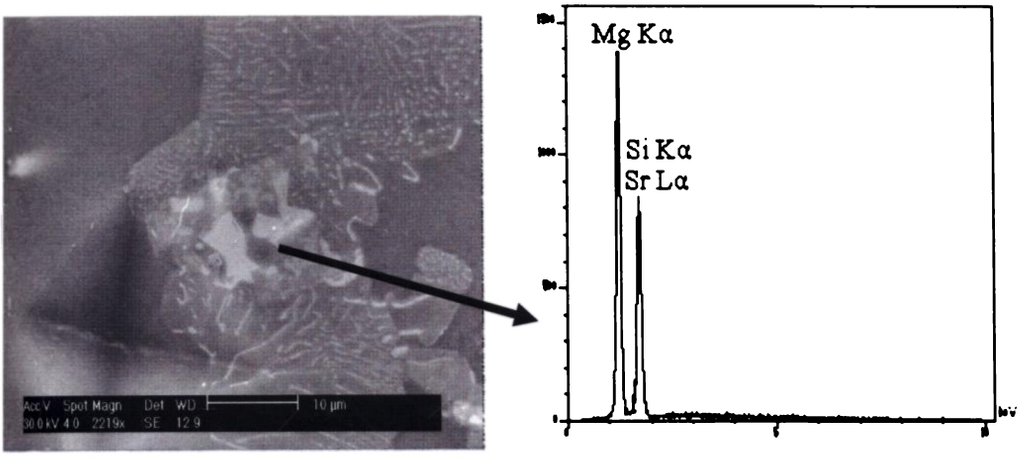

Figure 4.24: SEM photograph and EDS spectrum of Sr modified Mg_2Si intermetallic indicate the presence of Sr in it

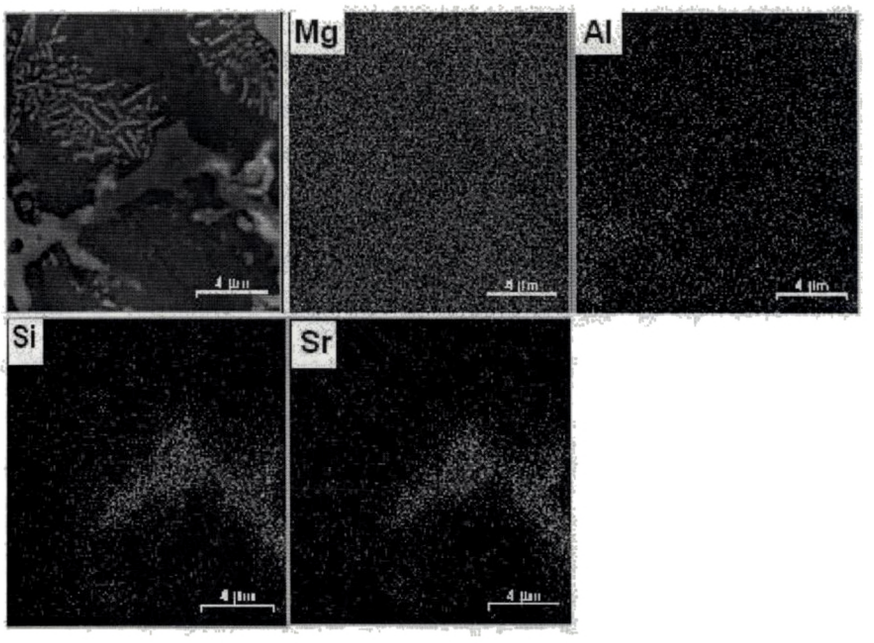

Figure 4.25: X- ray mapping taken on the modified Mg_2Si precipitate in Sr added AZ91+0.5% Si alloy indicates the distribution of Sr in Mg_2Si intermetallic

4.2 GRAIN REFINEMENT

This section of the chapter deals the effect of alloying additions on the grain refinement of AZ91 alloy. Apart from forming intermetallics, some of the elements added refine the base alloy grain size. With as cast microstructure, the grain boundaries of Mg-Al alloys are not revealed properly. The normal procedure to visualize the grain boundary is to solution treat the alloy at 410°C h for 28 h and ageing it at 200°C for 1h. [124, 270-272]. Ageing treatment enhances the delineation of grain boundaries. The boundaries can be then seen under microscope in etched condition. In the present study, the grain size was mainly measured by linear intersect method using image analyzer attached with the optical microscope. However, in some cases the grain sizes were measured by manually as well. The grain size of AZ91 alloy with and without different alloying elements in solution treated condition is presented in Table 4.2. Some of the alloy microstructures are also presented in Figure 4.26. All the microstructures show variation in grain sizes. Due to the large variation in grain sizes difficulties were encountered during the measurement. Minimum 5 measurements were carried out and average grain size is reported. It could be seen

that the addition of Si does not make much difference in grain size compared to the base alloy. But higher percentage of Sb and Sr additions show grain refinement ability to certain extent. The base alloy grain size of 80 ± 10 μm is reduced to 70 ± 15 μm with 0.5% Sb addition whereas it is further reduced to 63 ± 12 μm with 0.7% of Sb addition. When 0.2% Sr is added, the grain size has reduced to 65 ± 4; however, 0.5% Sr addition reduced the grain size to a minimum of 55 ± 5 μm. Not much appreciable change in grain size is observed with higher amount (0.7%) of Sr addition. Grain refinement is also seen with combined addition of Si and Sb & Si and Sr. In this case also Sr is seems to be more effective in grain refinement compared to Sb. The grain size of AZ91+0.5% Si+0.1% Sr alloy is 45 ± 5μm, which is almost 40-50% less than the grain size of base alloy.

Even though these elements are not much effective grain refiners as like as carbon inoculation, which consider as one of the prime grain refiner for Mg alloys particularly Al containing alloys, grain refinement due to these elemental additions may be the result of the formation of particles, which might have segregated in solidification front caused constitutional under cooling. This under cooling activates nucleant particles suspended in the melt [273]. The constitutional undercooling is simplified as the growth restriction factor (GRF) and defined as

$$GRF = \Sigma_i m_i C_{O,i}(K_i - 1)$$

where m is the slope of the liquidus line, C_o the initial composition, and k_i is the equilibrium partition coefficient for element i. A large GRF can result in effective grain refinement [274]. It is also possible that the intermetallics formed due to the additions might restrict the grain growth and thereby increases the nucleation site. The nucleation and growth are the main two influencing factors to determine the final solidification structure. Figure 4.27 illustrates the nucleation and growth rates for the early stage of solidification, in which the grain growth can be divided into two stages: stage (I) initial growth, during which nucleation and growth are competing processes, and stage (II) steady state growth, during which the nucleation rate is negligible. For a given alloy under identical solidification condition, a retarded grain growth would

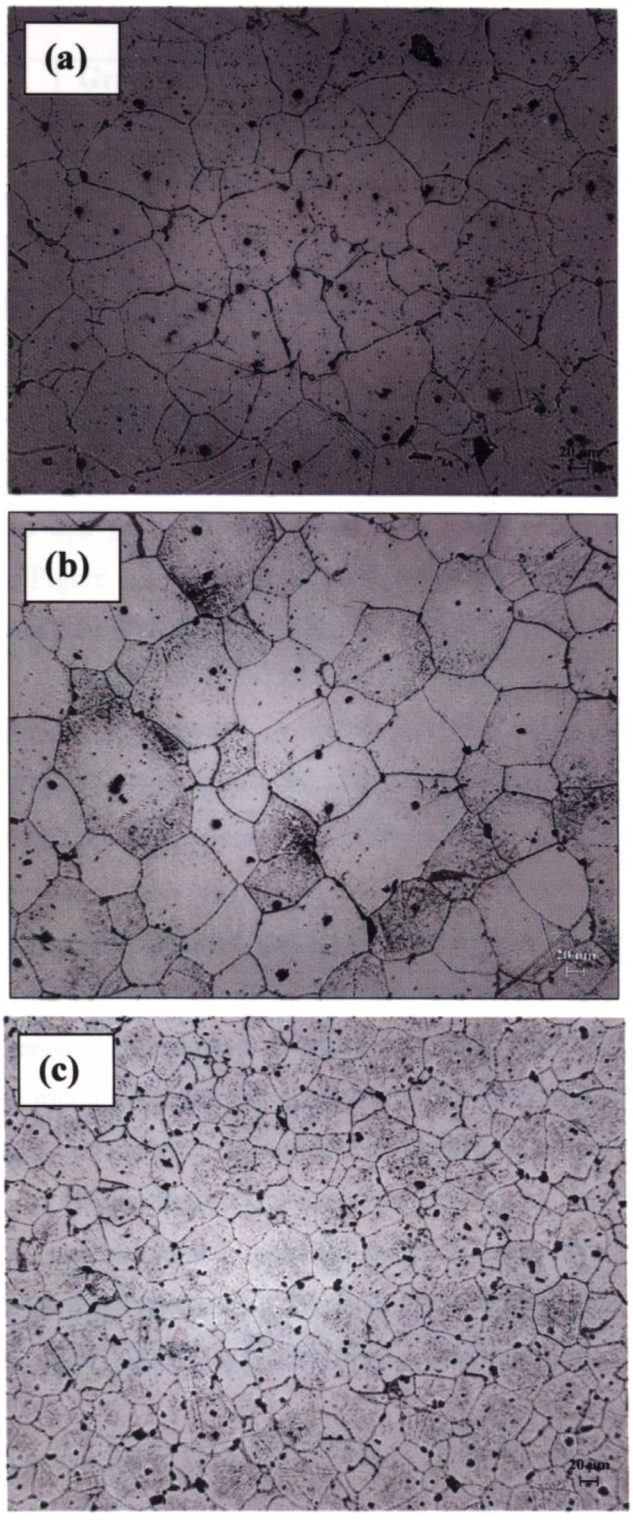

Figure 4.26: Optical microstructure showing grain size of different alloys in solution treated condition (a) AZ91 (b) AZ91+0.5% Si+0.2% Sb (c) AZ91+0.5% Si+0.1% Sr

Table 4.2: Grain size of various alloys at solution treated condition

Alloy	Grain size, μm	Alloy	Grain size, μm
AZ91	80 ± 10	AZ91+0.2% Sr	65 ± 6
AZ91+0.2% Si	70 ± 8	AZ91+0.5% Sr	55 ± 4
AZ91+0.5% Si	73 ± 10	AZ91+0.7% Sr	52 ± 8
AZ91+0.2%Sb	80± 5	AZ91+0.5% Si+0.2% Sb	60 ± 20
AZ91+0.5% Sb	70 ± 15	AZ91+0.5% Si+0.1% Sr	45 ± 5
AZ91+0.7% Sb	63 ± 12	-	-

result in enhanced and persistent nucleation with longer time for the initial grain growth. From the Figure 4.27 it could be seen that when the growth rate G' < G the nucleation rate would be N' > N [275].

Grain refinement due to the elemental additions in Mg alloys is reported in literature. [221, 222, 224, 231, 239, 276, 277]. Guangyin et al [221] noticed a grain size reduction of 115 μm to 80 μm with 0.5% Sb to AZ91 alloy. Lee et al [231] have reported that Si is also capable of refining the grain in Mg-Si binary alloys. Shuanug Shou et al. [224] also have reported that Ca addition to AZ91 alloy act as an effective refiner and the mechanism behind is that the added Ca segregates at the grain boundary and hence increases the constitutional super cooling. However, in this present study not much refinement is observed with Si addition. One possible reason for this is the purity of the melt. It is shown in literature that the grain size of AZ91 varies substantially depending on the purity of the ingots used to make the alloy [241]. It therefore appears that aluminium in combination with impurity elements affects the potency of the nucleants in the melt. This might be the reason for the low efficiency of Si in AZ91 alloy as a grain refiner in the present study.

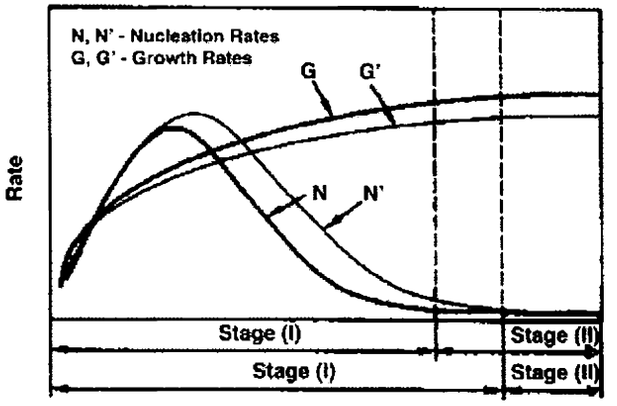

Figure 4.27: Schematic diagram illustrating the nucleation and growth rates during the early stage of solidification [274]

There are some ambiguities over the effect of Sr addition on the grain refinement of Mg-Al alloys. Hirai et al [222] have reported that Sr addition refines the grain size of AZ91 alloy. However, Peng Zhao et al. [239] have found that Sr addition has little effect of on the grain refinement on AM50 alloy. Y.C. Lee et al [277] also have reported that Sr addition has a significant grain refining effect only in low Al containing alloys and particularly in pure magnesium not with higher aluminium containing alloy like AZ91. The GRF parameters [m=-3.53, k=0.006 and m (k-1) = 3.51] values found in the literature [277] also indicate that the Sr has little effect on grain refinement. On the other hand, S.Lee et al [231] have found that Sr has a great effect on grain refinement (more than 50% reduction in grain size) in AZ91 alloy. They argued that Sr addition alters the precipitation process and thereby restrict the grain growth. More Al is precipitated as $Mg_{17}Al_{12}$ at the grain boundaries without growing into the matrix, which along with Mg-Al-Sr intermetallics hinders the movement of grain boundaries and the subsequent grain growth leading to the greater effect of grain refinement [231]. In the present study also it is observed during ageing treatment that more number of grain boundaries are seen with discontinuous $Mg_{17}Al_{12}$ intermetallic in Sr added AZ91 alloy.

4.3 HEAT TREATMENT

As cast microstructure of AZ91 alloy consists of many high aluminum rich eutectic regions apart from discontinuous precipitates at the grain boundary (ref. Table 4.1). During high temperature exposure, secondary precipitates (both continuous and discontinuous) form from the supersaturated areas [278]. It is believed that presence of discontinuous precipitates is detrimental to mechanical properties, particularly the creep [279]. Hence reduce the amount of discontinuous precipitate is essential to improve its mechanical properties. In order to study the effect of alloying additions on DP reaction and also its influence on the age hardening response, heat treatment studies were conducted on selected samples and its solution as well as aged microstructures were examined.

4.3.1 Solution Treatment

Solution treatment was carried out on all the alloy samples at 410°C for 48 h. Normally the eutectic $Mg_{17}Al_{12}$ dissolves into the matrix slowly due to its massive size in gravity cast alloys. It takes around 12 h for complete dissolution but for the homogenization of Al in the Mg matrix 48 h is required [134]. The microstructure of solution treated AZ91alloy shown in Figure 4.28 contains no massive $Mg_{17}Al_{12}$ but some Al-Mn intermetallic particles still could be seen as these particles are stable even at 410°C. Grain boundary is also seen but it is not completely revealed.

Figure 4.29 shows the solution treated microstructures of AZ91+0.5% Si, AZ91+0.5% Si+0.2% Sb, AZ91+0.5% Sb and AZ91+0.5% Sr alloys. It could be seen from the microstructures that all the intermetallics, Mg_2Si, Mg_3Sb_2 and Al_4Sr in Si, Sb and Sr added alloys respectively, are still appeared at the grain boundary even after 48 h of solution treatment, which indicates that these intermetallics are stable at high temperature. The main reason for the stability is that these intermetallics are having high melting point (Mg_2Si -1120°C, Mg_3Sb_2- 1228°C and Al_4Sr-1040°C) and low diffusivity in Mg compared to Al [280]. However, there are few undissolved $Mg_{17}Al_{12}$ intemetallic also seen in Sr added alloy (Figure 4.29 (d)).

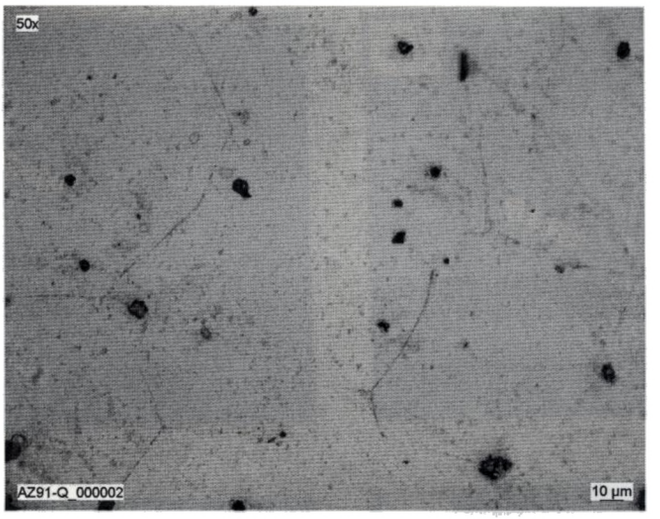

Figure 4.28: Microstructure of solution treated AZ91 showing no $Mg_{17}Al_{12}$ intermetallic

Even though the intermetallic is stable during solution treatment, refinement in Mg_2Si Chinese script morphology is observed in AZ91+0.5% Si alloy. Figure 4.30 shows a higher magnified view of Chinese script Mg_2Si intermetallic after solution treatment, which illustrate the linear branches of the Chinese script phase become disconnected and spheriodized due to the prolonged treatment at 410°C for 48 h. Refinement of Chinese script Mg_2Si precipitates during heat treatment in Mg-6Al-XSi alloy at 420°C is observed in earlier study [281]. Solution treatment principally influences the alloys in two ways (1) improving the vibration energy and the diffusion coefficient of the atoms, and (2) increasing the vacancies in the alloys. Due to this, the solutes will dissolve into the matrix, resulting in the decomposition of the intermetallic compounds. This mechanism is valid for $Mg_{17}Al_{12}$ because the solubility of Al increases at the high temperature. From the Mg-Si phase diagram (ref Figure 4.5), it could be seen that Si does not have much solubility in Mg matrix and hence the refinement mechanism must be different.

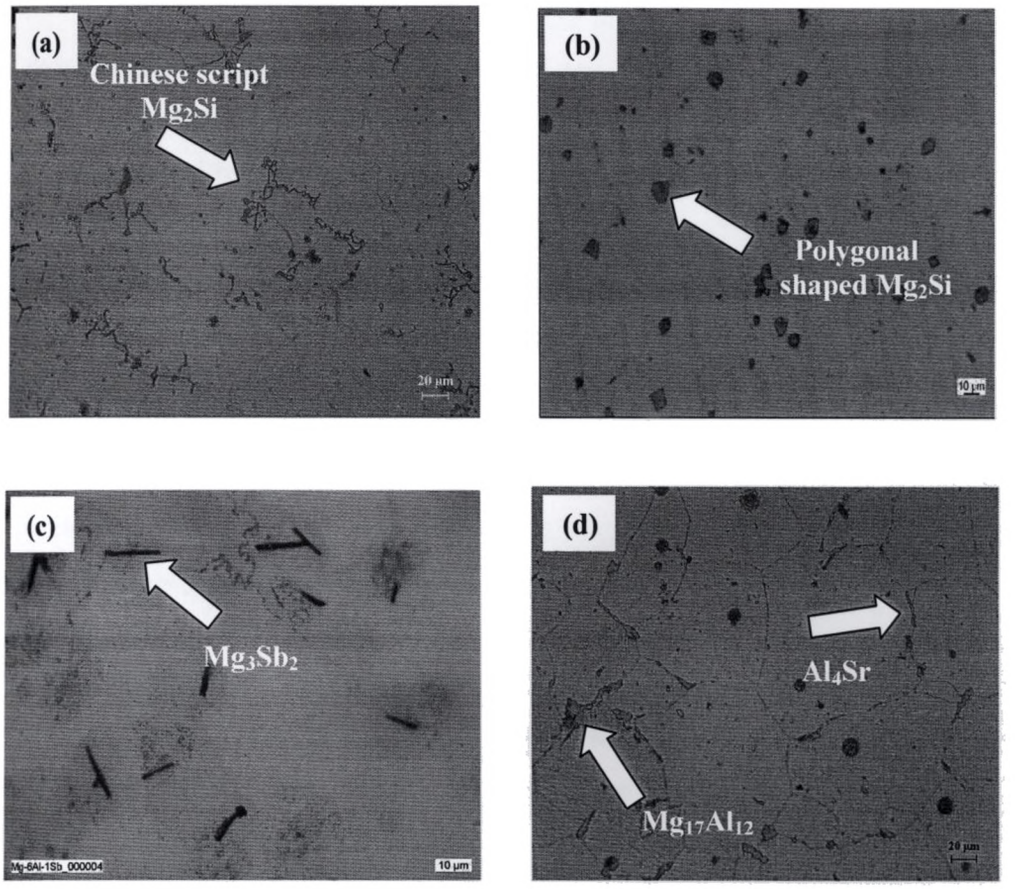

Figure 4.29: Microstructures of solution treated alloying element added AZ91 alloy showing Mg_2Si, Mg_3Sb_2, Al_4Sr intermetallics in (a) AZ91+0.5% Si (b) AZ91+0.5% Si+0.2% Sb (c) AZ91+0.5% Sb (d) AZ91+0.5% Sr respectively

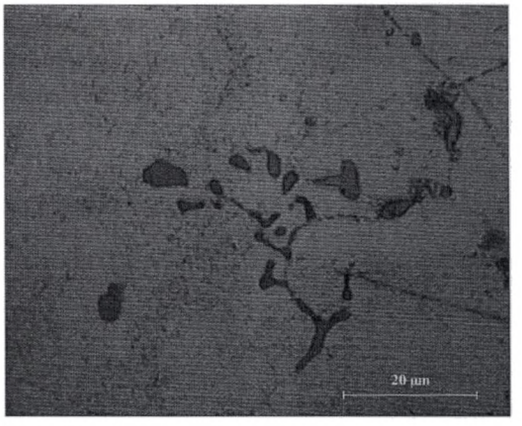

Figure 4.30: Solution treated microstructure of 0.5% Si added AZ91 alloy showing refinement in Mg_2Si intermetallic

Grain boundary and interface between the phases of alloys are containing lot of defects like dislocation and vacancies. Diffusion of atoms through these defects is easier and faster than the perfect matrix. So, it is obvious that the Mg_2Si/Mg interface plays an important role during the morphology changing of the Mg_2Si precipitates. Si atom movement within the precipitates is ruled out since Mg_2Si has congruent melting point and only exists at stoichiometric composition [282]. Therefore it is reasonable to believe that the Mg_2Si/Mg interface is the possible and only diffusion way for Si. Y.S. Lu [281] has proposed a mechanism of diffusion process at the interface of Mg_2Si/Mg during high temperature exposure. The process is illustrated in Figure 4.31. There always exist concaves and convexities on the particles along the interface, indicating different stress status as shown in Figure 4.31 (a). The interface tension made the nearby Si atoms escape from the Mg_2Si lattice and move coincidently. The Si atoms diffuse along the interfaces and enter the magnesium lattice in a new position to form Mg_2Si again, leading to the local decomposition and morphology changing of the Mg_2Si particles. As a result, the atom at the tip will move toward the middle, the concaves will become more sunken and convexities become smooth as shown in Figure 4.31 (b). It is believed that the straight part of the particle keep stable because the diffusion along the interface is homogeneous. Finally the linear particle will be broken near the concaves and the spheriodization of the sub-particles continues as shown in Figure 4.31 (c) and (d) [281].

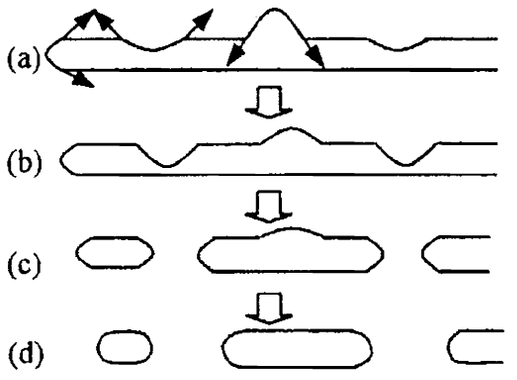

Figure 4.31: Schematic diagram illustrating the refinement mechanism for Mg_2Si intermetallic [281]

In Figure 4.29(c), it could be seen that, in addition to Al_4Sr intermetallic, there are some eutectic $Mg_{17}Al_{12}$ (but become smaller in size) appeared at the grain boundary in the solution treated condition (marked in the microstructure). Of course, only few particles of $Mg_{17}Al_{12}$ phase is seen, which means that the dissolution of this phase is not completely prevented but its stability slightly increases with Sr addition. It is also seen from Figure 4.32, which shows the higher magnified view of $Mg_{17}Al_{12}$ intermetallic in AZ91+0.5%Sr alloy, that its boundary has many curvatures. This indicates the dissolution of the phase into the matrix but slowly. This increase in stability is attributed to the fact that part of the added Sr dissolves in to the $Mg_{17}Al_{12}$ intermetallic. The EDS taken on $Mg_{17}Al_{12}$ confirms the presence of Sr in it. (ref Figure 4.18). The structure stability of intermetallic compound depends on its bond energy. It is believed that dissolved Sr might increase the bond energy of $Mg_{17}Al_{12}$ intermetallic and thereby increase its stability [239]. Similar kind of results is reported with Ca addition to AZ91 alloy [283, 284].

4.3.2 Ageing Behavior

The age hardening behaviour of AZ91 alloys with and without alloying additions at 200°C is shown in Figure 4.33. The Brinell hardness of heat treated alloys at different tempering conditions is presented in Table 4.3. The as cast hardness of AZ91 alloy (63.9 BHN) reduces slightly (57.8 BHN) with solution treated condition, which is due to the dissolution of hard $Mg_{17}Al_{12}$ phase in to the matrix. But the hardness is not reduced much since aluminium provides solid solution strengthening [285]. There are some studies, which report even a slight increase in hardness as well as the strength with solution treated condition due to the high percent of aluminium in solid solution compared to as cast condition [286]. But most of the data available in literature suggests solution treatment reduces the hardness [285, 287]. At peak aged condition the hardness increases to 83.8 BHN due to the re precipitation of $Mg_{17}Al_{12}$ phase as fine and evenly distributed continuous precipitates in the grain and laminar coarse discontinuous precipitates at the grain boundary. Even though, most of the age hardening is due to the formation of the fine continuous precipitates, discontinues precipitates are also contributes to the hardness to certain extent [136]. The peak hardness of the base alloy is reached around 900 min. The longer time taken to reach

the peak hardness even at 200°C indicates that the precipitation of $Mg_{17}Al_{12}$ intermetallic is a sluggish process. Moreover, the maximum hardness obtained at peak aged condition (the solution treated hardness increase from 57.8 BHN to 83.8 BHN at peak aged condition) suggests that the hardening response of AZ91 is poorer than that of many heat-treatable aluminium alloys, where a great improvement in hardness could be expected in peak aged condition. The major reason for this poor hardening response of AZ91 is the presence of less number of precipitates, which can be favourably oriented to obstruct the basal slip. Celotto [134] reported that rod or lath-shaped precipitates lying perpendicular or at an angle to the basal plane are more effective in preventing the basal slip than symmetric lozenge or lath-shaped precipitates lying parallel to the basal plane. It is also reported that only few precipitates are favourably orientated to obstruct the basal slip in AZ91 alloy [134].

From Figure 4.33, it can be seen that with all alloying additions the trend of the ageing curve is not changed to a large extent. Si addition both individual and combined with Sb increase the peak aged hardness considerably. The highest peak hardness of 102 BHN is obtained with AZ91+0.5% Si+0.2% Sb alloy. Even though the as cast and as solution treated hardness of 0.5% Sr added alloy is higher than the base alloy, at peak aged condition the hardness is not varying much with the base alloy. Reasonable increase in hardness is noticed with 0.5% Sb added alloy.

Increase in hardness at as cast and as solution treated condition with elemental additions are due to the combined effect of two factors: presence of hard intermetallic phase and grain refinement. The intermetallics like Mg_2Si, Mg_3Sb_2 and Al_4Sr are known to be harder and stable than both $Mg_{17}Al_{12}$ and α-Mg. Similarly, smaller the grain sizes higher the hardness. When the grain refinement takes place, the area of grain boundary increases and since at room temperature the grain boundary is stronger than the matrix, the grain refinement provide higher hardness. Superior age hardening response seen with AZ91+0.5% Si+0.2% Sb alloy over AZ91+0.5% Si alloy is attributed to the presence of fine and evenly distributed Mg_2Si precipitate and grain refinement noticed in the former alloy. When the precipitates are fine and evenly distributed throughout the microstructure the hardness greatly improves.

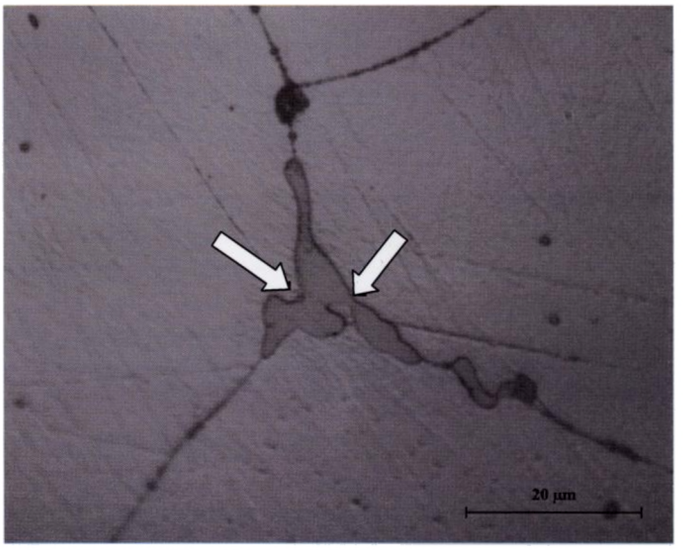

Figure 4.32: Solution treated 0.5% Sr added alloy showing retained $Mg_{17}Al_{12}$ intermetallic containing curvatures in boundaries

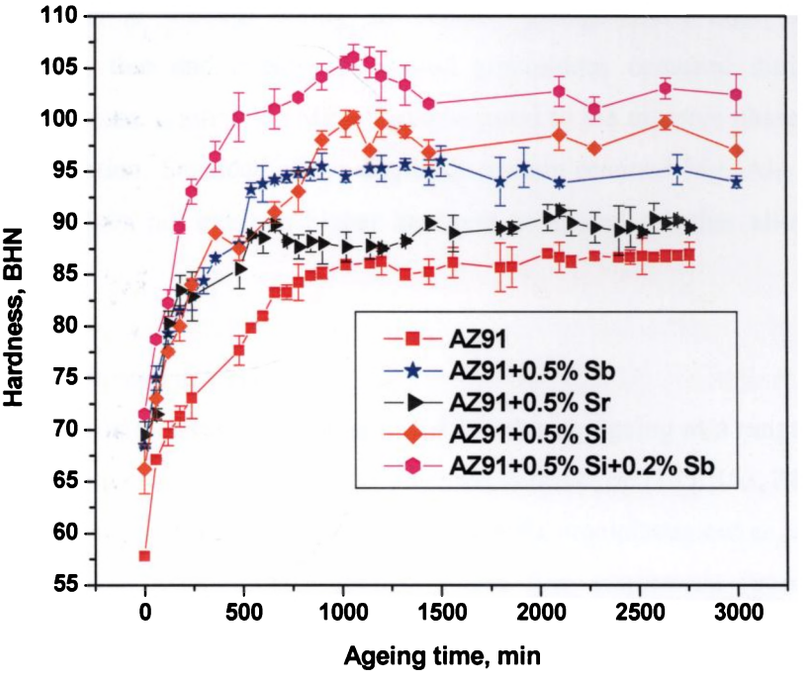

Figure 4.33: Ageing behavior of AZ91 with and without alloying additions at 200°C

Table 4.3: Hardness of various alloys at different tempering conditions

Alloy	Tempering condition			
	As cast, BHN	Solution treated, BHN	Peak aged, BHN	Time to reach peak ageing, min
AZ91	63.9	57.8	85.8	~900
AZ91+0.5% Si	68.4	66.2	99.2	~900
AZ91+0.5% Sb	73.5	68.5	95.4	~840
AZ91+0.5% Sr	72.2	69.5	89.54	~600
AZ91+0.5% Si+0.2% Sb	76	71.5	102	~780

Presence of hard intermetallics also leads to formation of large number of continuous precipitates during ageing by changing the precipitation process (as explained in section 4.3.3) and hence increases the peak aged hardness. The possible reason for the poor ageing behavior of Sr added alloy is attributed to the amount of Al available for the precipitation process during ageing. The microstructure of solution treated alloy shows the presence of Al_4Sr and some undissolved $Mg_{17}Al_{12}$ massive intermetallics. These intermetallics retain the aluminum and hence only part of the total aluminum then dissolves into the matrix during solution treatment and involves in the precipitation process during subsequent ageing. Since high hardness is associated with fine and evenly distributed precipitates occurred during ageing process (in this case, continuous $Mg_{17}Al_{12}$) compared to the massive phases occurred during solidification, Sr added alloy, despite it contain retained $Mg_{17}Al_{12}$ and Al_4Sr intermetallics, does not exhibits higher hardness compared to other alloys at peak aged condition.

4.3.3 Aged Microstructures

The microstructural development of AZ91 during ageing at a range of ageing temperatures is investigated and well documented in literature [135, 153, 288]. During ageing process the aluminum in supersaturated matrix precipitates out as $Mg_{17}Al_{12}$ in two forms: coarse discontinuous (cellular) and fine continuous (transrgranular) precipitates. Discontinuous precipitates are a cellular growth of alternating layers of $Mg_{17}Al_{12}$ phase and near equilibrium magnesium matrix at high angle grain boundaries. Growth of the discontinuous precipitation regions ceases relatively early

in the precipitation process. Continuous precipitation forms in the remaining regions of the matrix that are not already occupied by discontinuous precipitates [135, 153, 288]. In the present study the microstructural changes during the ageing treatment at 200°C is observed under light optical microscopy and SEM. Figure 4.34 shows the microstructure of AZ91 alloy samples aged for 60, 120 and 240 min. In the beginning i.e. 60 min aging time, the grain boundary thickening takes place, which associated with the initiation of DP [289]. Due to this, the boundary of the alloy is clearly seen compared to the solution treated condition (ref. Figure 4.28). Black appearance at some of the grain boundaries indicates that the DP process already started (marked in Figure 4.34 (a)). As the ageing time increases the amount of discontinuous phase is also increased. More number of the grain boundaries is seen with DP and the already formed discontinuous phases are grown in to the adjusted grains as evident from the microstructures of 120 and 240 min aged samples presented in Figure 4.34 (b) and (c). The boundary condition is important for the initiation of DP. Bradai et al. [145] have reported that DP initiation and growth occurs preferably at high angle grain boundaries. At the later stage of ageing, discontinuous precipitates are ceased and continuous precipitates forms as the degree of aluminum supersaturation reduced in the matrix. The microstructure of 1200 min aged AZ91 alloy sample given in Figure 4.35 clearly shows both well grown discontinuous precipitates at the grain boundaries and over aged coarse continuous precipitates at the grain interior.

The effect of alloying additions on the DP is seen from Figure 4.36, which shows 120 min aged microstructures of different alloys. From the microstructures it can be seen in general that the alloying additions reduce the amount of discontinuous precipitates at the grain boundary. The volume fraction of precipitates calculated using image analyzer for all the alloys aged for 120 min is given in Table 4.4. Since the DP is random along the grain boundaries in the microstructure, the calculated standard deviation is high. Ten microstructures taken at different locations of the sample were used to calculate the volume fractions. In spite of the large variation in standard deviation, it is evident that addition of Si, Sb and combined addition of Si and Sb reduces the DP greatly. However, Sr is not effective in suppressing the DP

compared to other elemental additions. In fact slightly higher volume of discontinuous precipitates is noticed with AZ91+0.5% Sr alloy as evident from Figure 4.36 (d).

Discontinuous precipitation is a solid-state decomposition reaction that converts the supersaturated solid solution α_o, into two phases α and β aggregate behind a migrating reaction front. Unlike any other solid-state heterogeneous process, the combination of precipitation and concurrent boundary migration in discontinuous precipitation necessitates a rather complex reaction mechanism to follow. Different kind of mechanism such as precipitate-matrix misfit, solute-solvent atomic size difference, solute segregation and diffusion coherency strain theory are proposed for discontinuous precipitation [290-292]. However, still it is not very clear that which mechanism dominates in Mg-Al alloys. Recently Kashyap et al. and Srinivasan et al. [293, 294] have reported that addition of Pb reduces the grain boundary precipitates in term of volume fraction and it is suggested that addition of Pb segregates at the grain boundary and reduces the grain boundary diffusion coherency strain, which in results reduce the movement of grain boundary. Bettles et al. [279] have also reported that gold addition in AZ91 alloy greatly reduces the formation of discontinuous precipitates during ageing process. They have suggested the tiny (up to 5 nm) gold particles presented throughout the matrix might have inhibited the movement of both atoms and grain boundaries.

In the present case, both the Si and Sb have very low solubility in Mg and it forms Mg_2Si and Mg_3Sb_2 intermetallics respectively. Hence the mechanism for the suppression of discontinuous precipitate due to these additions must be different. Recently, Yizhen Lu et al [295] have reported that addition of Si to Mg-6Al alloy reduces the DP during ageing due to the presence of hard Mg_2Si precipitates. It is suggested that the dislocations generated in the matrix around the hard Mg_2Si precipitates during cooling due to difference in co-efficient of thermal expansion between matrix and precipitate act as a heterogeneous nucleation sites for continuous precipitates. By this process, Si addition reduces the formation of discontinuous precipitate [295]. The same theory could be evoked for Sb addition also. Hence the

higher hardness obtained with Si and Sb addition at peak aged condition might also be attributed to the presence of more number of continuous precipitates.

It is found from the aged microstructure of Sr added alloy that more amounts of discontinuous precipitate forms in the initial stage of ageing. More number of boundaries is seen with DP compared to other alloys as shown in Figure 4.36 (d). The volume fraction of discontinuous precipitates calculated is slightly higher / equal compared to the base alloy (ref. Table 4.4). It could be also seen from Table 4.3 that Sr added alloy reaches the peak hardness little early than the base alloy. This is due to low amount of Al available in the solid solution. Nussbaum et al [238] and Lee et al [231] reported that Sr modifies the precipitation behavior of Mg-Al alloys by promoting more precipitates along the grain boundaries. However, the reason behind such occurrence is not known. On the other hand the formation of DP during ageing of Mg-Al is a combined effect of Al in the solid solution, grain size and ageing temperature [146]. High amount of Al, finer grain size (high angle grain boundary) and medium ageing temperature (150-250°C) leads to more DP in Mg-Al alloys. Hence, the boundary characterization of Sr added alloy is necessary to understand the precipitation mechanism.

Table 4.4: Volume fraction of discontinuous precipitates formed in 120 min aged Samples

Alloy	AZ91	AZ91+0.5 %Si	AZ91+0.5% Sb	AZ91+0.5%Sr	AZ91+0.5% Si+0.2% Sb
Volume fraction of discontinuous precipitates, %	8.5±4	2.7±2.2	4.1±3.6	10.2±5.2	3.5±2.8

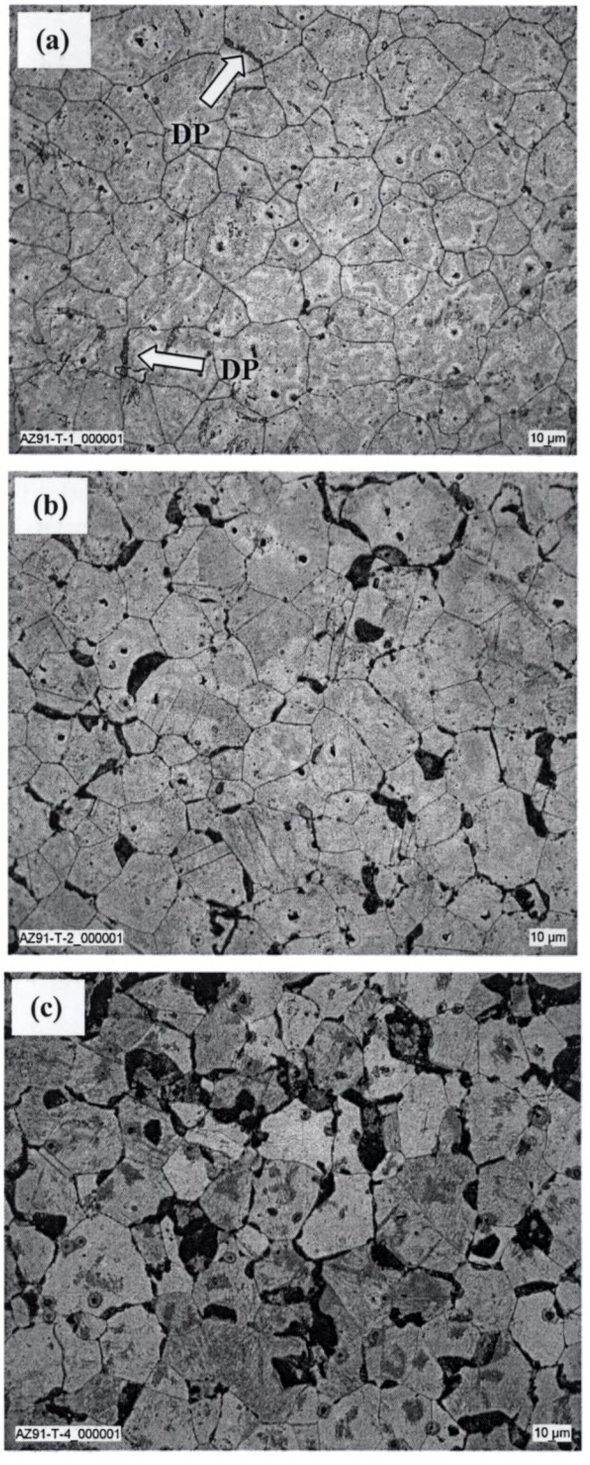

Figure 4.34: Aged microstructure of AZ91 for different time showing discontinuous precipitates at the grain boundaries (a) 60 min (b) 120 min (c) 240 min

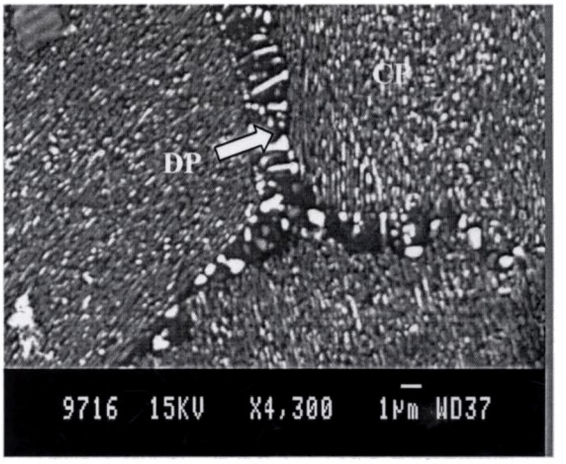

Figure 4.35: 1200 min aged microstructure of AZ91 showing both continuous and discontinuous precipitates

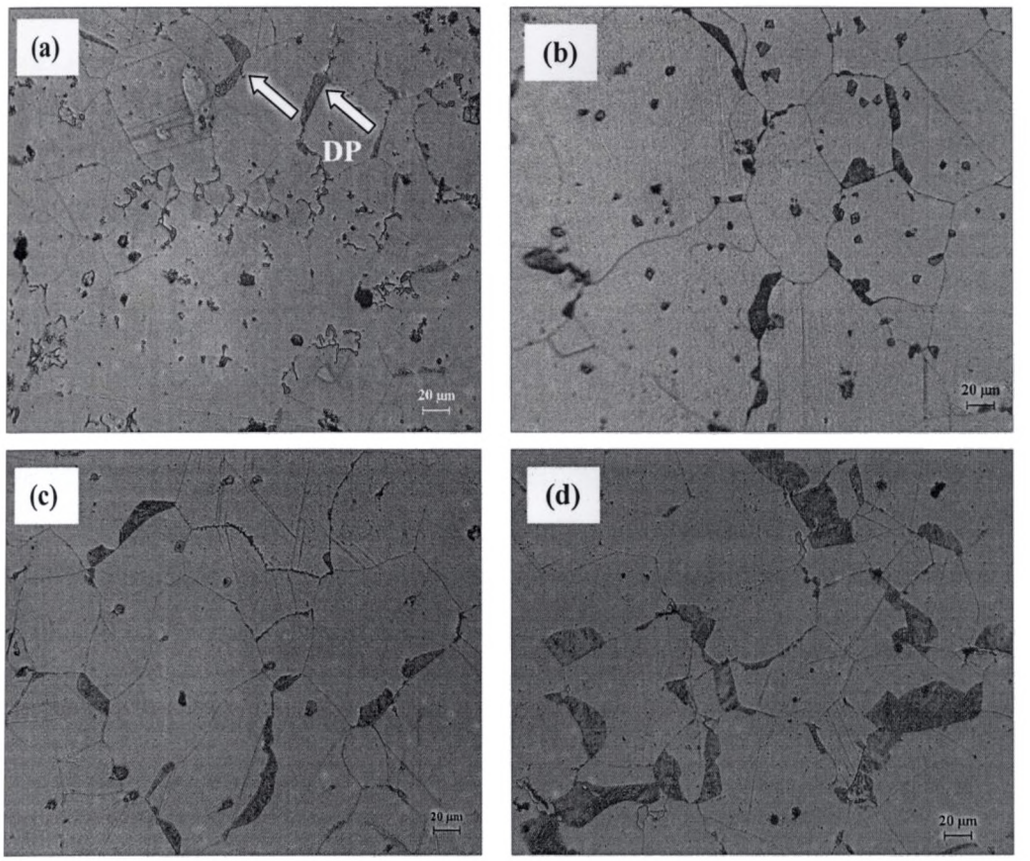

Figure 4.36: 120 min aged microstructures of AZ91 alloys with different alloying additions showing discontinuous precipitates (a) AZ91+0.5% Si (b) AZ91+0.5% Si+0.2% Sb (c) AZ91+0.5% Sb (d) AZ91+0.5% Sr

4.4 TENSILE PROPERTIES

The alloying additions, apart from introducing various intermetallics and refining the grain size, refines also the $Mg_{17}Al_{12}$ intermetallics in some cases (like Sr addition). These microstructural variations influence the tensile properties of AZ91 alloy. Hence, the tensile properties of AZ91 alloy with and without additions were evaluated, compared and presented in this section. Tensile samples were prepared in accordance with ASTM E8 standard and the tests were carried out at room as well as high temperatures (up to 200°C for base alloy and at 150°C for all remaining alloys). Five samples were tested for each alloy and the average value was reported. Extensometer was used to get the % elongation during room temperature testing but for high temperature tests, the values were manually calculated from the markings on the sample (25mm gauge length was used). Fractography studies were also carried out to identify the micro-fracture mechanism.

4.4.1 AZ91 Alloy

Figure 4.37 presents the ultimate tensile strength (UTS), yield strength (YS) and percentage of elongation (%E) of AZ91 alloy measured from the tensile test carried out at different testing temperatures (RT, 100, 150, 200°C). The tensile properties obtained in the present investigation are inline with the standard values reported in the Materials Science Hand Book [296] and published by International Magnesium Association (IMA), Canada [297]. In fact, the tensile properties obtained in the present study are higher than many published values in literature [41, 42, 48]. In general, the mechanical properties of AZ91alloy reported in literature are scatter in nature mainly due to the difference in the casting process variables, which alter the microstructural features like grain size, eutectic volume fraction, porosity and etc [298, 299]. Moreover, properties variation within casting is also noticed by many researchers [43, 155, 300-304]. E. Aghion et al [155] have reported that the tensile properties of die cast AZ91 alloy are highly sensitive to wall thickness. Considerable change in UTS, YS and %E is noticed with samples tested from different location along the wall thickness of casting. Yang et al [43] have also reported the same in gravity cast AZ91 alloy.

In the present study also variation in the tensile properties are noticed with the samples taken at the different locations of the casting. As shown in Figure 3.3 in chapter 3, the casting thickness obtained is around 40 mm. In order to check the variation in the tensile properties, samples from the centre of the casting are also evaluated and compared with the values of the samples taken near the wall of the casting. These values are given in Table 4.5. AS pointed out, these differences are owing to the change in the microstructural characteristics like grain size and % porosity, which are also given in Table 4.5. The higher tensile properties observed with the samples taken near the wall of the casting are due to less volume fraction of pores and finer grain structure. Magnesium alloys are more prone to shrinkage porosity due to their poor fluidity and hence difficulties are encountered to feed the molten metal at the end of the solidification [299]. Hence it is not surprise to have more porosity at the centre portion of the casting compared to the wall side of the casting. Cooling rate is also different along the thickness of the casting: the metal near the wall side of mould would cool very fast compared to the liquid metal in the middle. Hence variation in the grin size is seen along the thickness of the casting. Porosity and grain size have a great influence on both the room and high temperature properties of Mg alloys [298, 299]. Gutman et al. [299] have found a strong relationship between % porosities and strength properties of AZ91 alloy. Srinivasan et al. [77] also have reported an improvement in the strength properties of AZ91 alloy by improving the casting quality (finer microstructure and lesser porosities) using low pressure casting process.

From Figure 4.37, it can be seen that that the strength properties of the alloy shows a drop off as the testing temperature increases from room temperature to 200°C, which shows that the tensile properties of AZ91 alloy is highly sensitive to operating temperature. There is a sudden drop in strength properties above 150°C. At 200°C test temperature, the UTS reduced to 135 MPa from a value of 210 MPa at room temperature, which indicates the limitation on the usage of this alloy at high temperatures. In contrast, increase in %E is noticed with increase in test temperatures. High percentage of elongation of 20% is seen at 200°C compared to 4% at RT. Normally at room temperature magnesium alloys exhibit brittle failure due to the

limitations in number slip systems: only basal slip is active at room temperature. However, at high temperatures the alloy yields more ductility. This is due to the fact that additional slip systems such as prismatic and pyramidal slip planes are active in magnesium alloys at high temperatures. Cross slip takes place through these planes at high temperatures and introduce more ductility [305].

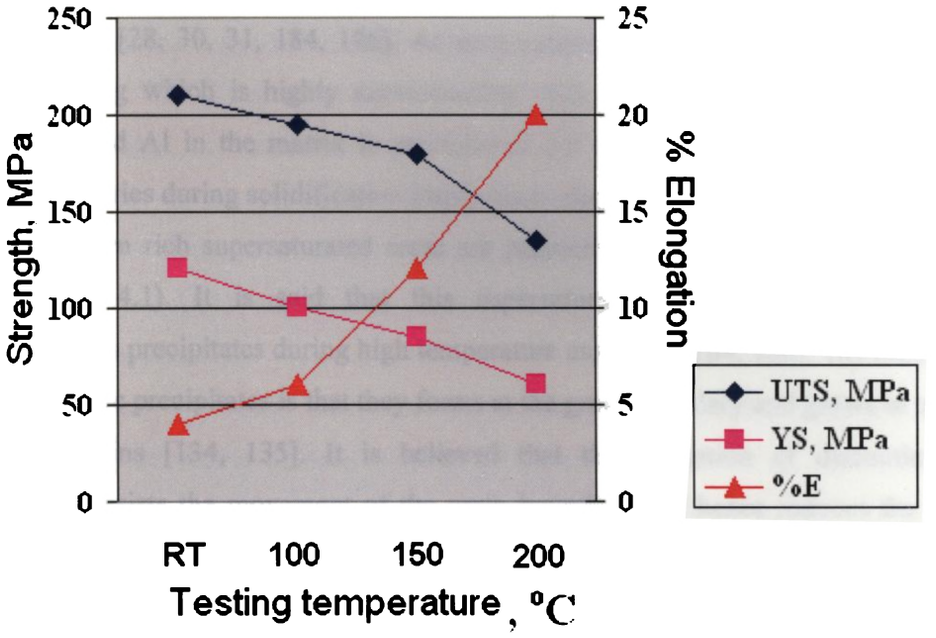

Figure 4.37: Tensile properties of AZ91 alloy at different temperatures

Table 4.5: Property variation along the wall thickness of the casting

Sample location	YS, MPa	UTS, MPa	%E	Grain size, µm	% Porosity
Center of casting	92	173	2.8	110	2.35
Wall side of casting	120	210	4	80	1.98

The major reason for the poor high temperature properties of AZ91 alloy is the microstructural degradation takes place at elevated temperature. As far as AZ91 alloy is concerned, the principal room temperature strengthening element is $Mg_{17}Al_{12}$ intermetallics. But this intermetallic has low melting point (437^0 C) and has higher diffusivity in Mg matrix. Hence, this coarsen at a faster rate and unstable at higher temperatures i.e. above 100°C and no longer acts as a barrier for dislocations [230, 78]. Moreover, $Mg_{17}Al_{12}$ has a cubic crystal structure due to which it is incoherent with the hcp magnesium matrix [29]. Therefore, presence of this phase leads to poor elevated temperature properties. In addition, the microstructure of AZ91 alloy is found to be unstable during high temperature exposure due to the dynamic precipitation [28, 30, 31, 184, 186]. As seen earlier, the as cast microstructure has eutectic α-Mg which is highly supersaturated with Al. Even though, most of the supersaturated Al in the matrix is precipitated out as discontinuous precipitates at grain boundaries during solidification itself, due to the slow cooling in gravity casting, still aluminum rich supersaturated areas are presented in the as cast microstructure (ref. Table 4.1). It is said that this supersaturated matrix decomposes into discontinuous precipitates during high temperature exposure [184, 186]. The nature of these dynamic precipitates is that they forms at the grain boundary and grows in to the adjacent grains [134, 135]. It is believed that the formation of discontinuous precipitate assists the movement of the grain boundary and hence reduces the high temperature properties [96]. However, this problem is more severe during creep deformation, where the material is exposed at high temperature for prolonged time rather than in high temperature tensile testing, which is a short-term test.

4.4.2 AZ91+XSi Alloys (X=0.2%, 0.5%)

The effect of Si addition to the tensile properties of AZ91 alloy is shown in Figure 4.38. The strength values are presented also in Table 4.6. At room temperature, the Si addition reduces the tensile properties compared to the AZ91 base alloy. Marginal reduction in both strength and elongation is observed with 0.2% Si addition. However, considerable reduction is observed with 0.5% Si. The presence of coarse Mg_2Si intermetallic in the Si added AZ91 alloys is the reason for such reduction in tensile properties, however substantial reduction obtained in 0.5% Si added alloy is

due to the presence of large amount of coarse Chinese script Mg_2Si intermetallic together with $Mg_{17}Al_{12}$. With 0.5% Si addition the UTS reduces from 210 MPa (base alloy value) to 188 MPa and the ductility reduces greatly from 4 to 1.8%. Since both $Mg_{17}Al_{12}$ and Mg_2Si are coarse and highly brittle in nature, the ductility gets affected greatly compared to the strength. It can also be observed that yield strength is not changed much with Si addition. At 150°C, as like base alloy, with Si addition too both yield strength and UTS reduces with increase in ductility. However, it could be noticed that percentage of reduction in strength with 0.2% Si addition is found to be less compared to the base alloy even though strength (YS, UTS) values obtained are lesser than the value of AZ91 alloy, which indicate that Mg_2Si intermetallic even though in Chinese script improves the high temperature resistance of AZ91 alloy to certain extent. This is due to the fact that Mg_2Si is hard and stable at high temperature compared to $Mg_{17}Al_{12}$ intermetallic.

Si is one of the prime alloying elements to magnesium next to Al. Many alloys like AS21 and AS41 etc., based on Mg-Al-Si system are developed for high temperature applications [66]. But these alloys are normally suitable only for die casting. In gravity casting form these alloys does not find applications due to the presence of unfavorable Chinese script Mg_2Si intermetallic. Cooling rate has a great influence on the morphology of Mg_2Si intermetallic. In gravity casting the cooling rate is slow and hence Si precipitates out in coarse Chinese script morphology [262-264]. On the other hand, due to a high cooling rate in pressure die casting more nucleation site is available for Mg_2Si and hence the size of the precipitates is finer. The coarse Chinese script morphology reduces the mechanical properties particularly the ductility. This is due to the fact that crack will easily nucleate and develop at the inter space between ductile Mg matrix and coarse Chinese script Mg_2Si precipitates. This along with the weak interface between α -matrix and the β -$Mg_{17}Al_{12}$ phase reduces the mechanical properties of the alloy and due to this reason the AS alloys are restricted to only die castings.

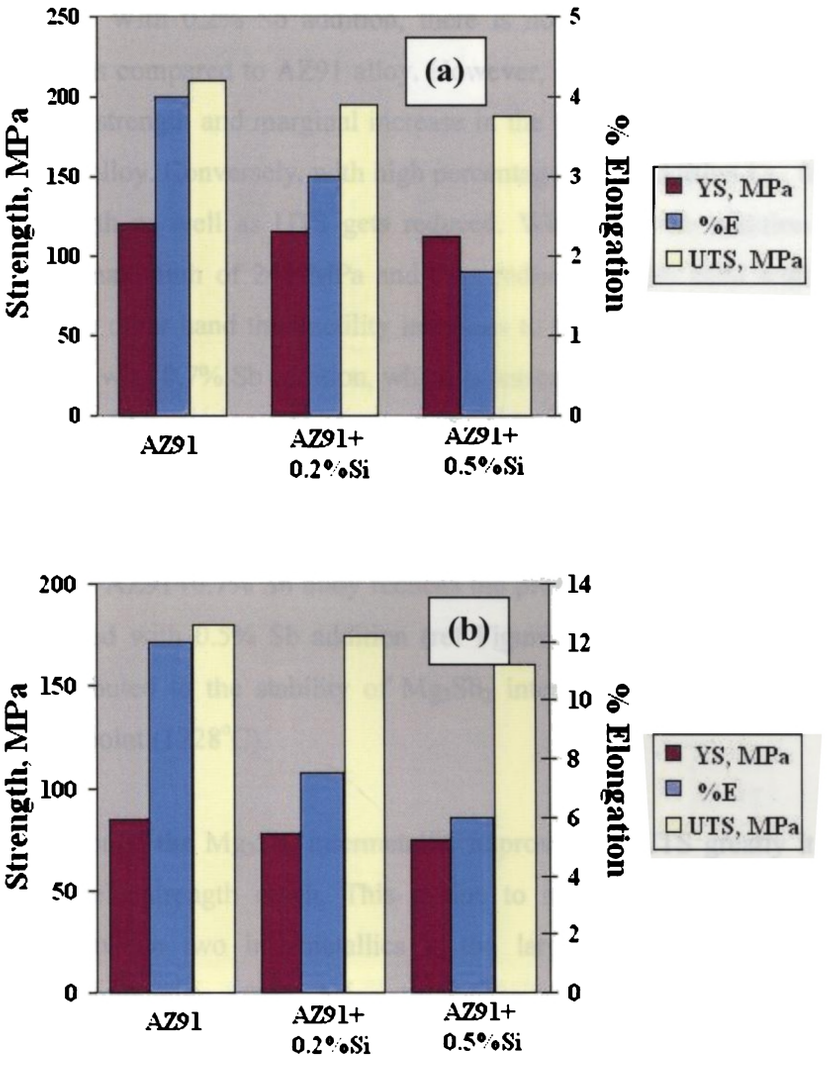

Figure 4.38: Tensile properties of Si added AZ91 alloy (a) at RT (b) at 150°C

Table 4.6: Tensile properties of Si added AZ91alloy in tabular form

Alloy	RT			At 150°C		
	YS	UTS	%E	YS	UTS	%E
AZ91	120	210	4	85	180	12
AZ91+0.2% Si	115	195	3	78	174	7.5
AZ91+0.5% Si	112	188	1.8	75	160	6

4.4.3 AZ91+XSb Alloys (X=0.2%, 0.5%, 0.7%)

Figure 4.39 presents the tensile properties of Sb added alloys at room as well as 150°C temperature in bar chart and their numerical values are given in Table 4.7 for comparison. With 0.2% Sb addition, there is no considerable improvement in tensile properties compared to AZ91 alloy. However, significant improvement in the ultimate tensile strength and marginal increase in the yield strength is observed with 0.5% Sb added alloy. Conversely, with high percentage of Sb addition i.e., 0.7%, both the yield strength as well as UTS gets reduced. With 0.5% Sb addition the UTS increases to a maximum of 242 MPa and then reduces to 206 MPa with 0.7% Sb addition. On the other hand the ductility increases to 5% with 0.5% Sb addition and reduces to 2.5% with 0.7% Sb addition, which is lesser than the base alloy ductility of 4%. Similar trend in properties is observed at 150°C testing temperature also. Grain refinement and Mg_3Sb_2 intermetallic is the reason for such improvement observed in 0.5% Sb added alloy. However, high volume fraction of needle shaped brittle Mg_3Sb_2 intermetallics in AZ91+0.7% Sb alloy reduces the properties [43]. The higher tensile strength observed with 0.5% Sb addition (ref Figure 4.39 (b)) at high temperature (150°C) is attributed to the stability of Mg_3Sb_2 intermetallics, which is due to its higher melting point (1228°C).

Even though the Mg_3Sb_2 intermetallic improves the UTS greatly it does not improve the yield strength much. This is due to it massive size in nature. The interspacing between two intermetallics is too large to achieve any significant dispersion -strengthening effect. Normally during plastic deformation due to the hardness difference between the hard intermetallics and the ductile matrix an internal stress develops which acts as a back stress for the dislocation movement and contributes to the tensile stress [306-308].

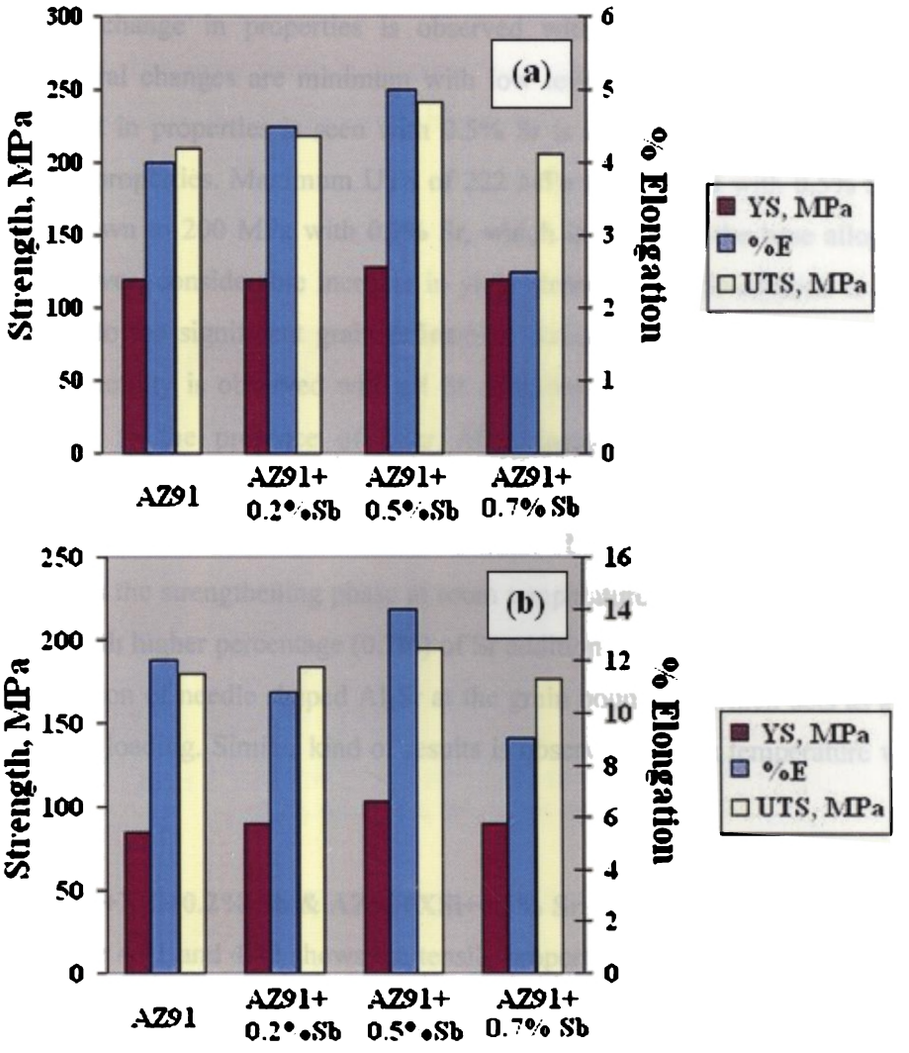

Figure 4.39: Tensile properties of Sb added AZ91 alloy (a) RT (b) 150°C

Table 4.7: Tensile properties of Sb added AZ91alloy in tabular form

Alloy	RT			At 150°C		
	UTS	YS	%E	UTS	YS	%E
AZ91	210	120	4	180	85	12
AZ91+0.2% Sb	218	120	4.5	184	90	10.8
AZ91+0.5% Sb	242	128	5	195	103	14
AZ91+0.7% Sb	206	120	2.5	177	90	9

4.4.4 AZ91+XSr Alloys (X=0.2%, 0.5%, 0.7%)

Figure 4.40 and Table 4.8 provides the tensile properties of Sr added alloys. In general the Sr additions have little effect on tensile properties of AZ91 alloy. Not appreciable change in properties is observed with 0.2% Sr addition, since the microstructural changes are minimum with low level of Sr content, whereas slight improvement in properties is seen with 0.5% Sr is addition. Further addition of Sr reduces the properties. Maximum UTS of 222 MPa is observed with 0.5% Sr and it has come down to 200 MPa with 0.7% Sr, which is less than the base alloy's UTS value. However, considerable increase in yield strength with Sr addition is noticed. This is due to the significant grain refinement obtained by Sr additions. Not much change in ductility is observed with all Sr additions. The improvement obtained in UTS is due to the presence of finer Al_4Sr intermetallic. However, not much improvement in UTS seen with Sr addition is due to the fact that the formation of Al_4Sr intermetallic reduces the volume fraction of $Mg_{17}Al_{12}$ phase, which is also considered as the strengthening phase at room temperature. The reduction in strength properties with higher percentage (0.7%) of Sr addition is due to the presence of more volume fraction of needle shaped Al_4Sr at the grain boundary, which acts as a stress raiser during loading. Similar kind of results is observed at high temperature with Sr additions.

4.4.5 AZ91+XSi+0.2% Sb & AZ91+XSi+0.1% Sr Alloys (X=0.2%, 0.5%)

Figure 4.41 and 4.42 shows the tensile properties of AZ91+XSi+0.2% Sb and AZ91+XSi+ 0.1% Sr alloys respectively. The tensile properties of all alloys are consolidated in Table 4.9. As mentioned earlier, the purpose of Sb and Sr addition to the Si containing alloys is to refine the Chinese script Mg_2Si precipitates. The change in the size and morphology of Mg_2Si precipitates improves the mechanical properties particularly the ductility. The ultimate strength and ductility of 0.2% Sb added AZ91+0.2% Si alloy are increased to 238 MPa and 6% respectively compared to the AZ91+0.2% Si alloy's value of UTS- 195 MPa and elongation- 3%. Improved UTS and ductility is also observed with 0.1% Sr modified AZ91+0.2% Si alloy and it is 220 MPa and 4.5% respectively. Yield strength is also improved in both cases. Improved tensile properties are also noticed with 0.5% Si added alloy containing Sb

and Sr due to the modification effect but the properties are lesser than that of modified 0.2% Si alloy. The same trend is observed with high temperature properties also. However, in all cases, the properties are higher with Sb modification compared to Sr modification.

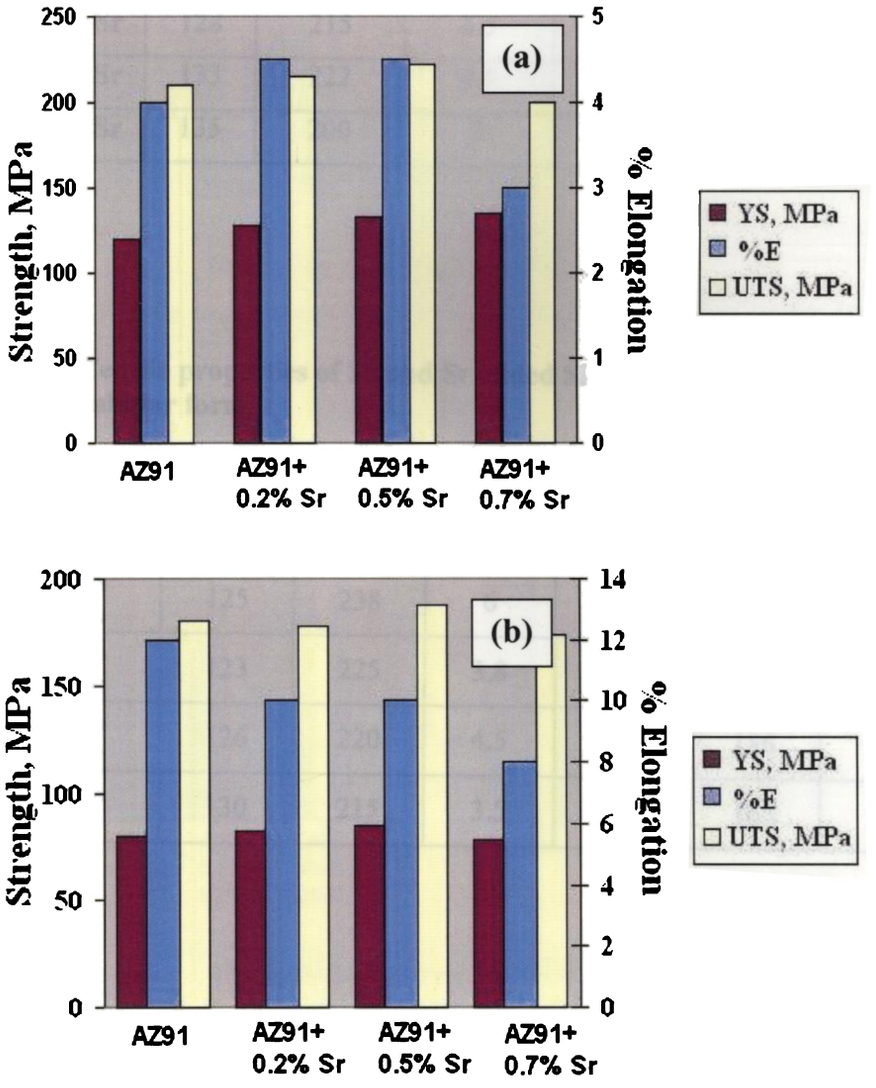

Figure 4.40: Tensile properties of Sr added AZ91alloy (a) RT (b) 150°C

Table 4.8: Tensile properties of Sr added AZ91alloy in tabular form

Alloy	RT			At 150°C		
	YS	UTS	%E	YS	UTS	%E
AZ91	120	210	4	85	180	12
AZ91+0.2% Sr	128	215	4.5	82	178	10
AZ91+0.5% Sr	133	222	4.5	85	188	10
AZ91+0.7% Sr	135	200	3	78	174	8

Table 4.9: Tensile properties of Sb and Sr added Si containing AZ91 alloys in tabular form

Alloy	At RT			At 150°C		
	YS	UTS	%E	YS	UTS	%E
AZ91	120	210	4	85	180	12
AZ91+0.2% Si+0.2% Sb	125	238	6	100	198	16
AZ91+0.5% Si+0.2% Sb	123	225	3.8	94	175	12
AZ91+0.2% Si+0.1% Sr	126	220	4.5	92	186	11.5
AZ91+0.5% Si+0.1% Sr	130	215	3.5	88	165	10

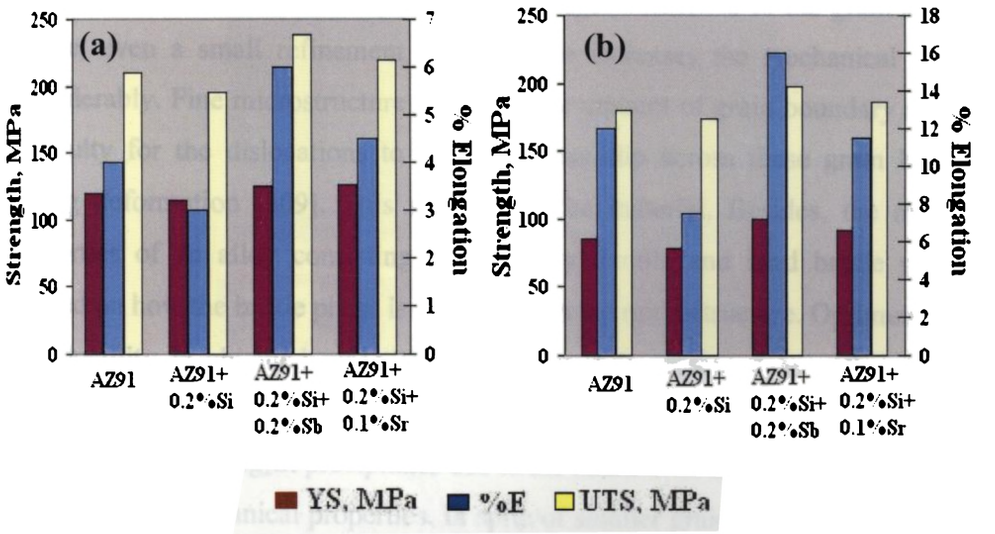

Figure 4.41: Tensile properties of AZ91+0.2% Si alloys modified by Sb and Sr (a) RT (b) 150°C

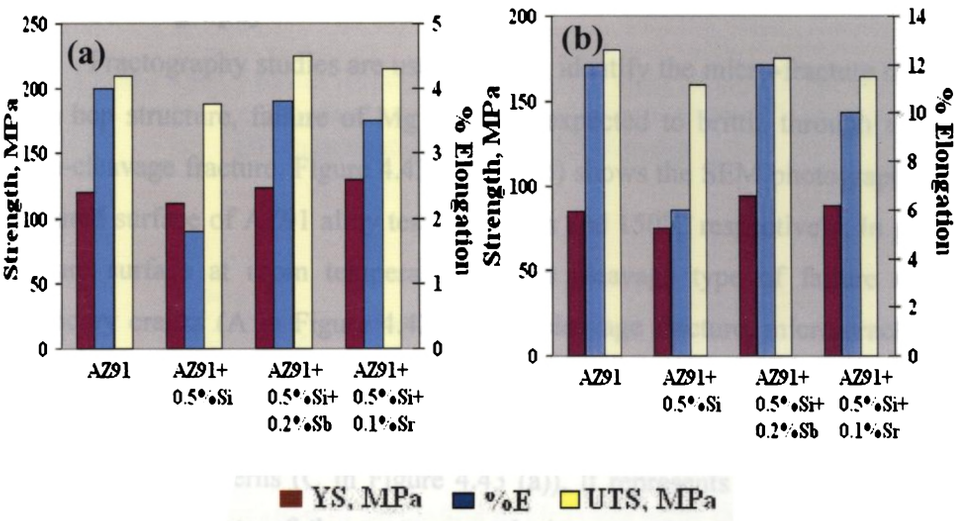

Figure 4.42: Tensile properties of AZ91+0.5% Si alloys modified by Sb and Sr (a) RT (b) 150°C

The improvements in tensile properties of combined additions are due to the combination effect of following reasons: reduction in grain size and modification in the morphology of Mg_2Si intermetallic. It is well recognized that finer grain size is beneficial for mechanical properties in cast materials. That too, since magnesium is HCP structure, its mechanical properties are highly sensitive to the grain size [164]. Hence, even a small refinement in grain size increases the mechanical properties considerably. Fine microstructure provide large amount of grain boundary areas. It is difficulty for the dislocations to do continuous slip across these grain boundaries during deformation [309]. This strengthens the material. Besides, the mechanical properties of an alloy consisting of relatively ductile and hard brittle phase will depend on how the brittle phase is distributed in the microstructure. Optimum strength and ductility is obtained when the brittle phase is presented as a fine dispersion uniformly distributed throughout the soft matrix [310]. In the present case, fine and evenly distributed Mg_2Si precipitates due to the addition of small amount of Sb and Sr improves the mechanical properties. In spite of smaller grain size, Sr modified alloys exhibits lesser properties compared to the Sb modified alloys, which is due to the presence of bigger sized Mg_2Si intermetallics in Sr modified alloys.

4.4.6 Fractography

Fractography studies are useful tool to identify the micro-fracture mechanism. With hcp structure, failure of Mg alloys is expected to brittle through cleavage or quasi-cleavage fracture. Figure 4.43 (a) and (b) shows the SEM photograph of tensile fractured surface of AZ91 alloy tested at room and 150°C respectively. In general the fracture surface at room temperature shows cleavage type of failure with some secondary cracks (A in Figure 4.43 (a)). In cleavage fracture, micro-cracks develop along certain crystal planes, which is normally (0001) for Mg. In the fracture surface many cleavage planes (B in Figure 4.43 (a)) are seen with cleavage steps of different sizes and river patterns (C in Figure 4.43 (a)). It represents steps between different local cleavage facets of the same general cleavage plane. River pattern steps are usually the result of cleavage along second-order cleavage planes or tearing and, to minimize the energy of fracture, they join like river tributaries in the direction of crack propagation. Schematic diagram given in Figure 4.44 illustrates the two mode

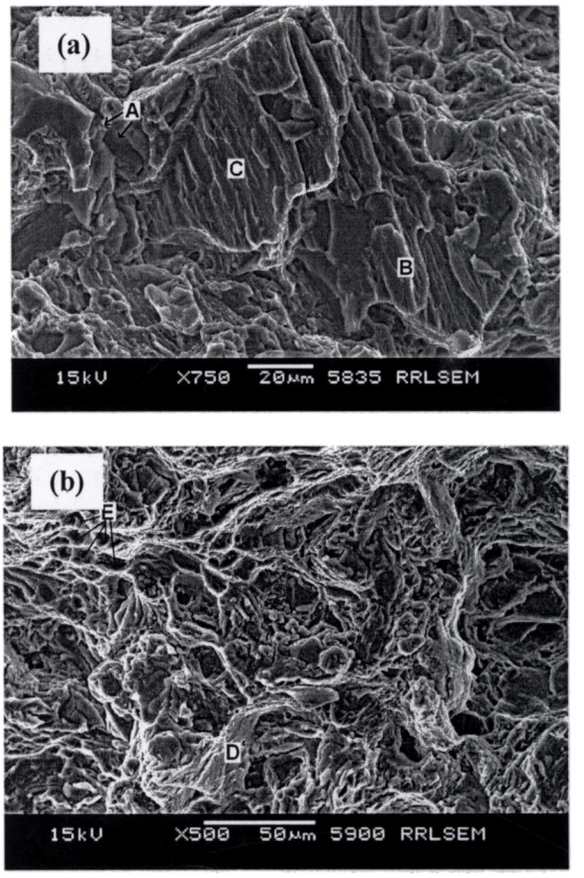

Figure 4.43: Tensile fractorgraph of AZ91 alloy at (a) RT (b) 150°C: (A) secondary crack (B) cleavage plane (C) river pattern (D) plastic deformation (E) dimples

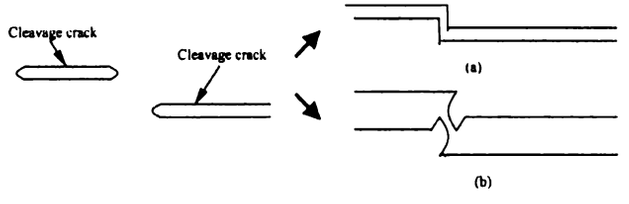

Figure 4.44: Illustration of formation of cleavage steps through (a) secondary cleavage (b) tearing [45]

of steps formation [45]. However, there are some cleavage planes, which have less or no river pattern in fracture surface.

In AZ91 alloy, the $Mg_{17}Al_{12}$ intermetallics present as massive form and coarse lump shape discontinuous form and is very susceptible to fracture because of their brittleness [231]. When load is applied, micro cracks are initiated here and they are readily connected to grain boundaries, thereby making the AZ91 alloy brittle. The longitudinal cross section near the room temperature tensile fracture surface of AZ91 alloy was examined and its microstructure is shown in Figure 4.45. It clearly shows that most of the $Mg_{17}Al_{12}$ particles are got severely fractured, which indicates that these particles and its interface play a major role during tensile deformation.

The improvement in ductility obtained during tensile test at 150°C can be correlated to the fracture surface, which shows more deformation zone (D in Figure 4.43 (b)). However, cleavage planes with secondary cracks noticed ensures still the fracture is a brittle kind. More cleavage facets connected with tearing ridges and shallow dimples is in agreement with the high elongation values obtained at 150°C temperature. This is likely due to the introduction of additional slip planes like pyramid and prismatic planes through which cross slip takes place at elevated temperature [188].

With 0.5% Si addition, well defined cleavage planes with multiple secondary cracks are observed (Figure 4.46). Cleavage planes without river pattern observed indicate that the grain may have been orientated at a right angle to the main tensile axis, causing the fracture to propagate very easily on a single plane [311]. Moreover the plastic zone is constrained due to the presence of Chinese script Mg_2Si phase. The coarseness and unfavorable Chinese script morphology of Mg_2Si along with $Mg_{17}Al_{12}$ increases the brittleness of the alloy and hence reduces the ductility greatly. The microstructure taken on the longitudinal section near the tensile fractured sample of 0.5% Si added alloy reiterate the claim, which shows multiple cracks on Chinese script Mg_2Si precipitates (ref Figure 4.47).

Modification of Mg_2Si precipitates and grain refinement by Sb addition changes the fracture mode of AZ91+0.5%Si alloy from complete cleavage to partial quasi cleavage, which is evident from the fracture surface of AZ91+0.5%Si+0.2%Sb alloy. Presence of large amount of plastic zones spread throughout the fracture surface could be seen in Figure 4.48. In quasi-cleavage fracture, cracks come to being in local areas, grow locally and finally form pits. The quasi cleavage fracture procedure is schematically shown in Figure 4.49 [312]. It is also a kind of brittle fracture but different from cleavage. It is rather complicated fracture pattern also. The planes on the fracture surface are not coherent with certain crystal orientation but formed through combination of locally formed micro cracks. During the combination, tearing ridges are formed. Hence, the bottoms of the pits are not strict cleavage planes but consist of several somewhat sunken planes with secondary cracks [312]. Many quasi cleavage facets connected by tearing ridges and shallow dimples ensure the high ductility and strength obtained in this alloy compare to base as well Si added alloys.

Figure 4.50 show the fracture surface of Sb added alloys, which reflects the tensile properties obtained in tensile test. The fracture surface of 0.5% Sb added alloy shown in Figure 4.50 (a) exhibits cleavage fracture in general. But the fracture surface consists of more quasi-cleavage planes and deformation zone. These fracture features ensures ductility, even though it fails in a brittle manner. In contrast, the fracture surface of 0.7% Sb added alloy (Figure 4.50 (b)) contains lot of cleavages planes with multiple deep secondary cracks. This is inline with the lesser tensile properties observed with 0.7% Sb added alloy. Figure 4.51 shows the fracture surfaces of 0.5% and 0.7% Sr added alloys. Fracture surface of 0.5% Sr added alloy shows many well defined cleavages with multiple secondary cracks. But still some plastic deformation bands and fine dimples are seen in the fracture surface. On the other hand, 0.7% Sr added alloy shows cleavage planes with lot of lengthy deep secondary cracks, which ensure brittle fracture. It possesses smallest deformation zone, exhibiting intergranular fracture feature. This is due to the presence of more number of needle shaped intermetallics at the grain boundaries, which acts as a stress raiser during the loading and promotes cracking along the boundaries.

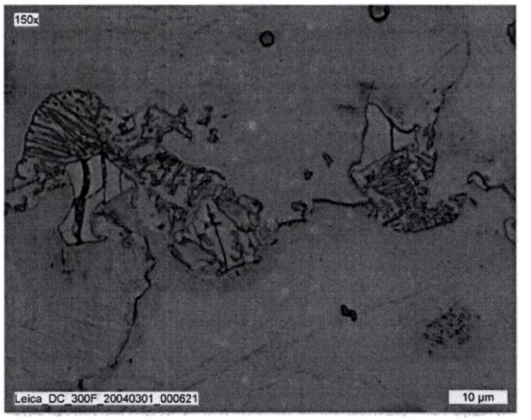

Fig. 4.45: Cross section near the tensile fractured surface of AZ91 alloy showing severely cracked $Mg_{17}Al_{12}$ intermetallic particle

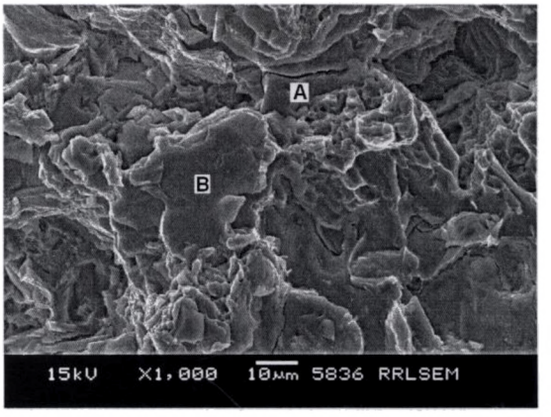

Fig. 4.46: Fracture surface of AZ91+0.5% Si alloy: (A) Secondary crack (B) cleavage plane

Figure 4.47: Tensile tested AZ91+0.5%Si alloy showing cracked Mg_2Si intermetallic

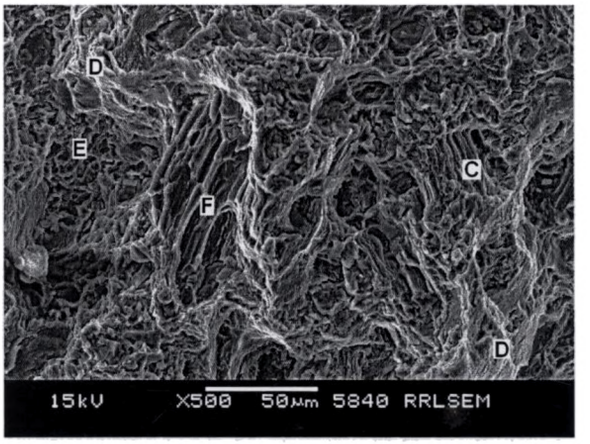

Figure 4.48: Fracture surface of AZ91+0.5% Si+0.2% Sb: (C) river pattern (D) plastic deformation (E) dimples (F) quasi-cleavage facet

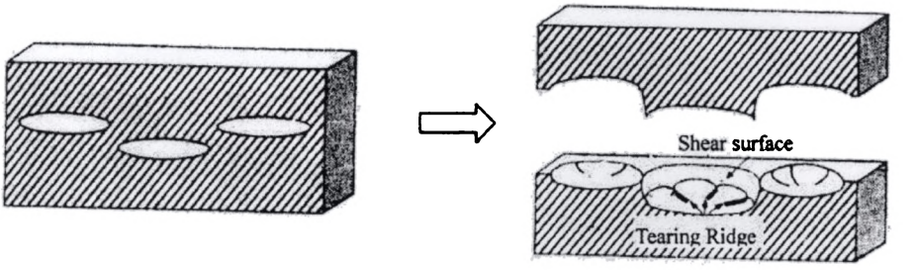

Figure 4.49: Schematic illustration of quasi-cleavage fracture [45]

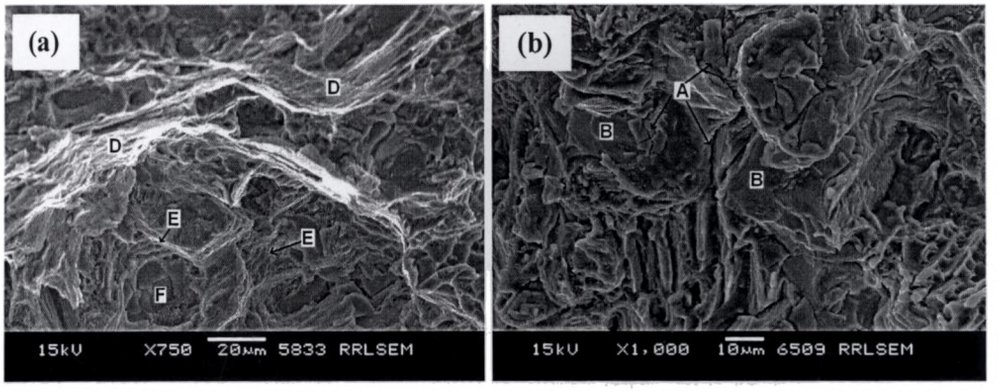

Figure 4.50: Fractograph of Sb added AZ91 alloy failed at RT (a) AZ91+0.5% Sb (b) AZ91+0.7% Sb: (A) secondary crack (B) cleavage plane (D) plastic deformation (E) dimples (F) quasi-cleavage

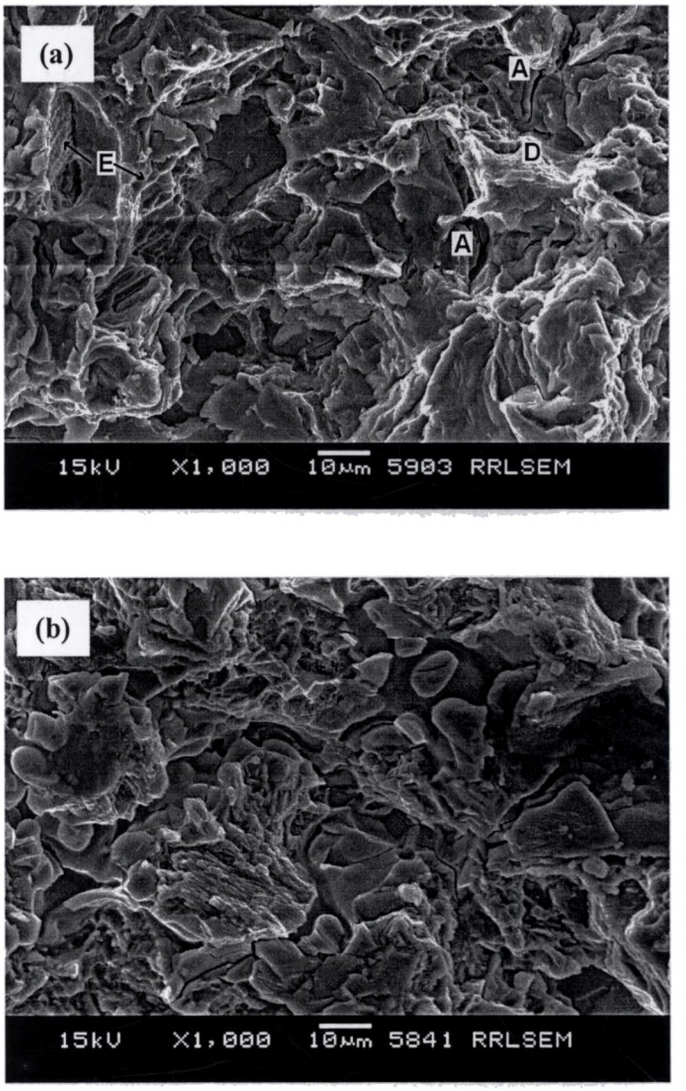

Figure 4.51: Fractorgraph of Sr addedAZ91 alloys failed at RT (a) AZ91+0.5% Sr (b) AZ91+0.7% Sr alloy (A) second crack (D) plastic deformation (E) dimples

4.5 CREEP BEHAIVOR

The role of different alloying additions to AZ91 alloy on its creep behavior is presented in this section. The creep behavior of alloys was investigated at 150 and 200°C with an initial stress of 50 MPa. Two type of creep testing was carried out in the present study: creep testing for 500 h (referred as short term test) and creep testing till fracture (referred as long term test). It is found that the base alloy's creep life at 150°C is around 6000 h, which means the creep testing is time consuming at 150°C. Hence, all the alloys were initially creep tested at 150°C for 500 h. Based on the result of 500 h test, few samples were selected and creep test till fracture was carried out. But in the present investigation, it is found that, in most of the cases, the steady stage creep is not reached even at 500 h. Variation in minimum creep rate is observed between 500 h test and long term testing. For example, the minimum creep rate of base alloy AZ91 at 150°C in short term test (500 h test) is 9.348 X 10^{-4} % h^{-1} whereas during long term test (till fracture) it is 5.9239 X 10^{-4} % h^{-1}. Similarly, the minimum creep rate of AZ91+0.5% Si alloy in short term testing is 5.0825 X 10^{-4} % h^{-1} compare to the value of 3.5803 X 10^{-4} % h^{-1} during long term testing. This indicates that secondary steady state creep reaches only after 500 h. However, it is interesting to note that the creep behavior of any two alloys, when compared to each other, exhibits similar trend in both testing i.e., the alloy showed lesser creep resistant in 500 h (in terms of minimum creep rate) compared to the other alloy, also showed lesser creep resistance in long time testing too. Moreover, most of the literature suggests that 100 h creep behavior could be taken as a comparative tool while comparing the creep behavior of different alloys [221, 313, 314]. Hence, in the present study, 500 h test was considered as a tool to select samples for long term creep testing. This procedure minimized the total testing time. Alloys, which exhibit good creep resistance at 150°C, were further subjected to creep testing at 200°C.

4.5.1 AZ91 Alloy

Figure 4.52 (a) show the creep curve of AZ91 base alloy obtained at 150°C with an initial stress of 50 MPa. It resembles a typical creep curve, which has a short primary and long secondary region followed by an extended tertiary creep region. The creep rate continuously decreases during primary stage to reach a constant creep rate

and is stabilized for longer time during secondary creep region. Finally the rate is increased drastically till failure during tertiary stage. The constant creep rate is known as secondary creep rate or minimum creep rate. Both secondary creep rate and creep extension is calculated from the creep curve and is presented in Figure 4.52 (a). The creep curve of AZ91 alloy tested at 200°C is presented in Figure 4.52 (b). It shows a short primary stage, secondary stage and long tertiary stage of creep. Comparing the creep behavior at both the temperatures, it is clear that the creep resistance of AZ91 alloy is drastically reduced with increase in testing temperature. The secondary creep rate increases from 5.9239 X 10^{-4} $\%h^{-1}$at 150°C to 4.871 X 10^{-2} $\%h^{-1}$at 200°C, which is almost two-fold increase. Creep extension also increases from 8.29% to 14.306%. Most importantly the total creep life is greatly reduced as the testing temperature increases from 150 to 200°C. A sample showed a creep life of 5817 h at 150°C withstands only up to 131 h at 200°C. These results reflect the poor creep behavior of AZ91 alloy above 150°C.

4.5.2 AZ91+XSi Alloys (X=0.2%, 0.5%)

Figure 4.53 shows the short term and long term creep curves of Si added AZ91 alloys at 150°C with an initial stress of 50 MPa. The creep properties like steady state creep rate, creep strain and creep rupture life of tested alloys are listed in Table 4.10. The creep curves of base alloy and 0.2% Si added alloy up to 300 h are similar at 150°C. After then, the curve of Si added alloy is started moving down from the base alloy curve indicating the alloy become hardening due to the presence of stable Mg_2Si intermetallic at grain boundary. However, lower creep rate is observed with 0.5% Si addition right from the beginning of the creep testing. The minimum creep rate is reduced from 9.348 X 10^{-4} to 5.0825 X 10^{-4} % h^{-1} with 0.5% Si addition in the short term test. This result contradicts with the tensile properties observed in the present study. It is found from the present study that with 0.5% Si addition the tensile properties are considerably decreased due to the unfavorable size and morphology of Mg_2Si intermetallic. The improved creep behavior of AZ91+0.5%Si alloy with same microstructure indicates that the deformation modes in both cases are different. In tensile testing, the load is applied at a rate of $\approx 10^{-3}$ to 10^{-4} s^{-1}, which is very high compared to the strain rate normally encountered in creep ($\approx 10^{-8}$ to 10^{-9} s^{-1}). This

difference in strain rate makes deformation mode different in two cases. Superior creep behavior of 0.5% Si added alloy over 0.2% Si added alloy is attributed to the high work hardening effect in 0.5% Si added alloy, which is due to the presence of higher volume of Mg_2Si precipitates.

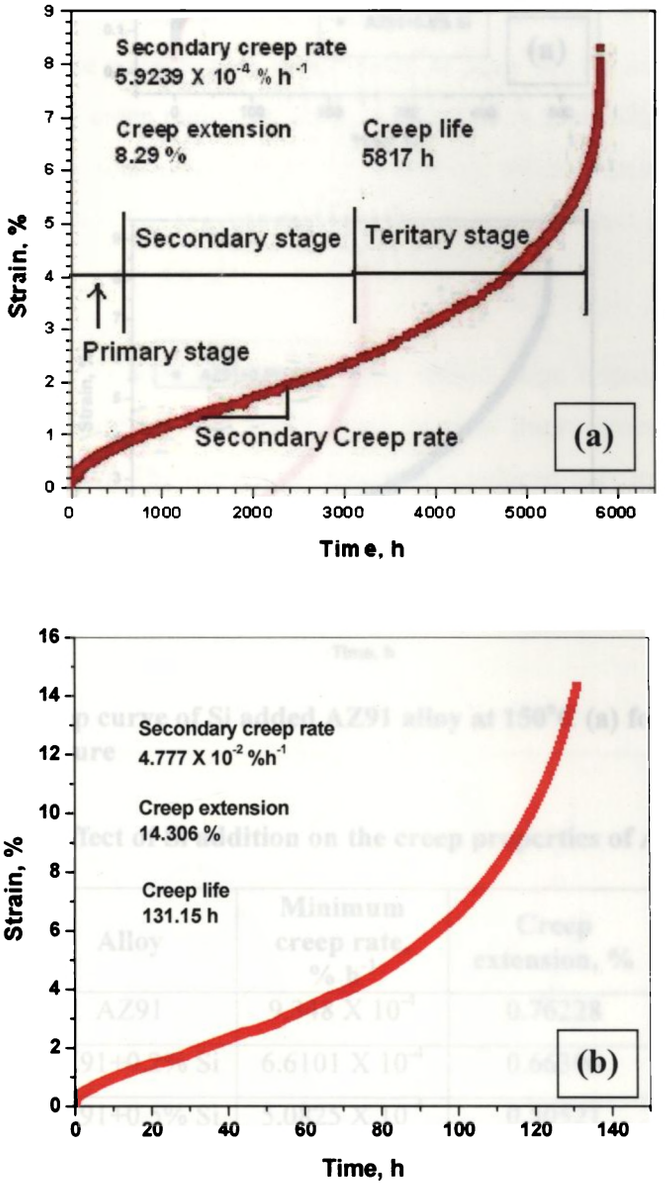

Figure 4.52: Creep curves of AZ91 alloy tested at different temperature (a) 150°C (b) 200°C

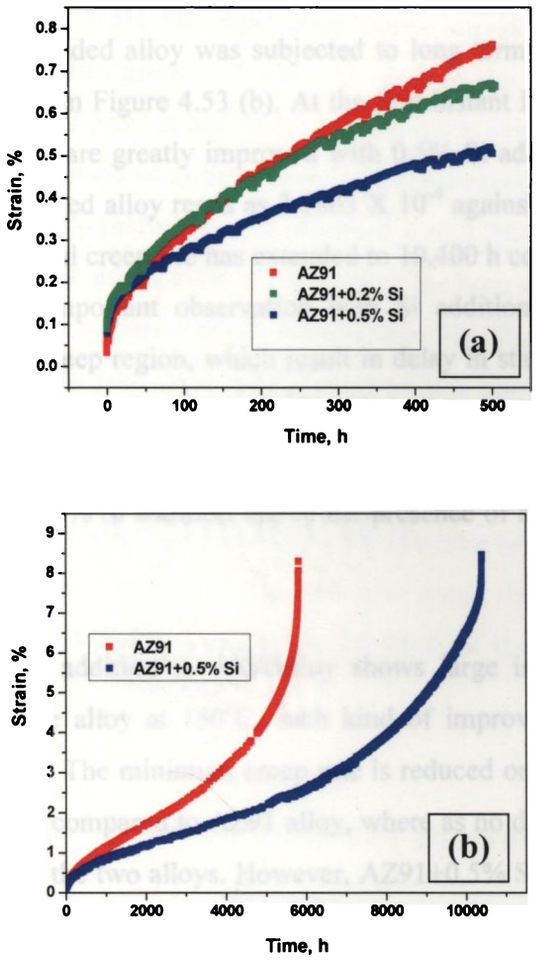

Figure 4.53: Creep curve of Si added AZ91 alloy at 150°C (a) for 500 h (b) till fracture

Table 4.10: Effect of Si addition on the creep properties of AZ91 alloy

Testing condition	Alloy	Minimum creep rate, % h^{-1}	Creep extension, %	Creep life, h
150°C, 500 h	AZ91	9.348 X 10^{-4}	0.76228	-
	AZ91+0.2% Si	6.6101 X 10^{-4}	0.66396	-
	AZ91+0.5% Si	5.0825 X 10^{-4}	0.50521	-
150°C, long term	AZ91	5.9239 X 10^{-4}	8.2908	5817
	AZ91+0.5% Si	3.5803 X 10^{-4}	8.46176	10400
200°C	AZ91	4.871 X 10^{-2}	14.306	131.15
	AZ91+0.5% Si	3.542 X 10^{-2}	10.388	133.46

AZ91+0.5% Si added alloy was subjected to long term creep testing and its creep curve is presented in Figure 4.53 (b). At the first instant itself, it could be seen that the creep properties are greatly improved with 0.5% Si addition. The minimum creep rate of 0.5% Si added alloy reads as 3.5803 X 10^{-4} against 5.9239 X 10^{-4} % h^{-1} of the base alloy. The total creep life has extended to 10,400 h compared to 5,817 h of base alloy. The most important observation with Si addition is the extension of secondary steady state creep region, which result in delay in start of the tertiary state of creep. The tertiary creep region for 0.5% Si added alloy starts after 5,700 h, which is almost equal to the total creep life of the base alloy, which indicates that the alloy become stronger with 0.5% Si addition due to the presence of hard and stable Mg_2Si intermetallic.

Even though Si addition to AZ91alloy shows large improvement in creep properties over the base alloy at 150°C, such kind of improvement is not seen at 200°C (ref Figure 4.54). The minimum creep rate is reduced only marginally in case of AZ91+0.5% Si alloy compared to AZ91 alloy, where as no difference is noticed in total creep life between the two alloys. However, AZ91+0.5% Si alloy shows slightly lesser creep extension to failure compared to AZ91.

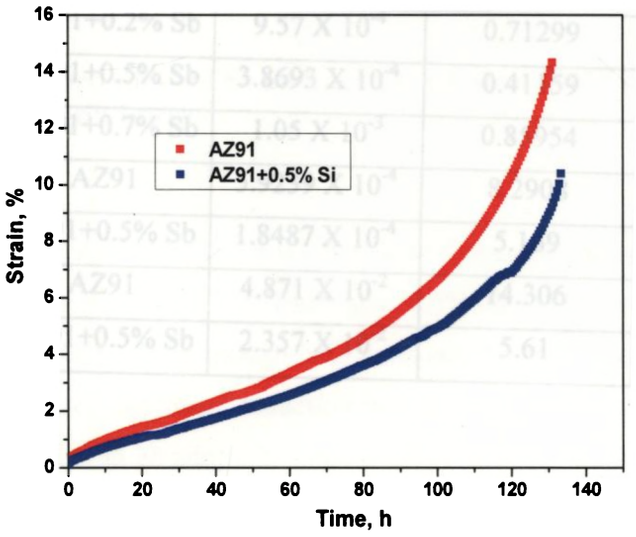

Figure 4.54: Creep curve of AZ91+ 0.5% Si alloy tested at 200°C

4.5.3 AZ91+XSb Alloys (X=0.2%, 0.5%, 0.7%)

Figure 4.55 shows the creep behavior of Sb added alloys at 150°C. The 500 h test indicates that the creep behavior of 0.2% Sb added alloy exhibits almost similar creep behavior whereas 0.5% Sb added alloy shows superior behavior to the base alloy. The creep properties given in Table 4.11 reads as the minimum creep rate of 0.5% Sb added alloy is 3.8693 X 10^{-4} % h^{-1} and the creep extension is only 0.411 %. The stable Mg_3Sb_2 intermetallic is the reason the improvement in creep behavior. On the other hand, poor creep performance is observed with 0.7% Sb added alloy. Indeed the creep rate of 0.7% Sb added alloy is higher than the base alloy. Presence of more volume fraction of needle shaped brittle intermetallic Mg_3Sb_2, which act as a stress raiser is the reason for the poor creep performance of high percentage Sb added alloy. Figure 4.55 (b) shows the long-term creep test curves of AZ91 alloy with and with out 0.5% Sb addition. The minimum creep rate is greatly reduces to 1.8487 X 10^{-4} % h^{-1} and its creep extension is only 5.16 % compared to the base alloy extension of 8.2 %. Extended secondary creep regions along with low creep strain indicate the alloy exhibits excellent creep resistance due to the presence of thermally stable Mg_3Sb_2 intermetallic.

Table 4.11: Effect of Sb addition on the creep properties of AZ91 alloy

Testing condition	Alloy	Minimum creep rate, % h^{-1}	Creep extension, %	Creep life, h
150°C, 500 h	AZ91	9.348 X 10^{-4}	0.76228	-
	AZ91+0.2% Sb	9.57 X 10^{-4}	0.71299	
	AZ91+0.5% Sb	3.8693 X 10^{-4}	0.41159	-
	AZ91+0.7% Sb	1.05 X 10^{-3}	0.85954	-
150°C, long term	AZ91	5.9239 X 10^{-4}	8.2908	5817
	AZ91+0.5% Sb	1.8487 X 10^{-4}	5.169	11264
200°C	AZ91	4.871 X 10^{-2}	14.306	131.15
	AZ91+0.5% Sb	2.357 X 10^{-2}	5.61	134.08

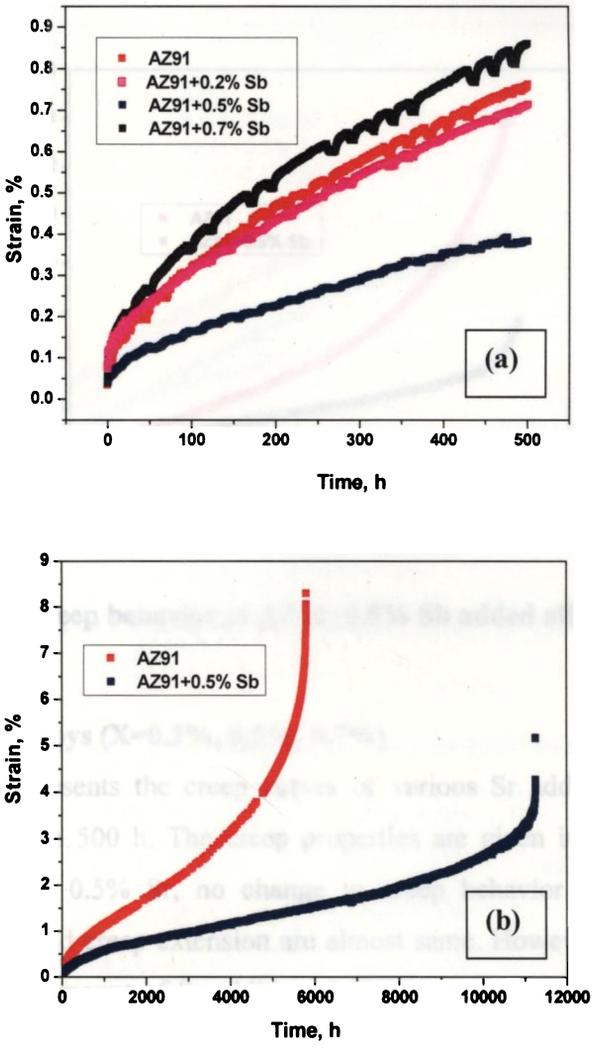

Figure 4.55: Creep curve of Sb added AZ91 alloys at 150°C (a) for 500 h (b) till fracture

Creep test on AZ91+0.5% Sb alloy at 200°C was carried out and the creep curve is presented in Figure 4.56. Interestingly, 0.5% Sb addition shows improved creep properties at 200°C. Even though both base and 0.5% Sb added alloys exhibit almost same creep life, significant reduction in minimum creep rate and total creep extension is observed with Sb addition. Almost 50% reduction in minimum creep rate is seen with Sb addition.

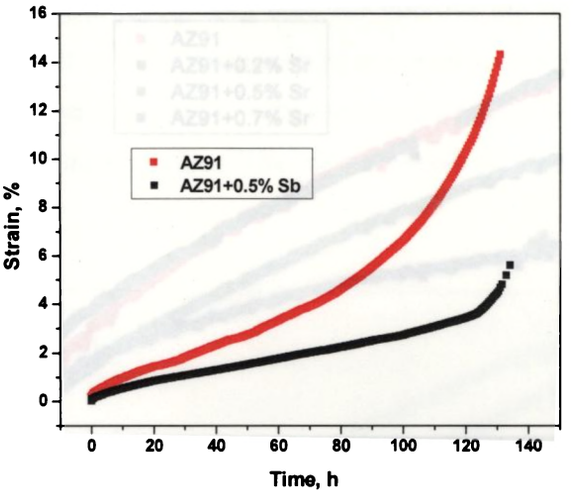

Figure 4.56: Creep behavior of AZ91+0.5% Sb added alloy at 200°C

4.5.4 AZ91+XSr Alloys (X=0.2%, 0.5%, 0.7%)

Figure 4.57 presents the creep curves of various Sr added AZ91 alloys at 150°C conducted up to 500 h. The creep properties are given in Table 4.12. With addition of 0.2% and 0.5% Sr, no change in creep behavior is observed. Both minimum creep rate and creep extension are almost same. However, improvement is observed with higher amount of Sr addition. 0.7% Sr addition reduces the minimum creep rate to 4.222 X 10^{-4} % h^{-1}. The creep extension for 500 h also greatly reduces to 0.4 11 mm with 0.7% Sr addition. These improvements are attributed to the presence of stable Al_4Sr intermetallic, which replaced the low melting point $Mg_{17}Al_{12}$ intermetallic. When 0.7% Sr is added, the tensile properties got reduced due to the presence of more number of Al_4Sr intermetallic, but it exhibits higher creep resistance. This shows that the stability of the intermetallics present in the microstructure is more important in creep.

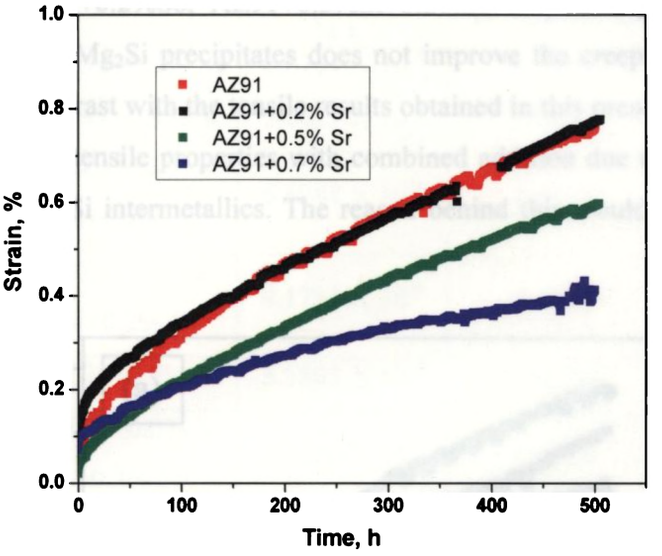

Figure 4.57: Creep curve of Sr added AZ91 alloys at 150°C for 500 h

Table 4.12: Effect of Sr addition on the creep properties of AZ91 alloy

Testing condition	Alloy	Minimum creep rate, % h^{-1}	Creep extension, %
150°C, 500 h	AZ91	9.348 X 10^{-4}	0.76228
	AZ91+0.2% Sr	1.02 X 10^{-3}	0.7779
	AZ91+0.5 % Sr	9.3184 X 10^{-4}	0.5976
	AZ91+0.7% Sr	4.222 X 10^{-4}	0.4115

4.5.5 AZ91+XSi+0.2% Sb Alloys (X=0.2%, 0.5%)

Creep testing was also carried out on combined addition of Si and Sb alloys. Figure 4.58 show the creep curves of AZ91+0.2% Si+0.2% Sb and AZ91+0.5% Si+0.2% Sb alloy tested at 150°C for 500 h. Creep curves of individual additions of Si to AZ91 alloys are also presented in the figure for comparison. The creep properties measured from the curves are presented in Table 4.13. From the results, it could be seen that addition of Sb to the Si containing alloys does not make much difference in creep behavior. For both the 0.2% and 0.5% Si added alloys, the creep rate values marginally differ with its counterpart

alloys AZ91+0.2%Si+0.2%Sb, AZ91+0.5%Si+0.2%Sb respectively. This suggests that modification of Mg_2Si precipitates does not improve the creep properties. This observation is in contrast with the tensile results obtained in this present investigation, which shows higher tensile properties with combined addition due to morphological modification of Mg_2Si intermetallics. The reason behind this would be discussed in section 4.5.7.2.

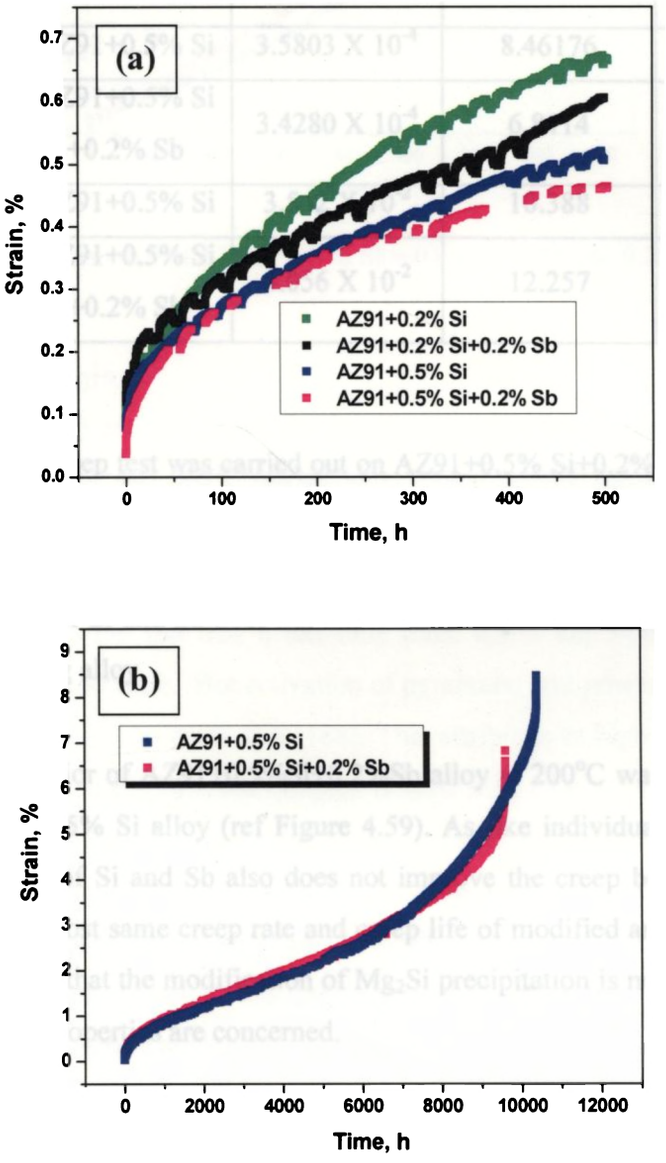

Figure 4.58: Creep curves of Si and Sb added AZ91 alloys at 150°C (a) for 500 h (b) till fracture

Table 4.13: Effect of combined addition of Si and Sb on the creep properties of AZ91 alloy

Testing condition	Alloy	Minimum creep rate, % h^{-1}	Creep extension, %	Creep life, h
150°C, 500 h	AZ91+0.2% Si	6.6101 X 10^{-4}	0.66396	-
	AZ91+0.5% Si	5.0825 X 10^{-4}	0.50521	-
	AZ91+0.2% Si+0.2% Sb	6.4988 X 10^{-4}	0.6052	-
	AZ91+0.5% Si+0.2% Sb	4.1781 X 10^{-4}	0.4178	-
150°C, long term	AZ91+0.5% Si	3.5803 X 10^{-4}	8.46176	10400
	AZ91+0.5% Si +0.2% Sb	3.4280 X 10^{-4}	6.8114	9612.5
200°C	AZ91+0.5% Si	3.542 X 10^{-2}	10.388	133.46
	AZ91+0.5% Si +0.2% Sb	4.056 X 10^{-2}	12.257	153

Long term creep test was carried out on AZ91+0.5% Si+0.2% Sb alloy and its creep behavior is compared with that of AZ91+ 0.5% Si alloy (Figure 4.58 (b)). It is again realized that the modification of Chinese script Mg_2Si into polygonal shape in combined addition of Si and Sb does not make much improvement in creep behavior of Si only containing alloy.

Creep behavior of AZ91+0.5%Si+0.2%Sb alloy at 200°C was compared with AZ91 and AZ91+0.5% Si alloy (ref Figure 4.59). As like individual addition of Si, combined addition of Si and Sb also does not improve the creep behavior of AZ91 alloy at 200°C. Almost same creep rate and creep life of modified and unmodified Si alloy again confirm that the modification of Mg_2Si precipitation is not much effective as far as the creep properties are concerned.

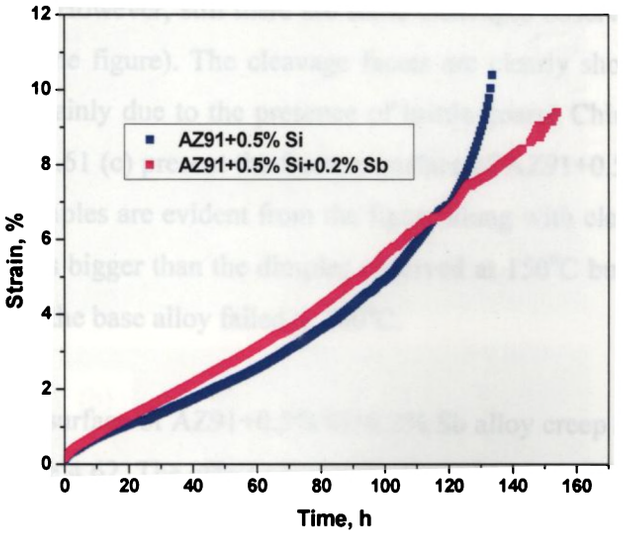

Figure 4.59: Creep curves of AZ91+0.5% Si with and with out 0.2% Sb alloy at 200°C

4.5.6 Creep Fractograph

Figure 4.60 (a) and (b) shows the fractographs of creep ruptured AZ91 alloy specimens tested at 150 and 200°C respectively, which exhibits ductile features. The large number of dimples with different sizes seen in the creep ruptured surface is consistent with high ductility obtained during creep. Normally, magnesium fails in brittle manner due to the fact that it has only three active slip systems (basal slip systems) at room temperature. But activation of pyramidal and prismatic slip systems at high temperature leads to cross slip [188]. This attributes to high ductility during creep. More number of bigger sized dimples is seen with base alloy failed at 200°C compared to 150°C. This is due to the coalescence of micro-voids accelerated at higher testing temperature. More uniform bigger sized dimples observed at 200°C are in consistent with higher ductility obtained at 200°C compare to 150°C. Oxidation is also seen with fracture surface of the specimens tested for creep. This is due to the exposure of fracture surface at elevated temperature for some time (after the sample is failed) in the furnace.

The creep fracture surfaces of AZ91+0.5% Si alloy tested at both 150 and 200°C is presented in Figure 4.61. The fractograph exhibits ductile features with large number dimples. The size of the dimples is similar with AZ91 alloy (ref figure 4.54 (a)). However, still there are some cleavages observed in the fracture surface (marked in the figure). The cleavage facets are clearly shown in the Figure 4.61 (b), which is mainly due to the presence of brittle coarse Chinese script Mg_2Si precipitates. Figure 4.61 (c) present the fracture surface of AZ91+0.5% Si alloy failed at 200°C. Coarse dimples are evident from the figure along with cleavage facets. The size of the dimples is bigger than the dimples observed at 150°C but smaller than the dimples observed in the base alloy failed at 200°C.

The fracture surface of AZ91+0.5% Si+0.2% Sb alloy creep ruptured at 200°C is presented in Figure 4.62. The effect of modification of coarse Chinese script Mg_2Si morphology is reflected in the fracture surface, which exhibits lot dimples of different sizes. Mainly two sizes of dimples are present: fine dimples observed in matrix and relatively coarse dimples initiated at the grain boundary. Figure 4.62 (b) and (c) shows the magnified secondary and back-scattered SEM image of the same area of the fractured surface. It clearly shows that most of the dimples are originated at Mg_2Si precipitates. There are some fine eutectic $Mg_{17}Al_{12}$ particles are also seen under dimples with or without fracture. Cracking and debonding of Mg_2Si precipitates are observed in some areas. Nevertheless, most of the particles are still firmly bounded in the matrix. Several matrix cracks around the particles are also seen.

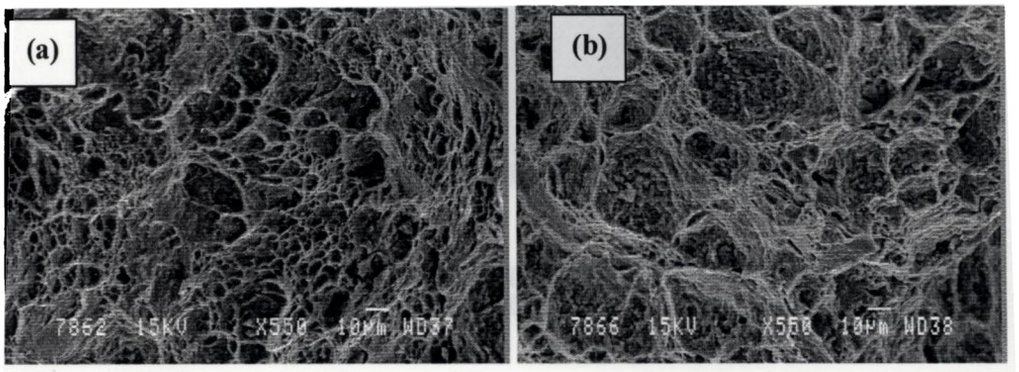

Figure 4.60: Fractographs of creep ruptured AZ91 alloy at (a) 150°C (b) 200°C

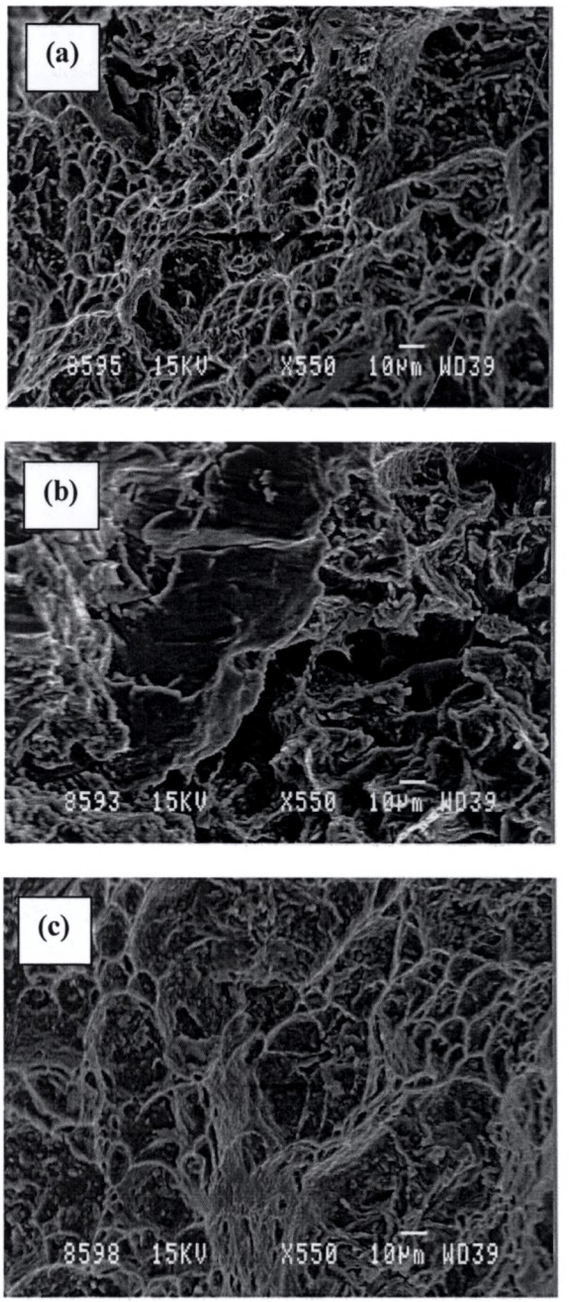

Figure 4.61: Fractographs of creep ruptured AZ91+0.5% Si alloy at (a) &(b) 150°C (c) 200°C

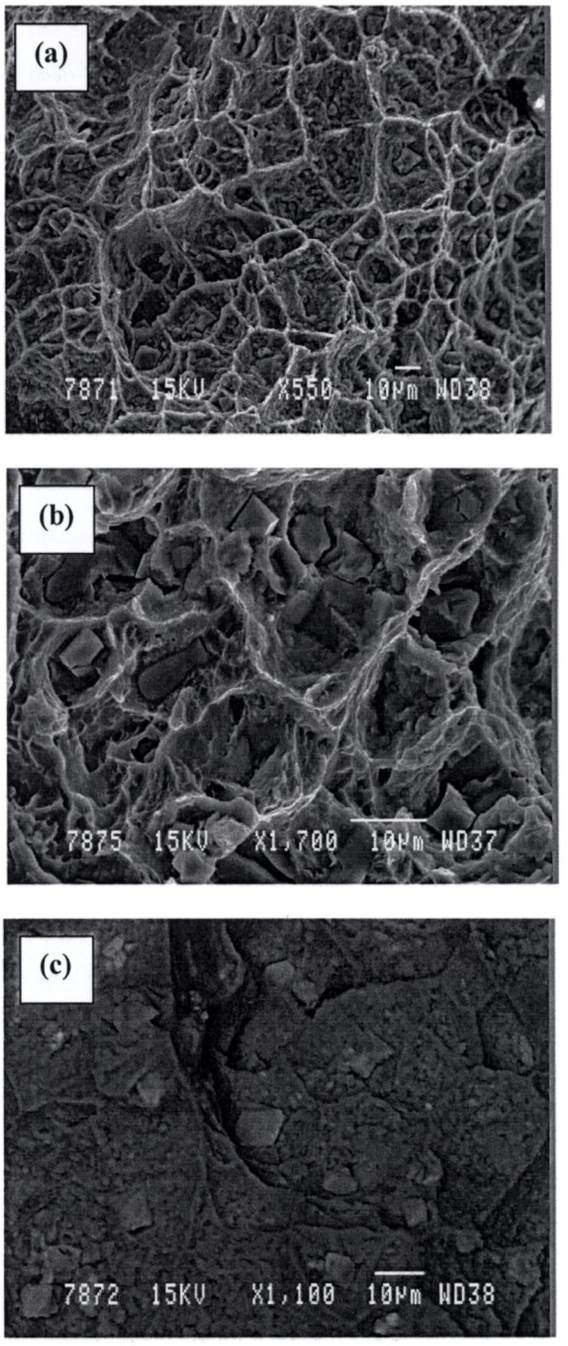

Figure 4.62: Fractograph of creep ruptured AZ91+0.5% Si +0.2% Sb alloy at 200°C (a) SE image lower mag. (b) SE image higher mag. (c) BSE image

4.5.7 Post Creep Microstructural Analysis

4.5.7.1 AZ91 alloy

The microstructure of as cast AZ91 alloy is unstable at high temperature due to the supersaturation of aluminum in the solid solution [28, 30, 31, 184, 186]. In the present study also many high aluminum concentrated areas are found in the as cast AZ91 microstructure (ref. Table 4.1). In the initial stage of creep the aluminum in solid solution provides solid solution strengthening against moving dislocations. Then secondary precipitates forms from the solid solution during creep exposure [184, 186]. Many literatures reported that the dynamic precipitation (continuous and/or discontinuous $Mg_{17}Al_{12}$) takes places during creep but it is still inconclusive that how these precipitates influence the creep behavior of this alloy. Dargusch et al [186] have reported that the dynamic discontinuous precipitation occurred at the grain boundary in the die cast AZ91 alloy leads to the grain boundary sliding whereas Regev et al [29] have reported that the continuous secondary precipitates occurred from the supersaturate eutectic matrix strengthens the ingot cast AZ91 alloy against creep deformation. The result of Blum et al [184] also suggest that continuous precipitates dominate during creep exposure of die cast AZ91 alloy and provide strengthening against creep.

In the present study, a detailed post creep test microstructural analyses were carried out to understand the structural changes due to the high temperature exposure. Figure 4.63 shows the microstructure of longitudinal cross section near the fracture surface of AZ91 alloy creep ruptured at 150°C, which contain lot of coarse continuous precipitates. Higher magnified view of the same sample (Figure 4.63) clearly shows the presence of continuous precipitates with random orientation, which occurred during creep. Similar kind of dynamic continuous precipitates are observed in all the tested alloys. These continuous precipitates would have formed at the initial stage of creep and become coarsen during the continuous exposure to high temperature. The interrupted microstructure of AZ91 creep tested at 150°C for 2000 h (secondary creep region) shown in Figure 4.64 contains finer continuous precipitates. These precipitates, in earlier stage of creep, block dislocation motion and encourage cross slip leading to strengthening [315]. Hence, hardening mechanism is changed from

solid solution strengthening to precipitation hardening. Then prolonged exposure leads to the coarsening of precipitates and it looses its ability to pin both the dislocations and boundary. As it is clear that the $Mg_{17}Al_{12}$ precipitates has low melting point (437°C) and aluminum has higher diffusivity in magnesium, coarsening takes place very easily and faster. Moreover the decomposition of $Mg_{17}Al_{12}$ at grain boundary during elevated temperature exposure increases the aluminum content in local areas. Subsequently this reduces the solidus temperature and hence increases the homologous temperature [316]. This represents the tertiary stage of creep. As long as the hardening mechanism dominates the creep rate decreases. Whereas, when softening mechanisms become dominant, the creep rate increases. The minimum creep rate measured is the point of balance between hardening and softening mechanisms, which happens during secondary stage of creep.

Apart from the coarsening effect, the massive $Mg_{17}Al_{12}$ particles are also involved in cavity formation. Figure 4.63 also shows most of the $Mg_{17}Al_{12}$ particles suffer from sever cracking and cavity formation at the matrix – precipitate interface. These cavities develop along the grain boundary since more coarse discontinuous precipitates are present in the grain boundary and finally introduce matrix cracking. One of the major reasons for the formation cavity is the weak interface between matrix and $Mg_{17}Al_{12}$ intermetallic. It is well known that the crystallographic lattices of Mg matrix and $Mg_{17}Al_{12}$ are different: the magnesium matrix has an hcp lattice, while the β-$Mg_{17}Al_{12}$ precipitates have a cubic lattice. It is also known that dislocations cannot pass as easily through hard precipitates as through the matrix. In such cases pileups of dislocations near the precipitates lead to increase in local stress concentration and resulted in cracking. Moreover cavity may forms at the grain boundary triple points. One such cavity at triple point in creep ruptured AZ91 alloy at 150°C is shown in the Figure 4.65. According to Regev [29], the intergranular cavitation and cracking also indirectly contributes to the softening process during creep. From dislocation theory, it is well known that cavitation enables dislocations to leave the bulk of the grain to the free surface without being blocked by obstacles. This prevents the activity of dislocation sources and hence, the number of pileups is reduced [29].

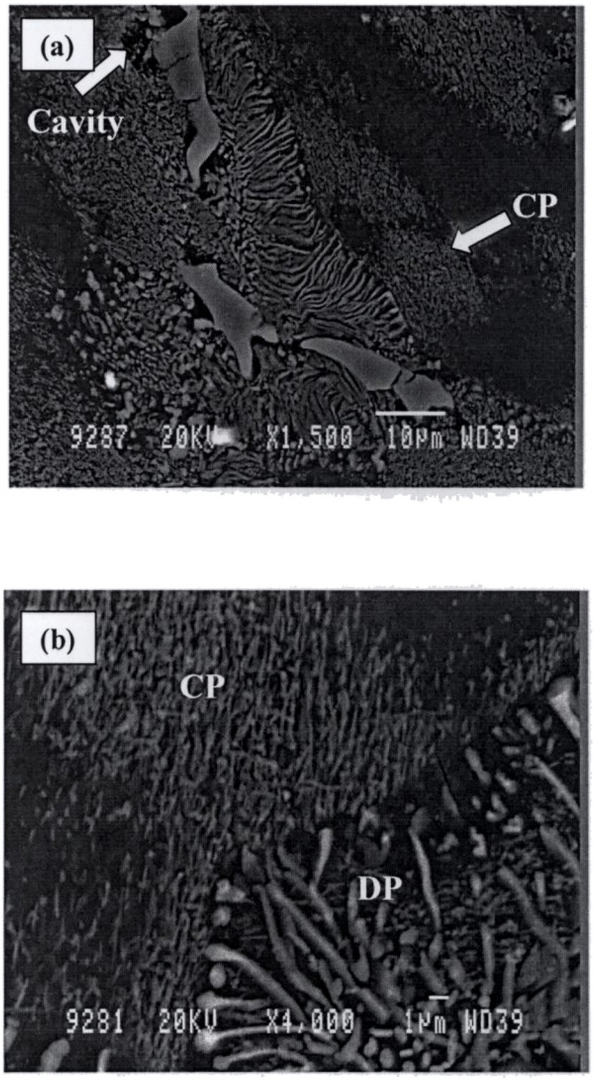

Figure 4.63: Longitudinal cross section near the fracture surface of AZ91 alloy creep ruptured at 150°C showing continuous precipitates (a) lower (b) higher magnification

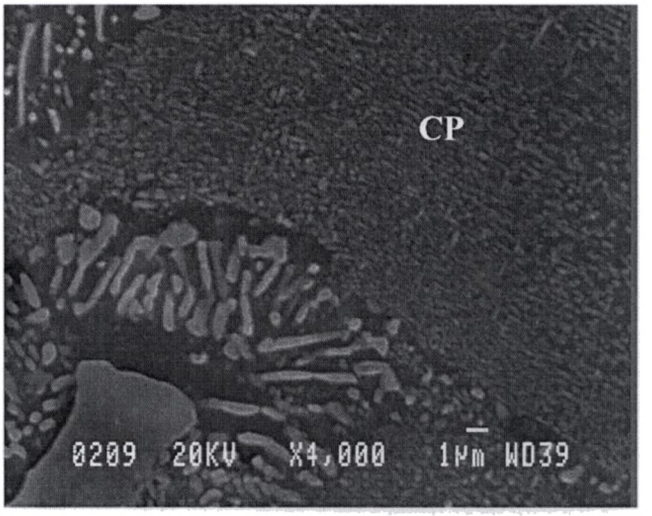

Figure 4.64: Interrupted microstructure of creep tested AZ91 alloy showing fine continuous precipitates

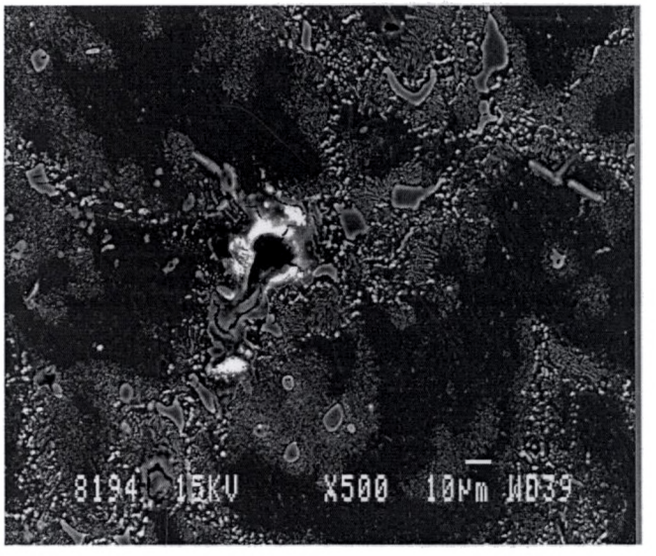

Figure 4.65: Cavity at gain boundary triple point in AZ91 alloy ruptured at 150°C

Hence it is clear from the present investigation that following microstructural changes lead to the poor creep behavior of AZ91alloy:

1. Coarsening and softening of continuous $Mg_{17}Al_{12}$ precipitates at the later stage of creep, unable to block the movement of dislocation and grain boundary

2. Incompatibility between the matrix and $Mg_{17}Al_{12}$ intermetallic leads to the cavity and crack formation, which propagate along the grain boundary

4.5.7.2 AZ91 with alloying additions

As seen earlier, cavity formation is generally observed feature of creep failure. Most of the cavity forms as a consequence of stress concentration at areas like grain boundary triple point junctions, which are the sites of greatest disorder and inherent weakness [317]. However, the presence of stable and hard intermetallic at the grain boundary may inhibit the sliding of one grain over another by reducing the atom movements across the grain boundary, and thereby reduce the opportunities for cavity formation at the triple points. It is understood that the $Mg_{17}Al_{12}$ intermetallic is not strong enough to prevent the cavity formation; perhaps it facilitates it due to its incompatibility with the matrix. On the other hand, the presence of stable intermetallics like Mg_2Si, Mg_3Sb_2 and Al_4Sr at the grain boundary reduces the activity of atom diffusion along the grain boundary. In addition to that, presence of these intermetallics introduces many dislocations nearby during solidification due to the difference in co-efficient of thermal expansion. These dislocations act as a heterogeneous nucleation site for the continuous precipitates [295]. Figures 4.66 show the microstructure of Si and Sb added alloys, which clearly indicates the presence of dense continuous precipitates near the intermetallics. These finely distributed coherent precipitates near the boundaries are more effectively reduce the atom movement across the grain boundary by diffusion. Since these precipitates form along the grain boundary dislocations it also effectively pinning them in place.

Apart from that, these intermetallics effectively obstruct the growth of the crack along the grain boundary, which already developed at the interface of matrix

and $Mg_{17}Al_{12}$ as explained earlier. The SEM photograph of cross section near the fracture surface of creep ruptured AZ91+0.5Si alloy is shown in Figure 4.67, it could be seen that many cracks are initiated from the massive as well as discontinuous precipitate of $Mg_{17}Al_{12}$ and spreads throughout the matrix. These cracks are obstructed by the Mg_2Si precipitates at the grain boundary. However, cavity formation and cracking at these intermetallics (Mg_2Si and Mg_3Sb_2) is the softening mechanism, which leads to the final fracture at last. Cracks and cavities at both Mg_2Si and Mg_3Sb_2 intermetallics are also seen in the crept microstructure of Si and Sb added alloys (see Figures 4.66 & 4.67). However, the interrupted microstructure of AZ91+0.5% Sb added alloy creep tested up to 6000 h at 150°C shown in Figure 4.68, indicate that the Mg_3Sb_2 intermetallic is intact. This gives rise to an extended secondary creep region. Hence, the final failure is decided by the intermetallics as how long it prevents the crack propagation.

In the present study, it is also found that both the morphologies (Chinese script and polygonal) of Mg_2Si intermetallic exhibits similar creep properties, despite the tensile properties are sensitive with the morphology, which indicates that the Chinese script does not affect the creep properties. Recently, Dargush et al. [318] also reported that the morphology of the Chinese script Mg_2Si is effective to hold the grain boundary against sliding during creep. As shown in Figure 2c, it has multiple arms extended into neighboring grains thereby restrict the grain boundary movement effectively. Another possible explanation is the difference in type of load applied during tensile and creep testing. The normal strain rate used for tensile testing is much higher (10^{-3} to 10^{-4} S^{-1}) than the strain rate encountered during creep testing (in the range of 10^{-7} S^{-1}). At higher strain rate, accumulation of dislocations at the interface of matrix and hard intermetallic is at a faster rate, which increases the local stress level and leads to cracking. On the other hand, dislocation pile up is at slower rate during creep and hence strengthening effect due to its multiple arm morphology, as it restricts the grain boundary movement, dominates. Due to this, the creep behavior of AZ91 improves by the presence of massive size Mg_2Si with Chinese script morphology even though it reduces tensile properties.

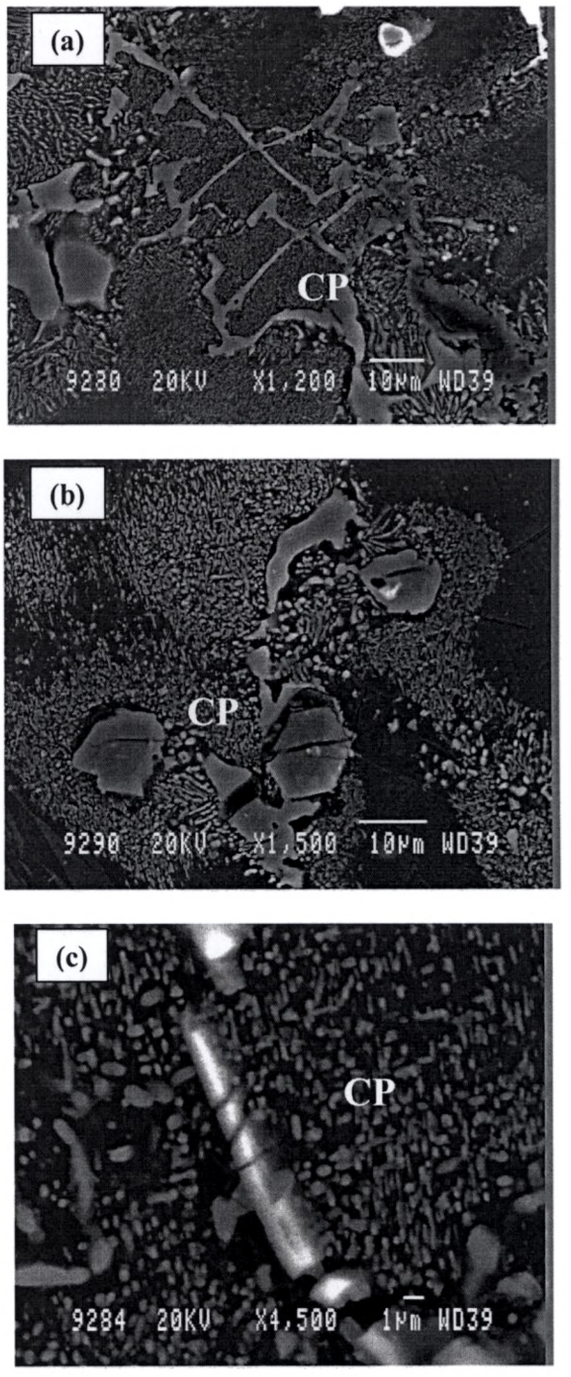

Figure 4.66: Continuous precipitates occurred around the intermetallics during creep at 150°C (a) AZ91 (b) AZ91+0.5% Si (c) AZ91+0.5% Sb

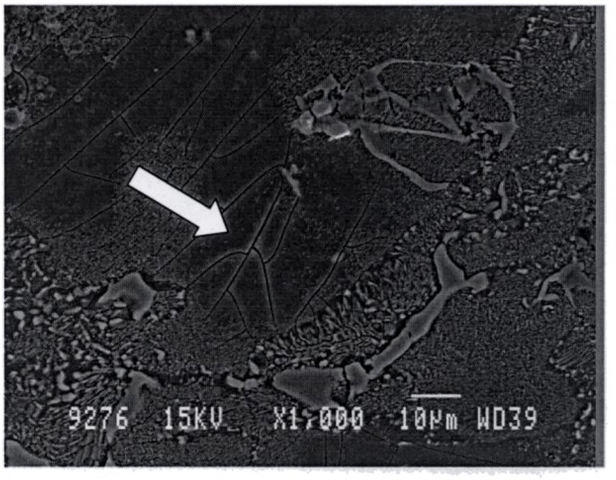

Figure 4.67: Photograph of creep ruptured AZ91+0.5% Si alloy at 150°C showing cracks arrested by Mg_2Si intermetallic

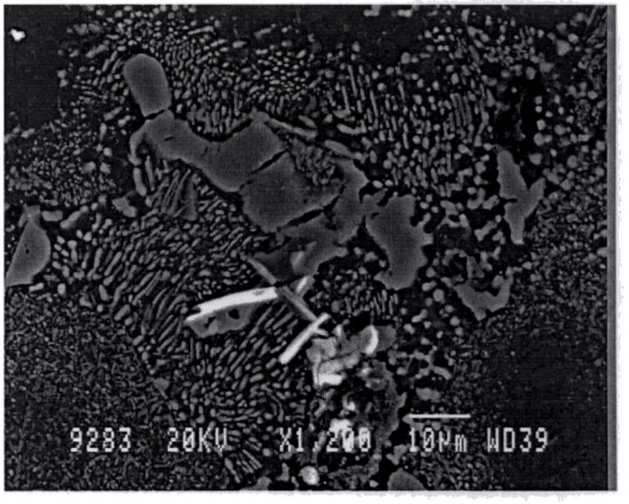

Figure 4.68: Photograph of AZ91+0.5% Sb subjected to creep testing at 150°C up to 6000 h showing Mg_3Sb_2 intermetallics remain intact

Superior creep behavior is observed with 0.5% Sb added alloy compared to all alloys studied. The effect of intermetallics on the properties can be related to its stability, shape and bonding with matrix. In general, the thermal stability of intermetallics is related to their melting points, higher the melting point, higher is the thermal stability [325]. The melting point of Mg_3Sb_2 intermetallic (1228°C) is slightly higher than the melting point of Mg_2Si intermetallic (1085°C) [43, 176]. Moreover, the lattice similarities exist between the Mg matrix and Mg_3Sb_2 intermetallic; both are hcp lattice structures. In contrast, Mg_2Si has cubic structure [316]. In that way Mg_3Sb_2 intermetallic is more effective compared to both Mg_2Si and $Mg_{17}Al_{12}$. Due to this reason 0.5Sb added alloy exhibit superior creep properties in the present study. However, in general, not much improvement in creep properties is observed with alloying additions at 200°C. This is attributed to the fact that the softening effect by the coarsening of $Mg_{17}Al_{12}$ is more predominant at 200°C due to the high mobility of aluminum atoms.

Even though long term test was not carried out for Sr added alloy, the 500 h test indicate that Sr addition are also capable of improving the creep resistance of AZ91 alloy. The above said intermetallic stability theory could be invoked to explain the improvement, since the melting point of Al_4Sr intermetallic (1040°C) is higher than the $Mg_{17}Al_{12}$. Moreover, from heat treatment studies it is found that Sr addition increases the stability of $Mg_{17}Al_{12}$ to certain extent. Many $Mg_{17}Al_{12}$ intermetallic is seen even after prolonged solution treatment at 420°C. This will also play a role during creep. A detailed study on Sr addition is included in the future course of work.

Hence, the improvement in creep properties of AZ91 alloy due to the alloying addition is attributed to the following reasons:

- Formation of thermally stable intermetallic, which pin the boundary against sliding
- Formation of more number of continuous precipitates thereby strengthen the grain boundary

4.6 CORROSION BEHAVIOR

Normally, the minor alloying additions such as Si, Sb, Sr, RE and etc., are carried out to improve the mechanical properties. However, these additions change the microstructure by introducing different intermetallics. From the literature, it is found that the corrosion behavior of AZ91 alloy is influenced by its microstructure. It is necessary and important to study the corrosion behavior of the alloying elements added AZ91 alloy. Corrosion test were carried out on the selected samples on each alloying additions. AZ91+0.5% Si, AZ91+0.5% Sb, AZ91+0.5% Sr and AZ91+0.5% Si+0.2% Sb samples were subjected to 100 h immersion test on 3.5% NaCl in solution and polarization and impedance test in ASTM 1348 (148 mg l^{-1} of Na_2SO_4, 138 mg l^{-1} of $NaHCO_3$ and 165 mg l^{-1} NaCl (pH≈8.3)) solution. Corrosion rate of all alloys is found out from the immersion test and its corrosion behavior is also derived from polarization and impedance test in ASTM 1348 solution.

4.6.1 Immersion Test

Figure 4.69 presents the effect of Si, Sb, Sr and combined addition of Si and Sb on the corrosion rate of AZ91D in 3.5% NaCl solution. The 100 h immersion test shows that alloying additions has different kind of influence on corrosion behavior of AZ91 alloy due to the difference in the microstructure. Individual addition of Si and Sr improve the corrosion resistance marginally. Substantial improvement in corrosion resistance is obtained for the combined addition of 0.5% Si and 0.2% Sb. The AZ91+0.5%Si+0.2%Sb alloy shows a corrosion rate of 155 mpy against the base alloy's value of 226 mpy. On the other hand Sb along added alloy shows slightly higher corrosion rate (262 mpy) compared to the base alloy.

4.6.2 Potentiodynamic Polarization Test

The polarization behavior of AZ91 alloy with and without alloying additions is presented in Figure 4.70. The polarization parameters measured from the polarization curves are listed in Table 4.14. The results show apparent changes in corrosion potential and corrosion current density of AZ91 alloy with alloying additions. All the alloying additions shift the corrosion potential more positive. At the same time, the corrosion current reduction is also noticed with Si, Sr additions.

Compared to individual addition of Si, combined addition of Si and Sb shifts the corrosion potential of base alloy more positive with less corrosion current. The corrosion potential shifts positive by 52 mV and corrosion current reduced by 2 X 10^{-6} A/cm^2. On the other hand, even though the corrosion potential is high with Sb added alloy, the corrosion current is also high, increased by 2.5X 10^{-6} A/cm^2, which indicates that the corrosion rate is high with Sb addition. These results are inline with the immersion test. From the cathodic region of the polarization curves (ref. Figure 4.70), it can be seen that at all the potential the cathodic current is high in case of Sb added alloy compared to other alloys, which suggests that the cathodic activity is high.

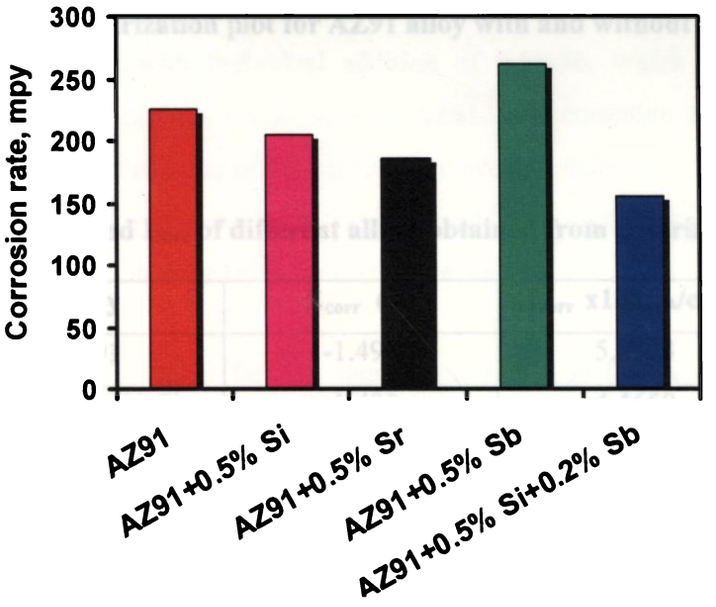

Figure 4.69: Corrosion rate of different alloys calculated from 100 h immersion test in 3.5% NaCl

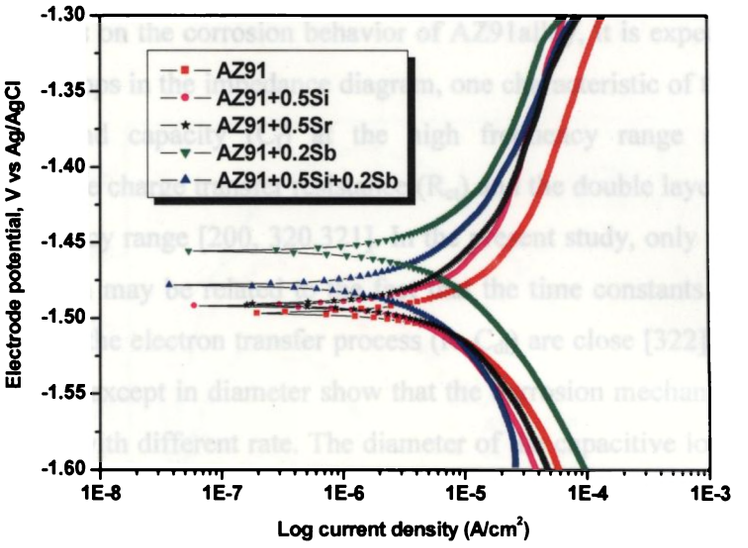

Figure 4.70: Polarization plot for AZ91 alloy with and without additions

Table 4.14: E_{corr} and I_{corr} of different alloys obtained from polarization curve

Alloy	E_{corr} (V)	I_{corr} x10^{-6}(A/cm^2)
AZ91	-1.497	5.8373
AZ91+0.5% Si	-1.490	4.4659
AZ91+0.5% Sr	-1.480	4.5827
AZ91+0.5% Sb	-1.445	7.369
AZ91+0.5% Si+0.2% Sb	-1.477	3.9276

4.6.3 Electrochemical Impedance Spectroscopy

Corrosion damage results from electrochemical reactions, so electrochemical measurement can often reveal the corrosion mechanism [220, 319]. Electrochemical impedance spectroscopy (EIS) is a useful technique in the study of corrosion. The simple electrochemical system consists of a double layer capacitance (C_{dl}), a solution resistance (R_s) and a charge-transfer resistance or polarization resistance (R_p) as shown in Figure 3.10. These electrochemical parameters obtained are summarized in

Table 4.15. The EIS results of AZ91 with and without alloying additions are presented in Figure 4.71 as Nyquist plot and Bode plot. The Nyquist plot given in Figure 4.71 (a) shows that all the alloys exhibit only one capacitive loop. According to previous studies on the corrosion behavior of AZ91alloy, it is expected to observe two semi-circle loops in the impedance diagram, one characteristic of the passive film resistance (R_f) and capacity (C_f) at the high frequency range and the other, characteristic of the charge transfer resistance (R_{ct}) and the double layer capacity (C_{dl}) in the low frequency range [200, 320,321]. In the present study, only one semi-circle is observed, which may be related to the fact that the time constants for the surface film (R_{Cf}) and for the electron transfer process ($R_{ct}C_{dl}$) are close [322]. Similarities in all EIS spectrums except in diameter show that the corrosion mechanism is same for all the alloys but with different rate. The diameter of the capacitive loop provides the corrosion rate [323]. The diameter of the capacitive loops of 0.5% Si and 0.5% Sr added alloy is almost same but slightly higher than the AZ91 base alloy, whereas it increases considerably with combined addition of Si and Sb. As expected lesser diameter is observed with individual addition of 0.5%Sb, which shows that Sb addition reduces the corrosion resistance of AZ91. The corrosion rate is inversely related to R_p. Higher the value of R_p, higher the corrosion resistance (lesser corrosion rate). Higher R_p value obtains with combined addition and lower value with Sb addition also reflects the alloy behavior during corrosion.

In general, C_{dl} value for the magnesium alloys is low and the reason is attributed to the formation of relatively thick and compact protective film on the metal surface [46, 324]. In this present investigation, it can also be seen that the increase in Rp value is not accompanied by a breakdown of the C_{dl} values, indeed the C_{dl} values are increase with increase in Rp values. Similar kind of observation has been made with La addition to AZ91 alloy by Yu Fan et al [46]. This shows that the alloys could not form an effective protective film in Cl environment. The Bode plot in Figure 4.71 (b) shows the low frequency impedance values of different alloys. Higher impedance value is noticed with individual addition of Si and Sr and combined addition of Si and Sb. Again, lesser impedance value noticed with Sb addition is matching with immersion and polarization test results.

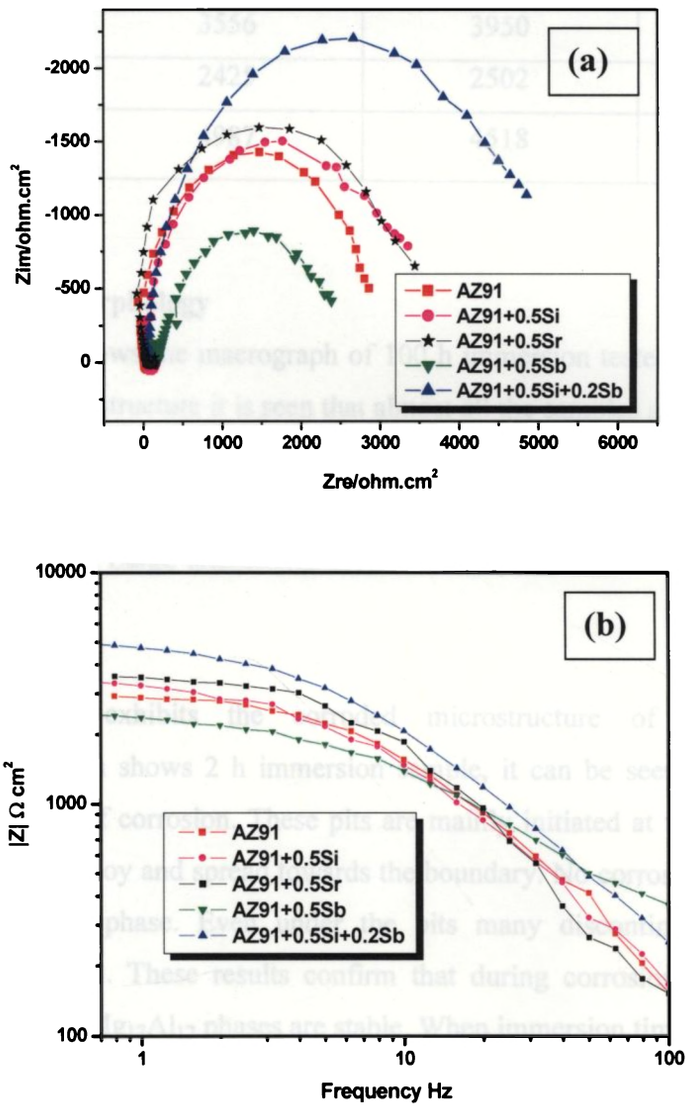

Figure 4.71: Electrochemical impedance spectroscopy measurements of different alloys (a) Nyquist plot (b) Bode plot

Table 4.15: Corrosion parameters obtain from EIS measurement for different alloys

Alloy	$\|Z\|$ ohm cm^2	R_p ohm cm^2	C_{dl} x10^{-6} μF/cm^2
AZ91	2910	3019	1.25
AZ91+0.5% Si	3450	3581	7.4
AZ91+0.5% Sr	3556	3950	7.2
AZ91+0.5% Sb	2425	2502	7.48
AZ91+0.5% Si+0.2% Sb	4987	4518	7.06

4.6.4 Corrosion Morphology

Figure 4.72 shows the macrograph of 100 h immersion tested samples in 3.5 NaCl. From the macrostructure it is seen that almost all the samples are similar due to the longer immersion time in aggressive Cl environment. However, it is noticed that the extent of corrosion in the Sb added alloy is more severe. The entire surface is attacked by corrosion. Large uncorroded areas are observed with combined addition of Si and Sb.

Figure 4.73 exhibits the corroded microstructure of AZ91. From Figure 4.73 (a), which shows 2 h immersion sample, it can be seen that the alloy exhibits pitting kind of corrosion. These pits are mainly initiated at the centre of α-Mg matrix of AZ91 alloy and spread towards the boundary. No corrosion is observed on the β $-Mg_{17}Al_{12}$ phase. Even under the pits many discontinuous $Mg_{17}Al_{12}$ intermetallics are seen. These results confirm that during corrosion process, both massive and lamellar $Mg_{17}Al_{12}$ phases are stable. When immersion time increases, the corrosion spread throughout the sample as seen from the figure 4.73 (b) which shows the corroded surface of 100 h immersed sample. Many massive eutectic and lamellar β $-Mg_{17}Al_{12}$ phases at the grain boundary are still appears intact at grain boundary. It is observed in the present study that all other intermetallics like Mg_2Si (both in Chinese script and polygonal), Mg_3Sb_2 and Al_4Sr are also stable even after 100 h exposure in the NaCl solution (ref. Figure 4.74).

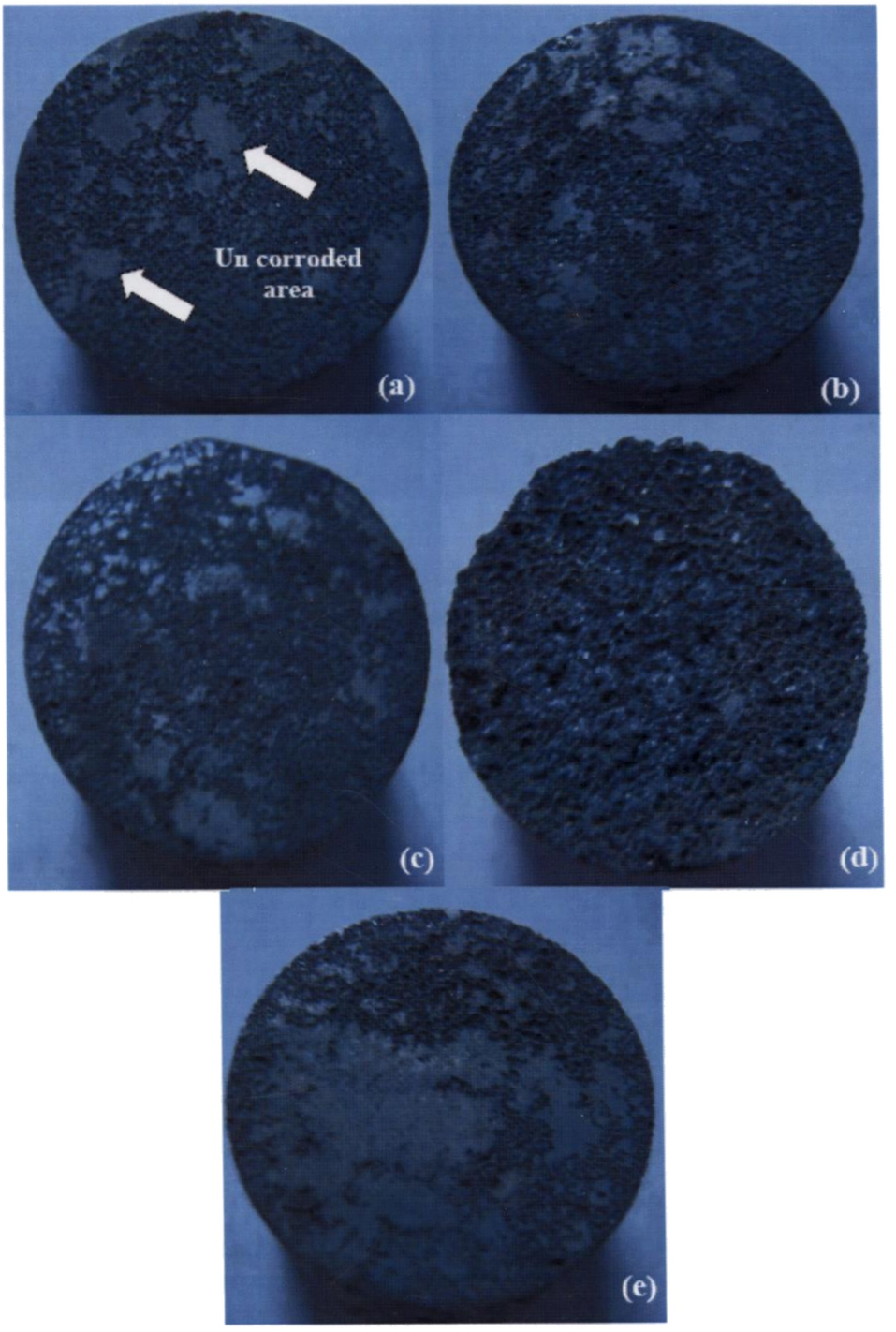

Figure 4.72: Photograph showing the macrostructure of corroded samples (a) AZ91 (b) AZ91+0.5% Si (c) AZ91+0.5% Sr (d) AZ91+0.5% Sb (e) AZ91+0.5% Si+0.2% Sb

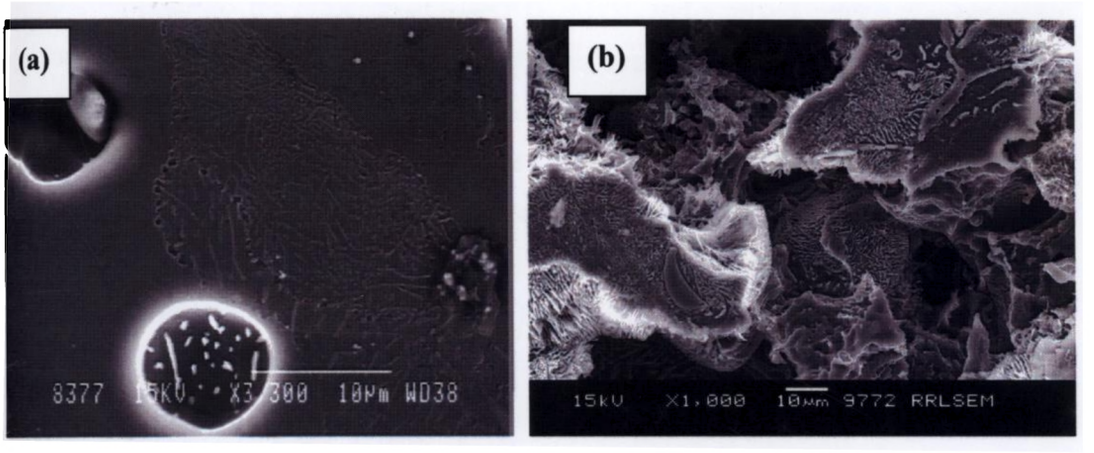

Figure 4.73: SEM photograph of immersion tested AZ91 alloy (a) 2 h immersed surface showing pitting type corrosion in the α-Mg matrix (b) 100 h immersed surface showing unaffected massive and discontinuous $Mg_{17}Al_{12}$ precipitates

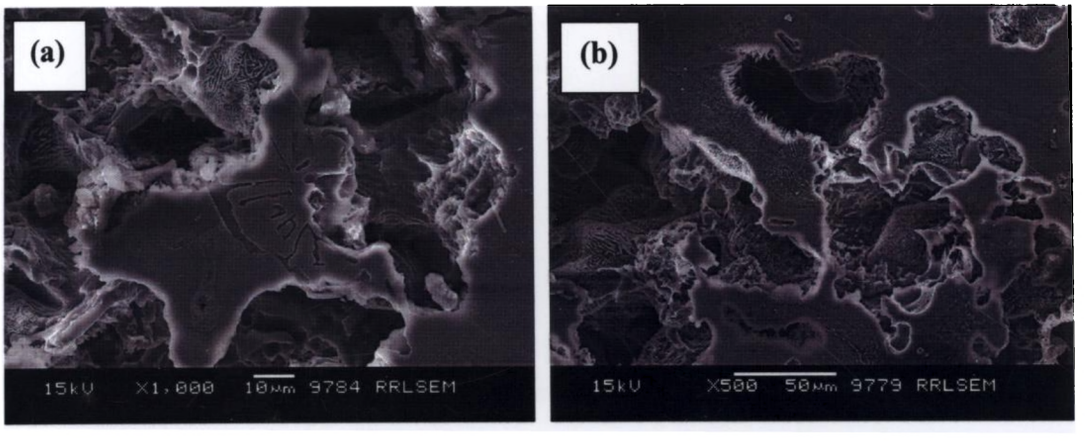

Figure 4.74: SEM photograph of different alloys immersion tested for 100h showing stable intermetallics (a) AZ91+0.5% Si alloy (b) AZ91+0.5%Sb alloy

4.6.5 XRD Analysis

XRD analysis was carried out on the corrosion product collected from immersion test conducted on various alloys and is presented in Figure 4.75. All the spectrums shows the presence of $Mg(OH)_2$, MgH_2 and a mixed oxides of magnesium and aluminum which has fallen from the surface. The JCPDS card shows that the $MgO:Al_2O_3$ ratio of this mixed oxide is 1:2.5 [325]. Similar kind of oxides is observed in previous study [36]. Some of the peaks for the intermetallics like β-$Mg_{17}Al_{12}$, Mg_2Si, Mg_3Sb_2 and Al_4Sr are also seen with respective alloys. This indicates that these intermetallics are stable in Cl environmental. During long exposure, due to the undermining of α-Mg matrix, these intermetallics are removed from the surface of the samples.

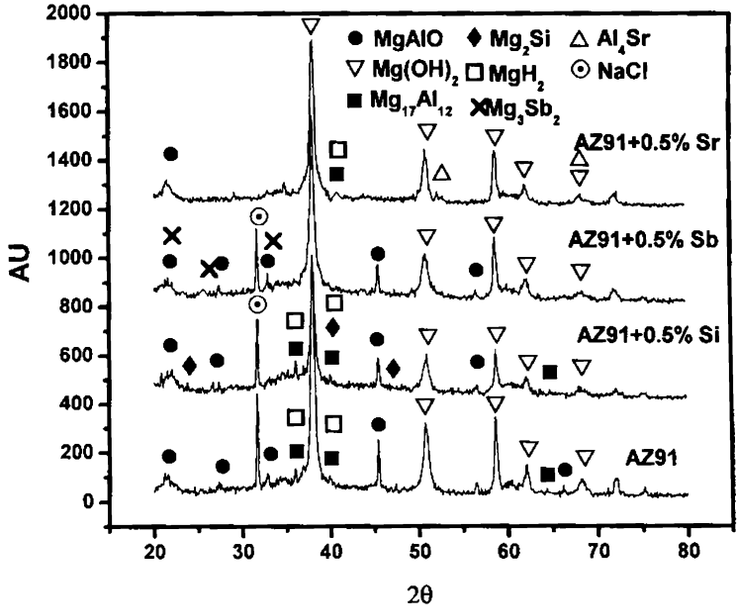

Figure 4.75: XRD patterns of particles collected from 100 h immersion test showing the presence of different oxides and intermetallics

4.6.6 Corrosion Mechanism

Presence of second phases have a pronounced influence on the corrosion of Mg alloys, because most of elements only affect the corrosion resistance of magnesium alloys after the formation of second phases [326]. The influence of microstructure constitutes on corrosion behavior of Mg-Al alloy is studied elaborately

by various authors and well documented in literature [36, 202, 208, 326, 327]. As discussed in chapter 4.1, the as cast microstructure of AZ91 alloy mainly consists of α-Mg matrix and β-$Mg_{17}Al_{12}$. This intermetallic is more corrosion resistant compared to α-Mg matrix due to the higher amount of Al in it. It is said that the β- $Mg_{17}Al_{12}$ intermetallic has a dual role in corrosion: effective barrier and active cathode to α- Mg matrix. It acts as an effective barrier when its volume fraction is high and inter-particle distance is not too large as like in die cast alloy. So the oxide film on the phase is continuous and hence the dissolution of α-phase is inhibited. On the other hand, if the β- phase is coarse and interparticle distance is very large, as like in gravity casting, the formation of networking is not possible. In this case the corrosion rate is increased by β- phase since it acts as a cathode with respect to less aluminium content α-Mg matrix. Moreover, undermining of β- phase occurred due to the corrosion of matrix near the phase [324].

Improvement in corrosion behavior of AZ91 alloy due to the alloying additions is reported in literature [46-50]. Elements like Ca and RE additions to Mg-Al alloys are beneficial to improve its corrosion behavior. The reasons attributed to such improvement are: (i) the added elements refine the β- phase and forms more continuous network, (ii) the added element suppresses the formation of β- phase by forming another intermetallic with Al which is less harmful to corroding α- Mg matrix, (iii) alloy elements may incorporate into the protective film and increase its stability.

In the present work, it can be seen from the microstructure that addition of Si to AZ91 alloy does not change the size and morphology of β- phase considerably. It is also seen that the addition of Si does not form any another component with Al but form a Chinese script Mg_2Si intermetallic at grain boundary and when it is added along with Sb, fine polygonal Mg_2Si which seems nobler than α- Mg matrix and behaves as a passive cathode. The E_{corr} for Mg and Mg_2Si are almost same (-1.65 V_{SCE}) [37]. Hence it is expected that Mg_2Si intermetallic does not have a detrimental effect on the corrosion resistance of AZ91 alloy. From the improved corrosion behaviour of combined addition over the individual addition of Si, it is understood

that the morphology and distribution of this phase has an influence on the corrosion behaviour. When the Mg_2Si precipitates in fine polygonal shape and distributed evenly along with $Mg_{17}Al_{12}$ at the grain boundary, it helps to form a continuous network which would help to inhibit the propagation of corrosion effectively from one grain to another grain and thereby improve the corrosion resistance greatly.

However, the improvement noticed with Sr added alloy is attributed to different reasons. Addition of Sr to AZ91 refines the grain as well as the β- phase and reduces the volume fraction of β- phase by forming Al_4Sr. It is well known that the β- phase is stable in NaCl solution due to the higher percentage of Al in it but act as an effective cathode to magnesium matrix in gravity castings. Hence replacement of this phase with less cathodic intermetallics improves the corrosion resistance of Mg-Al alloys. So, the intermetallic Al_4Sr plays very important role in corrosion improvement. This along with the refined β- phase provides effective protective thin layer on the surface.

It is seen that addition of Sb to AZ91 alloy does not change the size, morphology and volume fraction of β- $Mg_{17}Al_{12}$ intermetallic, rather it forms Mg_3Sb_2 intermetallic. From the figure and XRD analysis on the particle collected form the immersion test, it could be seen that Mg_3Sb_2 precipitates is also stable during corrosion process. However, the high corrosion rate observed with Sb addition in the present work indicates that the Mg_3Sb_2 phase seem to be an effective cathode along with β- $Mg_{17}Al_{12}$ to α- Mg matrix. This increases the number of galvanic sites and thereby increases the corrosion rate.

However, it is worth to mention that a detailed investigation particularly, the role of these elements on the surface film characteristics is needed to understand its role on corrosion behaviour of AZ91 which is included in the future coarse of study.

CHAPTER 5: CONCLUSIONS

In the present research work, individual and combined additions of Si, Sb and Sr to gravity cast AZ91 have been carried out. Their effects on the microstructure, ageing characteristics, tensile and creep properties and corrosion behaviour are studied. More emphasis has been given to the creep properties. Ageing treatment was carried out at 200°C. Tensile properties were evaluated both at room and high (150°C) temperatures. Creep testing has been carried out at 150 and 200°C. Initially all the alloys have been subjected to creep testing at 150°C for 500 h and selected alloys have been subjected to creep testing till fracture. Immersion test, polarization and impedance measurement are carried out on selected samples to study the effect of alloying additions on the corrosion behaviour of AZ91 alloy. This chapter summarizes all the major observations and the conclusions drawn from this study as well as highlights the significant contributions of this thesis to the existing knowledge. The avenues for future work are also identified.

1. The microstructure of the as cast AZ91 alloy consists of α-Mg solid solution, massive β-$Mg_{17}Al_{12}$ intermetallic and discontinuous precipitates of $Mg_{17}Al_{12}$ at the grain boundary.

2. Addition of 0.2% Si introduces Chinese script Mg_2Si intermetallic whereas 0.5% Si, addition leads to the formation of coarse Chinese script Mg_2Si in more volume. Si addition does not change the size and volume fraction of $Mg_{17}Al_{12}$ phase and it does not change the grain size much.

3. Addition of Sb combines with Mg to form needle/plate shaped Mg_3Sb_2 intermetallics at the grain boundary along with $Mg_{17}Al_{12}$ intermetallic. Significant grain refinement is noticed with 1%Sb addition. However, no change in volume and size of $Mg_{17}Al_{12}$ is observed with Sb addition.

4. Addition of 0.5% Sr leads to the formation of needle shaped Al_4Sr intermetallic at boundaries. Higher amount of Al_4Sr intermetallic is seen with 0.7% Sr addition. In the Sr added alloy, less amount of β- $Mg_{17}Al_{12}$ phase is noticed, which is due to consumption of more Al for the formation of Al_4Sr. In addition, refinement of grains is also noticed with Sr addition.

5. Addition 0.2% Sb to Si containing alloy has refined the coarse Chinese script Mg_2Si intermetallic into fine polygonal shaped particles and distributes it evenly. Moreover, 0.1%Sr addition also refines the Mg_2Si intermetallic but into a rectangular shape. Sb addition is found to be more effective in refining the Mg_2Si intermetallic compared to Sr addition. Grain refinement is also observed with both the combined additions. Addition Sb with Sr has suppressed the growth of Mg_2Si intermetallics during solidification and leads to the refinement

6. Solution treatment at 410°C for 48 h leads to complete dissolution of $Mg_{17}Al_{12}$ intermetallic in AZ91 alloy. During ageing at 200°C discontinuous precipitates are formed at the grain boundaries in the initial stage and later continuous precipitates are occurred in the remaining regions.

7. Even after 48 h of solution treatment, the intermetallic Mg_2Si, Mg_3Sb_2 and Al_4Sr are still appeared at the grain boundary. The coarse Chinese script Mg_2Si disintegrates into a fine round form. Dissolution of Sr into $Mg_{17}Al_{12}$ intermetallic increases its stability to certain extent and due to this still some of the $Mg_{17}Al_{12}$ particles are appeared after solution treatment.

8. Addition of Si and Sb suppresses the formation of discontinuous precipitates during ageing at 200°C whereas Sr addition slightly its volume. Higher hardness is observed with all alloying additions at all tempering conditions.

9. Individual addition of Si reduces the tensile properties, particularly the ductility, due to the presence of coarse Chinese script Mg_2Si intermetallic.

However, the addition of 0.5%Sb with 0.5%Sr increases the properties due to the presence of intermetallics and refinement of grains.

10. Higher percentage of Sb and Sr additions (0.7%) reduces the properties due to the presence of more volume fraction of needle shaped Mg_3Sb_2 and Al_4Sr intermetallics respectively, which acted as a stress raisers during loading.

11. With 0.2% Sb and 0.1% Sr, the AZ91+XSi (X= 0.2% and 0.5%) alloys exhibit improved tensile properties particularly the ductility due to the favorable morphological change of Mg_2Si intermetallic.

12. Improved high temperature (150°C) tensile properties are also noticed with alloying additions. As like at room temperature, higher percentage of additions leads to the reduction in properties.

13. The alloying additions greatly improve the creep properties of AZ91 alloy at 150°C whereas such improvement is not observed at 200°C. Addition of Si (0.2%, 0.5%), Sb (0.5%) and Sr (0.5%, 0.7%) improves the creep resistance of AZ91 alloy considerably at 150°C whereas 0.7% Sb additions reduce the creep properties. Among various additions, Sb addition has yielded higher creep properties.

14. Both AZ91+0.5% Si and AZ91+0.5% Si+0.2% Sb alloys exhibit similar creep behavior suggesting morphology of the Mg_2Si intermetallic (Chinese script and polygonal shape) does not have much effect on the creep properties.

15. Dynamic continuous precipitates from the supersaturated eutectic α-Mg solid solution occur during creep exposure. However, the additional intermetallics presented due to the alloying additions leads to the formation of more amounts of precipitates.

16. Cavity formation at the interface between the matrix and β-$Mg_{17}Al_{12}$ intermetallic due to the incompatibility between them and coarsening of continuous $Mg_{17}Al_{12}$ precipitates due to its low thermal stability are identified as the reasons for the poor creep resistance of AZ91 alloy.

17. The improvement in creep properties obtained due to the alloying additions is attributed to the presence of thermally stable intermetallics and more amounts of continuous precipitates, which effectively minimize the grain boundary damage.

18. Marginal improvement in corrosion resistance is noticed with Si and Sr additions whereas combined addition of Si and Sb improves its corrosion behavior significantly. In contrast, Sb addition alone reduces the corrosion resistance.

19. Both the morphology and distribution of Mg_2Si intermetallic have greater influence on the corrosion behavior of AZ91 alloy. Fine and evenly distributed polygonal shaped Mg_2Si intermetallic effectively inhibits the corrosion compared to the coarse Chinese script Mg_2Si.

20. The Mg_3Sb_2 intermetallic in Sb added alloy increases the cathodic activity and hence decreases the corrosion resistance of AZ91 alloy.

5.1 SIGNIFICANT CONTRIBUTIONS OF THE PRESENT INVESTIGATION TO THE KNOWLEDGE

1. A detailed post creep test microstructural analyses on AZ91 alloy with and without alloying additions has facilitated to understand the behavior of various intermetallics during creep.

2. Ca, P and Sb additions are carried out to modify the coarse Chinese script Mg_2Si intermetallic in gravity cast magnesium alloys. In the present work it is

found that Sr is also capable of modifying the morphology of Mg_2Si intermetallic.

3. It is well established that the Chinese script morphology of Mg_2Si intermetallic in magnesium alloys is detrimental to tensile properties. However, its effect on the creep properties is not known. Based on the results from the present investigation it is found that the Chinese script morphology effective in reducing the grain boundary movement during creep.

4. The improvement in the corrosion resistance of AZ91 alloy due to the addition of RE elements is well known. In the present study, the effect of Si, Sb and Sr additions on the corrosion behavior of AZ91 alloy are studied in detail.

5.2 AVENUES FOR FUTURE WORK

1. The idea adopted by various researchers in the process of developing new magnesium alloys for creep resistance is to reduce the aluminum content in order to reduce the volume of $Mg_{17}Al_{12}$ as well as by adding alloying elements, which introduce thermally stable intermetallics. Many alloy systems like Mg-2% Al-1% Si (AS21), Mg-4% Al-1% Si (AS41), Mg-4% Al-2% RE (AE42), Mg-5% Al-0.8% Ca, Mg-5% Al-1.2% Sr, etc., are developed based on this concept. In the present investigation, it is observed that the Sb addition is also capable of improving both tensile and creep properties of AZ91. Therefore it is worth to study the effect of Sb addition on the low Al (i.e., 3%, 6%, etc.,) containing Mg alloys to explore the possibility of developing cost effective high creep resistance magnesium alloys.

2. On the other hand the ill effect of Sb on corrosion resistance of magnesium alloys is also need to be investigated in detail to find out the possible remedy.

3. Long term creep testing need to be carried out to understand the strengthening mechanism due to Sr addition in AZ91 alloy

4. A detailed TEM study is required to understand the dislocation and creep mechanisms of AZ91 alloy with and without alloying additions

5. Detailed microstructural investigation and surface protective film characterization on the corroded sample of AZ91 alloy is needed to understand the role of alloying elements on the corrosion behavior.

REFERENCES

1. Luo: JOM, 2002, vol. 54, pp. 42-[illegible].
2. Javaid, E. Essadiqi, S. Bell and B. Davis: *Proc. Magnesium Technology 2006,* A. A. Luo, N. R. Neelameggham and R. S. Beals, eds., USA, March, 2006, pp. 7-[illegible].
3. Wilson, K. Clause, M. Earlam and J. Hillis: "*Magnesium and Magnesium alloys*", A Diges of useful Technical Data from Kirk-Othmer Encyclopedia of Chemical Technology, The International Magnesium Association, McLean, PA, USA, 1995, p.1.
4. M. Henstock: The Recycling of Non-Ferrous Metals, International Council on Metals and Environment, Ottawa, Ontario, Canada, 1966, p.213.
5. U.S. Geological Survey, "Magnesium-2004", Minerals Yearbook, 2004, 46.1-46.6
6. Katie Jereza, Ross Brindle, Steve Robison, John N. Hryn, David J. Weiss and Bruce M. Cox: *Proc. Magnesium Technology 2006,* A. A. Luo, N. R. Neelameggham and R. S. Beals, eds., USA, March, 2006, pp. 89-94.
7. Statecasts, Incorporated, AFS Metal casting Forecast and Trends 2005, American Foundry Society, Schaumburg, IL, 2004.
8. D. Eliezer, E. Aghion and F. H. Froes: *Proc. Magnesium 97*, E. Aghion and D. Eliezer eds., Dead Sea, Israel, Nov. 1997, pp.343-[illegible].
9. C. Sheldon Roberts: Magnesium and its alloys, John Wiley and Sons Inc., 1960, pp. 85-[illegible].
10. G. V. Raynor: The Physical Metallurgy of Magnesium and its Alloys, Pergamon press, New York, 1959, pp.-254-[illegible].
11. ASM metal hand book, vol.2, 10th edition, 1990, p457.
12. A.K. Dahle, D. H. St John and G. L. Dunlop, Materials Forum, 2000, vol. 24, pp. 167-[illegible].
13. Yeshuang Wang, Baode Sun, Qudong Wang, Yanping Zhu and Wenjiang Ding: Mater. Letters, 2002, vol. 53, pp. 35
14. Du Wenwen, Sun Yangshan, Min Xuegang, Xue Feng, Zhu Min and Wu Dengyun: Mater. Sci. Eng., 2003, vol. 356, pp. 1[illegible].

15. Per Bakke and Hakon Westengen: Adv. Eng. Mat., 2003, vol. 5, pp. 879.
16. Wole Soboyejo: Mechanical Properties of Engineering Materials, 2003, Marcel Dekker, Inc., chapter 15.8 (ISBN: 0-8247-8900-8).
17. A. Luo and M.O. Pekguleryuz: J. Mater. Sci., 1994, vol. 29, pp. 5259.
18. W.E. Marcer II: Technical Paper Series SAE Int. Congr. And Exp., SAE, Detroit, MI, 1990, paper no. 900788.
19. D.J. Sakkinen: Technical Paper Series SAE Int. Congr. And Exp., SAE, Detroit, MI, 1994, pp. 71
20. H. Gjestland, G. Nussbaum, G. Regazzoni, O. Lohne and Bauger: Mater. Sci. Eng., 1991, vol. A134, pp. 1197
21. T. K. Anue and H. Westengen: *Proc. Magnesium alloys and their application*, B. L. Mordike and F. Hehamann, eds., 1992, DGM Informationsgeselschaft m.b.H., pp. 221.
22. M. O. Pekguleryuz and M.M. Avedesian: J. Jpn. Inst. Light Met., 1992, vol. 42, pp. 679
23. M. O. Pekguleryuz, A. Luo, P. Vermette and M.M. Avedesian: *Pro. 50th Annual Meeting of IMA*, IMA, Washington, D.C., 1993, pp. 20.
24. T.K. Aune and T.L. Ruden: Technical Paper Series SAE Int. Congr. Exp. SAE, Detroit, MI, 1992, paper no. 920070.
25. C. Suman: Technical Paper Series SAE Int. Congr. Exp. SAE, 1991, Paper no. 91046.
26. L. Albright and T.K. Aune: Technical Paper Series SAE Int. Congr. Exp. SAE, Detroit, MI, 1991, Paper no. 910412.
27. K. Lovoid: Z Metalkd, 1976, vol. 67, pp 514
28. M.S. Dargusch, G.L. Dunlop and K.Pettersen: *Proc. Magnesium Alloys and Their Application,* B.L. Mordike and K.V. Kainer, eds., 1998, Wolfsburg, German, pp. 277.
29. M. Regev, E. Aghoin, A. Rosen and M. Bamberger: Metall. Trans. A, 2001, vol. 32A, pp. 1335.
30. W. Blum, B. Watzinger and P. Zhang: Adv. Eng. Mat, 2000, vol. 2, pp. 349

31. W. Blum, B. Watzinger and P. Weidinger: *Proc. Magnesium Alloys and Their Application,* B.L. Mordike, K.V. Kainer, eds., 1998, Wolfsburg, German, pp. 49
32. G. l. Maker and J. Kruger: Int. Mat. Rev., 1993, vol. 38, pp. 138
33. O. Lunder, J.E. Lein, T.Kr. Aune and K. Nisancioglu: Corrosion 1989, vol. 45, p. 741
34. G. Song, A. Atrens, D.St. John and L. Zheng: *Proc. Magnesium alloys and their applications,* K.U. Kainer, ed., Wiley-VCH, New York, NY, 2000, p.425.
35. G. Song, A. Atrens and M. Dargusch: Corrosion Science 1999, vol. 41, pp. 249
36. Rajan Ambat, Naing Naing Aung and W.Zhou: Corrosion Science, 2000, vol. 42, pp. 1433
37. G. Song and A. Atrens: Adv. Eng. Mat., 2003, vol. 5, pp. 837
38. A. A. Luo: Inter. Mater. Rev., 2004, vol. 49, pp. 13
39. E. Aghion, B. Bronfin, F. Von Buch, S. Schumann and H. Friedrich: JOM, 2003, Nov., pp. 30
40. Koray Ozturk, Yu Zhong, Alan A. Luo and Zi-Kui Liu: JOM 2003, Nov., pp. 40
41. Wang Qudong, Chen Wenzhou, Zeng Xiaoqin, Lu Yizhen, Ding Wenjiang, Zhu Yaping and Xu Xiaoping: J Mater. Sci., 2001, vol. 36, pp. 3035
42. Qudong Wang, Wenzhou Chen, Wenjiang Ding, Yanping Zhu and M.Mabuchi: Metall. Mater. Trans., 2001, vol. 32A, pp. 787
43. Yuan Guangyin, Sun Yangshan and Ding Wenjiang: Mater. Sci. Eng., 2001, vol. A308, pp. 38
44. Yuan Guangyin, Sun Yangshan and Zhang Weiming: J Mater Sci Let, 1999, vol.18, pp. 2055
45. Yizhen Lu, Qudong Wang, Xiaoqin Zeng, Wenjiange Ding, Chunquan Zhai and Yanping Zhu: Mat. Sci. Eng., 2000, vol. 278, pp. 66
46. Yu Fan, Guohua Wu, Hongtao Gao, Guanqun Li and Chunquan Zhai: J Mater. Sci., 2006 vol. 41, pp. 5409

47. Yu Fan, Guohua Wu and Chunquan Zhai: Mater. Sci. Eng., 2006, vol. A433, pp. 208-[illegible].
48. Guohua Wu, Yu Fan, Hongtao Gao, Chunquan Zhai and Yan Ping Zhu: Mater. Sci. Eng. 2005, vol. A408 pp. 255-[illegible].
49. Zhou Xuehua, Huang Yuanwei, Wei Zhongling, Chen Qiurong and Gan Fuxing: Corrosion Science, 2006, vol. 48, pp. 4223-[illegible].
50. F.Rosalbino, E. Angelini, S. De Negri, A. Saccone and S. Delfino: Intermetallics, 2005, vol. 13, pp. 55-[illegible].
51. Sarennah J. P. Longworth: M. S. Thesis, Cambridge University, August 2001.
52. S. Sugimoto: 53rd Annual Magnesium Congress, Ube City, Japan, 1996, p38
53. http://www.ford.com/servlet/ecmcs/ford/index
54. http://www.thenewsteel.com
55. P.D. Caton: *Proc. magnesium alloys and their applications*, May 1992, B.L. Mordike and F. Hehmann eds., Germany, 1992, p367.
56. Magnesium Electron Limited, Magnesium alloy database, MATUS Databases, Engineering Information Co. Ltd, 1992.
57. D. Eliezer, E. Aghion, and F.H. Froes: Advanced Performance Materials 1998, vol. 5, pp. 201-[illegible].
58. B. L. Mordike and T. Ebert: Mater. Sci. Eng., 2001, A302, pp. 37-[illegible].
59. E.F. Emley: Principle of Magnesium Technology, Pergamon press, First edition, 1966, pp. 218-[illegible].
60. ASM hand book, Volume-15, Casting, ASM International, 4th edition, 1998, pp. 798-[illegible].
61. Zeng Xiaoqin, Wang Quandang and Zhao Yhnhu: J Mater. Proc. Tech., 2001, vol. 112, pp. 17-[illegible].
62. Stephen. C. Erickson: Foundry Management &Technology, 1998, vol. 126, pp. 38-[illegible].
63. Zeng Yi-wen, Peng Li-ming, Mao Xie-min, Zeng Xiao-qin and Ding Wen-jiang: Mater. Sci. Forum, 2005, vol. 488-489, pp. 73-[illegible].
64. You Guoqiang, long Siyuan and Zha Jili: Mater. Sci. Forum, 2005, vol. 488-489, pp. 77-[illegible].
65. J. F. King: Magnesium Elektron Swinton, no. 3 (2003), p10.

66. M. O. Pekguleyuz: Mater. Sci. Forum, 2000, vol. 350-351, pp. 131 .
67. H. Friedrich and S. Schumann: J Mater Proc Tech, 2001, vol. 117, pp. 276 .
68. F. Czerwinski, A.Zielinska-Lipiec, P.J. Pinet and J. Overbeeke: Acta Materialia, 2001, vol. 49, pp. 1225 .
69. Y. Wang, G. Liu and Z. Fan: Acta Materialia, 2006, vol. 54, pp. 689 .
70. Z. Fan, G. Liu and Y. Wang: J Mater Sci, 2006, vol. 41, pp. 3631
71. Alfred Yu, Mohsen Masoumi, Naiyi Li and Henry Hu: *Proc. Magnesium Technology 2006*, A. A. Luo, N. R. Neelameggham and R. S. Beals eds., TMS 2006 Annual Meeting in Texas, USA, 2006, pp. 97 .
72. E. Cerri, P. Cavaliere, P. Leo and P. P. De Marco: *Proc. Magnesium Technology 2006*, A. A. Luo, N. R. Neelameggham and R. S. Beals eds., TMS 2006 Annual Meeting in Texas, USA, 2006, pp. 109
73. Li Xinggang, Xie Shuisheng, Jiang Yunxi and Li Lei: Mater. Forum, 2005, vols. 488-489, pp. 307 .
74. Yung Sen, Wang Wuxiao and Jiang Bailing: Mater. Forum, 2005, vols. 488-489, pp. 313 .
75. F. J. Edler, G. Lagrene and R. Siepe: *Proc. Magnesium and their application*, 2000, Wiley-VCH Verlag Gmbh, pp. 554 .
76. A. Srinivasan, U. T. S. Pillai and B. C. Pai: Int. J. Microstructure and Materials Properties, 2007, vol. 2, pp. 429
77. A. Srinivasan, U. T. S. Pillai,J. Swaminathan and B. C. Pai: Int. J Cast Metal Res, 2006, vol. 19, pp. 265 .
78. Polmear: *Proc. Magnesium Alloys And Their Application,* B.L. Mordike and F. Hehmann, ed.,1992, Garmisch-Partenkirchen, Germany, pp. 201
79. Smithells Light Metals hand book, E. A. Brandes, G. B. Brook, eds., Butterworth-Heinemann, 1998, p86 (ISBN 0 7506 3625 4)
80. Z. P. Luo, D. Y. Song and S. Q. Zhang: J Alloys and Compounds, 1995, vol. 230, pp. 109
81. M. Suzuki, H. Sato, K. Maruyama and H. Oikawa: Mater. Sci. Eng., 1998, vol. A 252, pp. 248

82. K. Maruyama, M. Suzuki and H. Sato: Met. Trans A, 2002, vol. 33, pp. 875

83. P. Abachi, A. Masoudi and K. Purazrang: Mater. Sci. Eng., 2006, vols. A435-439, pp. 653

84. G. Foerster: *Proc., 7th International Die casting Congress,* paper 9372, 1972, SDCE

85. B. R. Powell, V. Rezhets, M. Balogh and R. Waldo: *Proc. Magnesium technology 2001*, J. N. Hryn ed., warrendale, PA, TMS, 2001, pp. 175

86. H. J. Fuchs: UK Patent 847,992, published 1960.

87. M. O. Pekguleryuz and A. Luo: Patent Cooperative Treaty application WO 96/25529, 1996.

88. B. R. Powell, V. Rezhets, A. A. Luo, J. J. Bommarito and B. L. Tiwari: US Patent 6,264,763, 24 July 2001.

89. M. O. Pekguleryuz and E. Baril: *Proc. Magnesium Technology 2001*, J. N. Hryn ed., warrendale, PA, TMS, 2001, pp. 119

90. P. Labelle, M. O. Pekguleryuz, D. Argo, M. Dierks, T. Sparks and T. Waltmate: SAE Technical Paper 2001-01-0424, 2001, Warrendale, PA, Society of Automotive Engineers.

91. P. Labelle, M. O. Pekguleryuz, M. Lefebvre and R. Bouchard: SAE Technical Paper 2002-01-0079, 2002, Warrendale, PA, Society of Automotive Engineers.

92. E.F.Emley, "Principle of Magnesium Technology", Pergamon press, First edition, 1966, p925

93. M. O. Pekguleryuz, M. M. Avedesiaan and Sainte-Foy: *Proc. Magnesium alloys and their applications*, B.L. Mordike, F. Hehmann eds., April 1992, Germany, pp 213

94. Qin Hua, Deming Gao, Hongjun Zhang, Yuhui Zhang and Qijie Zhai: Mater. Sci. Eng., 2007, vol. 444, pp. 69

95. P. L. Schaffer, Y. C. Lee, A. K. Dahle: *Proc. Magnesium Technology 2001*, J. Hryn ed., The Minerals, Metals and Materials Society, pp.81

96. A. K. Dahle, Young C. Lee, mark D. Nave, Paul L. Schaffer and David H. St John: J Light Metal, 2001, vol. 1, pp. 61

97. O. Lunder, T. Kr. Aune and K. Nisancioglu: Corrosion, 1987, vol. 43, pp. 291 .

98. J. D. Hanawalt, C. E. Nelson and J. A. Peloubet: Trans. AIME, 1942, vol. 147, pp. 273

99. A. Luo: *Proc. 3rd International Magnesium Conference*, Manchester, UK, April 1996, pp449

100. M. D. Nave, A.K. Dahle and D.H. StJohn: *Proc. Magnesium technology 2000*, H. I. Kaplan, J.N. Hryn, B. B. Clow eds., The Minerals Metals and Materials Society (TMS), Warrendale, PA,USA, 2000, pp. 233

101. M. D. Nave, A.K. Dahle and D.H. StJohn: *Proc. Magnesium technology 2000*, H. I. Kaplan, J.N. Hryn, B. B. Clow eds., The Minerals Metals and Materials Society (TMS), Warrendale, PA,USA, 2000, pp. 243

102. I. G. Farbenindustrie: British Patent GB359,425, 1931.

103. C. E. Nelson: Trans. AFS, 1948, vol. 56, pp. 1

104. N. Tiner: AIME Tech. Pub., 1945, vol. 12, pp. 1

105. P. D. Webster, "Fundamentals of foundry technology", Redhill, Portcullis press, 1980, p190.

106. Y. Tamura, T. Haitani, E. Yano, T. Motegi, N. Kono and E. Sato: Mater. Trans. A, 2002, vol. 33A, pp.2784

107. E. F. Emley: Principle of Magnesium Technology, Pergamon Press, Oxford, United Kingdom, 1966, pp. 201

108. D. H. St John, Ma Qian, M. A. Easton, P.Cao and Z. Hildebrand: Mater. Trans. A, 2005, vol. 36A, 1669

109. R. T. Wood, The Foundryman, 1953, vol. 46, p98.

110. I. G. Farbenindustrie, Belgian patent, 444757, 1942.

111. G. B. Patridge, Production of magnesium technology, Oxford, Pergamon press, 1966, p203.

112. P. Cao, Ma Qian and D. H. StJohn: Scr. Mater., 2004, vol. 51, pp 125

113. R. Hultgren and D.W. Mitchell: Trans. AIME, 1945, vol. 161, pp. 323

114. A. Luo: Scr. Metall. Mater., 1994, vol. 31, pp. 1253

115. K. Achenbach, H. A. Nipper and E. Piwowarsky: Die Giesserei, 1939, vol. 26, pp. 597-604 and 621

116.C. H. Mahoney, A. L. Tarr and P. E. Le Grand: Trans. AIME, 1945, vol. 26, pp. 328

117.J. A. Davis, L. W. Eastwood and J. De Haven: Trans. AFS, 1945, vol. 53, pp. 352

118.M. Qian and P. Cao: Scr. Mater., 2005, vol. 52, pp. 415

119.Tammura Y Kono, T. Motegi and E. Sato: J Jpn Inst. Light Metals, 1998, vol. 48, p395.

120.T. Haitani, Y. Tamura, E. Yano, T. Motegi, N. Kono and E. Sato, J Jpn Inst. Light Metals, 2001, vol. 51, p403.

121.Y. Liu, X. Liu and B. Xiufang: Mater. Lett., 2004, vol. 58, pp. 1282

122.E. Yano, Y. Tamura, T. Motegi and E. Sato: J. Jpn. Inst. Light Met., 2001, vol. 51, pp. 594

123.Qinglin Jin, Jeong-Pil Eom, Su-Gun Lim, Won-Wook Park and Bong-Sun You: Scr. Mater., 2003, vol. 49, pp. 1129

124.D. O. Karlsen, D. Oymo, H. Westengen, P. M. D. Pinfold, and Stromhaug: *Proc. Light metals processing and applications,* 1993, pp. 397-408, Montreal, CIM.

125.T. Motegi, E. Yano, Y. Tamura and E. Sato: Mater. Sci. Forum, 2000, vols. 350-351, pp. 191

126.N. Ono, K. Nakamura and S. Miura: Mater. Sci. Forum, 2003, vols. 419-422, pp. 195

127.R. Dawalla, N. Coung and A. Stolnikov: *Proc. 6th Int. Conf. on Magnesium alloys and their application,* K. U. Kanier, ed., Wiley-VCH, Weinheim, 2004, pp. 803

128.R. K. Nadella, I. Samajdar and G. Gottstein: *Proc. 6th Int. Conf. on Magnesium alloys and their application,* K. U. Kanier, ed., Wiley-VCH, Weinheim, 2004, pp.1052

129.N. V. Ravi kumar, J. J. Blandin, C. Desrayaud, F. Monthellet and M. Suery: Mater. Sci. Eng., 2003, vol. A359, pp. 150

130.W. J. Kim and Y. K. Sa: Scr. Mater., 2006, vol. 54, pp. 1391

131.M.T. Perez-Prado, J.A. del. Valle and O.A. Ruano: Scr Mater, 2004, vol. 51, pp. 1093

132.M.T. Perez-Prado, J.A. del. Valle and O.A. Ruano: Scr Mater, 2005, vol. 59, pp. 3299

133. Q. Guo, H. G. Yan, Z. H. Chen and H. Zhang: Materials Characterization, 2007, vol. 58, pp.162

134.S.Celotto: Acta Meta, 2000, vol. 48, pp.1775

135.Clark J.B: Acta Meta, 1968, vol. 16 pp.141

136.J. Bettles, P. Humble and J. E. Nie: *Proc. 3rd International Magnesium Conference*, G. W. Lorimer, ed., Manchester, UK, 1996, pp. 403

137.A.F. crawley and K.S. Milliken: Acta Metall., 1974, vol. 22, p557.

138.A. F. Crawley and B. Lagowski: Metall. Trans., 1974, vol. 5, pp. 949

139.D. Duly, W. Z. Zhang and Audier: M., Phil. Mag. A, 1995, vol. 43, p187.

140.B. Lagowski and A. F. Crawley: Mater. Trans. A, 1976, vol. 7A, pp. 773

141.M. A. Gharghouri, G.C. Weatherly, J.D. Embury and J. Root: Phil. Mag. A, 1999, vol. 79, pp1671

142.Physical Metallurgy, Volume-II, Robert W. Cahn and Peter Hassen, eds., 4th edition, 1996, North-Holland publishers, p1451 (ISBN: 0 444 89875 1).

143.Marta Talach-Dumanska, Pawel Zieba, Andrzej Pawlowski, Joanna Wojewoda and Wolfgang Gust: Mater. Chem. Phy., 2003, vol. 80, pp. 476

144.I. Manna, S.K. Pabi and W. Gust, Int. Mat. Rev., 2001, vol. 46, pp. 53-91.

145.D. Bradai, M. Kadi-Hanifi, P. Zieba, W.M. Kuschke and W. Gust: J Mater. Sci., 1999, vol. 34, pp. 5331

146.D. Duly and Y. Brechet: Acta Metall. Mater., 1994, vol. 42, pp. 3035

147.D. Duly, M.C. Cheynet and Y. Brechet: Acta Metall. Mater. 1994, vol. 42, pp. 3843

148.K.N. Tu and D. Turnbull: Acta Metall, 1967, vol. 15, p1317.

149. K. N. Tu and D. Trunbull: Acta Metall., 1967, vol. 15, p369.

150. K. N. Tu, D. Trunbull: Metall. Trans., 1972, vol. 3, p2769.

151.G.R. Purdy and N. Lange, *Decomposition of alloys: the early stages*, P. Haasen et al, eds., Pergamon press, Oxford, 1984, p214.

152.R.A. Fournelle and J.B. Clark: Metall. Trans., 1972, vol. 3, p2757.

153.D. Duly, J. P. Simon and Y. Brechet: Acta Metall. Mater., 1995, vol. 43, pp. 101

154.M. Dargusch, M. Hisa, C.H. Cacares and G.C. Dunlop: *Proc. of the Third International Magnesium Conference*, G.W. Lorimer, ed., 1996, Manchest, U.K., pp. 153

155.E. Aghion, N. Moscovitch and A. Arnon: Mater. Sci. Eng. A, 2007, vol. A447, pp. 341

156.Choong Do Lee: Mater. Sci. Eng. A, 2007, vol. 459, pp. 355

157.C. H. Caceres: Scr. Metall., 1995, vol. 32, pp. 1851

158.M. K. Surappa, E. Blank and J. C. Januet: Scr. Metall., 1986, vol. 20. pp. 1281

159.C. H. Caceres, B. I. Selling: Mater. Sci. Eng. A, 1996, vol. A220, pp. 109

160.A. M. Gokhale and G. R. Patel: Scr. Mater., 2005, vol. 52, pp. 237

161.S. Jayalakshmi, S. V. Kailas and S. Seshan: J Mater. Sci., 2003, vol. 38, pp. 1383

162.Koichi Ishikawa, Hiroyuki Watanabe and Toshiji Mukai: Mater. Lett., 2005, vol. 59, pp. 1511

163.R. Armstrong, I. Codd, R. M. Douthwaite and N. J. Petch: Phill. Mag., 1962, vol. 7, p45.

164.K. Kubota, M. Mabuchi and K. Higashi: J Mater. Sci., 1999, vol. 34, pp. 2255

165.T. Mohri, M. Mabuchi, N. Saito and M. Nakamura: Mater. Sci. Eng., 1999, vol. A257, p287.

166.M. Mabuchi, T. Asahina, H. Iwasaki and K. Higashi: Mater. Sci. Technol., 1997, vol. 13, p825.

167.Y. H. Wei, Q. D. Wang, Y. P. Zhu, W. J. Ding, Y. Chino and M. Mabuchi: Mater. Sci. Eng., 2003, vol. 360, pp. 107

168.M. Mabuchi, H. Iwasaki, K. Yanase and K. Higashi: Scr. Mater., 1997, vol. 36, pp. 681

169.K. Hiratsuka, A. Enomoto and T. Sasada: Wear, 1992, vol. 153, pp. 361

170.A. Alahelisten, F. Bergman, M. Olsson and S Hogmark: Wear, 1993, vol. 165, pp. 221

171.H. Chen and A.T. Alpas: Wear, 2000, vol. 246, pp.106

172.W.Q. Song, P. Bggs and M. Brandt: *Proc. Engineering Materials 2001*, 23-26 September 2001, Melbourne, pp. 78

173.D.S. Mehta, S.H. Masood and W.Q. Song: J. Mater. Proc. Technol., 2004, vols. 155-156, pp. 1526

174.Peter J. Blau and Matthew Walukas: Tribology International, 2000, vol. 33, pp. 573

175.Introduction to Creep: R. W. Evans and B. Wilshire: The Institute of Materials, London, 1993, p19.

176.M. O. Pekguleryuz and A. Arslan Kaya: Adv. Eng. Mater., 2003, vol. 5, pp. 866-

177.W. J. MCG. Tegart: Acta Metall., 1961, vol. 9, p614.

178.R. B. Jones and J. H. Harrris: *Proc. Joint International Conference on Creep*, London, 1963, The Institute of Mechanical Engineers, vol. 1, p1.

179.K. Milicka, J. Cadek and P. Ris: Acta Metall., 1970, vol. 18, p.1071.

180.J. G. Crossland and R. B. Jones: Mater. Sci., 1972, vol. 6, p162.

181.S. S. Vegarali and T. G. Landgon: Acta Metall., 1981, vol. 29, p1969.

182.A. R. Chaudhuri, N. J. Grant and J.T. Norton: Trans. AIME, 1953, vol. 197, p712.

183.M. Regev, E. Aghion and A. Rosen: Mater. Sci. Eng., 1997, vols. 234-236, pp. 123

184.W. Blum, P. Zhang, B. Watzinger, B.V. Grossmann and H.G. Haldenwanger: Mater. Sci. Eng., 2001, vols. A319-321, pp.735

185.Willum K. Miller: Metall. Trans. A, 1991, vol. 22A, pp. 873

186.M. S. Dargusch, G. L. Dunlop: *Proc. Materials 98*, Michael Ferry ed., Institute of Materials Engineering, Wollongong, Australia, 1998, p.579.

187.P. Zhang and W. Blum: Z. Metallkd., 2003, vol. 94, pp. 716

188.M. Regev, E. Aghion, A. Rosen and M. Bamberger: Mater. Sci. Eng. A252, 1998, pp. 6

189.M. Regev, M. Bamberger, A. Rosen and E. Aghion: *Proc. Magnesium Alloys and Their Application*, B.L. Mordike and K.V. Kainer, eds., 1998, Wolfsburg, German, pp. 283

190.A. Finkel, M. Regev, E. Aghion, M. Bamberger and A. Rosen: *Proc. Magnesium 97*, E. Aghion and D. Eliezer eds., November, 1997, Dead Sea, Israel, pp.121-

191. S. Spigarelli, M. Cabibo, E. Evangelista, M. Regev and A. Rosen: *Proc. 2nd International Conference in Magnesium Science and Technology*, E. Aghion and D. Eliezer eds., Feb. 2000, Dead Sea, Israel, 293

192.Corrosion Engineering: M. G. Fontana, 3rd edition, McGraw-Hill Book Company, 1986, pp. 294-

193.H. H. Uhlig and R. Winston Revie: "Corrosion and corrosion control", Chap.20: 1985, New York, Wiley publisher.

194.C. H. Brun, J. Pagetti and J. Talbot: Mem. Sci. Rev. Metall., 1976, vol. 73, pp. 659-

195.L. Whitby: "Corrosion resistance of metals and alloys", 2 edn, 1963, p169, New York, Reinhold.

196.O. Khaselev and J. Yahalom: Corrosion. Science, 1998, vol. 40, pp. 1149.

197.D. Daloz, P. Steinmetz and G. Michot: Corrosion, 1997, vol. 53, pp. 944.

198.T. J. Warner, N. A. Thorne, G. Nussbaum and W. M. Stobbs: Surf. Interf. Anal, 1992, vol. 19, p386.

199.F. Hehmann, R. G J. Edyvean, H. Jones and F. Sommer: *Proc. Int. Conf. on Powder Metallurgy Aerospace Materials*, Lucerne, Switzerland, November 2-4, 1987, p. 46 (Shrewsbury, UK: Metal Powder Report Publishing Services, 1987).

200.N. Pebere, C. Riera and F. Dabosi: Electrochemical Acta, 1990, vol. 35, pp. 555.

201.G. Song and A. Atrens: Adv. Eng. Mat., 1999, vol. 1, pp. 11

202.G. Song: Adv. Eng. Mat., 2005, vol. 7, pp. 563-586.

203.G. Song, A. Atrens, X. Wu and B. Zhang: Adv. Eng. Mat., 1998, vol. 40, pp. 1769-

204.M. R. Bothwell, H. P. Godard, W.B. Jepson and I.R. Kane: The corrosion of Light Metals, Wiley and Sons., New York, 1967.

205.R. Baboian and J.E. Hills: Corrosion tests and standard: application and interpretation, Rober Baboian, ed., ASTM Manual Series MNL 20, Philadelphia, 1995.

206.K.N. Reichek, K.J. Clark and J.E. Hillis: SAE Technical paper series, 850417, 1985.

207.C. Suman: SAE Trans. 1990, vol. 19, pp.849-

208.G. Song, A.l. Bowlers and David H. StJohn: Mater. Sci. Eng., 2004, vol. A366, pp. 74

209.R.K. Singh Raman: Metall. Mater. Trans. A, 2004, vol. 35A, pp. 2525

210.D. E. Bartak, B. E. Lemieux and E. R. Woolsey, US Patent: 5470664, 1995.

211.T. F. Barton, US Patent: 5792335, 1998.

212.T. F. Barton, J. A. Macculloch and P. N. Ross, US Patent: 6280598, 2001.

213.O. C. Fruchtnicht, US Patent: 3620939, 1971.

214.G. L. Marker and J. Kruger, Int. Mat. Rev., 1993, vol. 38, pp.138

215.M. Avedesin and H. Baker,eds: Magnesium and Magnesium alloys, ASM Specialty Handbook, ASM International, Materials Park, OH, 1999.

216.H. A. Evangelides: Metal Finishing, 1951, vol. 7, p56.

217.A. J. Zozulin, D. E. Bartak, Metal Finishing, 1994, vol. 92, pp. 39

218.Z. Shi, G. Song, and A. Atrens: Corrosion Science, 2005, vol. 47, pp. 2760-

219.S. Akavipat, E. B. Hale, C. E. Habermann and P. L. Hagans: Mater. Sci. Eng., 1984, vol. 69, pp. 311-

220.C. Padmavathi, J. K. Sarin Sunder, S. V. Joshi and K. Prasad Rao: Mater. Sci. Tech., 2006, vol. 22, pp. 583-

221.Yuan Guangyin, Qudong Wang and Wenjiang Ding: J Mater. Sci., 2002, vol. 37, pp. 127-

222.Kinji Hirai, Hidetoshi Somekawa, Yorinobu Takigawa and Kenji Higashi: Mater. Sci. Eng. A, 2005, vol. 403, pp. 276-

223.Peijie Li, Bin Tang and E. G. Kandalova: Mater. Lett., 2005, vol. 59, pp. 671-

224.Shuang-Shou Li, Bin Tang and Da-Ben Zeng: J Alloys and Compounds, 2007, vol. 437, pp. 317-

225.Xue Feng, Min Xuegang and Sun Yangshan: J Mater. Sci., 2006, vol. 41, pp. 4725-

226.Bin Tang, Shuang Shou Li, Xi Shu Wang and Da Ban Zeng Rong Wu: J Mater. Sci., 2005, vol. 40, pp. 2931-

227.A. Sanschagrin, R. Tremblay and R. Angers: Mater. Sci. Eng., 1996, vol. A220, pp. 69-

228.. I.J. Polmear, Mater. Sci. Tech., 1994, vol. 10, pp. 1

229. Y. Li, H. Jones: Mater. Sci. Tech., 1996, vol. 12, p81.

230. I.J. Polmear, Material Transaction JIM, 1996, vol. 37, p12.

231.S. Lee, S H Lee and D H Kim: Metall. Mater. Trans. A, 1998, vol. 29A, pp. 1221

232.G. Pettersen, H. Westengen, R. Hoter and O. Lohne: Mater. Sci. Eng., 1996, vol. A207, pp.115

233.W Qudong, Lu Yizhen, Z Xiaoqin, D Wenjiang, Z Yanping, Li Qinghua and Lan Jie: Mater. Sci. Eng., 1999, vol. A271, pp. 109-

234.Y Wang, Q Wang, C Ma, W Ding and Y Zhu: Mater. Sci. Eng., 2003, vol. A342, pp. 178-

235.O. Lunder and K. Nisancioglu: *Proc. Progress in the Understanding and Prevention of Corrosion*, J. M. Costa, A. D. Mercer eds., Vol. 2, The Institute of Materials, London, 1993, p1249.

236.W. E. Mercer and J. E. Hills: SAE Technical Paper No. 920073, 1992.

237.J. H. Nordlien, K. Nisancioglu, S. Ono and N. Masuko: J Electrochemical Society, 1997, vol. 144, p461.

238.G. Nussbaum, P. Bridot, T.J. Warner, G. Regazzoni and J. Charbonnier: *Proc. Magnesium Alloys and Their Applicaionts,* B. Mordike and F. Hehmann, eds., Garmisch-Partenkirchen, DGM Informationsgesellshaft, Oberursel, 1992, pp. 351-

239.Peng Zhao, Qudong Wang, Chunquan Zhai and Yanping Zhu: Mater. Sci. Eng., 2006, vol. 444, pp. 318-

240.Smithells Light Metals hand book, E. A. Brandes, G. B. Brook, eds., Butterworth-Heinemann, 1998, pp. 168- (ISBN 0 7506 3625 4).

241.R. M. Wang, A. Eliezer and E. Gutman: Mater. Sci. Engg. A, 2002, vol. A344, pp. 279- .

242.N. Ageew and G. Sachs: Z.Phys., 1930, vol. 66, pp. 293- .

243.N. Ageew, M. Hansen andG. Sachs, Z. Phys., 1930, vol. 66, pp.350- .

244.Jeong-Min Kim, Bong-Koo Park, Joong-Hwan Jun, Keesam Shin, Ki-Tae Kim and Woon-Jae Jung: Mater. Sci. Eng. A, 2007, vols. 449-451, pp. 326- .

245.M. D. Nave, A. K. Dahle and D. H. St. John: Int. J. Cast Met. Res., 13, 2000, pp. 1- .

246.H. Cao, M. Wessen: Met. Mater. Trans. A, 35A, 2004, pp. 309-

247. JCPDS File, V.1.30, 1997, Card No. 01-1128.

248.E.F.Emley, "Principle of Magnesium Technology", Pergamon press, First edition, 1966, p947

249.J. J. Kim, D. H. Kim, K. S. Shin and N. J. Kim: Scr. Mater., 1999, vol. 41, pp. 333- .

250.S. J. park, J. J. Kim, D. H. Kim, C. S. Shin and N. J. Kim: U. S. Patent 6,146,584. Nov. 17, 2000.

251.S. Beer, G. Frommeyer and E. Schmid: *Proc. Magneisum Alloys and Their Applications,* B. L. Mordike and F. Hehmann, eds., Frankfurt, , pp. 317

252.E.F.Emley, "Principle of Magnesium Technology", Pergamon press, First edition, 1966, p945

253.ASM hand book, Volume-3, Alloy phase diagram, ASM International, 1992, p2.283

254.M. Pekguleryuz and P. Labelle: US patent No. 6322644, Nov 27th , 2001.

255.D. Argo, M. O. Pekguleryuz, P. Labelle, M. Dierks, T. Sparks and T. Waltematte: *Proc. Magnesium Technology 2001*, J. Hryn, ed., TMS, New Orleans, March 2001, pp. 125- .

256.Bai Jing, Sun Yangshan, Xun Shan, Xue Feng and Zhu Tianbai: Mater. Sci. Eng., 2006, vol. A 419, pp. 181- .

257.M. O. Pekguleryuz and E. Baril: Mater. Trans., 2001, vol. 42, pp.1258-

258.E. Baril, P. Labelle and M. O. Pekguleryuz: JOM, 2003, vol. 55, pp. 34-

259.F. Czerwinski and A. Zielinska-Lipiec: Acta Materialia, 2005, vol. 53, pp. 3433-

260.P. Chartrand and A. D. Pelton: J Phase Equilibria, 1994, vol. 15, p591

261.C. B. Alcock and V. P. Itkin: Bull. Alloy Phase Diag., 1989, vol. 10, p624.

262.S. L. Couling: Met. Eng. Qtly, 1972, vol. 12, p7.

263.G. S. Foerster, *Proc. Conf. 33rd International Magnesium Association (IMA) Annual Meeting*, IMA, 1976, p35.

264.M. O. Pekguleryuz, A. Luo and C. Aliravci: *Proc. Light Metals Processing and Applications*, The Metallurgical Society of CIM, 1993, pp. 409-

265.M. S. Yoo, K.S. Shin and N.J. Kim: Mat tran A, 2004, vol. 35A, pp.1629-

266.G. Y. Yuan, Z. L. Liu, Q. D. Wang and W. J. Ding, Mater. Lett., 2002, vol. 56, pp. 53-

267.Lihua Liao, Xiuqing Zhang, Haowei Wang, Xianfeng Li and Naiheng Ma: J Alloys and Compounds, 2007, vol. 430, pp. 292-

268.B. Closset and J.E. Gruzleski, Metall. and Mater. Trans. A, 1982, vol. 13A, p945.

269.G.E. Byczynski and D.A. Cusinato, Int. J. Cast Metals Res., 2002, vol. 14, p315.

270.G. Petzow, Metallographic etching, 2nd edition, ASM International, materials Park, Ohio, 1999, 114-

271.M. Bamberger: Mater. Sci. Technol., 2001, vol. 17, pp.15-

272.Fox FA, Lardner E: J. Inst Met, 1945, vol. 71, pp. 1-

273.J. E. Hutt and D. H. St John: Mater. Sci. Technol, 1999, vol. 15, p495.

274.J. Hunt: Mater. Sci. Eng., 1984, vol. 65, pp. 75-

275.A. Luo: Can. Metall. Q., 1996,vol. 35, pp. 375-

276.Y. C. Lee, A. K. Dahle and D. H. St. John: *Proc. Magnesium Technology 2000,* H. I. Daplan, J. Hryn, B. Clow, eds., TMS, The Minerals, Metals & Materials Society, Warrendale, PA, 2000, pp. 211-

277.Y. C. Lee, A. K. Dahle and D. H. St. John: Metall. Mater. Trans. 2000, vol. A31, pp. 2895-

278. P. Zhang, B. Watzinger and W. Blum: Phys. Stat. Sol., 1999, vol. 175, pp. 481-

279.C. J. Bettles: Mater. Sci. Eng., 2003, vol. A348, pp. 280-

280.Emley: 'Principles of Magnesium Technology', Pergamon press, London, 1966, p. 945 and 947.

281.Y. Z. Lu, Q. D. Wang, X. Q. Zeng, Y. P. Zhu and W. J. Ding: Mat. Sci. Eng., 2001, vol. A301, pp. 255-

282.A. A. Nayeb-Hashemi and J. B. Clark: Bull. Alloy Phase Diagrams, 1984, vol. 5, p584.

283.X. G. Min, Y. S. Sun, W. W. Du and X. Feng: Dongnan Daxue Xuebao, 2002, vol. 32, pp. 409-414 (in Chinese).

284.X. G. Min, W. W. Du, X. Feng and Y. S. Sun: Chin. Sci. Bull., 2002, vol. 47, pp. 1082-

285.G. Nussbaum, P. Sainfort, G. Regazzoni and H. Gjesland: Scr. Metall., 1989, vol. 23, p1079.

286.Foseco Non-Ferrous Foundryman's hand book, John R. Brown, ed., 11th edition, Butterworth-Heinemann, p219.

287.L. Cizek, M. Greger, L. Pawlica, L. A. Dobrzanski and T. Tanski: J Mater. Process. Techn., 2004, vols. 157-158, pp. 466-

288.J.P. Zhou, D.S. Zhao, R.H. Wang, Z.F. Sun, J.B. Wang, J.N. Gui and O. Zheng, Materials Letters, 2007, vol. 61, pp. 4707-

289.C. J. Bettles and C. J. Rossouw: Micron, 2000, vol. 31, p651.

290.M. S. Sulonen: Acta Metall., 1964, vol. 12, pp. 749-

291.K. R. Lee, Y. J. Baik and D. N. Yoon: Acta Metall., 1987, vol. 35, pp. 2145-

292.M. Hillert: Acta Metall., 1982, vol. 30, pp. 1689-

293.K.T. Kashyap, C. Ramachandra, M. Sujatha and B. Chatterji: Bull. Mater. Sci. 2000, vol. 23, pp. 39-

294.A. Srinivasan, U.T.S. Pillai and B.C. Pai: Mater. Sci. Eng. A, 2007, vols. 452-453, pp. 87-

295.Yizhen Lu, Qudong Wang, Xiaoqin Zeng, Wenjiang Ding and Yanping Zhu: J. Mater. Sci. Let., 2001, vol. 20, pp. 397-

296.Practical hand book of Materials Science, Charles T. Lynch, ed., CRC. Press, 1989, p473 (ISBN: 0-8493-3702-X).

297.Robert S. Busk: Magnesium products design, International Magnesium Association, Marcel Dekker Inc., 1987, pp. 267-

298.E.M. Gutman: J Mater. Sci. Let., 1998, vol. 21, pp. 1787-

299.E.M. Gutman, Ya Unigovski, M. Levkovich, Z.Koren, E. Aghion and M. Dangur: Mater. Sci. and Eng. 1997, vols. A234-236, pp. 880-

300.C. H. Caceres, W. J. Poole, A. L. Bowles and C. J. Davidson: Mater. Sci. Eng., 2005, vol. 42, pp. 269-

301.G. Schindelbacher, R. Rosch: *Proc. Magnesium Alloys and Their Applications*, B. L. Mordike and K. U. Kainer, eds., Frankfurt, 1998, pp. 247-

302.W. P. Sequeira, G. L. Dunlop, M. T. Murray*: Proc. 3rd International Magnesium Conference*, G. W. Lorimer, ed., London, The Institute of Metals (London), 1997, pp. 63-

303.A. L. Bowles, T. J. Bastow, J. R. Griffiths, P. D. D. Rodrigo: *Proc. Magnesium Technology 2000*, H. I. Kaplan and J. Hryn, B. Clow, eds., Warrendale, PA, 2000, pp. 295-

304.A. Stich, H. G. Haldenwanger: *Proc. Magnesium 2000*, E. Aghion and D. Eliezer, eds., Dead Sea, MRI, 2000, pp. 27

305.Jayalakshmi, S.V. Kailas, S. Seshan, Composites part A, 2002, vol. 33, pp.1135-

306.E. Blank, M. Kaspar and M. Rappaz: *Proc. Strength of Metals and Alloys,* Vol. 1, Montreal, Canada, Pergamon Press Ltd., Oxford, UK, 1985, pp. 87

307.L. M. Brown and W. M. Stobbs: Phil. Mag., 1971, vol. 23, pp. 1185-

308.L. M. Brown and D. R. Clarke: Acta Metall., 1975, vol. 23, pp. 821

309.R. E. Smallman and R. J. Bishop: Metals and Materials: Science, Processes and Application, Butterworth-Heinemann Ltd., Oxford, UK, 1995, pp. 228-

310.George E. Dieter: Mechanical Metallurgy, 2nd ed., McGraw-Hill, New York, NY, 1976, pp. 218-

311.*Metal Handbook*, vol. 9, *Fractography and Atlas of Fractographs*, 8th ed., ASM, Metals Park, OH, 1974, pp. 64

312.L. Engel and H. Klinger, Translated by X. M. Meng, *An Atlas of Metal Damage*, Mechanical Publishing House, Beijing, 1990, pp. 30-31 (in Chinese).

313.Jing Bai, Yangshan Sun, Feng Xue, Shan Xue, Jing Qiang and Tianbai Zhu: J Alloys and Compounds, 2007, vol. 437, pp. 247

314.Yeon Jun Chung and Kwang Seon Shin:Proc. Magnesium Technology 2005, N.R. Neelameggam, H.I. Kalpan and B. R. Powell, eds., TMS, 2005, pp. 425

315.M. Regev, O. Botstein and A. Rosen: *Proc. Magnesium 2000, 2nd International Conference on Magnesium Science and Technology*, E. Aghion and D. Eliezer, eds., Dead Sea, Israel, 2000, pp. 301

316.Norbert Hort, Yuanding Huang and Karl Ulrich Kainer: Adv. Eng. Mater., 2006, vol. 8, pp. 235

317.C. J. Bettles and M. A. Gibson: Adv. Eng. Mater., 2003, vol. 5, pp. 859-865.

318.M.S. Dargusch, A.L. Bowles, K. Pettersen, P. Bakke and G.L. Dunlop: Mater. Trans., 2004, vol. 35A, pp. 1905

319.N. N. Aung and W. Zhu: J. Appl. Electrochem., 2002, vol. 32, pp.1397

320. G. Baril, C. Deslouis, N. Pebere: *Proc. Seventh symposium of electrochemical methods in corrosion research*, CD-Rom paper no. 007; 2000.

321.G. Baril, C. Blanc and N. Pebere: J Electrochem Soc, 2001, vol. 148, p489.

322.G. G. Kumar and N. Munichandraiah: J Solid State Electrochem, 2001, vol. 5, p8.

323.ASM hand book, Volume-13A, Corrosion, ASM International, 2003, pp. 453

324.R. Udhayan and D.P. Bhatt: J Power Sources, 1996, vol. 63, p103.

325.JCPDS File, V.1.30, 1997, Card No. 10-0238.

326.R. Ambat, N. N. Aung and W. Zhou: J App. Electro chemistry, 2000, vol. 30, pp. 865

327.S. Mathieu, C. Rapin, J. Steinmetz and P. Steinmetz: Corrosion Science, 2003, vol. 45, pp. 2741

PUBLICATIONS BASED ON THE PRESENT RESEARCH WORK

International Journals

1. "Microstructure and mechanical properties of Si and Sb added AZ91 magnesium alloy" **A. Srinivasan,** U. T. S.Pillai, and B. C. Pai, **Metallurgical and Materials Transaction A,** Vol 36A, No. 8, **2005**, 2235-2243.

2. "Observation of microstructural refinement in Mg-Al-Si alloys containing strontium", **A. Srinivasan,** U. T. S. Pillai, J. Swaminathan, S. K. Das and B. C. Pai, **Journal of Material Science,** Vol 41, **2006,** 6087-6089

3. "Modification of Mg_2Si precipitates in Si added AZ91 magnesium alloy", **A. Srinivasn,** U. T. S. Pillai and B. C. Pai, **AFS Transactions,** Vol. 114, **2006,** 737-746

4. "Combined addition of Si and Sb on the microstructure and creep properties of AZ91 magnesium alloy", **A. Srinivasan**, J. Swaminathan, U. T. S. Pillai, G. Krishna and B. C Pai, **Material Science and Engineering A** (in press)

5. "Effect of alloying additions on the corrosion behavior of AZ91 magnesium alloy', **A. Srinivasan**, S. Ningshen, U. Kamachi Mudali, U. T. S. Pillai, and B. C. Pai, **Intermetallics** , 15, **2007**, 1511-1517

6. "Effect of intermetallics on the creep behavior of AZ91 magnesium alloy" A. Srinivasan, J. Swaminathan, U.T.S. Pillai, G. Manoj and B.C. Pai, **Metallurgical and Materials Transaction A** (communicated)

National Journals

1. "Role of minor alloying addition to AZ91 magnesium alloy", N. Balasubramani, K. Raghukandan, U. T. S. Pillai, **A. Srinivasan** and B. C. Pai, **Indian Foundry Journal**, Vol 50, No.3, **2004**, 19-25.

2. "Magnesium cast alloys and its foundry practices" N. Balasubramani, **A. Srinivasan,** U. T. S. Pillai, K. Raghukandan and B. C. Pai, **Indian Foundry Journal,** Vol. 50, No. 10, **2004,** 30-35

3. "Creep behavior of Mg-Al alloys – An overview", G. Venkatesan, **A. Srinivasan,** K. Raghukandan, U. T. S. Pillai and B. C. Pai, **Indian Foundry Journal,** Vol. 51, No. 10, **2005,** 31-38.

4. "Improved mechanical properties and corrosion behaviour of AZ91 magnesium alloy for automotive applications", **A. Srinivasan**, U.T.S. Pillai, J. Swaminathan, S. Ningshen, U. Kamachi mudali and B.C. Pai, **Indian Foundry Journal**, vol. 53, No. 7, **2007,** 27-32

National/International Conference Presentation

1. "High temperature behavior of Pb and Sb added AZ91 alloy", **A. Srinivasan**, U. T. S. Pillai, S. G. K. Pillai, T. Soman and B. C. Pai, published and presented at **International Symposium on Research Scholars (ISRS-2004)**, Indian Institute of Technology, Chennai, Dec. 20 - 22, 2004.

2. "Fracture behavior of AZ91 magnesium alloy", **A. Srinivasan**, P. Prabahara rao, K. Sukumaran, U. T. S. Pillai, and B. C. Pai, presented at the Annual Technical Meeting of the Indian Institute of Metals **(NMD-ATM-2004)**, Trivandurm, India, Nov. 2004.

3. "Investigation on microstructure and mechanical properties of Si and Sb added AZ91 alloy", **A. Srinivasan**, J. Swaminathan, T. Soman, U. T. S. Pillai, and B. C. Pai, presented at the Annual Technical Meeting of the Indian Institute of Metals **(NMD-ATM-2004)**, Trivandurm, India, Nov. 2004.

4. "Studies on ageing behavior and mechanical properties of Sr added AZ91 alloy", **A. Srinivasan**, U. T. S. Pillai and B. C. Pai, published and presented in International Conference on Advanced Materials Design & Development **(ICAMDD)**, 14-16 Dec **2005**, Goa, India

5. "Improvement in creep properties of AZ91 Alloy by Pb addition", **A. Srinivasan**, J. Swaminathan, U. T. S. Pillai and B. C. Pai, presented at Annual Technical Meeting of the Indian Institute of Metals **(NMD-ATM-2005)**, IIT Madras, Chennai from 14-17 November 2005

6. "Effect of Si addition on microstructure and creep properties of AZ91 magnesium alloy", **A. Srinivasan,** J.Swaminathan, U. T. S. Pillai, Krishna Gugloth, Manoj Gunjan and B. C. Pai, presented at Annual Technical Meeting of the Indian Institute of Metals **(NMD-ATM- 2006),** Jamshedpur, India, Nov. 13-16, 2006

7. "Influence of alloying additions on microstructure, mechanical properties and corrosion behavior of AZ91 magnesium alloy", **A. Srinivasan,** S. Ningshen, J. Swaminathan, U. Kamachi Mudali, U. T. S. Pillai and B. C. Pai, presented at International conference on Recent Advances in Materials and Processing **(RAMP-2006)**, PSG Tech, Coimbatore, Dec.15-16, 2006

8. "Effect of intermetallics on the creep behavior of AZ91 magnesium alloy", A. Srinivasan, G. Manoj, U. T. S. Pillai, J. Swaminathan, G. Krishna and B. C. Pai, presented at National Conference on **Advance Material for Hostile Environments –Present Scenario and Future Prospects** held at Regional Research Laboratory, Trivandurm, 1-2 March, **2007**

ERRATUM

Page 3: Table 1.1	The expansion for the abbreviation of **RE** is **"Rear Earth "**
Page 57: Figure 2.26	The expansion for the abbreviation of **HSC is "Hot Crack Susceptibility Co-efficient"**
Page 5 : Para 2: Line 10	Corrosion starts from the centre of the **Grain**
Page 8: Para 2: Line 2	Magnesium density is **one forth of steel density**
Page 21: Para 2: Line 6	The yield strength increases with addition of Al whereas UTS increase up to 6% and **become less sensitive to Al addition.**
Page 22: Figure 2.5	% Elongation axis is made in Figure 2.5
Page 24: Para 1: Line 5	In a slow cooled alloy, when casting cools from eutectic to the room temperature, the solid **transformation** takes place, in which the highly super saturated eutectic Mg decompose into alternative layers of solute deployed Mg and $Mg_{17}Al_{12}$ phase
Page 29: Para 2: Line 5	Explained to the Examiner during Viva-Voce examination
Page 44: Para 1: Line 8	Explained to the Examiner during Viva-Voce examination
Page 45: Para 1: Line 4	Explained to the Examiner during Viva-Voce examination
Page 51: Figure 2.22 b	Arrow mark is made to show corrosion products
Page 64	The materials supplier is **"Exclusive Magnesium" Hyderabad, India**
Page 70	Explained to the Examiner during Viva-Voce examination
Page 77	Explained to the Examiner during Viva-Voce examination
Page 121 to 124	Explained to the Examiner during Viva-Voce examination

Page 125: Para 1	Explained to the Examiner during Viva-Voce examination
Page 133: Para 4: Line 7	Arrow mark is made on Figure 4.47 to indicate the cracks
Page 144: Para 1: Line 3	Explained to the Examiner during Viva-Voce examination
Page 145	Explained to the Examiner during Viva-Voce examination
Page 179 onwards	Correction is made on the respective pages